SILICON IN A ONE-DIMENSIONAL POROUS NANOTUBE STRUCTURE AND ITS EVALUATION AS DRUG DELIVERY VECTOR *IN VITRO*

by

NGUYEN TAN KHANH LE

Bachelor of Science, 2015
Texas Christian University
Fort Worth, TX, USA

Submitted to the Graduate Faculty of
College of Science and Engineering
Texas Christian University
in partial fulfillment of the requirements
for the degree of

Doctor of Philosophy

May 2021

ACKNOWLEDGEMENTS

Table of Contents

LIST OF FIGURES

xiii

xiv

LIST OF TABLES

Chapter I

Literature Review

1.1   Introduction

At the "Winter Meeting of the West" of the American Physical Society at Caltech in 1959, the general notion of "nanotechnology" was first introduced to the scientific community by the famous theoretical physicist, Richard Feynman, whose talk is often credited with initiating the idea that it is possible to manipulate materials at the nanoscale in conjunction with new size-dependent physiochemical properties.[1] While nanoscience has flourished for the past few decades, interestingly, these size-dependent properties have actually existed for thousands of years as evidenced by selected ancient artifacts remaining today.[2] To date, scientists have been able to trace the origins of the unique physical features of these materials. One of the most famous examples is the medieval church windows in the Altenberg Cathedral at Germany that display magnificent ruby red and deep yellow colors. Careful analyses revealed that the presence of gold and silver nanoparticles (NPs) embedded in the glass matrix are responsible for the red and yellow hues, respectively, of these elegant glass windows (Figure 1).[3] In contrast to bulk materials of the same composition, such unique features stem from metal particles with structural dimensions limited to the nanoscale.[2]
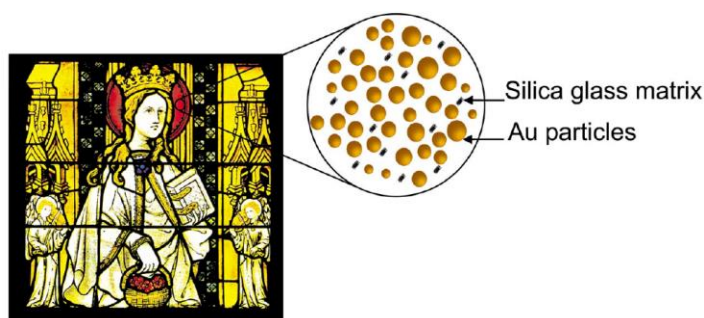
Figure 1. Nanoparticles utilized in a medieval church window in the Altenberg Cathedral (adapted from ref. 4).

To date, nanotechnology has played a prominent role in various aspects of our lives. With advances in characterization technology, particularly in high resolution microscopy, along with continuously growing knowledge of the physiochemical properties of nanoscale materials, an increasing number of studies and diverse applications, including energy and nanoelectronics, that involve nanomaterials has now been explored.[2, 5, 6] In terms of biomedical sciences, the emergence of nanotechnology has offered tools and methods to understand the complex behaviors of biological systems and therefore promote an interdisciplinary field, that is now referred to as nanomedicine.[2, 7]

With particular regard to drug delivery, nanotechnology has also contributed a remarkable evolution to the field by enabling treatments of several incurable diseases while alleviating adverse side effects that are largely stemmed from non-specificity of the free drugs.[8, 9]

For the past 30 years, a myriad of studies employing diverse nanoformulations have been presented in an attempt to address challenges encountered in multiple deleterious pathological diseases.[9-11] The first nanoformulation that received the Food and Drug Administration (FDA) approval was Doxil in 1995, which utilizes nanoscale liposomes modified with polyethylene glycol (PEG) to encapsulate and deliver the anti-cancer drug doxorubicin for treatment of ovarian cancer or AIDS-related Kaposi's sarcoma.[12] While organic-based delivery vectors, such as liposomes, have achieved exceptional results and many have even successfully obtained FDA approval,[13] inorganic nanoparticles (NPs) have recently emerged as appealing options owing to often simpler synthetic routes and the ease of scale-up production.[14-16] Since administered materials need to be eliminated from the body after completing their therapeutic functions, biodegradable NPs are invariably required.[17] Among the few inorganic NPs present today that are capable of resorption in biological media, porous silicon is an ideal delivery candidate for multiple diseases.[18]

In this chapter, the first section focuses on the role of inorganic NPs in nanotechnology with an emphasis on nanomedicine. The review describes some of the selected categories of NPs with fundamental properties relevant to therapeutic applications. Challenges in drug delivery regarding nanoparticle interactions with biological environments will be disscused along with future directions for effective clinical translation. The final section will focus on the fundamental aspects of biodegradable nanostructured porous silicon (pSi) with an emphasis on properties relevant to nanomedicine.

1.2   Inorganic Nanoparticles in Biology and Medicine

1.2.1   Compositions and Structures of Nanoparticles and Related Biological Applications

Compared to bulk counterparts, nanoscale particles possess a relatively high surface area along with size-dependent physiochemical properties. In particular, metallic NPs of gold (Au) and silver (Ag) offer a tunable color that can be varied by tuning the particle size owing to the surface plasmon resonance (SPR).[3] The surface charge built up from such interactions results in a restoring force that causes resonant density oscillation of electron charge at a specific frequency.[19, 20] When the particle size is within the nano regime, the absorption of light resulted from the SPR phenomenon falls within the visible region of the spectrum. As the particle size decreases, the absorption wavelength is blue shifted.[20]

Based on this unique SPR feature, a large number of immunoassays and biosensors employing AuNPs for detecting oligonucleotides and proteins with high sensitivity have been achieved.[21] Interestingly, in terms of therapeutics, owing to ability of colloidal Au NPs to absorb and scatter in the near infrared (NIR) region with a higher molar absorption coefficient compared with that of NIR absorbing fluorophores, the Au NPs can emit heat locally upon irradiation, thereby enhancing cell death by disrupting the cell membrane.[16, 22] An example of this is an

ultrathin Au nanoshell (surrounding a silica (SiO2) core) that enables enhanced optical contrast for bioimaging while effectively suppressing tumor growth *in vivo* via noninvasive external NIR irradiation (Figure 2).[23, 24] This novel technology has been commercialized by Nanospectra Sciences (Houston, Texas); clinical trials of prostate cancer treatment utilizing this approach are underway.[25]
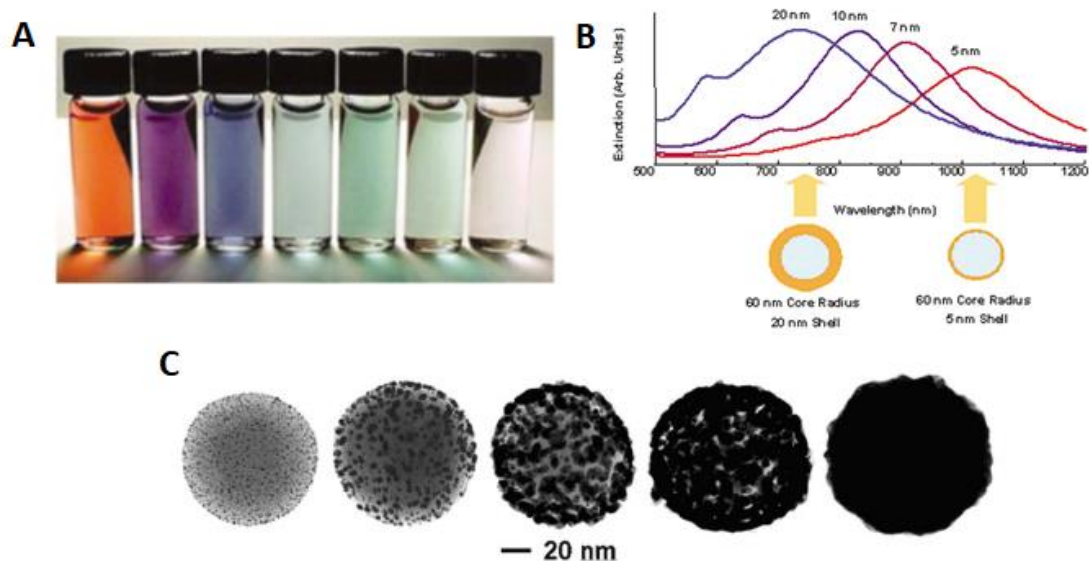
Figure 2. Gold-silica core shell structures: A) Tunable colors and B) Extinction spectra of the composites with different Au shell thickness; C) Transmission electron microscopic (TEM) imaging of SiO2-Au nanocomposites (adapted from ref. 26).

For tracking a given material after administration into a biological environment, the intrinsic size-dependent fluorescence properties stemming from quantum confinement of selected semiconductors, (so-called quantum dots (QDs)) offer the feasibility of monitoring the distribution of the NPs in real time.[27] Since the sizes of these dots are smaller than the exciton-Bohr radius (typically less than 10 nm), the band gap of QDs is inversely proportional to particle size ($1/R^2$). One can take advantage of tuning the size of QDs to achieve photoluminescence (PL) of specific energies (Figure 3A). To date, QDs have not only been one of the popular options for bioimaging

owing to tunable PL properties, but several promising therapeutic delivery options employing QDs also suggest potential merits of these materials in nanomedicine.[28, 29]

While UV light is normally used to excite QDs, the surrounding tissues and cells can potentially be damaged by this excitation source, thus posing legitimate concern in biosafety. On the other hand, a lower-energy NIR source that can penetrate deeper into the tissue and generate lower background signals, is an appealing safer choice for bioimaging.[30] In this manner, a unique class of lanthanide-doped materials, so called upconversion nanoparticles (UCNPs), that can efficiently convert two or more of the absorbed photons with a relatively low energy (i.e. NIR) into a higher-energy photon (i.e. visible or UV), have demonstrated exceptional potential in high-quality bioimaging and related-applications (Figure 3B).[31]
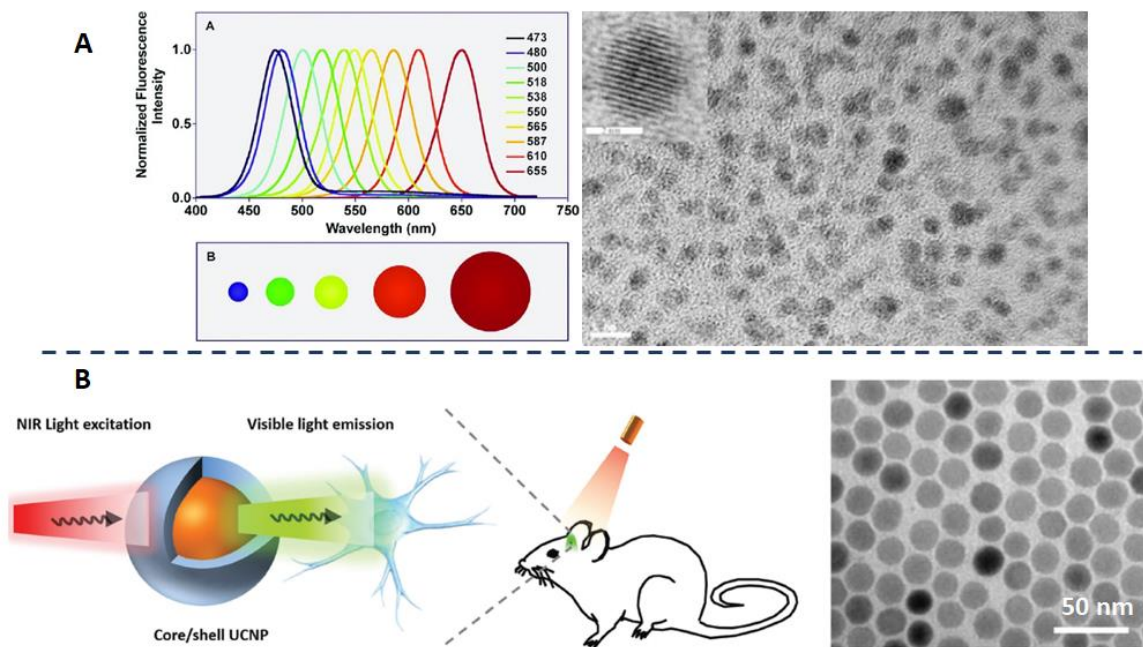
Figure 3. A) Emission spectra of QDs with various sizes and TEM imaging of CdTe/CdS/ZnS core/shell/shell QDs (adapted from ref. 32, 33) (scale bar: 2 nm) and B) Diagram showing conversion of NIR light to visible light and its application in stimulation of neurons and TEM imaging of NaYF$_4$:Yb/Er UCNPs (adapted from 34).

In addition to some of the selected examples of inorganic NPs presented above, a large number of other NPs with diverse compositions and unique properties, such as biocompatible superparamagnetic Fe_3O_4,[35] carbon-based NPs (e.g. carbon nanotubes)[36] and nanohybrids (e.g. alloys),[37] have been introduced. These nanomaterials have been shown to exhibit various distinctly unique physiochemical properties suitable for a broad range of bio-related applications, thereby suggesting a large library of inorganic NPs potentially available for nanomedicine.

In terms of nano-delivery, several studies to date have explored the advantages of employing inorganic-based NPs as robust delivery vectors to enhance bioavailability, pharmacokinetics and therapeutic efficacy of the free drug entities.[38] For instance, NPs endowed with a porous morphology (e.g. porous silica, SiO_2), have been exploited to efficiently entrap active species (e.g. biologics) inside the pores, and therefore, protect them from the external environment (Figure 4).[38] In addition, enhanced bioavailability of the insoluble crystalline drugs is also feasible due to nanoconfinement rendered by the small pore size of the matrix that effectively restrains the crystallization process and thus retain the amorphous form of the drug molecule.[39]

With the versatile surface chemistry of inorganic materials, a diverse range of molecular moieties endowing additional functions to the NPs can be readily grafted onto the particle surface.[40] A relevant example is utility of pH-sensitive linkers to deliver and facilitate drug release in a controlled-manner via cleavage of the linker as a response of changes in pH gradient within biological environments.[41] So far, several multifunctional particles have been demonstrated, and enhanced therapeutic efficacy in treatments of various disease models have been achieved in pre-clinical studies.[42, 43]
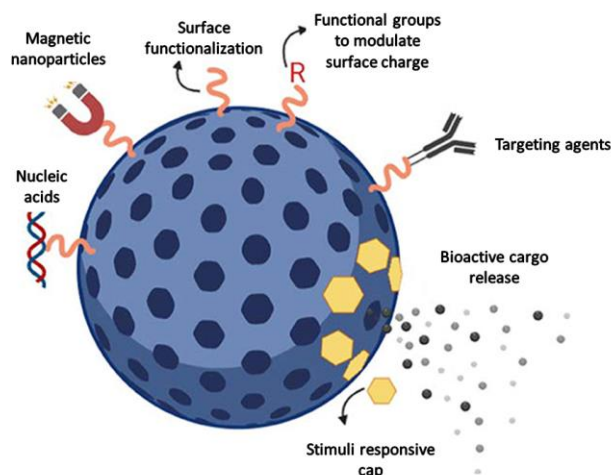
Figure 4. Schematic representation of various designs of mesoporous materials for drug delivery (adapted from ref. 44).

Unlike conventional organic-based nanocarriers, which face challenges in manufacturing scale-up along with limited shelf-life, inorganic NPs can be readily fabricated in a high quantity at low cost and exhibit high stability for a long period of time.[45] However, although many inorganic NPs (e.g. magnetic iron oxide) for biosensors and bioimaging are currently in clinical trials,[46-48] most inorganic-based nanomaterials envisioned for therapeutic delivery still remain in the pre-clinical stage of development owing to a large number of complex biological barriers.[49]

1.2.2 Biological Barriers in Drug Delivery

Multiple nanoparticle-based drug delivery platforms have demonstrated great therapeutic potential in pre-clinical studies.[50, 51] However, several nanotech-based delivery systems have failed to satisfy the stringent requirements for translation to human medical use. In particular regard to cancer therapy, which has been the focus of many delivery platforms, a recent analysis summarizing delivery efficiency of several therapeutic delivery systems in the literature for the past 10 years, suggested that only 0.7 % (median) of the injected dose of NPs can successfully reach the tumors.[49]

Such limitations are a consequence of multiple physiological barriers that NPs encounter upon systemic administration, thereby hampering delivery efficiency and clinical translation. These barriers to acquiring effective dosage at target sites (e.g. cancerous tumor) include: phagocytic sequestration and renal clearance, margination, extravasation from the blood vessels, cellular internalization and endosomal/lysosomal escape (Figure 5).[52]
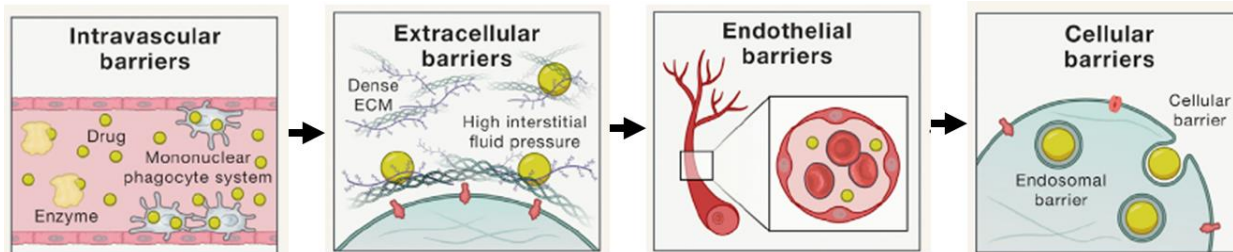
Figure 5. Biological barriers of drug delivery (adapted from ref. 53).

a) Clearance by Mononuclear Phagocytic and Renal Systems

In order for NPs to reach the pathological tissues after systemic administration, it is imperative that the nanoconstructs must be able to exhibit a sufficiently long circulation lifetime. Although NPs can readily be engineered with well-characterized physical and chemical properties (size, shape and surface chemistry), upon exposure to a dynamic extracellular environment, the presence of a protein corona (a layer of proteins adsorbed on NP surface) with composition dictated by cell conditioning (e.g. media and cell phenotype) and physiochemical features of the NPs creates a bioactive interface, which consequently determines cellular responses and circulation time in the blood stream.[54, 55] Such formation of a protein corona is not only detrimental to particle stability by alternating the surface charge but also hinders chemical reactivity of the moieties grafted onto the NP surface, hence significantly diminishing the functions originally designed for the construct.[56, 57] In addition, the protein corona also mediates sequestration of the NPs by the

mononuclear phagocytic system (MPS), which is responsible for engulfing and removing foreign substances (e.g. viruses and bacteria) from the host body as a part of its defense mechanism.[58, 59]

The physiochemical features of nanomaterials, particularly surface charge, have been shown to influence the likelihood of NP sequestration by MPS. Evaluation of circulation lifetimes of NPs as a function of the surface charges have indicated that positively charged NPs are more prone to be cleared from the body, whereas those possessing a slightly negative or neutral surface exhibit a relatively longer circulation lifetime and therefore have a higher chance of reaching the disease sites.[52] Based on this principle, recent FDA-approved lipid NPs for delivery of therapeutic small interfering RNA (siRNA), namely Onpattro, has been shown to exhibit remarkable delivery efficacy owing in part to the relatively neutral surface charge that ultimately inhibits nonspecific protein adsorption.[60]

In addition, surface modifiers are also involved in modulating the biological identity of the synthetic material. For instance, PEG molecules are among the most popular surface grafting agents that are capable of reducing non-specific protein binding via the formation of the hydrated shell around the NP core, thus camouflaging the nanoparticulate from systemic clearance recognized by the macrophages as well as extending circulation time in the bloodstream.[61] Since PEG is among a few polymers that have FDA approval owing to its biocompatibility and lack of immunogenicity, this surface functionalization is relevant to several types of NPs designed for drug delivery.[62]

Among the factors mentioned above, NP size is also one of the critical parameters that dictate systemic clearance of the NPs. Whereas NPs with a hydrodynamic diameter smaller than 5.5 nm are rapidly cleared out of the body through the renal (kidney) system, larger NPs are subjected to entrapment within the liver and spleen of the MPS.[49] Owing to the physiological

features of the liver, NPs are likely to be passively captured inside the liver sinusoid via extravasating through the gaps between the adjacent endothelial cells, so called endothelial fenestration, of the liver blood vessels.[63] The Kupffer cells, which are the macrophages of the liver, lining inside the capillaries readily take up the NPs by binding to the opsonins, such as immunoglobulins, adsorb onto the NP surface via the complementary receptors present on the cell membrane and therefore reduce the circulation half-life of NPs.[49, 56] Although the endothelial fenestration (5 μm) of the spleen is significantly larger than that of the liver (~ 100 nm), NPs are more likely to accumulate within the liver rather than the spleen owing to the significantly higher blood flow rate through the liver relative to that through the spleen.[64]

Thus, understanding of the biological systems responsible for reducing circulation lifetimes of the administered nanomaterials is imperative to rationally design NPs that can circumvent such rapid clearance.

b) Flow Dynamics of Nanoparticles in the Bloodstream

While *in vitro* studies commonly employ a static cell growth condition, NP *in vivo* studies are subjected to complex blood flow dynamics, thereby affecting margination (i.e. the movement of the NPs towards the endothelium and propensity to adhere to the vascular wall).[65] Such interactions with vessel wall are unequivocally desirable in drug delivery due to the need of extravasation of NPs from the blood vessel to accumulate within the pathological sites and efficient interactions with vascular biomarkers in the case of NPs decorated with targeting moieties, thereby influencing overall biodistribution of the materials.[65, 66]

In blood vessels, a variety of forces, such as gravity, van der Waals and hydrodynamic forces, act on NPs and influence their movement in the blood stream.[65] These forces, however, are highly dependent on the characteristics of NPs, such as size and geometry, and therefore determine

the overall outcomes of drug delivery.[66] Here, although the optimal size required for efficient margination varies depending on the experimental models and the characteristics of the blood vessels, it is generally observed that the relatively small NPs (less than 100 nm) are more likely to be trapped between the red blood cells (RBC) and move along with them in the center of the flow streamlines, therefore, it is more difficult for the NPs to escape from the flow and move towards the endothelium.[65] On the other hand, larger NPs (greater than 500 nm) exhibit a relatively higher margination degree, and gravity-driven margination also becomes more prominent at this size range (Figure 6A).[65]

As mentioned above, NP shapes are also involved in determining overall margination dynamics of the materials. In early studies, NPs were commonly synthesized in a spherical geometry which are inclined to flow parallel to and away from the blood vessels and therefore unlikely to marginate.[66] With advances in synthetic methodologies, a variety of non-spherical NPs with complex movements under fluid flow have been demonstrated in a number of models that mimic blood flow dynamics in the microcirculation.[67, 68]

In contrast to spherical NPs, the movements of the non-spherical counterparts are characterized with oscillation and tumbling owing to the non-uniform distribution of forces (i.e. lateral, longitudinal and torque) exerted by the blood flow on the particles (Figure 6A).[67, 69] Decuzzi and coworkers have indicated an increase in aspect ratio (AR) of NPs also increases lateral drift velocity, thereby favoring margination.[70] Thus, these NPs are more likely to transport across the vessel walls and thereby interact with the endothelial walls. In another careful study of the influence of NP geometry on margination dynamics using a parallel-plate flow chamber setup, Decuzzi and coworkers compare the flow patterns of porous silicon (pSi) particles (Section 1.3.1) in different shapes: discoid, quasi-hemisphere, and sphere.[67] As expected, different flow dynamics

associated with each particle shape observed with discoidal particles were more likely to move to the vessel walls (i.e. marginate) than the other shapes (Figure 6B). Although biological interactions of free-standing pSi-based nanorods or nanotubes have not been evaluated in a systematic manner, earlier studies have shown that Au nanorods exhibit favorable flow dynamics (i.e. more likely to marginate)[71]. Thus, compared with spherical NPs, non-spherical NPs exhibit higher contact points with endothelial cells, favoring tumor accumulation and promoting interactions between the vascular receptors and the ligands decorated on the NP surface (Figure 6B).
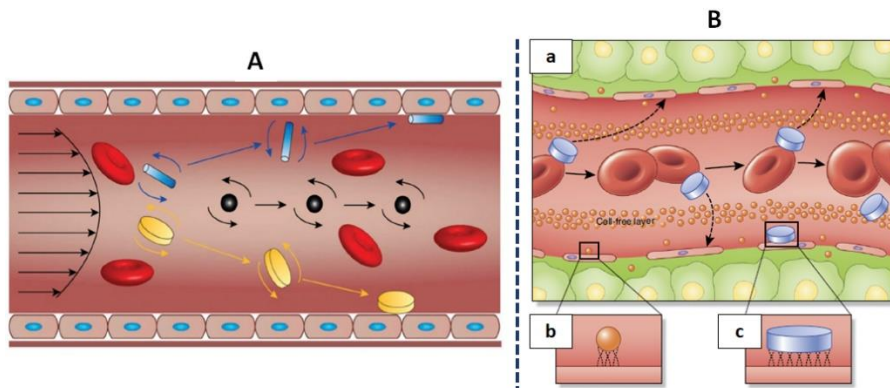
Figure 6. A) Flow dynamics of NPs of different shapes and sizes (adapted from ref. 66) B) a. Margination of particles in discoidal geometry and contact surface area of b. spherical and c. discoidal particles (adapted from ref. 72).

While the key physical characteristics of NPs described above dictate the transportation pattern within the blood stream and margination trends, other physiological conditions, such as the local concentration of RBCs and the shear rates, also significantly influence the flow dynamics of a given material.

c) Extravasation of Nanoparticles from the Blood Vessels

Upon systemic administration, NPs must be able to accumulate in the target sites to deliver therapeutic agents. This requires efficient extravasation of NPs from the blood vessels to the target

area. In normal vascular tissues, endothelial cells create a layer with tight junctions (~ 1 nm) that allow diffusion of certain small molecules, such as oxygen, salt and metabolic waste products.[49] On the other hand, in cancer, due to aggressive growth of tumor cells, additional blood vessels are produced to acquire more nutrition and oxygen. In contrast to normal blood vessels, these newly formed angiogenic vessels are highly disorganized and characterized with the inter-endothelial gaps (or fenestra) whose sizes are commonly within the range of 100-500 nm, present across the vessel wall that allow NPs of particular size range to extravasate through and into the pathological sites, such as the tumor interstitium (Figure 7A).[73] In addition, owing to dysfunctional lymphagiogenesis along with a high density of tumor cells that compresses the lymphatic vessel, lymphatic drainage is significantly impaired; therefore, NPs are highly retained in the interstitial fluid after extravasation (i.e. escaping) from the capillary vessels.[52] This phenomenon described herein was discovered by Maeda and Matsumura and is called enhanced permeability and retention (EPR) effect or passive targeting, which has been extensively exploited in cancer therapy to facilitate accumulation of NPs at the tumor sites.[56]

Although EPR is common in cancer, fenestrations (or pores) are also present on the blood vessel wall of inflamed tissues in heart diseases and infections.[64] As cells undergoing inflammation, they become contracted and therefore induce formation of pores on the capillaries (Figure 7B). In addition, some molecules, such as 56 kilodaltons protease secreted by *Serratia marcescens* pathogens, are also responsible for inducing fenestration in blood vessels, thereby facilitating vascular permeability.[74] However, it should be noted that in contrast to tumors, owing to a lack of aggressive cell growth, the lymphatic drainage system in inflammation and bacterial infections remains normal relative to that of the healthy tissues. Overall, such a unique EPR effect can be harnessed as a route to facilitate extravasation of NPs through the leaky endothelium.[64]
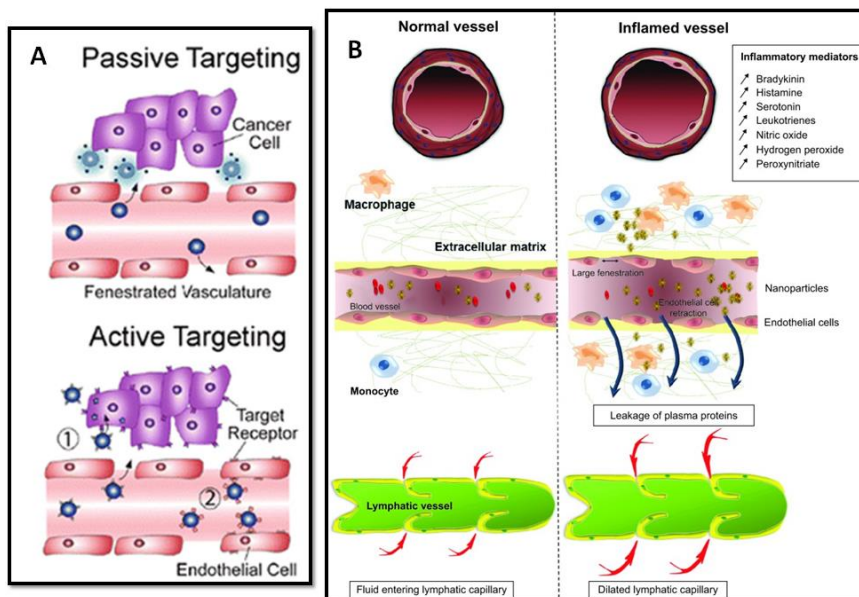
Figure 7. Fenestrations in blood vessel wall of A) cancer (adapted from ref. 75) and B) inflamed tissues (adapted from ref. 64).

Since pore size distribution and the degree of vascularization depend on the type of tumors as well as the stage of cancer,[52] delivery systems designed specifically for a particular cancer treatment is envisioned. However, due to heterogeneous distribution of the endothelial gaps on the blood vessel wall, non-uniform extravasation of NPs is typically observed, creating critical challenges in the passive (non-specific) targeting strategy.[49]

Since some organs of the MPS, such as the liver, also possess fenestration features as described previously, nonspecific accumulation of NPs in non-targeted organs and tissues is discerned as a challenging issue.[49] While NPs in passive targeting are only coated with stabilizing or antifouling agents, in active targeting, targeting moieties, such as ligands and antibodies, are decorated onto NPs, to specifically bind to the complementary species present on the target sites such as peritumoral area (i.e. area surrounding the tumor) or intracellular targets. In this fashion, compared to passive targeting that solely relies on EPR, active targeting has achieved a statistically higher delivery efficiency in cancer therapy owing to preferential accumulation at the target sites

15

and enhanced cellular uptake.[49] Nevertheless, formation of a protein corona mentioned previously also potentially compromises the targeting features by masking the these moieties, thus posing critical challenges that must be promptly addressed.

After extravasation, NPs are expected to distribute within the tumor tissues for subsequent cellular internalization. However, due to the heterogeneity of the tumor microenvironment (composed of stromal cells and diverse components of the extracellular matrices, such as collagen, proteoglycans and fibrin), a non-uniform distribution of drug-nanocarriers at the pathological sites is normally observed.[49, 76] Moreover, the movement of the vectors to the distal region (i.e. beyond the proximity of the blood vessel) is highly compromised owing to the abnormally high interstitial fluid pressure resulted from high proliferation rate of the cancer cells particularly in tumors, and therefore they are more likely to remain in the cell areas close to the blood vessels.[49] In order to mitigate such elevated pressure, some drugs (such as angiogenic and antifibrotic agents) have been utilized to facilitate diffusion of NPs by normalizing the blood pressure.[52]

d) Cellular Internalization

Upon accumulation in the pathological areas, drug carriers now must be able to transverse the cell membrane to release therapeutic agents inside the cells. Since the lipid bilayer of the cell membranes only permits diffusion of small, hydrophobic molecules, NPs are typically engulfed in membrane invagination and encapsulated inside cytoplasmic vesicles, so-called endosomes.[77]

Endocytosis consists of a variety of pathways that are specialized in internalizing different types of materials: clathrin-medicated endocytosis, caveolae-mediated endocytosis, pinocytosis and phagocytosis (Figure 8).[78] Upon internalizing inside the cell, the materials are typically subjected to an acidic and enzyme-rich environment of the lysosome, which is detrimental to the

stability of drugs and genetic materials. Therefore, NP designs that facilitate endosomal escape are of utmost necessity.

To date, two main endosomal escape pathways have been the mainstay of designing nanomaterials: flip-flop mechanism and proton sponge effect. In the flip-flop pathway, lipids and polymers with cationic components can interact with the negatively charged endosomal membrane, thereby triggering membrane flipping and facilitating material release.[79] Conversely, the proton sponge effect is observed with the materials containing a high density of protonatable amine groups that trigger an osmotic pressure imbalance inside the endosomes and therefore burst the vesicles.[80, 81]

Since surface chemistry dictates interactions with cell membrane, these functionalities are involved in mediating recruitment of protein components and molecules of endocytosis, thereby influencing the entry pathways. In this manner, surface functionalities involved in internalization routes that circumvent lysosome, such as caveolae-mediated endocytosis pathway, have been currently studied and integrated in NP designs to eschew complex endosomal escapes.[82]

In addition to challenges to ensure NPs can escape from or avoid the endosome and release therapeutic agents intracellularly, multidrug resistance stemming from drug efflux pumps and effective delivery of therapeutic species to the target cellular compartments (e.g. cytoplasm vs. nucleus) are also worthy of being emphasized in therapeutic delivery.[52]

Nature Reviews | Molecular Cell Biology
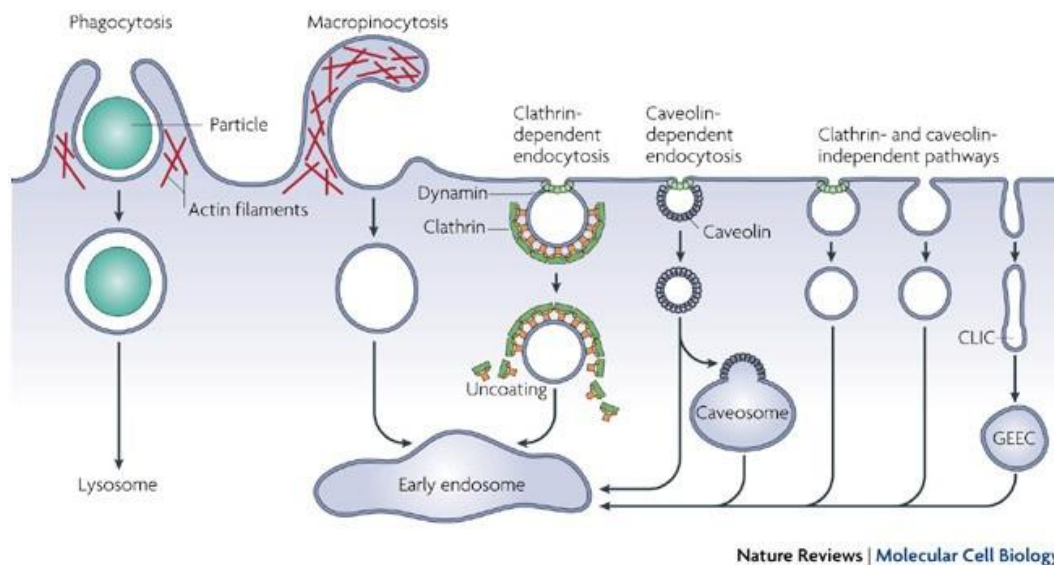
Figure 8. Pathways of cellular internalization of NPs (adapted from ref. 78).

All in all, the complex influences of biological environments on the performance of nanocarriers reinforce the notion that any NP design must address such fundamental challenges described above to guarantee robust performance of the vectors.

1.2.3 Influence of Nanoparticle Shape on Biological Functions

The shapes of NPs not only impact on flow dynamics of the vectors in the bloodstream but also play a dynamic role in cellular internalization, intracellular trafficking, as well as influencing various cellular pathways and functions.
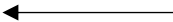
While surface chemistry of NPs along with cell phenotype determine the efficacy of NP internalization, the initial interface between NPs and cell membrane is a critical factor;[83] in other words, the wrapping time of the cell membrane around the particle required for initiating the uptake hinges on the local alignment of the particle on the cell membrane.[66]

Since non-spherical NPs exhibit diverse orientations relative to the cell surface along with different surface adhesion energies, various uptake outcomes are certainly expected.[84] For instance, considering the interactions between macrophages and NPs of different shapes (i.e.

18

spherical and cylindrical), a relatively longer wrapping time was observed in the case of cylindrical NPs interacting with cells via the major axis.[83] In addition, since a given nano-cell interface instigates the binding of the targeting moieties to the biomarkers expressed on the cell surface, internalization of NPs is regulated accordingly. Generally, a local contact area that generates a sufficient density of ligand-receptor sites is required for initiating the internalization process.[85] [52]

For non-spherical NPs, the aspect ratio (AR) (length : width) of NPs is involved in the outcomes of endocytosis. Considering macrophage uptake, since non-spherical NPs inhibit the formation of actin cups required for initiating phagocytosis, this type of structure is less likely to be internalized by the macrophages relative to the spherical counterparts (Figure 9A).[83, 86] Hence, this unique uptake behavior suggests non-spherical NPs are an appealing option to effectively preclude clearance by the macrophages.

Table 1. Influence of NP shape (SiO_2 NPs) to cell functions (A375 cells) (adapted from ref. 83).

Cell function	Order of Impact
Cellular uptake	LR ≫ SR ≫ > S
	←———————
	Increasing cellular uptake
Cell Cytoskeleton	LR ≫ SR = S
	←———————
	Increasing disorganization of F-actin
Cell adhesion and adhesion molecule expression	S ≫ > SR ≫ > LR
	←———————
	Increasing the number of cells adhered on the cell plates.
	——————→
	Decreasing melanoma cell adhesion molecule (MCAM) expression
Cell migration	S ≫ > SR ≫ > LR
	←———————
	Increasing migration
Cell viability and apoptosis	LR ≫ > SR = S
	←———————
	Increasing cytotoxicity and apoptosis

LR = long rods [AR = 4], S = short rods [AR = 2], S= spherical [AR = 1]

However, owing to the complex physiological conditions and physiochemical properties of NPs that collectively dictate nano-bio interfaces, there is no general consensus in cellular uptake patterns applied for all NPs as well as cell lines and disease models. For instance, whereas gold nanorods were shown to accumulate inside HeLa cervical cancer cells at a lower density than the spherical counterpart, a higher concentration of PEGylated silica nanorods with a relatively high AR was internalized compared with that of the spheres and the shorter nanorods.[83] Such drastic differences might be attributed to variation in surface chemistry, aggregation state, and hydrodynamic size of the materials in the biological media. Therefore, NP internalization should be carefully evaluated in the context of both cell phenotype and NP properties.

As indicated above, besides surface chemistry and size of NPs that collectively influence cellular functions, NP shapes also have diverse impacts on the integrity of the plasma membrane and multiple cellular functions, including cell migration, cytoskeleton, cellular spreading and cytotoxicity (e.g. SiO_2 NPs, Table 1).[83] In some studies, NPs with a high AR, such as nanowires (AR > 1000) were shown to readily pierce through and disrupt the cell membrane, thus potentially triggering unexpected consequences to overall cellular functions (Figure 9B).[87, 88] Given NPs with the same chemical composition but with different shapes, cellular structures and pathways are affected differently. For instance, while spherical SiO_2 NPs strongly affect cell migration, the SiO_2 nanorod structure causes more profound effects on the cytoskeleton.[89, 90] Thus, an understanding of the impact of a given NP design to overall cellular functions is needed to address any adverse pathological responses resulted from NP administration.
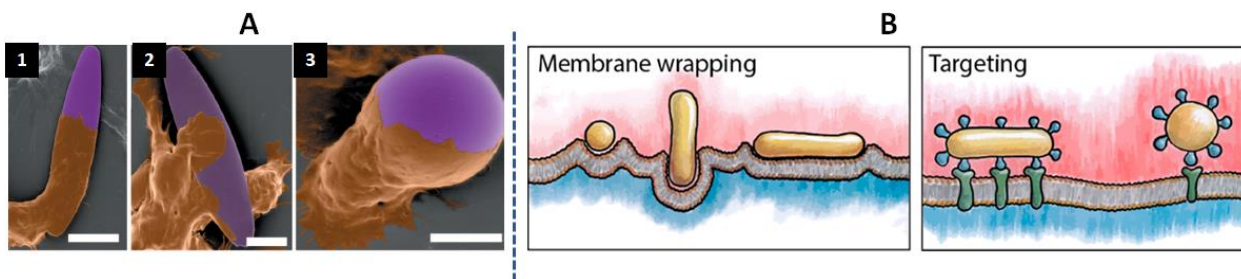
Figure 9. A) Macrophages internalizing polystyrene particles of different shapes (scale bar: 5 μm) (adapted from ref. 86) and B) Schematic illustrating interactions of NPs of various geometries with cell surface (adapted from ref. 91).

Upon internalization, intracellular distributions of NPs are also governed by NP shape probably owing to its influence on diffusion movement of the materials in the viscous cytoplasm. For instance, after cellular uptake, spherical poly(lactic-co-glycolic acid) (PLGA) NPs are more likely to accumulate closer to the nucleus than the elliptical discs counterpart.[92]

Since biodegradable materials are popular choices for drug delivery carriers, it is noteworthy to emphasize the impact of the degradation process to the structural dynamics of the materials. Here, as degradation proceeds, physiochemical properties of the platform also change accordingly, causing complications in determining the biological impact of the materials in a predicted manner.

Therefore, considering the involvement of shape in multiple complex cellular pathways and delivery efficacy, the concept "form follows function" must be the principle of NP design in nanomedicine, and understanding in structural characteristics of a given nanomaterial is imperative to evaluate downstream cellular pathways and ultimate functions *in vivo*.

1.3   Nanostructured Silicon

Bulk crystalline silicon has been the major element in electronic and photovoltaic industries; nevertheless, they are unfavorable for biomedicine largely due to a lack of dissolution

in biological-relevant environments.[93, 94] It was not until the 1990s when the unique biodegradation properties of Si particles with a nanoporous architecture was discovered by Professor Canham, thus paving a way to a new era of pSi-based nanomedicine.[18] Owing to tunable physiochemical properties of pSi and the bioinert degradation byproduct (i.e. orthosilicic acid, $Si(OH)_4$), there is a growing enthusiasm for employing this material to tackle multiple challenges in drug delivery as described above and therefore implying future clinical applications, which are currently limited to organic-based materials.[95, 96]

In this section, a brief overview of fabrication strategies of pSi commonly employed in biomedically-relevant studies and methods to control particle shape are presented. Next, a comprehensive review of several unique bio-relevant properties of pSi is presented, namely tunability of surface chemistry, biodegradation and biocompatibility, followed by some selected examples of nanocarriers based on pSi platforms with promising *in vitro* and *in vivo* results.

1.3.1 Pore Formation and Control of Silicon Particle Geometry

To date, porous silicon can be fabricated via a number of preparative routes.[97] However, to be able to control formation of porous architecture as well as achieve reproducible etching results, electrochemical etching method, in which Si is etched in an anodization cell in the presence of HF and a platinum cathode, is highly preferred and has been commonly employed by numerous research groups to fabricate pSi particles of defined porous structures.[98]

In anodic etching, the pore morphology is highly directional and perpendicular to the (100) crystal plane of the Si wafer. By controlling etching parameters as well as doping level of the Si wafer, a broad range of surface areas, pore sizes (abbreviated as d) and porous morphologies can be achieved. Typically, a dendritic porous structure is commonly observed in both micro ($d < 2$ nm) and mesoporous Si (2 nm $< d < 50$ nm), while a columnar architecture is normally associated

with the macropores (d > 50 nm).[99] Since porous structure of pSi determines drug loading capacity along with the release profile, such initial control of the porous architecture is imperative to capitalize on this etching strategy.

Similar to any NPs designed for drug delivery applications, tunability of particle size is also of utmost interest. For anodized-pSi, after etching, the film is lifted off and is subjected to ultrasonication and/or grinding to obtain micro and nano-sized particles.[100] However, this method normally yields a large size distribution and often requires additional ultrafiltration or centrifugation step to obtain the target particle size, such as submicron-pSi for therapeutic delivery, therefore inevitably lowering the yield (Figure 10A). To circumvent this issue, an alternative anodic etching-based strategy, namely electrochemical perforation etching, developed by the Sailor group, has been demonstrated to readily program the size via etching parameters without affecting the final yield of the product.[101]

In perforation method, high porosity (65 % porosity) layers of tens of nanometers, or so-called perforations, are created by periodic pulses of high current density (e.g. 400 mA.cm^{-2}) during the etching and separated by thicker primary layers with relatively lower porosity (42% porosity), whose thickness essentially determines the particle size (160-350 nm). Since the porosity of the perforation layer is relatively higher than that of the primary layer, they are prone to cleavage during ultrasonic fracture, thus precluding exhaustive ultrasonication step and yielding a more uniform size distribution. Since the target particle size can readily be achieved using this method without further ultrafiltration or centrifugation, a five times higher yield relative to the those prepared with no intervening perforated layers was obtained (Figure 10B).[101]
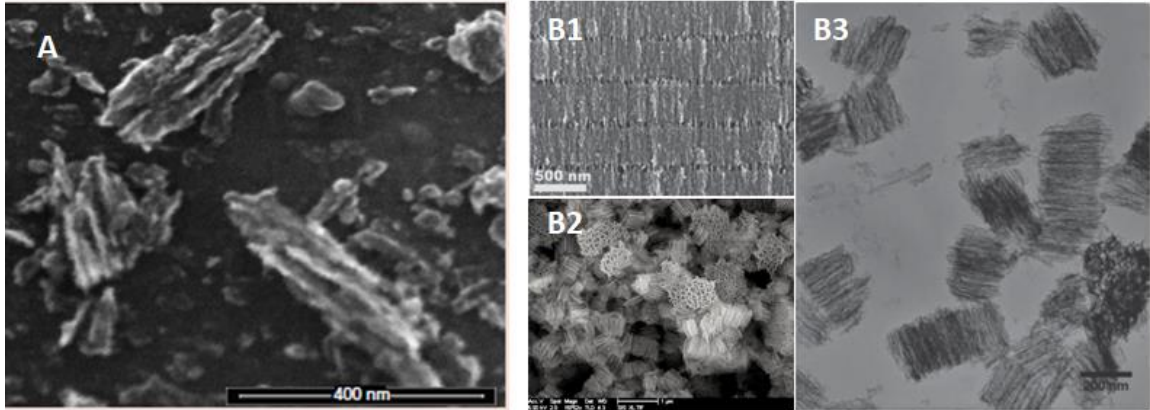
Figure 10. Anodized pSi A) after ultrasonication and size selection by centrifugation (adapted from ref. 102) and B) produced by perforation etching method: Scanning electron microscopic imaging showing perforation layers (B1) and particles after sonication (B2); TEM imaging showing high resolution of porous architectures (B3) (adapted from ref. 101).

Although anodic etching, including the perforation method, enables control of porous architecture along with particle size, irregular-shaped particles are typically produced. In the field of nanomedicine where the particle shape plays pivotal roles in various physiological interactions, particles with a well-defined geometry are therefore a desired target. Thus, this motivation has spurred investigations of a number of synthetic methods to sensitively manipulate the shapes of pSi particles, and in recent years, a number of pSi in remarkably controlled geometric shapes has been successfully fabricated via intricate synthetic routes.

To achieve well-defined NP geometry, one of the strategies in which photolithography employed prior to anodic etching is demonstrated, such that the final shapes of pSi particle are precisely controlled via the unit shapes created on lithographic patterns.[100, 103] In this manner, while the porous structure is readily achieved via electrochemical etching, this photolithographic route offers flexibility to obtain a large selection of micron and submicron-scaled pSi in various shapes: hemispheres and discoids along with tunable diameter, thickness and porosity (Figure 11A and

B).[100, 104] However, a main challenge of this strategy is poor yield that precludes it from practical clinical trials.

In contrast to the pSi shapes (typically 2 dimensional (2D)) presented thus far, one dimensional (1D) Si nanostructures, such as nanowires (NW) (AR > 1000), can also readily be achieved via a vapor-liquid-solid (VLS) method. Since Si nanowires typically possess a highly crystalline structure with a smooth surface morphology that results in a lack of favorable resorption in physiologically relevant environments, the range of applications of solid Si NW in nanomedicine is unfortunately limited.[87, 105] Alternatively, a novel strategy combining photolithography and metal-assisted chemical etching (MACE) has been employed to produce pSi in 1D nanoneedles (NND) form; therefore a high loading of therapeutic molecules in conjunction with favorable biodegradability and biocompatibility stemming from the porous structure can be achieved (Figure 11C).[106] While therapeutic loading in pSi NND is confined within the porous structure, an alternative 1D construct, namely nanotubes, offers additional encapsulation of the cargos inside a hollow structure, thereby ideally protecting the therapeutic species from the external environment.[107] In recent years, multiple synthetic routes have been demonstrated to produce a 1D nanotube structure of Si; further discussions of SiNT fabrication, along with associated therapeutic implications will be described in detail in the chapters that follow.
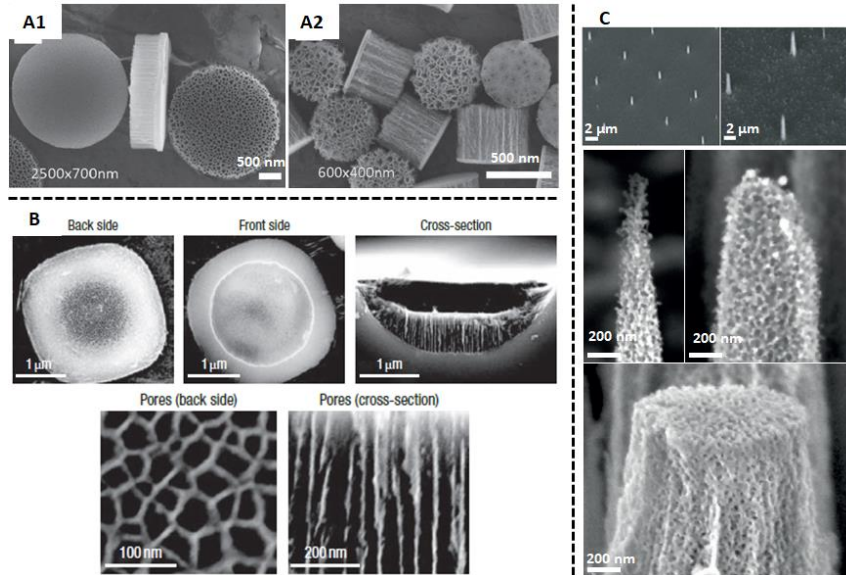
Figure 11. Porous silicon in various geometric shapes: A) Discoidal pSi (A1: 2500 x 700 nm, A2: 600 x 400 nm) (adapted from ref. 103) B) Hemispherical pSi (adapted from ref. 104) and C) Porous nanoneedles (adapted from ref. 108).

In general, while a vast variety of synthetic methods can be used to generate pSi of desired structures, depending on the target biomedical studies, the overall structure of pSi must be carefully controlled to achieve desirable delivery outcomes.

1.3.2 Surface Chemistry and Chemical Modification Strategies

The original surface chemistry of the as-prepared pSi is determined by the selected pSi fabrication method. In particular, fabrication methods involving electrochemical etching generally produce pSi with a native hydride-terminated surface, whereas chemical conversion of silica to silicon typically generates an outer oxide layer.[109] Since SiH_x species (x = 1-3) of the hydride-terminated pSi are strong reducing agents and susceptible towards oxidation in both ambient air and aqueous environments, this native surface creates complications in evaluation of the biofate of the materials in both *in vitro* and *in vivo* studies.[110] In addition, careful *in vitro* studies performed by the Voelcker group suggested cytotoxicity of the hydride-terminated pSi, particularly towards

human lens epithelial cells (SRA 01/04), owing in part to the presence of the reactive oxygen species generated from the material after exposure to cell culture medium. Hence, these observations emphasize the urgent need for surface modifications to enhance biocompatibility and stability of the material.[111]

Depending on the target applications, a suitable surface modification method is chosen to activate/passivate the surface of pSi, thus tuning degradation kinetics as well as endowing suitable surface functionality for further modification (or biological targeting). To date, several surface modifications, such as thermal oxidation (Figure 12A) and thermal hydrocarbonization, have been established to readily modify hydride-terminated pSi in a well-controlled manner and impart distinct hydrophobicity/hydrophilicity on the material depending on the surface functionality.[110] In particular, whereas freshly anodic etched pSi is hydrophobic, oxidized pSi is hydrophilic, thereby suggesting feasibility of integrating biologics and hydrophilic drugs to this platform.[110]

Considering surface functionalization of the oxidized pSi, organophosphonates functionalization and silanization have been commonly performed to endow additional functionality to the pSi matrix.[112] In the specific case of silanization, the silanol groups on the template are covalently bonded to the hydrolyzed anchoring moiety of the organo-alkoxysilane molecules via a condensation reaction, therefore creating a stable siloxane bond between the coupling agent and pSi surface (Figure 12B). Due to a large variety of the tail groups of the silane molecules, a variety of additional molecules of interest can be linked to the pSi template via the coupling agents. Among possible linkers, silane molecules with an amino group at the distal ends have been extensively utilized to extend surface functionality and conjugate with biomolecules of interest via either covalent bonds (e.g. PEGylation) or simple electrostatic interactions (e.g. nucleic

27

acids).[110, 113] Thus, such versatile surface functionality of pSi has significant implications in diverse bio-relevant applications.
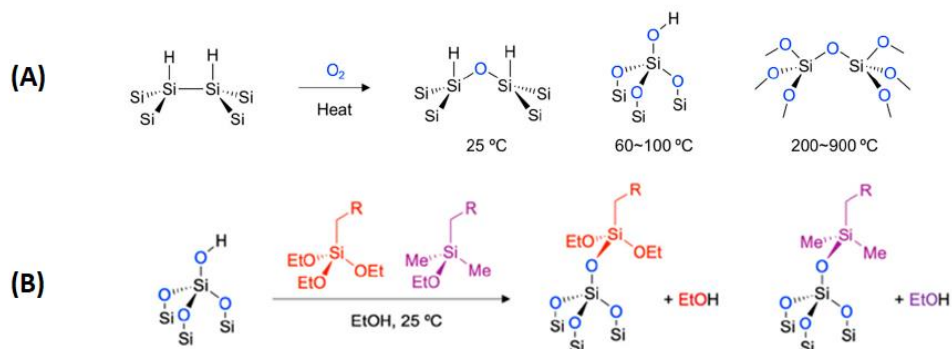
Figure 12. A) Surface oxidation of the hydride-terminated pSi and B) surface modification of the oxidized pSi via hydrolytic condensation with organo-alkoxysilane molecules (adapted from ref. 114)

1.3.3 Bio-relevant Properties

a) Dissolution of Porous Silicon

Accumulation of NPs in the body after administration for an extensive period of time can potentially trigger harmful pathological responses, such as inflammation. Thus, a drug delivery system capable of degrading and resorbing/excreting in a biocompatible manner to avoid invasive surgical removal procedure is an attractive option. The discovery of *in vitro* biodegradability of pSi in simulated body fluid (SBF) by Professor Canham in the mid 1990s and the follow-up *in vivo* studies demonstrating both biodegradability and biocompatibility of the material have remarkably inspired pSi-based nanomedicine.[18] Owing to the nanoarchitecture with a relatively high surface area, upon exposure to physiological media, pSi is readily resorbed via surface oxidation followed by hydrolysis of Si-Si bonds to release a non-toxic and soluble orthosilicic acid [$Si(OH)_4$], which is readily eliminated from the body via the renal system (Figure 13).[115] Interestingly, the $Si(OH)_4$ byproduct has not only been shown to be non-toxic to the body but also

benefit bone growth and collagen synthesis. Recent studies have also demonstrated the remarkable implications of $Si(OH)_4$ in combating Alzheimer's disease via reducing aluminum uptake.[116]
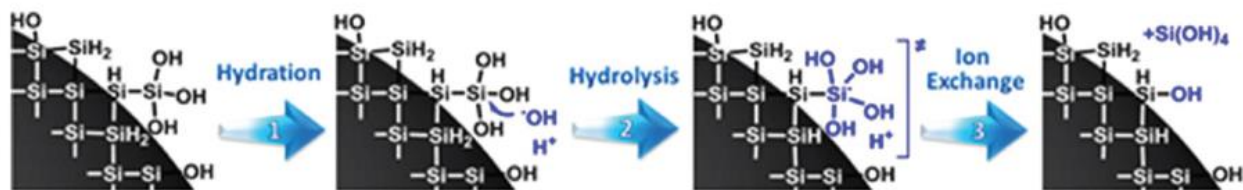
Figure 13. Dissolution mechanism of pSi (adapted from ref. 117).

Although pSi is a bioresorbable material, a fast degradation may decrease the half-life of the platform upon administration *in vivo* and thus diminish therapeutic efficiency of the system. For the past decade, a great number of studies have demonstrated the impact of pore size, surface functionality and Si skeletal dimension (or feature size) of pSi on its degradation kinetics.[115] Hence, by controlling these features, adequate dissolution rate can readily be obtained.

While a large selection of porous structures can be produced via tuning fabrication parameters, dissolution of pSi is generally accelerated as the surface area increases due to enhanced diffusion of the medium throughout the Si skeleton. In addition, owing to versatile surface chemistry, the degradation profile of a modified pSi also differs from that of the original material as a result of the impact of the surface functionality.[115] In particular, while hydride terminated pSi is susceptible to oxidation that leads to fast degradation rate, a passivation SiO_2 layer significantly slows down the dissolution. Also, modifying agents grafted on the pSi surface are also responsible for changing dissolution behavior of the material. For instance, for the case of commonly-employed PEG, the Ferrari group observed that pSi dissolution rate decreased as the molecular weight of PEG molecules increased, presumably attributed to the steric hindrance of the chain length of PEG molecules that inhibits diffusion of $Si(OH)_4$ dissolution byproducts from the pore, thereby reducing resorption rate.[118]

Besides those factors mentioned above, there are other physical features of pSi, such as particle size and crystallinity, which dictate dissolution rates and have been described thoroughly in several comprehensive reviews of pSi.[117] In general, owing to tunable dissolution properties of a given pSi architecture, there is a great utility in drug delivery where the platform is designed for delivery and cleared from the biological systems after completing its functions. Although it is generally assumed drug release is primarily facilitated by the dissolution of the platform, Tasciotti and co-workers suggested that drug release profile is also significantly influenced by the intrinsic chemical properties of the cargos (e.g. solubility and surface chemistry) and pore filling, which is primarily determined by the pore size. [119]

In addition, it is also worthwhile to point out that while dissolution kinetics of pSi can be readily tuned via fabrication conditions, complex biological environments, particularly *in vivo* conditions, composed of diverse biochemical species and different pH gradients also significantly affect the dissolution rate of a given material, and thus one can expect the degradation kinetics of a given material is varied as a result of biodistribution of the particles.[116, 120]

Thus, the interplay between cargos, platform structures and the biological environment in determination of the therapeutic outcome must be carefully considered rather than decoupling these components separately. Also, careful evaluation in both *in vitro* and *in vivo* studies are necessary to understand the biological dynamic behaviors of the materials prior to any clinical studies.

b) **Dissolution Patterns of pSi Particles in Well-defined Shapes**

As described in the previous section, a large selection of pSi in diverse geometrical shapes (i.e. hemispheres, discoids and nanoneedles) has been synthetically achieved to date and contributed to our understanding the biological outcome of the materials upon administration.

These well-defined structures not only elucidate the movement dynamics in the blood stream, but also provide information regarding evolution of the particle shape as the dissolution occurs, thus sensitively having an impact on drug release kinetics as well as biological interactions, that is challenging to obtain from irregularly shaped particles.

While the pore diameter of all the structures become larger over time as a result of decreasing wall thickness upon dissolution, the degradation patterns of each particle shape are drastically different. While the disc morphology becomes thinner as dissolution progresses (Figure 14A), the outer layer of the hemispheres is first subjected to dissolution followed by the central core and the final pore collapse (Figure 14B).[103, 119] On the other hand, for the nanoneedle structure, as the pore size increases as the degradation progresses, the defined needle structure eventually collapses owing to insufficient structural integrity, and only the solid stumps remain after 24 h (Figure 14C).[108]

Hence, by understanding the evolution of structural shapes upon dissolution, the impacts of the nanostructure on nano-bio interface can be thoroughly evaluated, especially with respect to delivery efficacy.
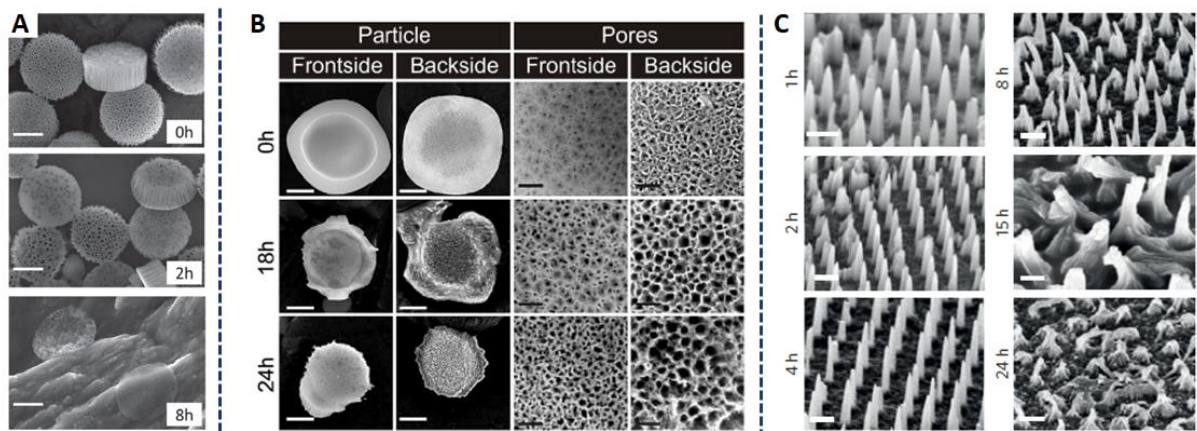
Figure 14. Dissolution patterns of A) hemispherical pSi (adapted from ref. 119); B) discoidal pSi (adapted from ref. 103) and C) nanoneedle pSi (adapted from ref. 108).

c) Biocompatibility of pSi

While nanostructured pSi can readily degrade into nontoxic byproducts to avoid long-term accumulation, pSi in micro and nanosize can readily interact with and penetrate into body tissues and organs in various manners and therefore result in complicated body responses.[121] In the late 1990s, studies of pSi implantation in the guinea pig showed no evidence of chronic inflammation, thereby indicating the first evidence of biocompatibility of pSi *in vivo*.[122]

To date, a multitude of pSi-based platforms with intricate designs has been developed to address several hurdles in drug delivery and therefore pose critical challenges to draw a solid conclusion regarding the biocompatibility of all pSi structures for every disease model. Owing to the complex nature of the biological systems, the structural parameters (e.g. shape and size) as well as the surface chemistry of the materials that are generally responsible for possible changes in cell homeostasis, biological responses can vary among different cell lines and animal models.[123] Interestingly, in earlier studies, injection of pSi microparticles (hydrosilylated and oxidized surface) into the vitreous of rabbit eyes and implantation of pSi membranes (amino and oxidized terminated surface) under the conjunctiva of rats triggered insignificant inflammatory responses and did not cause any damages to animals' eyes, thus suggesting biocompatibility of pSi with different surface chemistry to eye tissues.[124]

All in all, while *in vitro* studies are imperative to evaluate the impacts of a given pSi-based platform at the cellular level, more *in vivo* and clinical studies are required owing to the complex aspects of the living systems, such as immune responses.[123] In addition, a systemic evaluation of the biointerface of a given pSi structure is imperative in order to understand the biological responses upon administration of the materials and also to allow reasonable comparison of the impacts of different types of pSi structures on biological systems.

1.4 Nanostructured Silicon as A Therapeutic Platform

1.4.1 Bio-relevant Applications

Owing in part to the unique tunable resorption characteristics, pSi nano and microparticles have become a prominent candidate in multiple nanomedicine applications.[110, 125] While biosensing and non-invasive implants using pSi-based materials have been demonstrated and achieved considerable successes, pSi is also indicated as exceptional therapeutic delivery platforms.[96, 110, 126]

In general, pSi is designed for loading, providing protection, delivery and facilitating the release of the therapeutic cargos at the targeted disease sites. In particular, the porous architecture of pSi has been exploited not only to increase drug loading capacity but also to enhance bioavailability of the drugs as described in section 1.2.1. Owing to tunability of the porous morphology, drug release profile can ideally be controlled accordingly. For the past few decades, a multitude number of studies have exploited the porous architecture of pSi to deliver insoluble drugs, such as anti-cancer drug camptothecin and anti-inflammatory drug celecoxib.[127] Recently, our group has demonstrated an exciting eco-friendly delivery route comprised of plant-derived mesoporous pSi and anti-inflammatory drugs extracted from horsetail. By confining within the porous structure of Si platform, drug solubility was enhanced significantly and increased anti-inflammatory effect relative to the free drug was observed.[128]

In addition, since a vast number of therapeutic species, particularly nucleic acids and proteins, are susceptible to degradation by the complex biological environments, multiple designs of pSi-based platforms have been introduced to confine and protect the cargos within the porous architecture, thus indicating potential merits of pSi in delivery of biologics.[129, 130]

Interestingly, while pSi has been employed to deliver various therapeutic agents for treatments of cancer and infection diseases, there is a growing evidence suggesting pSi with certain surface chemistry (i.e. thermally oxide and thermally hydrocarbonized pSi) can act as adjuvants by inducing maturation of dendritic cells and stimulating cytokine secretions involved in differentiation of immune cells, hence implying remarkable potential uses of pSi in immunotherapy.[131]

1.4.2 pSi particle - cell Interaction

As described in earlier sections, after systemic administration, nanomaterials are subjected to complex interaction dynamics with various biological constituents. While there are multiple factors that determine therapeutic efficacy of a given material, a focus on the influence of some of the selected physiochemical properties, namely surface chemistry and particle geometry, of pSi materials at the nano-cell interface is described herein with an emphasis on cell functions and delivery efficacy.

To date, surface chemistry is one of the most important characteristics that dictate the outcome of any therapeutic treatment. Not only blood circulation half-life but systemic clearance is also significantly determined by the chemical functionality grafted on the NP surface. Hence, critical assessment of the effect of surface chemistry of a given pSi particle is necessary to address any potential adverse side effects.

Upon administration into the body, pSi particles are expected to interact with immune cells prior to reaching to the target sites and subsequently trigger immune responses. In a series of careful studies by the Santos group, the influence of pSi with a diverse range of surface chemistry on various immune cell lines have been elucidated (Figure 15). As expected, positively charged particles generally exert adverse impacts on cells due to disruption of cell membrane integrity,

whereas negligible effects were observed in the remaining carriers (i.e. TOPSi, TCPSi, THCPSi, THPSi, defined in Figure 15). In addition, while NPs possessing a hydrophobic surface are generally compatible to cell functions (e.g. low ATP depletion and genotoxicity), it was shown that the biocompatibility of the hydrophilic oxidized pSi stems from its hydrophilicity and the favorable resorption of the material into nontoxic $Si(OH)_4$.[110, 132]

Additionally, in another study using irregular-shaped pSi to exclude shape factor, the same group also observed that pSi of certain surface chemistry, particular those with higher density of C-H structures on the surface, are likely to act as adjuvants that can synergistically trigger immune responses, thus implying tremendous potential in delivery of immune-stimulative drugs. On the other hand, other pSi such as APTES-functionalized pSi particles, which lack ability to exert immune responses, offer advantages in delivery of immune-suppressive molecules. Therefore, these results collectively highlight the impact of pSi on immune systems.[133]
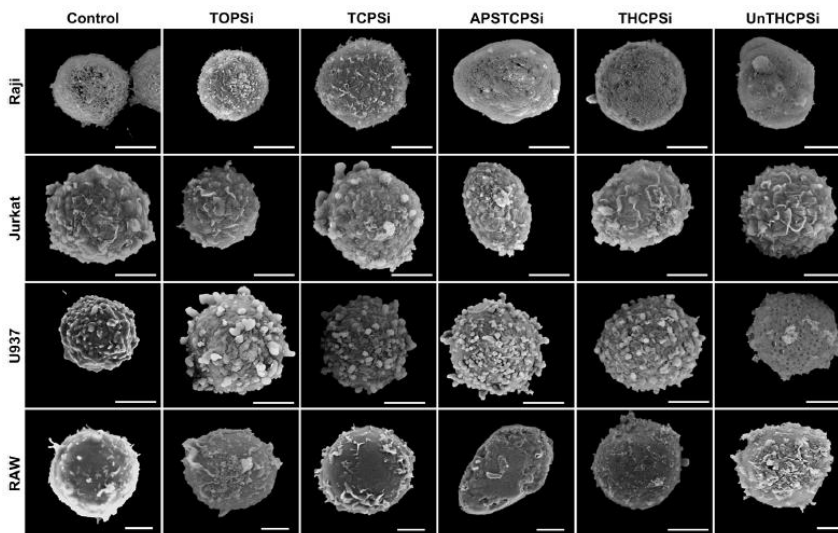
Figure 15. Impact of surface chemistry of pSi to morphology of immune cells (TOPSi: thermally oxidized pSi, TCPSi: thermally carbonized pSi, APSTCPSi: APTES-functionalized thermally carbonized pSi, THCPSi: thermally hydrocarbonized pSi and THPSi: undecylenic functionalized pSi) (adapted from ref. 132).

Besides surface chemistry, particle shape has been explored as a critical structural parameter responsible for any changes in cellular responses and therapeutic outcomes. With the emergence of well-defined nanostructured pSi in recent years, the influence of particle geometry on nano-bio interface can be thoroughly interpreted. While particle shapes have been shown to influence biodistribution, a focus on the interactions between pSi particles and cells is presented herein.

As mentioned in the previous sections, local alignment of the particles relative to the cell surface invariably determines the efficacy of particle uptake. With advances in microscopic technique endowing high resolution imaging, particle association with cells has been explored, providing details regarding internalization pathways. In addition, well-defined structures of pSi readily allow distinguishing particles from cells and other biological interference. For instance, via scanning electron microscopic (SEM) imaging, phagocytosis of discoidal microparticles by murine bone marrow-derived dendritic cells (BMDC) was shown, as evidenced by formation of an actin cup engulfing the particles surface.[134]

The exploration of the biointerface using pSi in a well-defined 1D structure paves the way to understanding the distinct nano-cell interactions produced by the high AR of the particles. Similar to the aforementioned SiNWs, which insignificantly creates adverse impact on cell viability despite cell penetration observed after exposure to NWs with relatively high AR (Figure 16A), biocompatibility of the noninvasive porous Si nanoneedles has also been indicated. [106, 108] Owing to biodegradability of the material, temporary exposure to cells presumably exerted negligible damage.

Here, detailed interactions between the array of needles and cells were evaluated via the cross-sections obtained from the focused ion beam scanning electron microscopic imaging (FIB-

SEM), which outlines needle-cell interface (Figure 16 B1 and B2). While initial studies suggest penetration of Si needles creates access to cytoplasm and thereby facilitates delivery of cargos (e.g. nucleic acids and quantum dots), Stevens and colleagues indicated a tight interface is created between the nanostructure and cell membrane upon interaction and thus deforms the cell membrane rather than completely piercing through the cell structure (Figure 16 C1 and C2). As the cell membrane becomes deformed owing to the physical interactions, numerous signaling proteins, such as caveolin-1 and clathrin light chain, participating in endocytosis processes are recruited locally at the needle-cell interface, thereby initiating the endocytosis, presumably via mechanical stimuli. However, since a high delivery efficiency was achieved despite the payloads (i.e. siRNA) co-localized with endolysosome, which readily degrades the cargos, the delivery might also be stemming from an alternative pathway, which remains to be evaluated.[135]
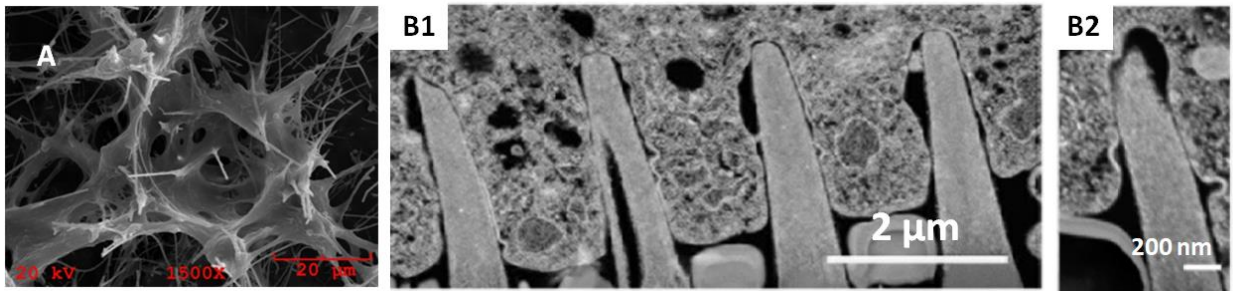
Figure 16. Association of 1D Si structure with cells. A) mouse stromal cells interacting with vertical SiNW array (adapted from ref. 87); B1) Cross section imaging showing high-resolution cell-needle interface between porous silicon nanoneedles and human mesenchymal stem cells and B2: clathrin-like vesicles formed at the interface (adapted from ref. 135).

While the majority of cellular interactions with 1D structures of Si up to date have focused on interactions with the whole array, only a few studies have focused on cellular responses upon exposure to free-standing structures, which affect cell viability in different manners. For instance, unlike SiNW and needle arrays, cell proliferation after treatment with free-standing particles is

significantly dependent on the dose, presumably owing to toxicity-induced aggregations and interference with cell functions.[136] Also, diverse orientation of free particles when comes into contact to cell surface creates complications in evaluations of internalization of the materials. Thus, to compare the platform with those are currently existing, such as nanodiscs and platelets, systematic studies regarding the impact of a given free-standing 1D Si structure on the nano-bio interface and intracellular delivery is needed.

1.4.3   Current Design Strategies of pSi-based Drug Delivery Systems and Outcomes

To address multiple biological hurdles, the designs of pSi-based delivery platforms have become increasingly intricate over the years. Whereas earlier studies mainly focused on controlling drug release and relied on the EPR effect to enhance particle accumulation, recent years have witnessed an increasing number of studies which focus on active targeting strategies to enhance specificity.[130] For instance, pSi decorated with peptides[130] and small molecular ligands[137] that selectively target specific moieties expressed on the target cell membrane have been demonstrated and achieved exceptional results.

While foreign materials are subjected to clearance by the MPS, particle design with an additional biomimetic outer layer, particularly derived from the cell membrane with specific surface molecules and lipid compositions , have enabled the materials to camouflage and evadethe MPS by prolonging circulation time.[138] Here, Santos and coworkers have developed strategies to effectively encapsulate thermally oxidized pSi NPs within cell membrane derived from various cell lines,[139] and pSi-based nanovaccine, which involves coating acetylated dextran@pSi platform with cancer cell membrane (CCM) has demonstrated several promising immunomodulatory properties. Since cancer cells of every patient exhibit different selection of antigens, a personalized vaccine can be envisaged (Figure 17A).[140] Besides cell membrane, biomimetic exosome coating

also renders NPs enhanced stability in the blood stream along with immunocompatibility and enhanced cellular uptake. In this manner, a biocompatible exosome coated drug@pSi nanocarriers have been achieved via exocytosis of the drug-loaded particles by human hepatocarcinoma tumor cells, and the system has been demonstrated to significantly enhance anti-cancer activity *in vivo* (Figure 17B).[141]
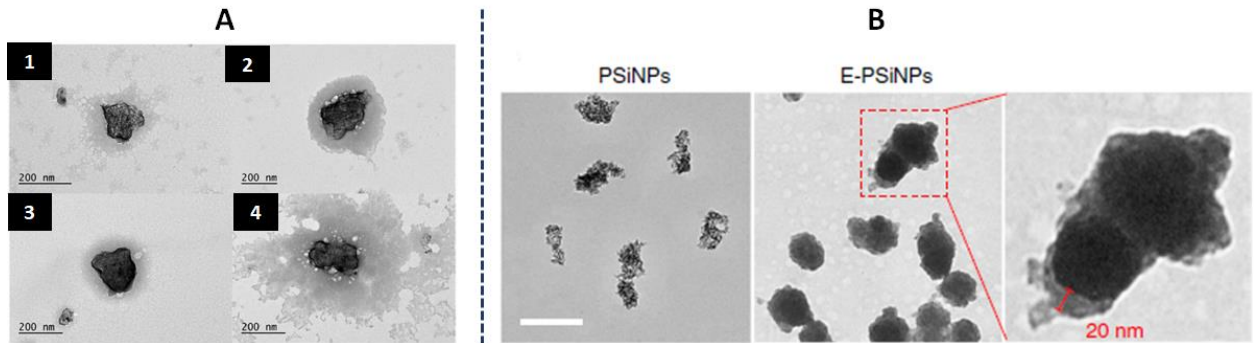
Figure 17. Biomimetic pSi nanoparticles: A) pSi coated with cell membrane derived from different cell lines (1. A549, 2. MCF-7, 3. MBA-MD-231, 4. PC3MM2) (adapted from ref. 139); B) pSi coated with exosome (adapted from ref. 141).

In addition to some of the selected designs described above, several other remarkable nanoconstructs have been presented to tackle multiple hurdles encountered upon systemic administrations, such as coating with amino-rich molecules (e.g. dendrimers)[142] or fusogenic lipids[130] to overcome the endosomal barriers, thus emphasizing flexibility of manipulating a given pSi material to satisfy stringent requirements for specific disease models and achieve optimal therapeutic outcomes. While a diverse selection of surface grafting molecules can be synthesized and decorated on pSi in various manners, the pSi core remains the utmost important component that influences the therapeutic outcome of the whole nanocomposite given by tunable dissolution properties and nanoarchitectures. Therefore, a system composed of a central pSi component with a well-defined structure is an appealing target in therapeutic applications.

Chapter II

One Dimensional Nanostructure of Silicon and Bio-relevant Properties of the Nanostructures

2.1   Introduction

One dimensional (1D) structures of silicon have offered numerous opportunities to study the impact of these nanoconstructs on cellular functions and contributed to knowledge in nano-bio interfaces.[135, 136] Among 1D structures, nanotubes are an attractive option owing to additional lumen that endows enhancement in cargo loading.

Although single-walled Si nanotubes (SiNTs) have yet to be produced (due to their inability to retain sp^2 hybridization in the same fashion as carbon nanotubes), nanotube constructs of cubic phase Si have been successfully fabricated via various synthetic routes.[143, 144] However, earlier synthetic methods, such as alumina membrane template and gas phase condensation methods, typically encountered complicating issues involving contamination with byproducts (e.g. solid Si nanowires) and homogeneity of the SiNT structures.[145, 146] With advances in nanotechnology, methods that endow SiNTs with tunable structures and high levels of reproducibility have been demonstrated, thereby providing ease in systematic evaluation of the impacts of these structures, especially on biological systems.[107, 147]

With a focus on the platforms designed for intracellular delivery via controlled interactions with cells, a unique delivery strategy using vertically aligned SiNTs have been demonstrated recently. Via a combination of direct e-beam lithography and deep reactive ion etching (EBL-DRIE), an array of open-ended SiNTs with well-defined structures (e.g. 300 nm inner diameter, 2 μm length and 5 μm pitch) that are uniformly distributed on the Si substrate are presented.[147] These delivery platforms are not only biocompatible to the tested primary cell line (i.e. Mouse embryonic fibroblast cells) but also have shown to trigger endocytotic pathways for intracellular delivery of biomolecules in a similar fashion to that of the porous Si nanoneedles (Si NNDs) as described in

Chapter 1. Owing to the unique hollow inner space, the authors also pointed out that additional functionalization was not necessary to achieve high loading.

Whereas pSi NNDs have demonstrated efficient therapeutic delivery via high surface area and bio-relevant properties (i.e biodegradability and biocompatibility) imparted by the porous morphology;[106, 108] SiNT arrays presented above readily mediate mechanodelivery (delivery via disturbance of the plasma membrane by mechanical force) via the unique hollow structure. Thus, these selected platforms are not only applicable to several therapeutic treatments including nanoinjection and cell-based therapy for their capability of delivering a large selection of therapeutic cargoes (e.g., nucleic acids and Cas9 ribonucleoprotein), but they are also beneficial to explore complex biological pathways triggered via interactions with 1D nanoconstructs at close proximity with cells.

While SiNT arrays produced by EBL-DRIE are endowed with controlled wall thickness, smooth side walls are typically achieved. Alternatively, an approach developed by our group, the so called sacrificial ZnO template route (Figure 18), not only yield SiNTs with tunable structural parameters (shell thickness and inner diameter), but the surface morphology of the nanoconstructs can readily be modulated via controlling the conditions of chemical vapor deposition (CVD).[107] Typically, a unique porous morphology is accompanied with a thin Si side wall (10-12 nm) obtained at a relatively low temperature (~ 540 °C) and a short reaction time (typically 5 min), whereas reactions operating at a higher temperature for a longer period of time usually yield thicker shells and a smoother surface.
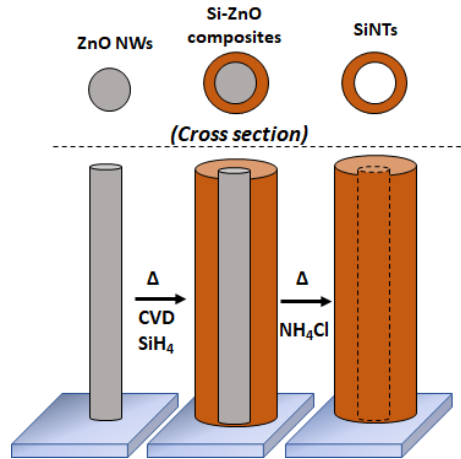
Figure 18. Synthetic scheme of SiNTs produced via a sacrificial ZnO template method.

For porous SiNTs (pSiNTs), the unique arrangement of pores on the side wall distinguishes this porous morphology from the dendritic mesopores and columnar macropores of other pSi structures typically obtained from anodic etching. In contrast to other pSi materials, SiNTs produced herein are typically amorphous presumably owing in part to lattice mismatch at the ZnO/Si interface. Nevertheless, highly crystalline nanotubes can readily be obtained by performing additional annealing step at a relatively high temperature (600-650°C). In addition, since this sacrificial template method excludes the need of corrosive reagents (e.g. HF) and intricate lithographic methods, the ease of use of this strategy is recognized.

With regard to bio-relevant properties, tunable degradation kinetics along with *in vitro* biocompatibility of the unmodified SiNTs with healthy human cell line (e.g. human embryonic kidney cells, HEK 293) have been demonstrated.[148] More importantly, resorption patterns of the amorphous pSiNTs in phosphate buffered saline (PBS) have been shown to be similar to that of the bioactive anodized pSi materials, thus collectively demonstrating potential merits of SiNTs with a porous morphology in drug delivery.[107]

Since biodegradable freestanding nanostructures are of utmost importance for systemic delivery of the therapeutic cargoes to the pathological sites and subsequent elimination from the body in a controlled manner,[17] it is of great importance to assess therapeutic implications of such biodegradable pSiNTs. Thus far, we acknowledge that there have been no reports regarding evaluation of the therapeutic potentials of Si in freestanding nanotube structure. Therefore, any assessments of pSiNTs as delivery matrices will be exciting opportunities to gain insight into applicability of this new class of nanoconstructs in nanomedicine.

Whereas inner diameter and shell thickness of SiNTs have been well-characterized in earlier studies, the lack of demonstration of systematic control of nanotube length suggests necessity of evaluating this feature prior to any bio-relevant studies.[107] In terms of cellular interactions, since membrane wrapping and cellular penetration are presumably influenced by the AR of the non-spherical nanoconstructs,[149] manipulation of pSiNT length is, therefore, essential to achieve optimal therapeutic outcomes. In addition, although pSiNTs are produced as an array of uniform individual nanotubes, investigations into size control of the freestanding pSiNT arrays are critical. Besides, since various aforementioned biological factors and physiochemical properties generally dictate the biofate of the materials, evaluation of the effects of biological media and surface functionality on biodegradability patterns of pSiNTs are also needed.

For these reasons, in this Chapter, control of nanotube length and fragmentation of nanotube arrays are thoroughly described, followed by assessment of degradation behavior of unmodified and functionalized pSiNTs in biological media. Additionally, cytotoxicity of functionalized pSiNTs to cancer cells is also detailed herein.

2.2   Experimental

2.2.1   Fabrication of SiNTs via A Sacrificial ZnO Template Method

a)   Growth of ZnO Nanowires (ZnO NWs)

ZnO NWs templates presented herein were fabricated via a hydrothermal method. A Fluorine-doped tin oxide (FTO) glass or Si wafer was cut into 1×1.5 cm pieces, which were immersed in 10% HCl and sonicated in acetone for 1 h and 40 min respectively. ZnO nanocrystals (or seeds) were prepared by stirring (400 rpm) a mixture of 0.01 M $Zn(CH_3CO_2)_2$ (12.5 ml), MeOH (25 ml) and 0.03 M NaOH (6 ml) for 2 h at $60^{\circ}C$. The final clear ZnO solution was cooled to room temperature before further use.

ZnO seeds were deposited on the substrates by a spin coating method: the substrate surface (conducting side for FTO glass) was coated with the above ZnO seed solution (3-4 drops) and was spun for 20 s at 3000 rpm; this process was done twice. After spin coating, the substrates were annealed in air at $260^{\circ}C$ for 40 min. After the samples were cooled down to room temperature, the spin coating and annealing steps were repeated one more time.

For growing ZnO NWs, a solution of 0.08 M $Zn(NO_3)_2$ (50 ml) and 0.08 M hexamethylenetetramine (HMTA) (50 ml) was prepared, and the rack containing the substrates with the ZnO-coated surface facing downward was immersed in the solution (Figure 19A). The sample was incubated at $95^{\circ}C$ for 1.5 h, 3 h, 6 h and 9 h. pSiNTs utilized in studies described in sections 2.4 – 2.6 were all produced using 1.5-h ZnO NW cores. It should be noted that for ZnO NWs that are grown longer than 3 h, the reaction was replenished with a fresh solution of $Zn(NO_3)_2$ and HMTA every 3 h. After the reaction was done, the substrates were rinsed with deionized (DI) water and dried in air.
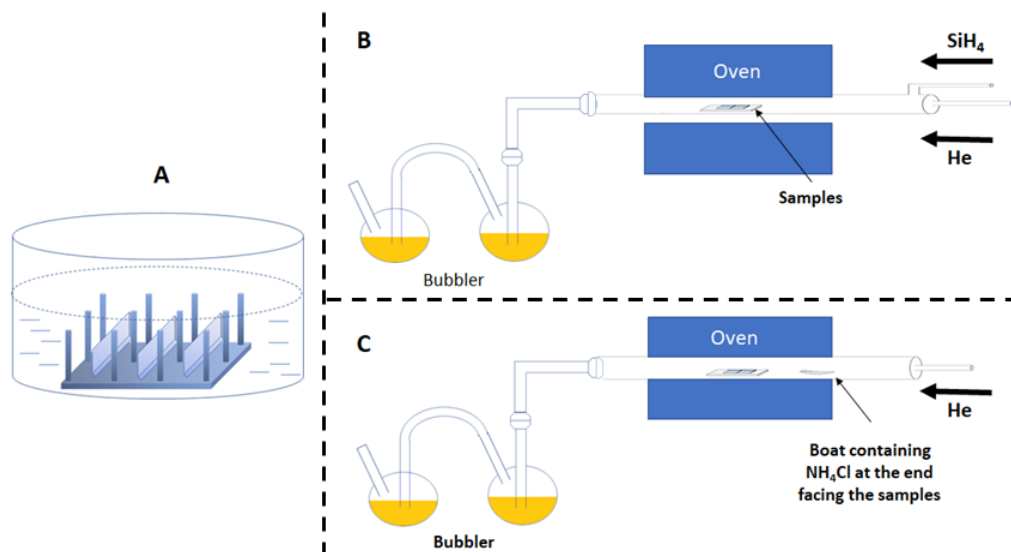
Figure 19. Set-ups of ZnO NW growth of the substrates precoated with ZnO nanocrystal seeds (A), Si deposition (B) and gas-phase etching (C).

b) **Silicon Deposition of ZnO NWs**

Chemical vapor deposition (CVD) in which silane (0.5 % SiH_4 in He) (20 sccm) diluted further in pure (5.0 UHP) He (250 sccm) was used to deposit Si on ZnO NWs (Figure 19B). To achieve a porous morphology, CVD was performed at 540 ^{o}C for 5 min.

c) **Gas-phase Etching of ZnO NW Cores**

Final removal of ZnO NWs was performed via etching with NH_4Cl at 500°C for 2 h in He (5.0 UHP) (180 sccm). The etching reactor was configured as shown in Figure 19C. The final pSiNT products were quickly rinsed with DI H_2O, acetone and gently dried with N_2 gas to remove any residue from the etching reactions.

2.2.2 Fragmentation of pSiNT Arrays

In these studies, pSiNTs obtained from 1.5-h grown ZnO NW template were utilized. The substrates were wetted with EtOH (95%), and the SiNT arrays were gently scraped off from the surface of the substrate. The solution of SiNT arrays was incubated *in vacuo* to remove any trace

EtOH solvent. To fragment SiNT arrays into smaller sizes, 2 ml of DI H_2O was added, and the solution containing SiNT arrays harvested from 3-4 substrates ($m_{SiNTs(total)}$ = 100-200 μg) was subjected to ultrasonication using Branson Sonifier (80 watt, 20 % Duty Cycle) for 10 s, 3 min, 5 min, and 10 min in an ice bath. It should be noted that the solution was mixed every 2 min by inversion.

2.2.3   Characterization of pSiNTs

Structural parameters (inner diameter, shell thickness and length) and the morphology of pSiNTs were characterized by transmission electron microscope (TEM) imaging (JEOL JEM-2100 electron microscope equipped with a GENESIS XM2 imaging EDX spectrometer). To prepare TEM samples, pSiNTs in EtOH were briefly sonicated (~10 s) in an ice bath by ultrasonication, and a drop the solution was added onto the carbon coated side of a TEM grid. After the solution was dried, the addition was repeated 2 more times.

To characterize the size of SiNT arrays after fragmentation, 1-2 drops of the SiNTs after fragmentation at each time point was added onto a clean Si wafer substrate mounted on an Al thimble and were dried in air prior to imaging. Particles were characterized by Field emission scanning electron microscope (FE SEM) imaging (JEOL JSM-7100F).

2.2.4   Surface Functionalization of pSiNTs and Characterizations

pSiNTs remained attached to the substrates were incubated in 2% 3-aminotriethoxysilane (APTES) or N^1-(3-Trimethoxysilylpropyl)diethylenetriamine (Abbreviation: triamine) (Gelest) in toluene for 4 h at room temperature with constant stirring (120 rpm) (Figure 20 and Figure 21). After incubation, the substrates were washed with toluene, acetone and then dried in air. For long-term storage, the substrates or the freestanding functionalized pSiNTs were stored in 95 % EtOH.
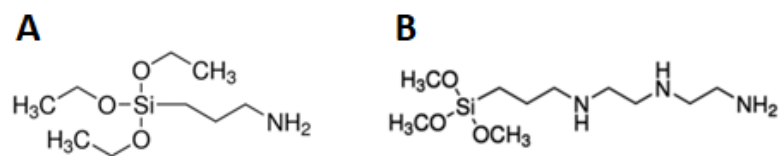
Figure 20. Molecular structures of A) APTES and B) triamine.
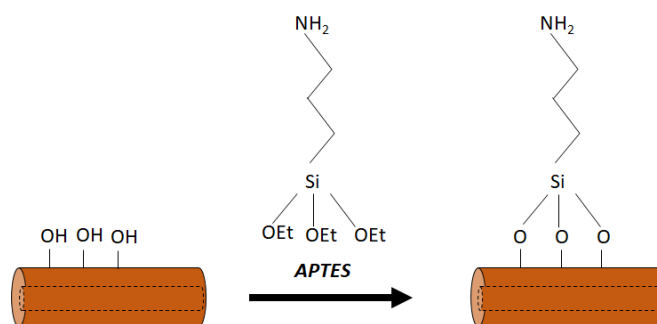
Figure 21. Synthetic scheme for surface functionalization of SiNTs with APTES.

Zeta Potential Analysis

Functionalized pSiNTs were mixed with 2 ml ultrapure water (water was purified using Purelab Classic, Elga) and the solution was briefly sonicated in an ice bath (~ 10 s). The zeta potential measurements were performed using ZetaPALS Zeta Potential Analyzer (Brookhaven) The zeta potential values were collected at room temperature (RT = ~ 20 °C) (10 runs, 30 cycles/run and fit to *Smoluchowski's* model, which is used for determination of electrophoretic mobility of particles dispersed in aqueous media)).[150] For the optimal measurement, the amount of pSiNTs should be kept at minimal such that the sonicated solutions should have a very faint yellow color.

2.2.5   Degradation of Unmodified and Functionalized pSiNTs in Biological Media

Unmodified and functionalized pSiNTs were fabricated on Si wafers (ZnO growth time: 1.5 h) and they were cut into equal pieces. The samples (~ 10 μg/wafer) were incubated in PBS or cell growth culture supplied with fetal bovine serum (FBS) (complete medium) (3 ml) for 6 h, 24

48

h and 48 h in a humidified incubator (37ºC, 5% CO_2). The morphologies of the nanotubes before and after incubation at each time point were characterized by FE SEM imaging (15 kV).

2.2.6 Cellular Interactions with Functionalized pSiNTs and the Corresponding Cell Viability

HeLa cervical cancer cells were maintained in Dulbecco's modified Eagle's medium (DMEM) supplemented with 10 % heat-inactivated fetal bovine serum (FBS), penicillin (88 U/mL), streptomycin (88 µg/mL), glutamine (0.88 mM) and 1/100 minimum essential medium (MEM) non-essential amino acids. Cells were maintained at 37 °C with 5 % CO_2 in air, in a humidified incubator. Cells were split when they reached 80-90 % confluence.

For a typical viability assay, 5000 HeLa cells were seeded in each well of a 96-well plate and incubated for 24 h. Next day, cells were treated with different doses of APTES-pSiNTs and Triamine-pSiNTs (ZnO NW growth time: 1.5 h) for 36 h. To prepare a pSiNTs solution, the samples were sterilized with EtOH and dried *in vacuo* for 2-3 h. Prior to cell treatment, the materials were sonicated in sterilized water for 5 min as described previously. The target concentrations of nanotubes were prepared by further dilution in sterilized water. After 36-h incubation, cell viability was evaluated by luminescence CellTiter-Glo assays, which quantify the amount of ATP in viable cells. Luminescence measurements were acquired with a BMG Labtech FLUOstar Omega fluorescence/luminescence plate reader.

2.3   Results and Discussion

2.3.1   Fabrication of pSiNTs

a)   Porous Morphology of SiNTs

According to earlier reports, surface morphology and shell thickness of SiNTs produced by the ZnO template method can be readily adjusted by modulating CVD parameters (i.e.

temperature and time).[107] By operating the above CVD process at 543 ± 2 °C for a short but fixed period of time (i.e. 5 min), SiNTs with porous side walls can readily be obtained. It is noteworthy to point out that since a orange/brown color is a typical feature of pSi,[151] formation of the porous side walls can readily be probed via visual inspection of the color of the substrates post CVD. Due to fluctuations in the heating rate/local temperature, different color intensities can be obtained, thus indicating variations in the shell thickness and the associated morphology (Figure 22A). In the case of pSiNTs with a light-yellow hue (#1), a thin wall in conjunction with a highly porous morphology, presumably resulting from a relatively low local temperature (of the above defined range), were observed owing to a relatively low density of Si islands. In this regard, the distribution of the Si domains is relatively broad with thin Si protrusions (diameter = ~ 20 nm) randomly distributed across the wall (Figure 23-1).

At a relatively higher local temperature (of the above defined range), the growth of Si islands via an Ostwald-type coalescence was induced,[107] thus increasing shell thickness and reducing the porosity (Figure 23-2 and 23-3). In addition, disappearance of the thin Si protrusions in these samples is likely a consequence of the fusion of the structures with a high density of the smaller nearby Si islands in order to achieve a lower surface energy. Also, the relatively high operating temperature along with a high gas flow rate might also contribute to the collapse of these physically unstable protrusions. Therefore, a smoother sidewall together with a narrower size thickness are typically observed in SiNTs with darker colors (Figure 22 A and B).

For investigations described later, pSiNTs with color intensities #2 and #3 were utilized since those with an ultrathin shell (#1) were shown to be highly fragile under physical manipulations.
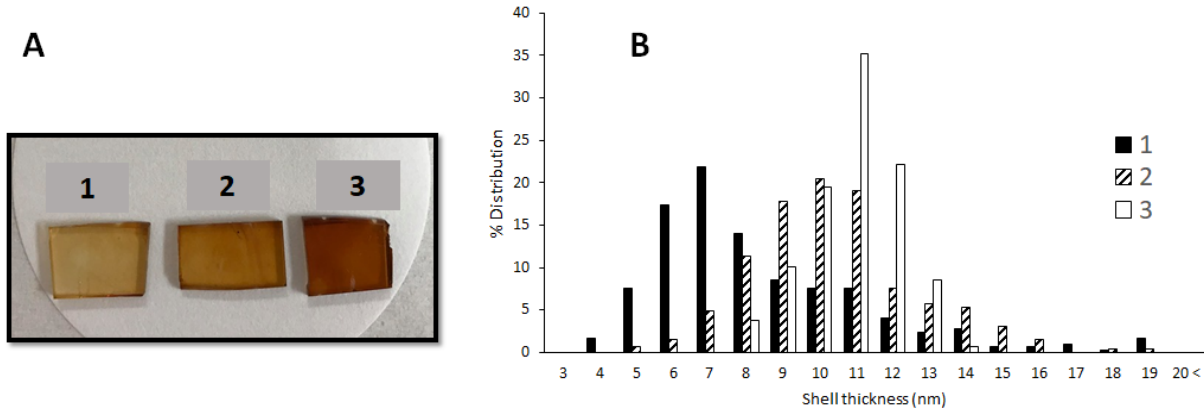
Figure 22. Porous silicon nanotubes. A) Color of the substrates after CVD (substrates: FTO glass) and the corresponding B) distribution of shell thicknesses.
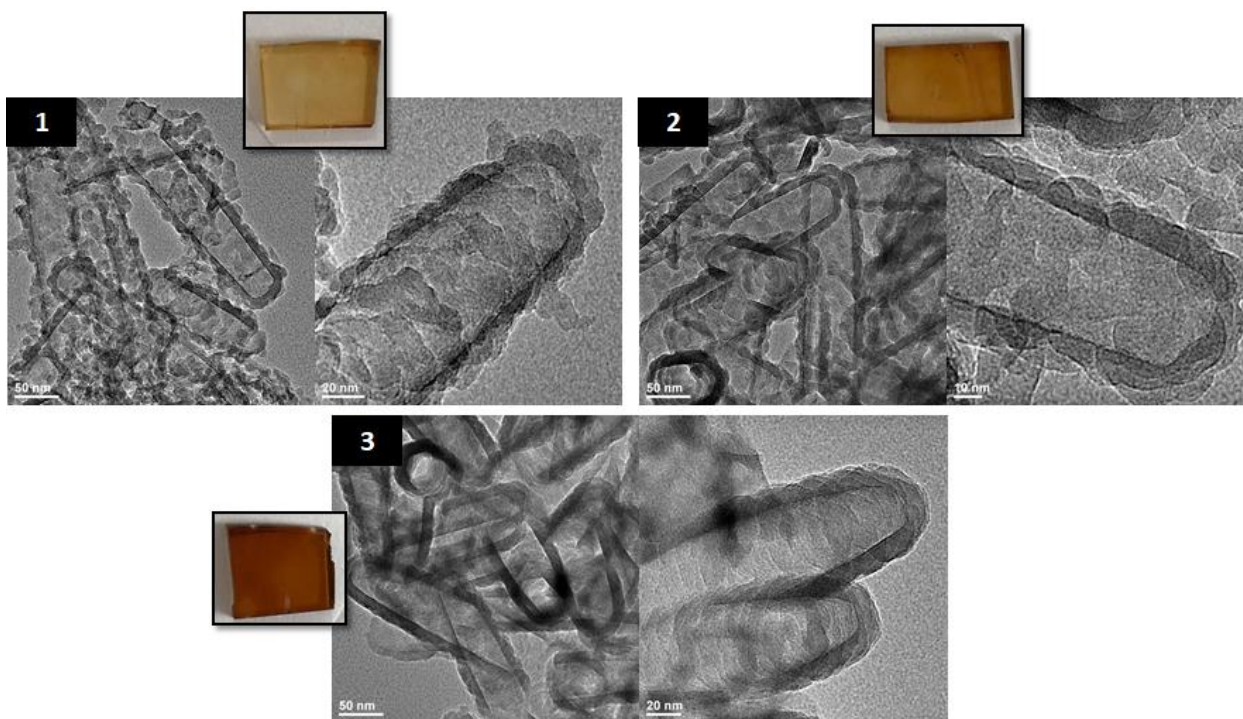
Figure 23. TEM imaging of pSiNTs with different shell thicknesses. Scale bars (from left to right): 50 nm and 20 nm (1); 50 nm and 10 nm (2); 50 nm and 20 nm (3). Inset: corresponding images of associated films.

Table 2. Shell thickness of pSiNTs

Shell thickness (nm)	1	2	3
Average ± Stdev	10.0 ± 3.2	10.9 ± 2.2	11.4 ± 1.2
Min	3.8	5.5	8.0
Max	28.3	19.2	14.2

b) **Control of SiNT Lengths**

Since the ZnO NW core template dictates the resultant hollow nanostructures of SiNTs, the length of SiNTs can be controlled via modulating the growth of ZnO NWs. With the polar plane (0001) of ZnO in the wurtzite crystal structure being metastable, growth along c-axis is more favorable than other directions.[152] Therefore, by tuning the growth time of ZnO NWs, the length of the 1D structure can therefore be controlled.[153] In other words, the longer the reaction time, the more extended the length of the NWs or SiNTs. Here, by keeping the same concentrations of the reactants (i.e. $Zn(NO_3)_2$ and HMTA) but increasing the growth time from 1 h to 9 h, longer NWs were achieved as indicated in the lengths of the final pSiNT products (Figure 24). It is also necessary to point out that the lateral growth of ZnO NWs (or the inner diameter of SiNTs) also increased as a result of a longer reaction time (Table *3*). Hence, using this method, a pSiNTs with length ranges from 100 nm – 3.5 μm can readily be achieved (Figure 25).

With an interest in therapeutic applications, nanotubes with submicron lengths are of utmost relevance due to the small size relative to that of most animal cells (~ 10 - 20 μm in diameter)[154], thus suggesting beneficial implications in enhanced cellular uptake and other related interactions.
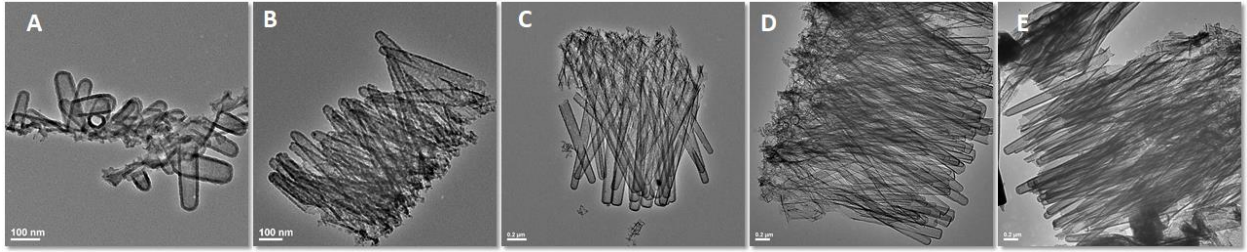
Figure 24. pSiNTs of different lengths achieved by tuning the growth time of ZnO NWs A) 1h, B) 1.5 h, C) 3h, D) 6 h and E) 9 h.
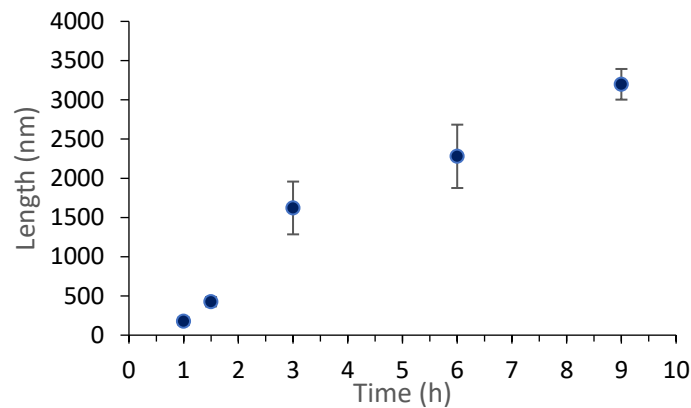
Figure 25. SiNT length increases as a function of ZnO growth time (average from ~100 measurements/time point).

Table 3. Inner diameters of pSiNTs determined by the growth time of ZnO NW templates.

Inner diameter (nm)	1 h	1.5 h	3 h	6 h	9 h
Average ± Stdev	44.3 ± 12.8	34.9 ± 8.1	96.2 ± 30.4	103.3 ± 34.6	125.5 ± 45.9
Min	14.5	14.0	35.0	34.9	28.9
Max	75.3	50.8	200.4	199.6	245.8

c) Fragmentation of SiNT Arrays

Since drug delivery using pSiNTs in freestanding form is envisaged, size characterization of the materials after detachment from the arrays are imperative. Here, upon detachment from the substrates, large fragments of nanotube arrays are collected, whose widths (bundles or aggregates)

range from 100 nm to 300 μm, thus emphasizing the necessity of more controlled fragmentation to achieve smaller sizes along with a narrow distribution (Figure 26 and Figure 27A). It is also important to note that the length of the nanotubes employed in these studies was limited to the submicron regime due to the length of the ZnO NW template.

By mechanically fracturing the arrays via ultrasonication, the size of the nanotube array films was reduced significantly relative to the original film dimensions (Figure 26). Instead of discrete singular nanotubes, it is clearly evident that the arrays are be broken into smaller bundles of SiNTs while retaining the same length as those of the arrays before fragmentation and preservation of the interconnecting opened-end structures (Figure 27). For a 5 min-sonication period, the majority of the bundles (75 %) was in submicron range, with less than 2 % of the bundles within 2-3 μm (Figure 27 D). After 10 min, a higher percentage of submicron bundles (82 %) was achieved (Figure 27 E). It is necessary to point out that from SEM and TEM imaging, even being subjected to a relatively high sonication power for 10 min, almost all the particles still maintained the well-defined, intact nanotube structures as well as the porous morphology, suggesting negligible mechanical damage to the given nanotube structure (Figure 28).

Since the submicron particles are demonstrated to be beneficial in therapeutic delivery owing to favorable cellular internalization and prolonged circulation lifetime *in vivo*,[65, 83] sonication times longer than 5 min are necessary to achieve the greatest number of submicron bundles composed of submicron-length pSiNTs.
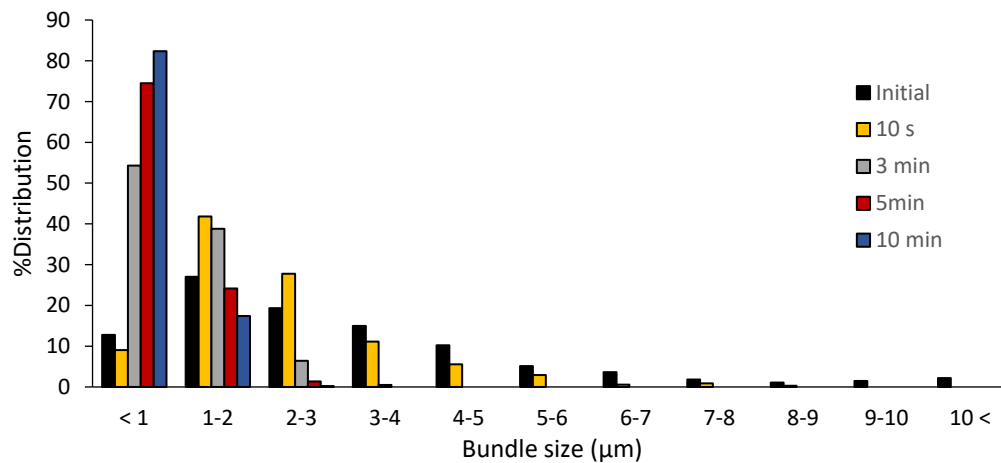
Figure 26. Size distributions of Unmodified-pSiNTs (U-pSiNTs).
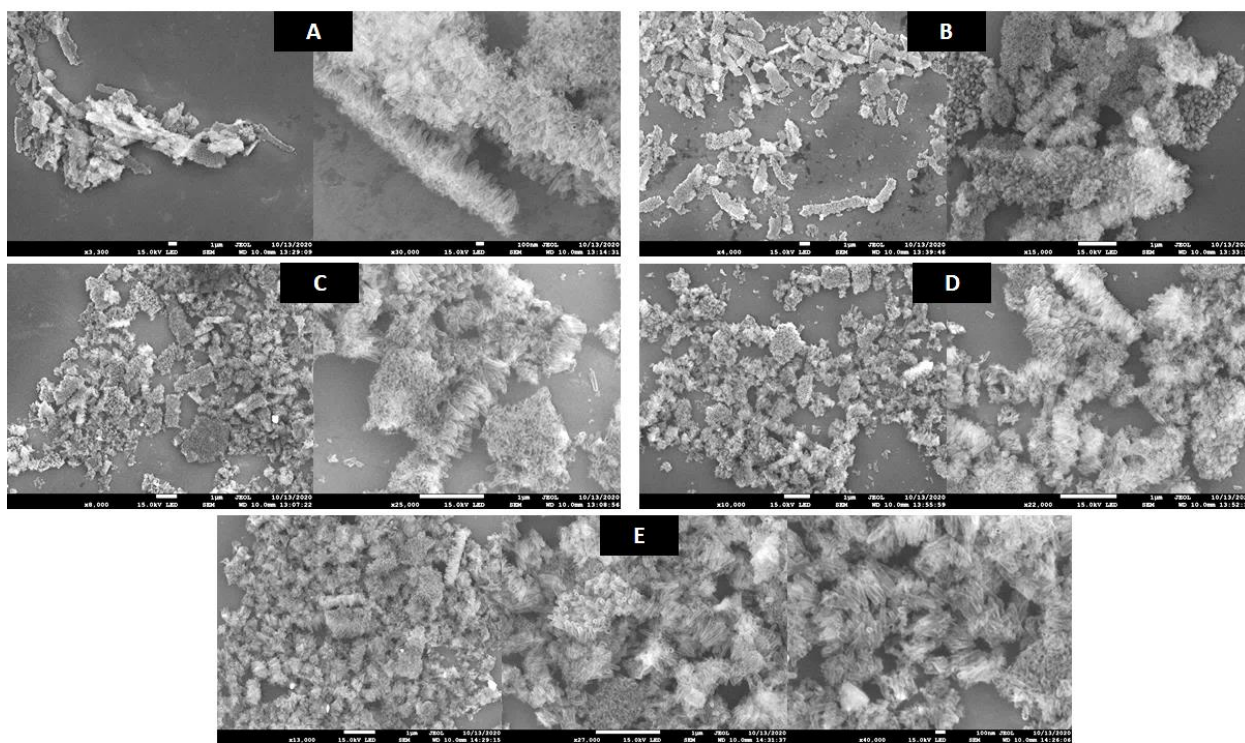
Figure 27. SEM imaging of U-pSiNT arrays before (A) and after ultrasonication for 10 s (B), 3 min (C), 5 min (D) and 10 min (E). Scale bars: A) 1 μm and 100 nm (from left to right); B) 1 μm; C) 1 μm; D) 1 μm; E) 1 μm, 1 μm and 100 nm (from left to right).
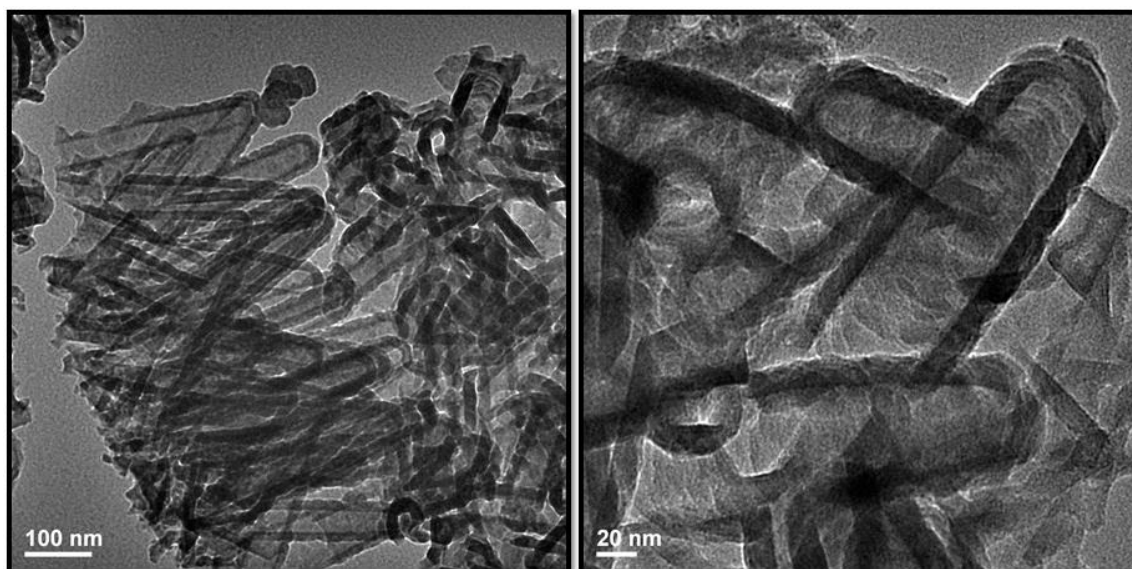
Figure 28. TEM imaging of U-pSiNTs after 10-min sonication.

2.3.2 Surface functionalization of pSiNTs

With regard to surface modification to extend functionality necessary for facilitating conjugation with additional moeities, it is essential to point out that in contrast to hydrophobic hydride-terminated pSi obtained from electrochemical anodization, all types of SiNTs (i.e. smooth and porous side wall) produced by ZnO method are hydrophilic with an oxygen-terminated surface owing to relatively high reactivity of Si in the presence of oxygen. Therefore, SiNTs can be readily functionalized with organo alkoxysilane molecules without the need of an extra oxidation step. Since silane molecules with amino group are advantageous for conjugation with additional moieties via covalent bond formation and electrostatic interactions,[148] APTES and triamine molecules are selected for functionalizing pSiNTs.

In order to probe successful surface modification, zeta potential measurements were performed to evaluate electrophoretic mobility and the corresponding zeta potentials, which subsequently reflect the surface charge of the materials. Here, a highly negative zeta potential value was observed for unmodified pSiNTs owing to the tendency of the silanol groups to

56

deprotonate (pKa = 2.0)[155] in ultrapure water (pH range is presumably 2-7). Conversely, since amino group of APTES or triamine (pKa = 9.6) are protonated within this pH range,[156] the surface charges of both materials became positive as indicated in the positive zeta potentials. Although zeta potential analyses performed herein were of a qualitative nature, changes in the sign of the zeta potential values from negative to positive after surface modification sufficiently indicated successful functionalization (Table 4).

Table 4. Zeta potential measurements.

	Zeta Potential (ζ) (mV)
Unmodified pSiNTs	-20 ± 1
APTES-pSiNTs	$+24 \pm 1$
Triamine-pSiNTs	$+27 \pm 1$
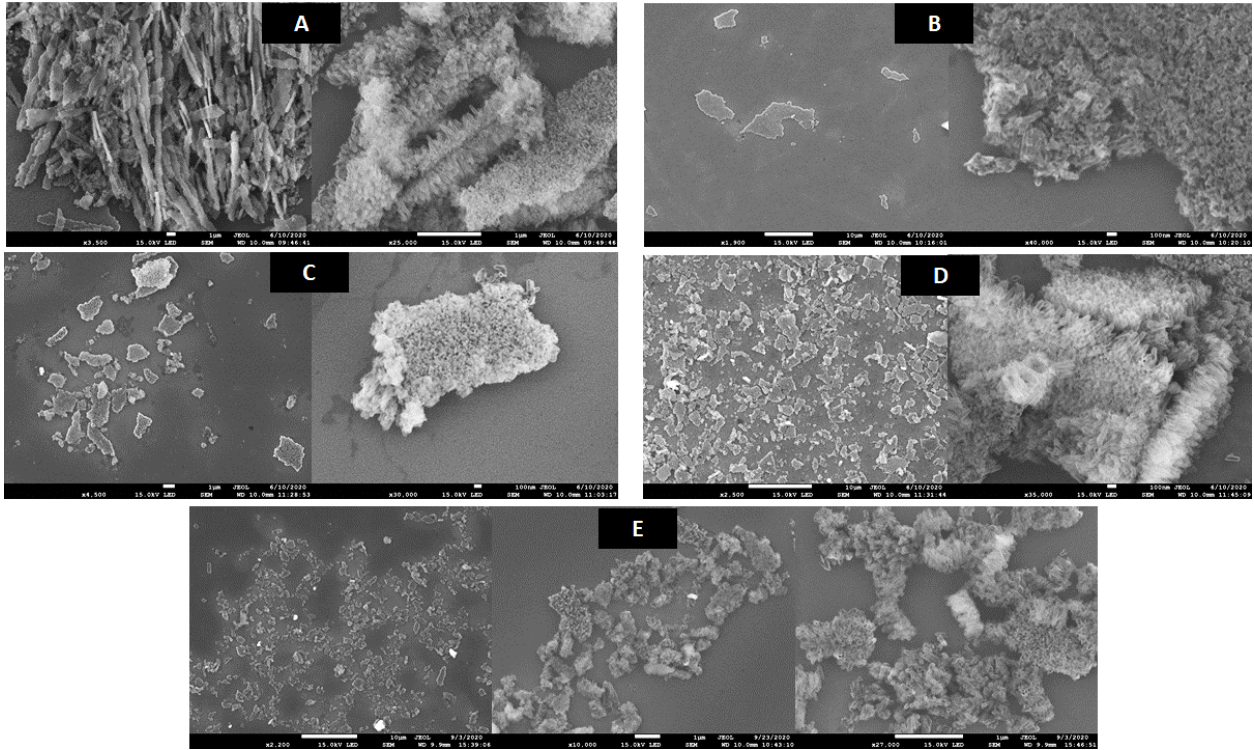
Figure 29. SEM imaging of APTES-pSiNT arrays before (A) and after ultrasonication for 10 s (B), 3 min (C), 5 min (D) and 10 min (E). Scale bars: A) 1 μm; B) 10 μm and 100 nm (from L to R); C) 1 μm and 100 nm (from L to R); D) 10 μm and 100 nm (from L to R); E) 10 μm, 1 μm and 1 μm (from L to R).

For producing freestanding SiNT bundles, functionalized SiNT arrays were also subjected to fragmentation by ultrasonication as described above. Similar to U-pSiNTs, 5 and 10-min sonication yielded the majority of the bundle sizes in the submicron regime (Figure 29 and Figure 30). By measuring zeta potential values before and after 10-min fragmentation, the surface charge of the particles remained positive. In spite of differences in particle sizes in these measurements, the results obtained from zeta potential measurements qualitatively indicated the amino group density remaining on the nanotube surface after 10 min sonication sufficiently conferred an overall positive surface charge to the materials (Table 5).
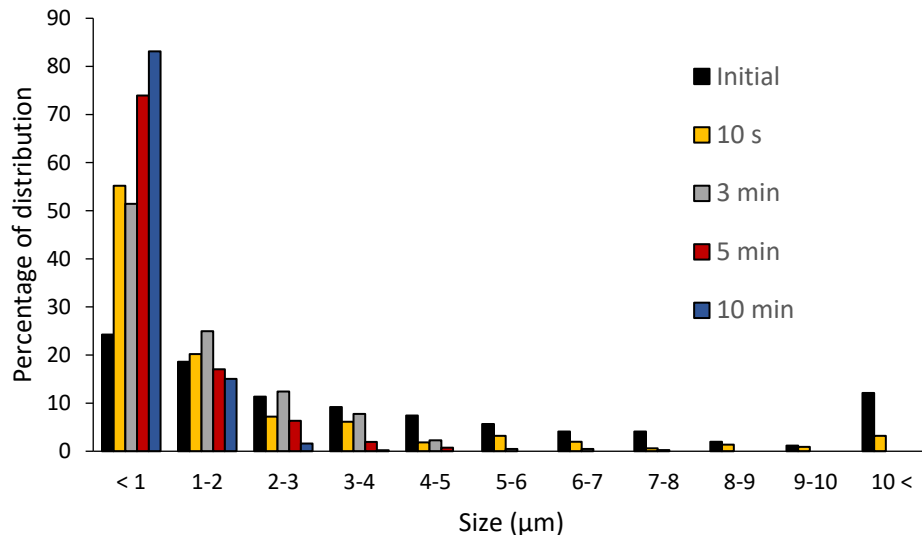
Figure 30. Size distribution of APTES-pSiNT bundles.

Table 5. Zeta potential measurements of APTES-pSiNT bundles after 10-s and 10-min ultrasonication.

	Zeta Potential (ζ) (mV)
10 s	+ 14 $\pm$ 1
10 min	+ 24 $\pm$ 2

2.3.3   Biodegradation of pSiNTs

While degradation kinetics of a large selection of SiNTs in aqueous media have been investigated in earlier studies,[107, 148] understanding the structural evolution of the constructs upon degradation in biological media is essential to evaluate the dynamic behaviors of the nanomaterials relevant to therapeutic studies. Since pSiNTs are of interest owing to the favorable dissolution kinetics, degradation patterns of U-pSiNTs and APTES-pSiNTs in biological media (i.e. PBS and cell culture medium) were assessed.

From SEM imaging, there was no evidence indicating degradation in PBS occurred in both types of pSiNTs even after 48 h (Figure 31). However, it should be noted that since the studies

59

presented herein were not done under sink conditions (i.e. re-supplying fresh medium after each time point) as reported in earlier studies, accumulation of silicic acid byproducts (condensation into SiO_2) over time might have inhibited dissolution of the material.

In contrast, in cell culture medium, dissolution of U-pSiNTs and APTES-pSiNTs were significantly enhanced with complete degradation after 48 h (Figure 32). Such relatively faster degradation rates presumably resulted from the presence of multiple complex components (e.g. (i.e. amino acids and proteins) of the growth medium and FBS that have been shown previously to induce degradation of pSi.[100, 119] Here, for U-pSiNTs after 6-h incubation in the growth medium, small hollow structures, presumably enlarged pores, appeared on the nanotube surface, thus indicating signs of degradation. After 24 h, not only did pores presented on the remaining tubes became larger, but the well-defined nanotube geometry of almost all the tubes also completely collapsed, leaving behind the hollow structures as remnants. Similar to U-pSiNTs, the majority of APTES-pSiNTs also degraded after 24 h. However, the nanotube largely remained intact after 6 h, and the enlarged pores that appeared after 24 h were also slightly smaller than that of the degraded U-pSiNTs. These differences in structural changes as a function of surface chemistry for a given medium might stem from the presence a silica - derivative layer formed by condensation of APTES molecules that slightly increased the shell thickness, thereby inhibiting diffusion of the medium and therefore slowed down dissolution of the functionalized nanotube surface (Figure 33).
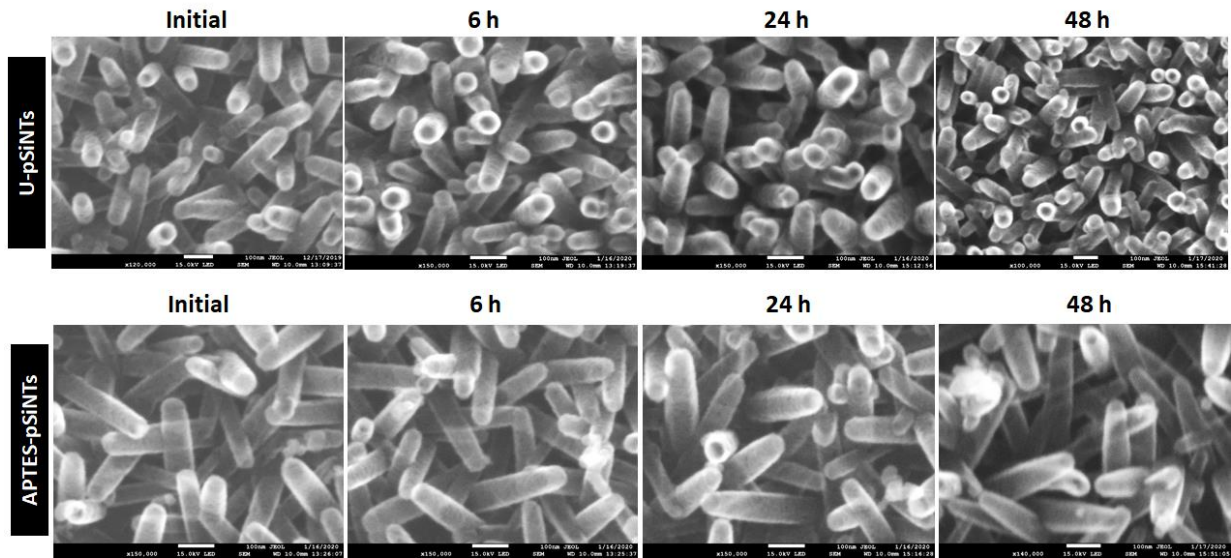
Figure 31. SEM imaging of U-pSiNTs and APTES-pSiNTs before and after incubation in PBS at 37 C for 6 h, 24 h and 48 h. Scale bars: 100 nm.
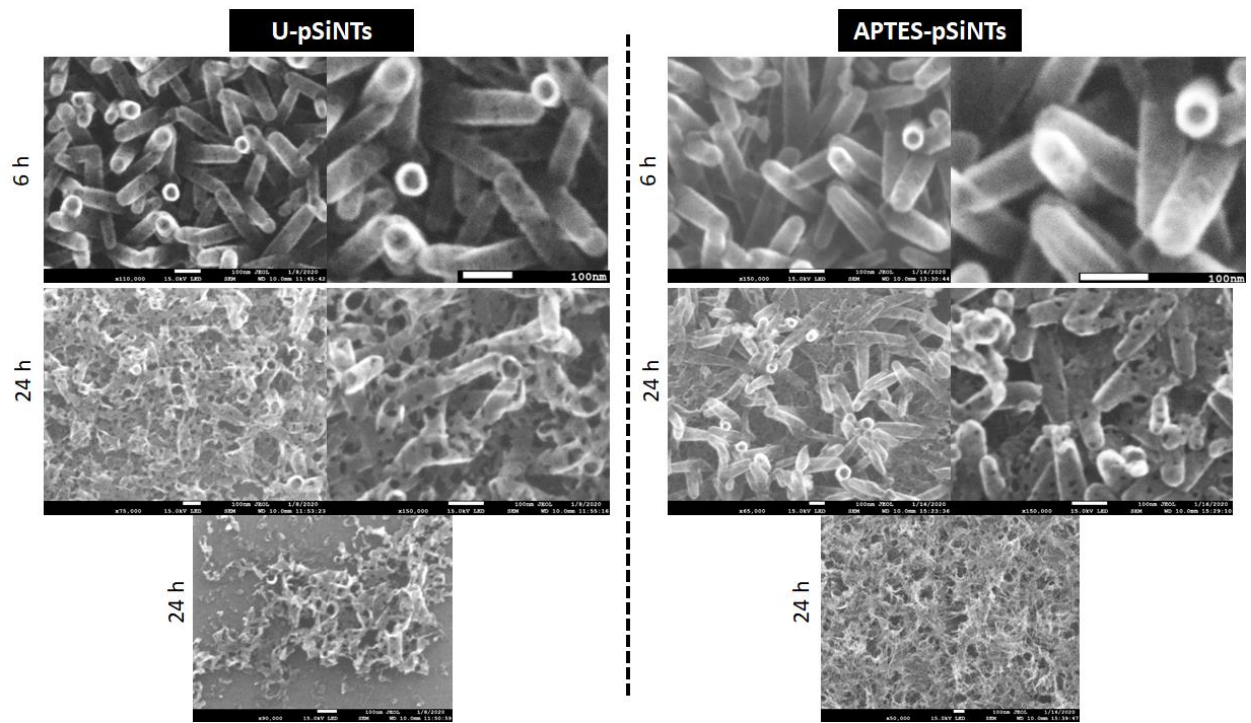
Figure 32. SEM imaging of U-pSiNTs and APTES-pSiNTs before and after incubation in cell culture medium at 37 °C for 6 h and 24 h. Scale bars: 100 nm.
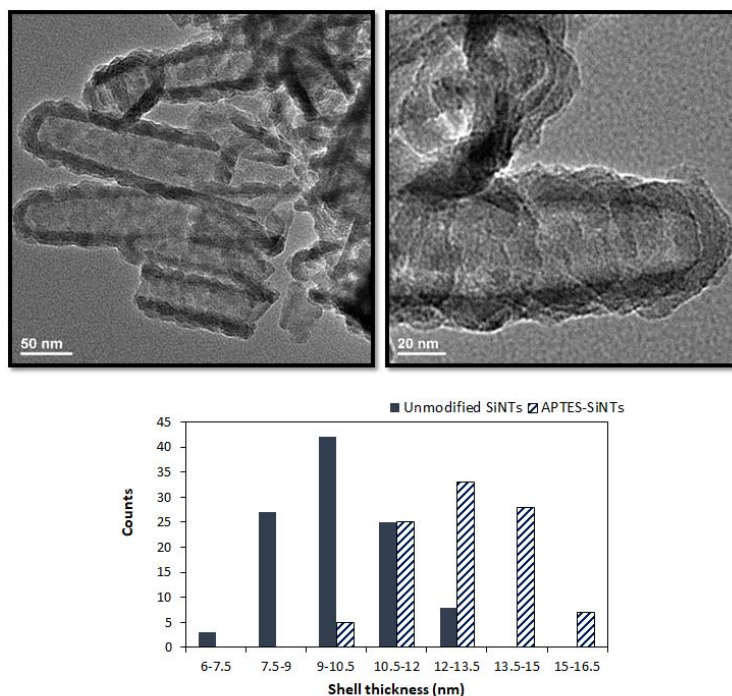
Figure 33. Surface morphology of APTES-pSiNTs after functionalization and distribution of shell thickness before and after functionalization.

2.3.4 Cellular Interactions with Functionalized pSiNTs

Since biocompatibility of a given nanomaterial is partly influenced by its surface chemistry,[157] it is important to evaluate the impact of the functionalized pSiNTs on cancer cells in order to address any potential adverse effects originating intrinsically from a given platform prior to any studies involving release of an anti-cancer drug. Here, cytotoxicity of APTES and triamine-functionalized pSiNTs to HeLa cervical cancer cells was evaluated. After 36 h, the functionalized pSiNTs appeared to accumulate around the nuclei and did not significantly affect cell morphology when compared to the no-treatment control (Figure 34). In addition, viability assays suggested the materials negligibly exerted toxicity to the cells after 36 h, thus indicating biocompatibility of the materials at the tested concentrations (Figure 35).

With biodegradability of the pSiNTs in the cell culture medium demonstrated, it is necessary to assess the morphology of the degraded pSiNTs in the presence of cells along with the metabolic byproducts. Using TEM imaging, the morphology of the remaining nanotubes harvested by cell lysis after the treatments were evaluated (Figure 36). Consistent with SEM imaging studies, APTES-pSiNTs readily degraded after 36 h as indicated in the disappearance of the defined nanotube construct. On the other hand, Triamine-pSiNTs remained intact after the same period of time. The lack of degradation is originated from the relatively higher amino group density compared with that of APTES-pSiNTs, thus creating a relatively higher local acidic environment on the nanotube surface and reducing its dissolution rate. In addition, presumably owing to steric hindrance of the longer alkyl chain of the triamine molecules, medium diffusion might also be hampered.

Therefore, by probing the nanotube morphology via TEM imaging, the dissolution rate of Triamine-pSiNTs was qualitatively demonstrated to be slower than that of APTES-pSiNTs. In addition, together with the viability studies presented above, it can be concluded that the degradation byproducts also negligibly exert adverse effects to viability of the type of cancer cells studied herein.
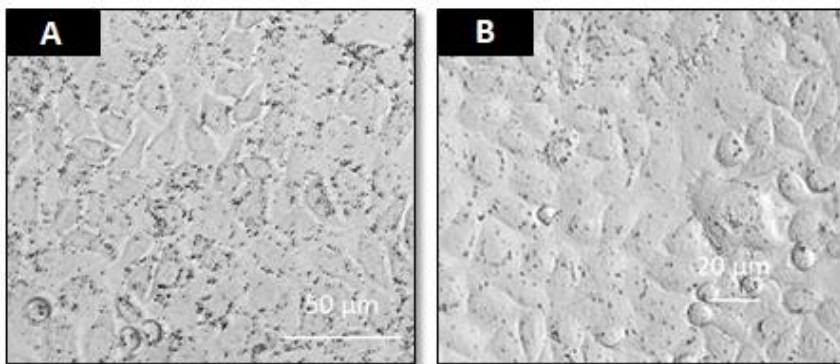
Figure 34. Cellular interactions with A) APTES-pSiNTs and B) Triamine-pSiNTs.
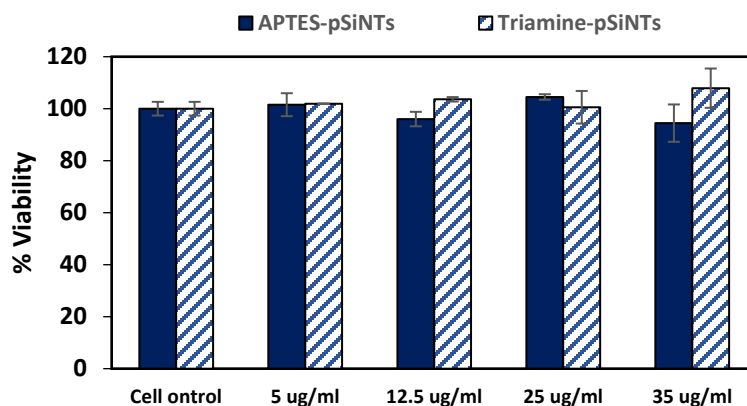
Figure 35. Cytotoxicity of APTES-pSiNTs and Triamine-pSiNTs after 36-h treatment.
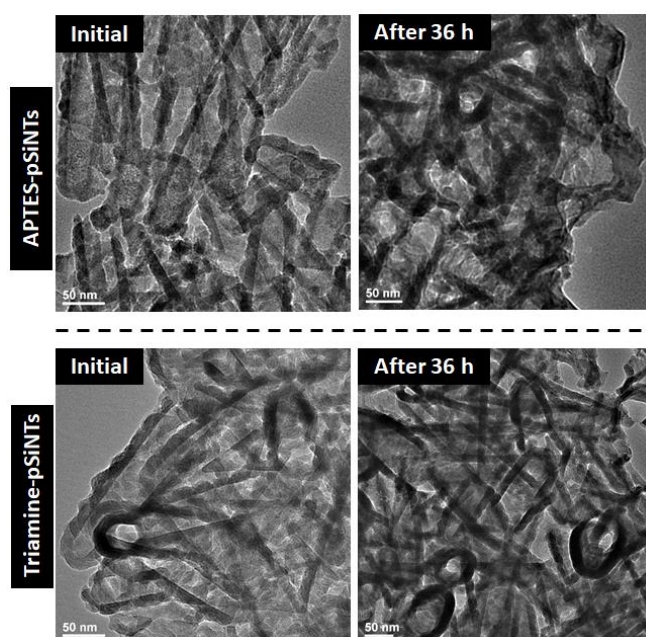
Figure 36. TEM imaging of APTES-pSiNTs and Triamine-pSiNTs before and after 36-h exposure to cancer cells in the complete growth medium. Scale bars: 50 nm.

2.4 Summary

This Chapter describes a facile method for controlling nanotube length via modulating ZnO NW growth time, thus suggesting feasibility of tuning an additional structural parameter of

nanotubes along with inner diameter, shell thickness and surface morphology to be suitable for the target applications. In the context of therapeutic delivery, the majority of the pSiNTs bundles in the sub-micron regime can readily be achieved by simple ultrasonication.

In addition, bio-relevant properties of pSiNTs and the functionalized materials including biodegradability and biocompatibility were described in this Chapter. Although, the current stage of the studies presented herein is still in its infancy, recognizing the need for evaluations of genotoxicity and *in vivo* studies to fully confirm biocompatibility of pSiNT and its derivatives, these preliminary results provide important information regarding the impacts of pSiNTs *in vitro* and encourage future studies involving pSiNT as the therapeutic platforms.

Chapter III

Formation of Platinum Nanocrystals on Porous Silicon Nanotube Templates

3.1   Introduction

Pt-based metal complexes, notably cisplatin, $Pt(NH_3)_2Cl_2$, are among the anticancer agents commonly used for treatment of a variety of cancers, including lymphomas and carcinomas, by exerting damage to DNA.[158] Nevertheless, several therapeutic delivery systems, such as polymers and inorganic nanoparticles, have been designed to locally deliver a high concentration of the drug while minimizing adverse side effects partly imparted by non-specificity.[42, 159]

Since biocompatibility and degradability of pSiNTs have been demonstrated in earlier chapters, these initial results encouraged us to evaluate the use of the materials as a delivery vector for cisplatin. One initially envisioned approach was to coordinate cisplatin to the amino moieties of APTES linker grafted on pSiNTs surface, thereby locally concentrating the therapeutically-active $[Pt(NH_3)_2]^{2+}$ species on the nanotube surface, which can be modified or loaded with other entities (i.e. targeting peptides or magnetic nanoparticles) designed for targeted delivery. Interestingly, in reactions where an established high-purity cisplatin (Sigma-Aldrich) was utilized, a relatively low amount of platinum species [2 wt % (TEM-EDX)] is detected that was not visually observable by TEM imaging; in stark contrast, a significantly higher density of ultrasmall crystalline Pt species [45 wt % (TEM-EDX)] were surprisingly observed when using cisplatin prepared and donated by a local small contract research firm. Further investigations into impurities present in the latter cisplatin have led to the intriguing discovery of a facile synthetic method for platinum nanocrystals (Pt NCs) uniformly deposited on pSiNT matrices.

In this Chapter, a series of experimental studies and results that tell the story behind the discovery of this novel synthetic route is described. Also, an evaluation of possible factors that contribute to formation of Pt NCs is presented, followed by a discussion of strategies for systematic control of the concentration of Pt NCs clusters formed on pSiNT templates.

3.2 Experimental

APTES-pSiNTs utilized in all experiments described in this Chapter were produced by functionalizing pSiNTs (1.5-h ZnO NWs) with APTES according to the protocol described in Chapter 2 unless otherwise stated. Zeta potential analyses were also performed to validate functionalization processes.

3.2.1   Initial Experiments with Cisplatin Obtained from Different Sources

   a) Conjugation of Cisplatin to APTES-pSiNTs

APTES-pSiNTs adhered to a given substrate (i.e. FTO glass) were incubated in cisplatin solution (3.32 mM, 2 ml) at room temperature (RT ~ 20 °C) for 24 h with constant stirring (200 rpm on a Fisher Scientific hot plate-stirrer). After incubation, the samples were washed with DI H_2O, EtOH and dried in air. Cisplatin utilized herein was obtained from two different sources: one was purchased from Aldrich Chem Co (Purity: 99.9%). and the other was received as a donation from a local contract research firm that had been prepared by that organization.

   b) Evaluation of Cisplatin Purity

Purity of cisplatin was evaluated using a UV absorption spectral method, where the absorption spectra of the stock solutions (prepared in deionized water) (1 mg/ml) were recorded using a Beckman Coulter spectrophotometer (DU 800), and the absorbance λ_{300}: λ_{247} ratio was evaluated. Cisplatin with acceptable purity should not have a ratio of less than 4.5.[160]

   c) Identification of Impurities in Cisplatin

The two components of Magnus's salt, $[Pt(NH_3)_4]^{2+}$ and $[PtCl_4]^{2-}$, were tested as the possible major impurities in cisplatin.[161, 162] Here, APTES-pSiNTs remained attached to the

substrates (i.e. FTO) were incubated in $[Pt(NH_3)_4]Cl_2$ (3.3 mM) or K_2PtCl_4 (3.3 mM) at RT for 24 h with constant stirring (200 rpm). The samples were washed with DI H_2O, EtOH and dried in air.

3.2.2 Control experiments

a) Influence of the Amino Groups to Formation of Pt NCs

To evaluate the roles of the NH_2 groups, unmodified-pSiNTs (U-pSiNTs) were incubated with potassium tetrachloroplatinate (K_2PtCl_4) solutions (prepared in DI H_2O) of different concentrations (0.5 mM, 1.5 mM and 3.3 mM) for 4 h and 24 h at RT with constant stirring (200 rpm). After incubation, the substrates were washed with DI H_2O, EtOH and then dried in air.

b) Synthesis of Silica Nanotubes (SiO$_2$ NTs)

Silica nanotubes (SiO$_2$ NTs) were synthesized using the sol-gel based procedure developed by Yin and co-workers.[163] Cyclohexane (15 ml) was added to a round-bottom flask containing Brij 58 (8.5 g) and the mixture was stirred at 50 $^{\circ}$C until the surfactant was completely dissolved. Then, $NiCl_2$ solution (0.8 M, 1.9 ml) was added into the mixture. After $NiCl_2$ was completely dissolved, hydrazine hydrate (0.45 ml) was added dropwise into the mixture. After 3 h, diethylamine (1 ml) was added into the solution and tetraethyl orthosilicate (TEOS) (3 ml) was added dropwise. After 2 h, the mixture was centrifuged and washed extensively with isopropanol to remove any residues. Next, the product (0.4 g) was stirred in HCl (1 M, 30 ml) to remove the $NiCl_2$-hydrazine core and yield a hollow SiO$_2$ NT structure. The as-prepared SiO$_2$NTs were then calcined in air at 500 $^{\circ}$C for 4 h to remove any remaining organic residue from the samples.

3.2.3 APTES Functionalization and Synthesis of Pt NCs on SiO$_2$ NTs

The calcined SiO$_2$ NTs (5 mg) were functionalized in 2 % APTES solution (2.5 ml) (solvent: toluene) for 4 h with constant stirring (200 rpm). Then the sample was centrifuged and

washed with toluene 3 times and acetone 2 times. The functionalized materials were dried *in vacuo* overnight.

Unmodified SiO_2 NTs or APTES-functionalized SiO_2 NTs were incubated in K_2PtCl_4 (2 mL, 1.5 mM) at RT for 24h. The product was centrifuged, washed with deionized water and finally dried with ethanol.

3.2.4 Quantification of the Density of NH_2 Groups (from APTES) Grafted on SiO_2 NTs

The well-known Kaiser test was adapted from Soto-Cantu's procedure (with some minor modifications) for the purpose of estimating the density of amine moieties present on silica nanotube surfaces.[164] In this method, ninhydrin reacts with the amino group of APTES and produces a blue-purple product or "Ruhemann's purple." Here, APTES-functionalized SiO_2 NTs (2 mg in 0.5 mL deionized water) were mixed with EtOH (3.5 mL). The sample was briefly sonicated in an ice bath for 10 s, and a ninhydrin solution prepared in EtOH [0.35 % (w/v), 1 ml], was added into the vial. The mixture was heated in an oil bath at 65°C for 30 min. After the samples were cooled down to RT (about 15 min), the mixtures were centrifuged, and the absorbance of the supernatant was measured at 574 nm using a Beckman Coulter spectrophotometer (DU 800). To construct a calibration curve, the above procedure was performed with a series of standard glycine solutions of known concentration (Figure 37).
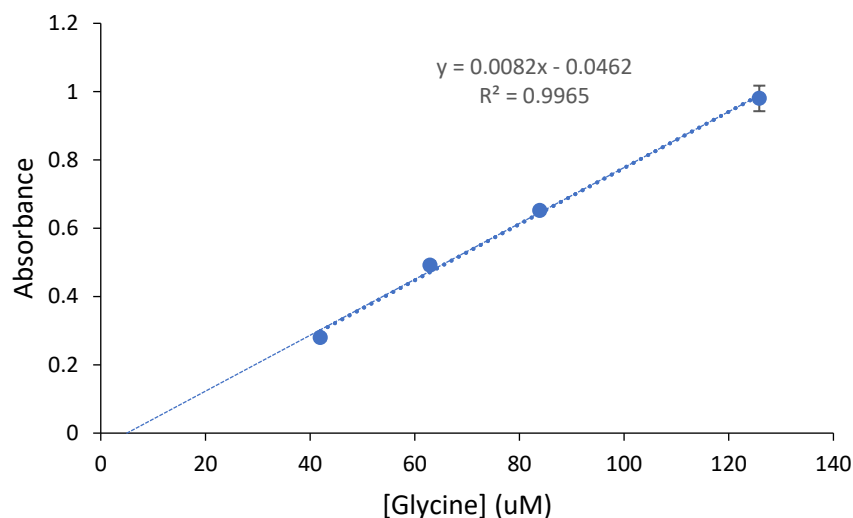
Figure 37. Calibration curve showing absorbance as a function of glycine concentration (Note: some errors bars are too small to be visible in the graph).

3.2.5 Control of Platinum Nanocrystals (Pt NCs) Density on APTES-pSiNTs

APTES-pSiNTs attached to a given substrate were incubated in K_2PtCl_4 solutions (prepared in DI H_2O) of different concentrations (0.5 mM, 1.5 mM and 3.3 mM) for 4 h and 24 h at RT with constant stirring (200 rpm). After incubation, the substrates were washed with DI H_2O, EtOH, and then dried in air.

For determination of Pt content in SiNT samples using Transmission electron microscopy - energy dispersive X-ray analysis (TEM-EDX), the EDX analysis method employed here uses a Pure Element Intensity Factor (PEIF) to calculate the k-ratio, which is then corrected by ZAF to determine the composition of a sample. All EDX spectra were consistently acquired using 200 kV, 80,000 magnification, and a ~700 nm x 700 nm scanning area.

3.3   Results and Discussion

3.3.1   Initial Experiments with Cisplatin Obtained from Different Sources

For the initial experiments regarding conjugation of cisplatin to APTES-pSiNTs via a linker strategy, the presence of cisplatin was evaluated by probing the Pt content using TEM imaging and energy dispersive X-ray analysis (TEM-EDX). In the case of the functionalized nanotubes incubated with the commercial cisplatin, the morphology of the nanotubes was similar to the untreated-materials, presumably owing to the small molecular size of the intact cisplatin molecules in conjunction with a low conjugation efficiency (2 wt % Pt) (Figure 38 A1). Conversely, with the non-commercial cisplatin, a highly uniform and dense clusters of ultrasmall platinate (i.e. Pt^0) species deposited on the nanotube surface was observed (Figure 38 B1). At sufficient magnification, these species exhibited characteristic lattice spacings associated with Pt (d = 0.24 nm), proof of the existence of crystalline Pt nanoparticles (Figure 39).

In order to elucidate such drastic differences in the cisplatin/APTES-pSiNT products, the purity of cisplatin was validated by using standard spectrometric assays of the $\lambda_{300}/\lambda_{247}$ ratio, whose value of 4.5 or higher indicates satisfactory purity.[160] Here, while the purity of the commercial cisplatin was confirmed ($\lambda_{300}/\lambda_{247}$ = 4.58) and agreed with the manufacturer's claim (99.9% purity), the non-commercial product, however, did not achieve the acceptable purity level (Figure 38 A2 and B2), thus suggesting the impurities in the cisplatin obtained from donation might possibly be responsible for the formation of the crystalline Pt species.
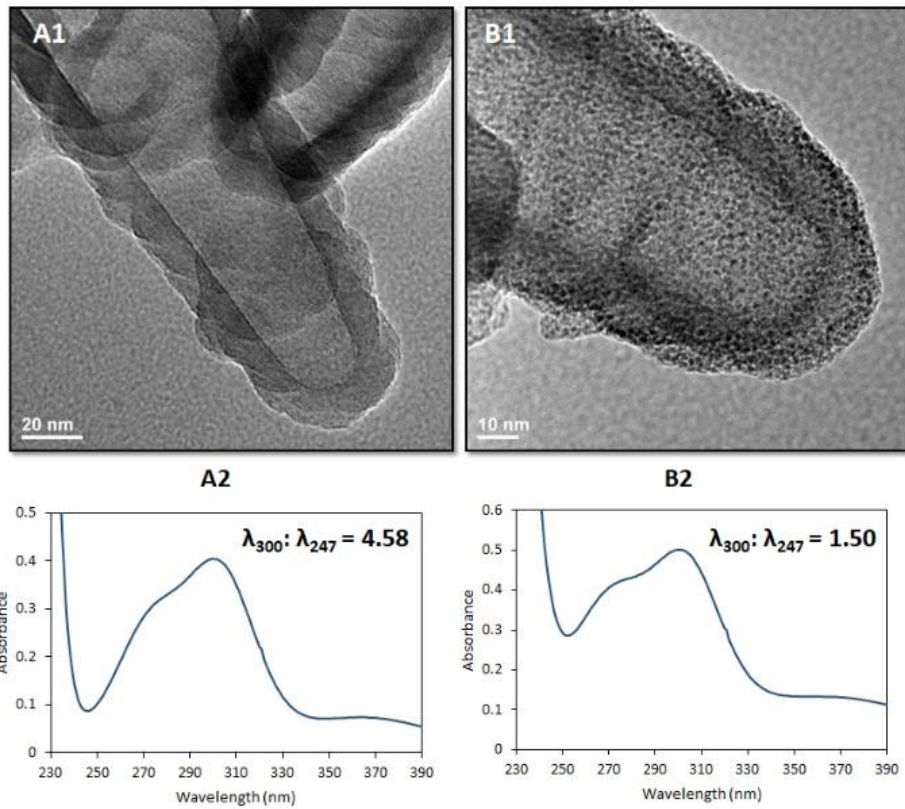
Figure 38. TEM imaging of APTES-pSiNTs after incubation in two different solutions of cisplatin (3.3 mM) and the corresponding UV-Vis spectrum of each cisplatin solution: commercial cisplatin (A1 and A2); non-commercial cisplatin (B1 and B2).

	Weight%
O	15.82 ± 0.84
Si	38.39 ± 4.65
Pt	44.74 ± 4.94
Cl	1.06 ± 0.26
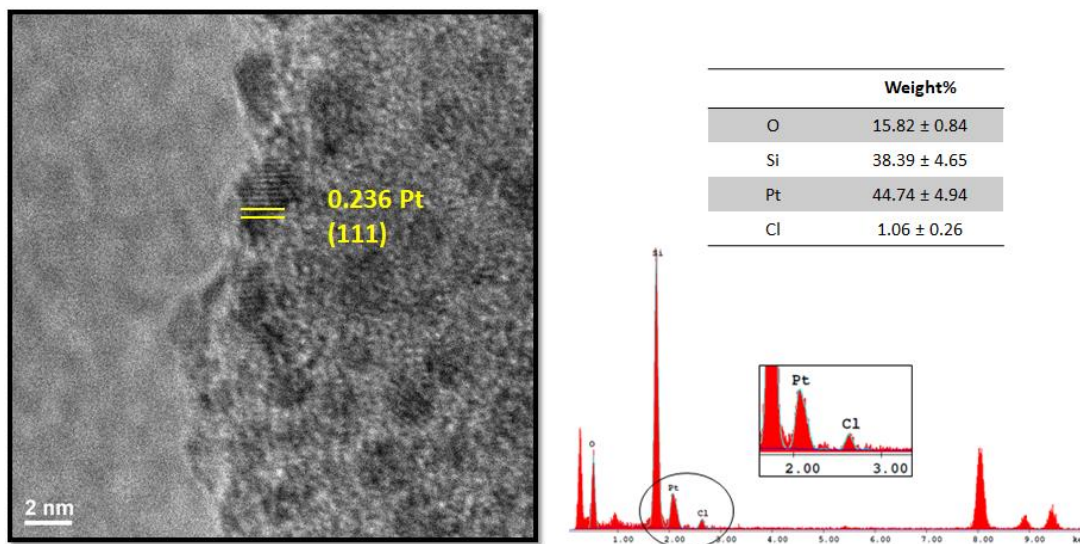
Figure 39. HR-TEM imaging of Pt species formed on the functionalized pSiNTs after 24-h reaction with the non-commercial cisplatin; The associated TEM-EDX spectrum and elemental quantification confirmed the high concentration of Pt species.

Identification of the Major Impurities in Cisplatin

To date, multiple synthetic routes of cisplatin have been explored with K_2PtCl_4 commonly employed as the starting material. One of the approaches to yield cisplatin reported in earlier studies involves direct addition of ammonia, NH_3, to the Pt salt precursor; nevertheless, this procedure inevitably yields Magnus's green salt, which is composed of $[Pt(NH_3)_4]^{2+}$ and $[Pt(Cl)_4]^{2-}$ as a side product.[161, 162] Thus, Magnus's green salt along with the excess K_2PtCl_4 might be the major impurities in the non-commercial/donated cisplatin and possibly facilitated the formation of a high density of metallic Pt species.

Here, whereas the reaction with $[Pt(NH_3)_4]^{2+}$ component of the Magnus's salt yielded a negligible amount of Pt (~1 wt %); interestingly, a uniform coverage of Pt species (60 wt%) with relatively high crystalline domains was observed in the case of K_2PtCl_4 (Figure 40), thereby suggesting $PtCl_4^{2-}$ is the major constituent in the non-commercial/donated cisplatin responsible for the generation of the ultrasmall Pt NCs on APTES-functionalized pSiNTs.

74
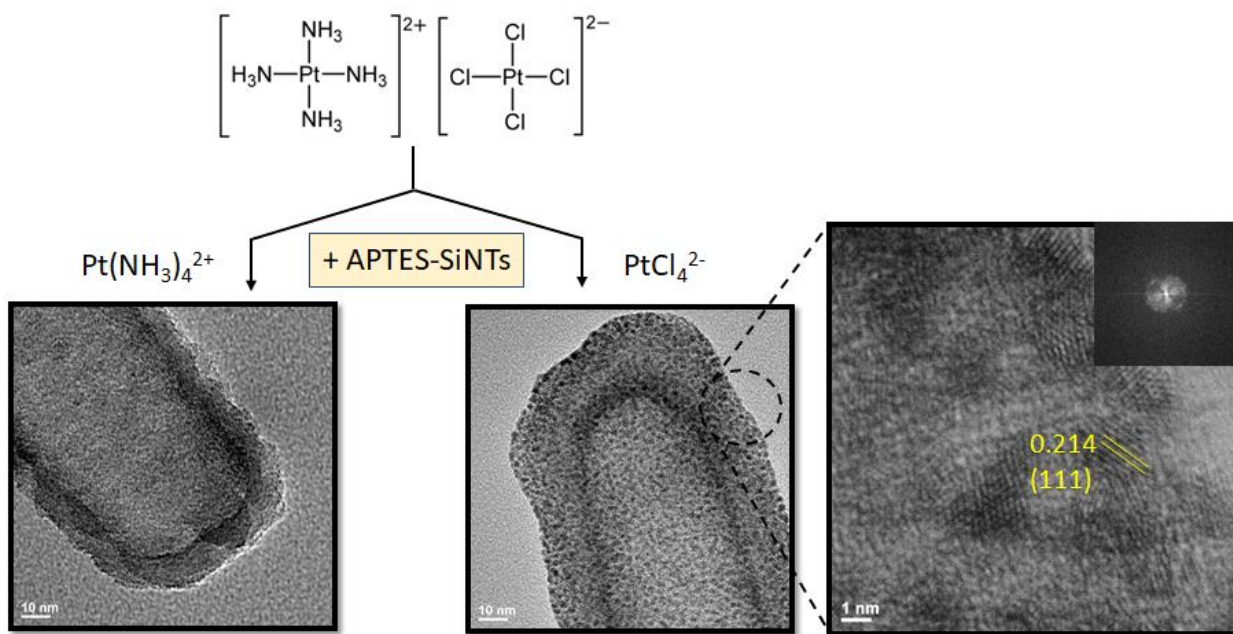
Figure 40. Molecular structures of Magnus's green salt and TEM imaging of the functionalized pSiNTs after reactions with $[Pt (NH_3)_4]^{2+}$ and $[PtCl_4]^{2-}$. HR-TEM imaging showing lattice spacing of the crystalline Pt NCs formed on the nanotubes after incubation in $PtCl_4^{2-}$.

3.3.2 Control Experiments

Since Pt NCs form on the functionalized pSiNTs in the absence of any external reducing agents, the logical question of what is the most likely species responsible involved in reduction of Pt^{2+} to the metallic Pt^0 emerges. Possibilities include: 1) network of Si-Si bonds; 2) polyols (i.e. silanol (Si-OH) moieties); 3) the amine moieties emanating from APTES. To address options (1) and (2) the following controls, unmodified pSiNTs and SiO_2 NTs produced via a sol-gel method, were assessed to identify the impact of Si-Si bonds and polyols, respectively. [165]

a) Formation of Pt Species on Unmodified pSiNTs

It has been demonstrated that Si-Si bonds, along with Si-H species, of pSi can act as efficient reducing agents to effectively mediate deposition of various metals (e.g. Cu, Pt and Ag) on pSi template in immersion plating methods.[166, 167] While pSiNTs produced here are oxide

75

terminated, Si-Si bonds were presumably involved in facilitating the formation of Pt^0. The exposure of U-pSiNTs to dilute $PtCl_4^{2-}$ solutions resulted in a trace amount of Pt species that randomly deposited on the nanotube surface. In addition, varying reaction time and concentration of the Pt salt precursor also did not significantly enhance the density of Pt species (Figure 41 and Table 6), thus suggesting any exposed Si-Si bonds in the nanotube framework played a minor role in the formation of Pt NCs.
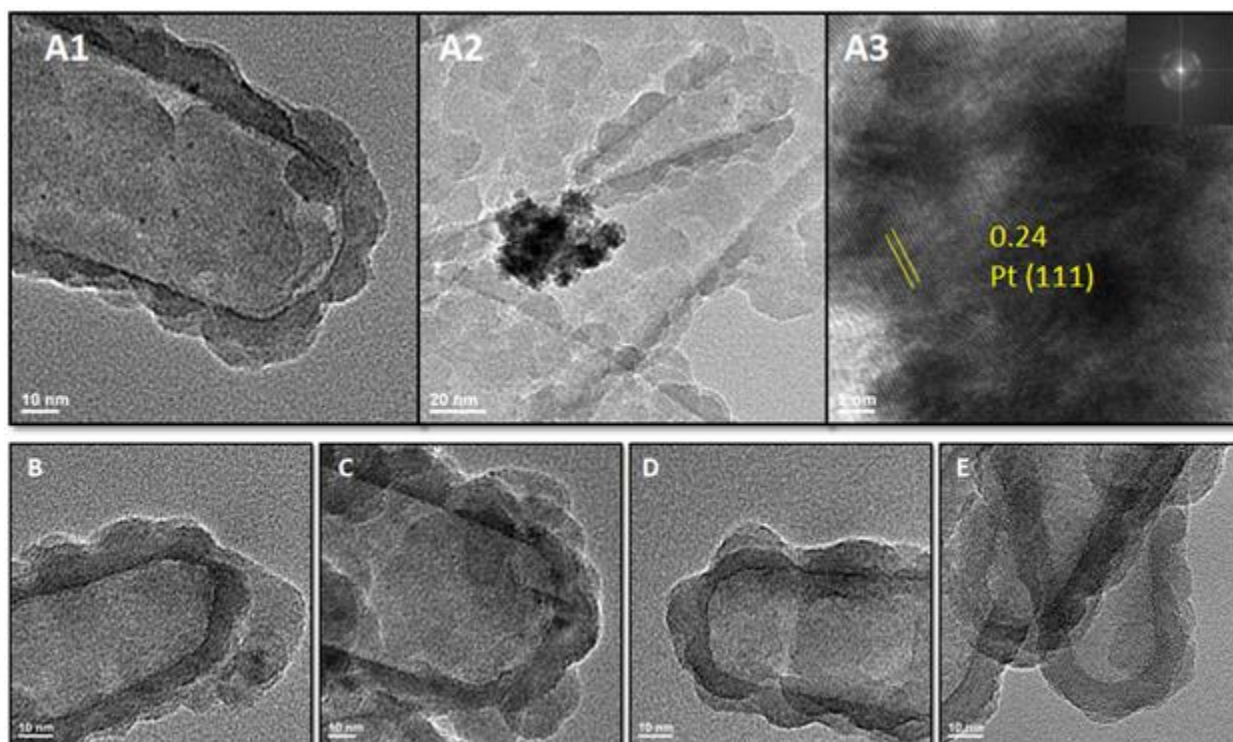
Figure 41. TEM imaging showing U-pSiNTs incubated in various concentrations of K_2PtCl_4 for different time periods: A1-A3 3.3 mM (24 h), A3: HR-TEM imaging showing lattice spacing of a cluster of Pt species deposited on the nanotube surface; B) 0.5 mM (4h), C) 24h, D) 1.5 mM (4h) and E) 1.5 mM (24h).

Table 6. Elemental analysis (wt %) of platinate species deposited on U-pSiNTs.

Time (h)	[K_2PtCl_4] (mM)	Si	O	Pt	Cl
4h	0.5	76.66 ± 2.72	21.97 ± 2.40	0.69 ± 0.47	0.68 ± 0.23
4h	1.5	66.89 ± 3.31	32.09 ± 3.47	0.57 ± 0.16	0.53 ± 0.23
24h	0.5	73.46 ± 5.99	24.84 ± 4.70	0.28 ± 0.57	1.42 ± 0.89
24h	1.5	75.10 ± 1.27	22.52 ± 1.14	0.67 ± 0.53	1.71 ± 0.56
24h	3.3	71.04 ± 1.57	27.12 ± 1.27	1.28 ± 0.05	0.56 ± 0.35

b) Synthesis of SiO$_2$ NTs and APTES-functionalized SiO$_2$ NTs

Since polyols (commonly from glycolic solvents) have been demonstrated to mediate the formation of various metal NPs,[168] SiO$_2$ NTs (length = 200 nm; inner diameter = 20 nm and shell thickness = 7 nm) produced via a sol-gel method were evaluated as the control to assess the reducing ability of the polyols, i.e. silanol groups in this case (Figure 42, Figure 43 and Table 7).

Here, only a negligible amount of Pt species was detected on the unmodified SiO$_2$ NTs upon exposure to PtCl$_4^{2-}$, thus indicating the insignificant role of the silanol groups in the reduction of Pt^{2+}. Conversely, an appreciable density of Pt species (19 wt% Pt) was only observed on the functionalized SiO$_2$ NTs, confirming the pivotal role of the primary amine moieties in facilitating the generation of Pt NCs (Figure 44 and Table 8).

Since various amines, such as oleyl amine and triethylamine, have been employed as efficient reductants to synthesize metallic Au NPs,[169-171] we propose that the amino groups stemming from the APTES moieties not only coordinate with PtCl$_4^{2-}$ species but also presumably serve as reducing agents to convert Pt^{2+} to Pt^0. In addition, based on the quantitative colorimetric Kaiser's tests performed with the functionalized SiO$_2$ NTs, a density of (2.73 ± 0.89) x10^4 NH$_2$ moieties/nanotube or 0.767 ± 0.025 NH$_2$ groups / nm^2 was sufficient to yield the metallic Pt species

(calculation method adapted from ref. 172 with minor modifications. Note: nanotubes are assumed as hollow cylinders with closed ends).
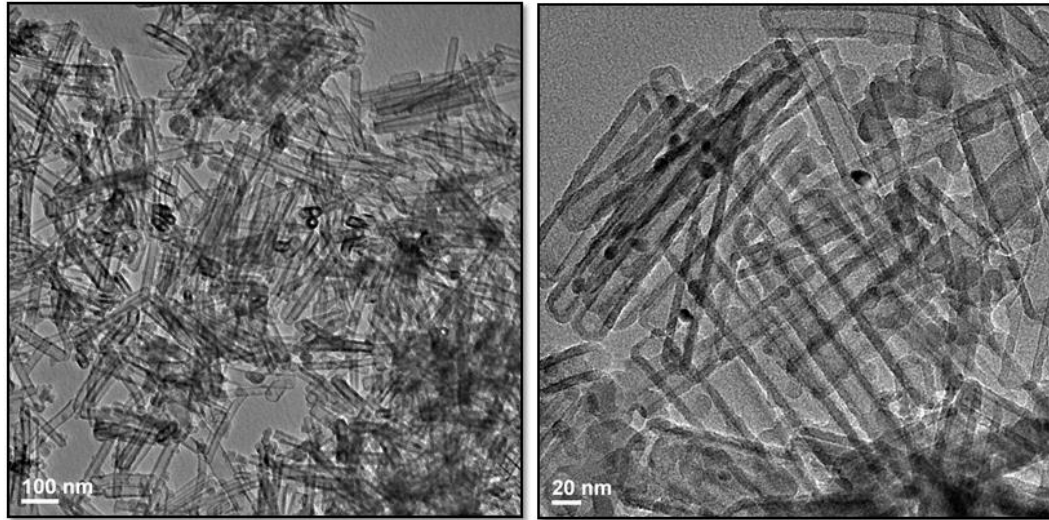
Figure 42. TEM imaging showing structural morphology of SiO_2 NTs.
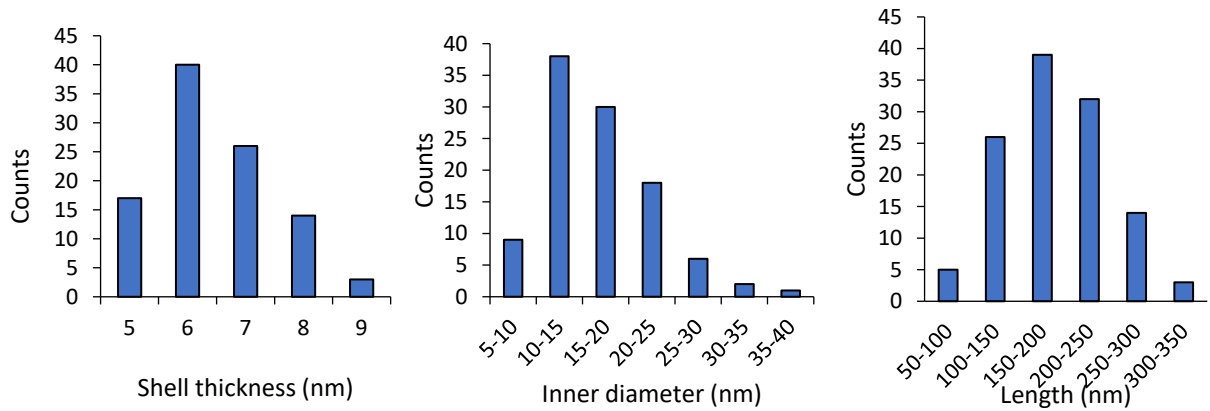
Figure 43. Size distributions of shell thickness, inner diameter and length of SiO_2 NTs.

Table 7. Summary of size distributions of structural parameters of SiO_2 NTs.

	Inner diameter (nm)	Shell thickness (nm)	Length (nm)
Average ± Stdev	16.7 ± 5.9	6.9 ± 1.0	188.5 ± 55.6
Min	6.4	5.3	56.7
Max	38	9.7	333.4
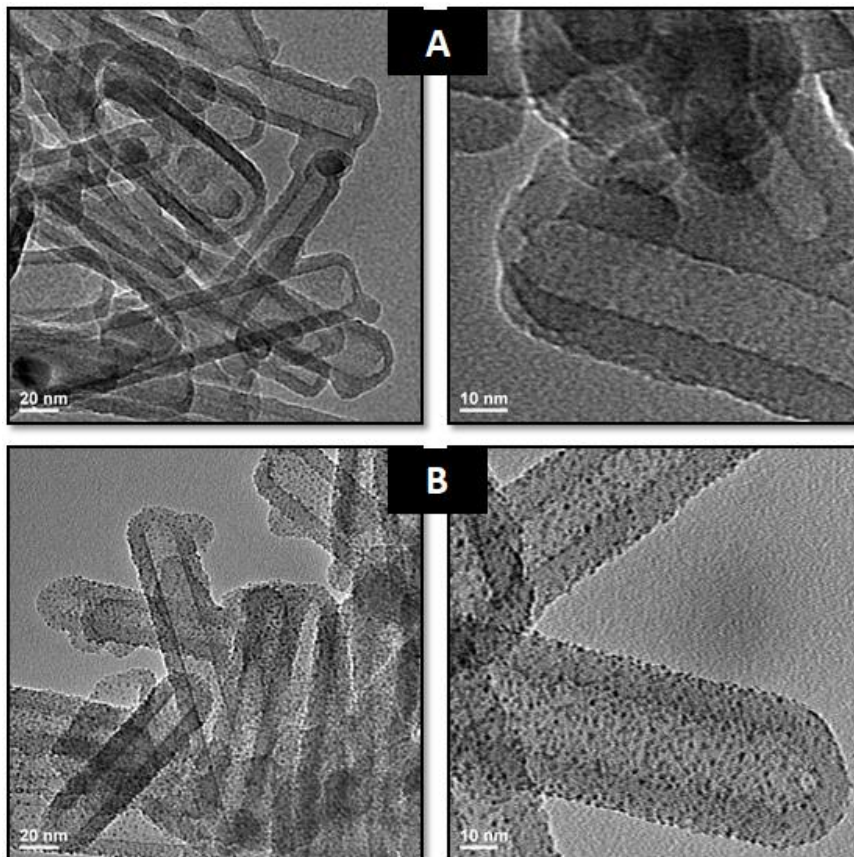
Figure 44. TEM imaging of A) U-SiO$_2$NTs and B) APTES-SiO$_2$ NTs after incubation in K$_2$PtCl$_4$ (3.3 mM) for 24 h.

Table 8. TEM-EDX analysis of the elemental contents of SiO$_2$ NTs after incubation in 3 mM K$_2$PtCl$_4$.

U-SiO$_2$ NTs	Wt %	At %	APTES-SiO$_2$ NTs	Wt %	At %
Si	43.15 ± 0.95	30.46 ± 0.96	Si	36.79 ± 2.03	31.64 ± 2.21
O	56.22 ± 1.13	69.51 ± 0.91	O	43.49 ± 3.22	65.53 ± 2.50
Pt	0.55 ± 0.48	0.06 ± 0.05	Pt	19.05 ± 2.96	2.37 ± 0.44
Cl	0.07 ± 0.08	0.04 ± 0.04	Cl	0.68 ± 0.20	0.47 ± 0.15

3.3.3   Characterization of Pt NCs-pSiNT composites prepared using K$_2$PtCl$_4$

Common synthetic methods for crystalline Pt nanoparticles typically involve addition of reducing agents, such as NaBH$_4$ and ascorbic acid, to facilitate the reduction of Pt^{2+}. In order to

maintain stability of the freestanding nanoparticles, especially for long term storage, addition of surfactant cetyltrimethylammonium bromide (CTAB) or polymeric stabilizers such as polyvinylpyrrolidone (PVP) are necessarily critical.[173, 174] For synthesizing ultrasmall Pt particles with diameters of a few nanometers (< 3 nm) (i.e. Pt NCs), more sophisticated reaction conditions are often required to yield a narrow size distribution while preserving particle stability. To date, some strategies, such as phase transfer method(s) or use of templates (e.g. dendrimers), have been demonstrated to successfully achieve Pt NCs as small as 1 nm.[175, 176] In our case, we have explored a facile reductant-free method, in which the functionalized pSiNTs are not only capable of serving as a solid support to achieve a uniform distribution of ultrasmall PtNCs (1-3 nm) but also effectively stabilize and minimize cross-fusion of the resulting NCs owing to the unique porous morphology of the platforms.

Further investigation into the tunability of Pt concentration suggests that the amount of Pt NCs deposited on the nanotubes can readily be modulated by controlling the reaction time and K_2PtCl_4 concentration. In this manner, the density of Pt NCs can be modulated in the range from 20 to 60 wt%.[165] Interestingly, for samples obtained after 24-h incubation, a relatively higher density of crystalline platinate species compared to 4-h samples was observed.

In addition to K_2PtCl_4, another Pt salt precursor, namely potassium hexachloroplatinate (K_2PtCl_6) also yielded a high density of Pt species on the functionalized pSiNTs. The lower concentration of Pt NCs (33 wt % Pt) compared to that obtained from K_2PtCl_4 (60 wt % Pt) might presumably attributed to a higher reduction potential required for reducing Pt^{4+} to Pt^0.
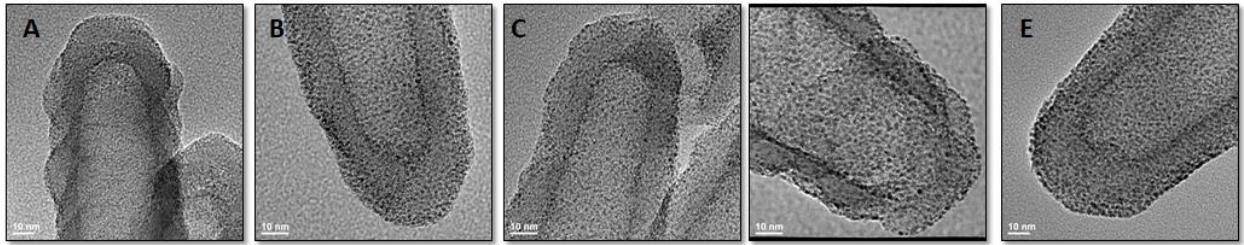
Figure 45. SiNTs with uniform coverage of different concentration of Pt NCs after being immersed in Pt salt precursor for different lengths of time. a) $K_2PtCl_4 = 0.5$ mM (4 h), b) $K_2PtCl_4 = 0.5$ mM (24 h), c) $K_2PtCl_4 = 1.5$ mM (4 h), d) $K_2PtCl_4 = 1.5$ mM (24 h), e) $K_2PtCl_4 = 3.3$ mM (24 h). Scale bar = 10 nm.
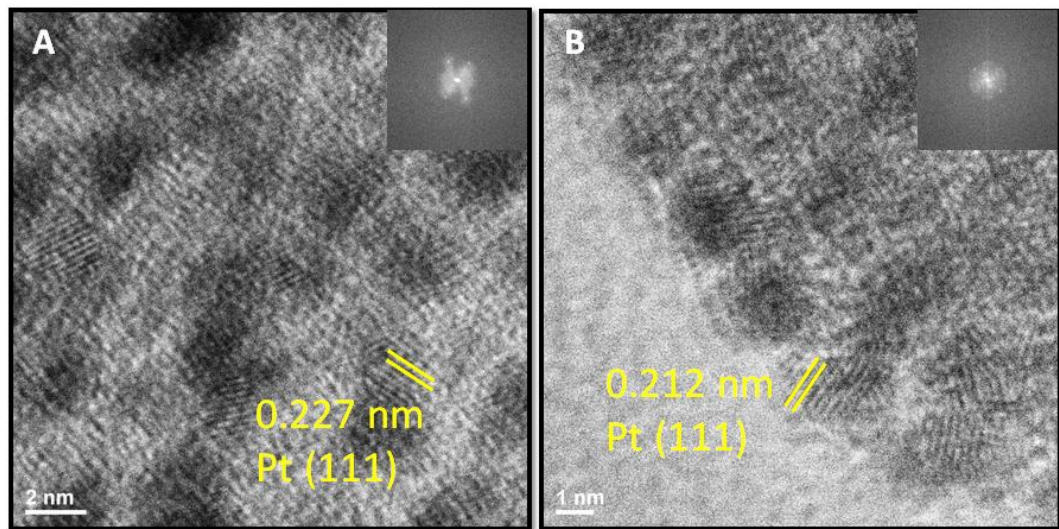
Figure 46. HR- TEM imaging provides insight into sizes and lattice spacing of Pt NCs (APTES-SiNTs were immersed in (A) 1.5 mM and (B) 3.3 mM K_2PtCl_4 for 24 h.

Table 9. Elemental analysis (wt %) of Pt-SiNTs composites prepared under different reaction conditions ([K$_2$PtCl$_4$] and immersion time in Pt precursor) (adapted from ref. 165).

Time (h)	[K$_2$PtCl$_4$] (mM)	Si	O	Pt	Cl
4h	0.5	62.3 ± 1.7	17.5 ± 1.3	18.4 ± 0.8	1.8 ± 0.3
4h	1.5	45.4 ± 2.3	14.4 ± 0.4	37.1 ± 2.0	3.1 ± 0.5
24h	0.5	48.2 ± 1.2	11.7 ± 2.2	37.3 ± 2.3	2.8 ± 0.5
24h	1.5	32.2 ± 1.6	9.7 ± 1.2	54.8 ± 1.4	3.3 ± 0.5
24h	3.3	20.3 ± 0.4	11.3 ± 2.3	63.0 ± 2.3	5.4 ± 0.5
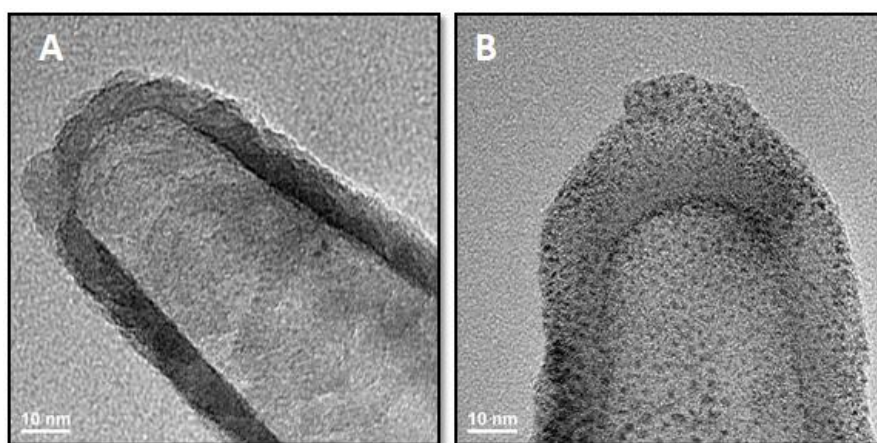
Figure 47. Formation of platinate species on A) U-pSiNTs and B) APTES-pSiNTs using K$_2$PtCl$_6$ (3.3 mM, 24 h) as the Pt salt precursor.

Table 10. Elemental analysis of Pt-SiNTs composites deposited on U-pSiNTs and APTES-pSiNTs prepared with K_2PtCl_6 (3.3 mM, 24 h).

U-pSiNTs	Wt %	At %	APTES-pSiNTs	Wt %	At %
Si	69.01 ± 4.39	60.07 ± 1.99	Si	46.05 ± 2.04	55.36 ± 2.54
O	25.46 ± 2.95	38.80 ± 2.29	O	16.56 ± 1.47	34.89 ± 2.28
Pt	4.82 ± 6.61	0.65 ± 0.93	Pt	33.16 ± 2.51	5.75 ± 0.61
Cl	0.56 ± 0.25	0.39 ± 0.20	Cl	4.10 ± 0.66	3.89 ± 0.55
K	0.14 ± 0.09	0.09 ± 0.05	K	0.14 ± 0.09	0.12 ± 0.07

3.4   Summary

In this Chapter, a facile method of synthesizing Pt NCs using pSiNTs as a scaffold has been explored. In the context of therapeutics, Pt NPs, especially those with ultrasmall size (i.e. < 3 nm) have demonstrated exceptional anticancer property (i.e. overcome the chemoresistance in hepatocellular carcinoma), owing in part to the high surface area.[177, 178] Since tunable payload of Pt NCs can be achieved and stabilized by SiNTs, a novel delivery system was envisioned, in which the biocompatible pSiNT component can serve as an effective biodegradable delivery vector for the therapeutic Pt NCs. Hence, inspired by the preceding therapeutic studies, anti-cancer activity *in vitro* of this nanocomposite was assessed and described in detail in Chapter 4.

Chapter IV

In vitro Anticancer Activity of Pt Nanocrystals-Porous Silicon Nanotube Nanocomposites

4.1 Introduction

Platinum nanoparticles (Pt NPs), both free-standing as well as anchored on various surfaces, have attracted widespread attention in nano-catalysis (e.g. fuel cells) and electronics.[179, 180] However, in recent years, the potential merits of Pt NPs in therapeutics and diagnostics have also been recognized. In terms of anticancer therapy, Pt NPs have been demonstrated as NIR II-photothermal agents (strong absorption in the 1000 -1350 nm region) that effectively induce local heating upon NIR irradiation and thus ablate the target cancerous tumors.[181-183]

In addition, more recent reports have explored the intrinsic anticancer properties of Pt NPs which stems from cytotoxic Pt^{2+} leaching from the corrosive Pt surface upon exposure to a cellular environment.[177, 178, 184, 185] Owing to the high surface area associated with its ultrasmall size, especially those with sub-10 nm diameter, these NPs are readily oxidized since an increase in Pt^{2+} density with decreasing particle size is evidenced in earlier X-ray photoelectron spectroscopy (XPS) studies.[186] Upon endocytosis and subsequent entrapment within the intracellular vesicles (i.e. endosomes and lysosomes), the dissolution of the corroded Pt NPs was enhanced owing to the acidic environment of these organelles, thus eliciting damage to cellular functions.[184] Whereas cisplatin and other related Pt complexes exert damage to DNA via initial chelation with DNA base heteroatoms, several studies regarding Pt NPs exposure to cells suggest arrested growth and programmed cell death (apoptosis)a consequence of DNA platination and enhanced strand-breaks initiated by the leaching Pt^{2+} (Figure 48).[42, 187, 188] Recently, the Hyeon group successfully identified multiple genes (critical for proliferation of hepatocarcinoma cancer cells) that are downregulated after treatment with Pt NPs.[178] Interestingly, Pt nanocrystals (Pt NCs), whose size is less than 3 nm, trigger a higher reduction in cell viability than those with larger size, presumably owing to a relatively greater exposed surface area for dissolution.[178, 184, 185, 189] Since Pt NCs can

effectively overcome chemoresistance acquired by hepatocellular carcinoma after treatment with traditional anticancer drugs, such as cisplatin, Pt NCs are therefore an attractive alternative in cancer therapy.[178]

Figure 48. Schematic illustration of cytotoxic mechanism exerted by A) cisplatin and B) Pt NPs. (adapted from ref. 187)

In order to achieve optimal therapeutic outcomes with Pt NCs, drug carriers are not only required to encapsulate and deliver a controllable payload inside the cells, but they also must ideally be capable of maintaining high dispersity of the small-sized crystals to preserve their therapeutic activity.[185] To address these issues, Pt NCs immobilized in dendrimers[184] and pH-sensitive polymeric matrices[178] have been developed recently, and superior therapeutic efficacy to Pt-based metal complexes (e.g. cisplatin) have been achieved both *in vitro* and *in vivo*.

As described in previous chapters, delivery vectors with well-defined structures are of utmost interest in order to overcome multiple biological barriers. Thus, since pSiNTs with tunable

structures can readily serve as a facile template for formation and uniform distribution of a tunable concentration of Pt NCs (1-3 nm) (Chapter 3), therapeutic potential of this novel nanocomposites is suggested. In this Chapter, a time-dependent cytotoxicity exerted by Pt NCs-pSiNT to HeLa cervical cancer cells is described, followed by cellular uptake studies that elucidate the mechanisms of Pt species in eliciting cellular damage.

4.2   Experimental

4.2.1   Fabrication of Pt NCs-pSiNTs and Free-standing Pt NCs

a) Pt NCs-pSiNTs

Pt NCs/APTES-pSiNT composites were synthesized according to the procedure described in Chapter 3. Here, two different concentrations of Pt NCs formed on APTES-pSiNTs were obtained by incubating the functionalized nanotubes in 1.5 mM K_2PtCl_4 for 4 h and 24 h at room temperature. The resulting Pt NCs-pSiNTs were characterized by TEM imaging and TEM-EDX.

b) Freestanding Pt NCs

Small-sized freestanding Pt NPs were synthesized using a protocol adapted from Wu's method.[190] In particular, K_2PtCl_6 (1 mL, 8 mM) and sodium citrate (0.5 mL, 40 mM) were diluted in DI H_2O (18.5 mL), and the solution was stirred vigorously at room temperature for 30 min (400 rpm). Then $NaBH_4$ (100 μL, 50 mM) was slowly added dropwise into the above solution, and the resulting solution was continuously stirred for 1 h at room temperature. Pt NPs were characterized by TEM imaging and TEM-EDX.

4.2.2   Viability Assays

HeLa cells were maintained in complete cell growth medium: Dulbecco's modified Eagle's medium (DMEM) supplemented with 10 % heat-inactivated fetal bovine serum (FBS), penicillin

(88 U/mL), streptomycin (88 µg/mL), glutamine (0.88 mM) and 1/100 minimum essential medium (MEM) non-essential amino acids. Cells were maintained at 37 °C with 5 % CO_2 in air, in a humidified incubator.

HeLa cells were seeded at a density of 2000 cells/well (100 µl complete medium) in a 96-well plate, and the cells were incubated at 37 °C in the humidified incubator for 24 h. Next day, cells were treated with Pt NCs-pSiNTs, which were dispersed in the complete medium by ultrasonication (5 min in ice bath). The final concentrations of Pt NCs-pSiNTs in the wells were 35 µg/mL and 50 µg/mL. Cells were incubated for 48 h, 72 h and 96 h at 37 °C, 5 % CO_2.

CellTiter-Glo assays were performed to assess cell viability. After incubation for a specific period of time, the medium was removed, and cells were washed with PBS to discard any excess nanoparticles. Then the complete medium (50 µl) was added into each well, followed by the CellTiter-Glo reagent (Promega) (50 µl). The samples were mixed and incubated at room temperature for 5 min and 10 min respectively. The samples were then transferred to a 96-well black plate (clear bottom), and the luminescence measurements were acquired with a BMG Labtech FLUOstar Omega fluorescence/luminescence plate reader.

Cells were also treated with the following controls: U-pSiNTs (17.5 µg/mL, 25 µg/mL and 35 µg/mL), Pt NPs and K_2PtCl_4 ((10 µg/mL, 17.5 µg/mL, 25 µg/mL and 35 µg/mL)) and the viability assays were performed as described above.

4.2.3 Caspase 3/7 Assays

Cells were seeded and treated with Pt NCs-pSiNTs and U-pSiNTs as described above. After incubation, cells were washed with PBS to remove any excess nanoparticles. Caspase 3/7 activity was evaluated by using Caspase 3/7 Glo assays. Specifically, fresh complete medium (50 µl) followed by Caspase 3/7 Glo reagent (Promega) (50 µl) was added into each well. The samples

were mixed briefly for 30 s at room temperature, and the plate was incubated at room temperature for 1 h and covered in aluminum foil to protect the samples from light. Then the samples were transferred into a 96-well white plate (opaque bottom), and the luminescence was recorded. The caspase activity was normalized based on the cell number determined from cell viability assays.

For the control, caspase 3/7 assays were performed on cells after treatment with U-pSiNTs (25 μg/mL and 35 μg/mL).

4.2.4   Cellular Uptake Studies

a)   Non-fluorescent Labeling Method

Cells were seeded at a density of 1×10^4 cells/1ml/well in a 24-well plate and incubated at 37 °C with 5 % CO_2 in a humidified incubator for 24 h prior to treatment. Next day, cells were treated with Pt NCs-pSiNTs (35 μg/mL), and were incubated for 24 h, 48 h and 72 h. After incubation, the medium was removed and washed with PBS (1 mL) to remove excess composites, fresh complete medium (500 μL) was added into the well, and cells were observed using Zeiss Axiovert 200 microscope (in brightfield mode).

b)   Fluorescent Labeling Method

Pt NCs-pSiNTs were labeled with Alexa Fluor 594 NHS ester tris(triethylammonium salt) (Molecular Probes) by incubating the materials, which remained attached to the substrates, in a solution of excess Alexa Fluor 594 at 4 °C overnight. Samples were washed with DI H_2O and stored at 4 °C until uses. Prior to cell studies, the samples were scraped off from the substrates and sterilized in 95 % EtOH.

Cells were seeded at a density of 2×10^4 cells/mL (500 μl) on a cover slip placed in a well of a 6-well plate for 30 min, and complete medium (1 ml) was then added into the well. Cells were incubated and treated with Pt NCs-pSiNTs in a similar manner described previously. After

89

incubation, CellTracker Green BODIPY (8-chloromethyl-4,4-difluoro-1,3,5,7-tetramethyl-4-bora-3a,4a-diaza-S-indacene) dye (0.5 mL, 10 μM) (Molecular Probes) was added into each well and incubated at 37 °C for 30 min. Then cells were washed with PBS 3 times to remove excess dye. The coverslip was mounted on a glass slide and cells were observed using Zeiss LSM 710 laser scanning confocal microscope. In conjunction to staining cells with Green BODIPY, cell samples without Green BODIPY dye labeling was also analyzed.

4.2.5 Dissolution of Pt NCs-pSiNTs in the Complete Growth Medium

The medium obtained after cell incubation with Pt NCs-pSiNTs and PBS washing were saved, centrifuged (5 min, 10000 rpm) and washed with DI H_2O twice to collect the remaining composites. The morphologies of the samples were characterized by TEM imaging and TEM-EDX.

4.3 Results and Discussion

4.3.1 Formation of Pt NCs-pSiNTs and Freestanding Pt NPs

To evaluate the anticancer activity of the Pt NCs-pSiNT composites, two candidates with different ranges of wt % Pt (determined by TEM-EDX) were selected: 30-35 wt% Pt (1.5mM/4h) and 45-50 wt % Pt (1.5 mM/24h). As described previously in Chapter 3, Pt NCs formed on pSiNTs possess an ultrasmall size (1-3 nm) and are uniformly distributed on the nanotube templates (Figure 49). In order to evaluate the therapeutic effects of the Pt NCs, ultrasmall freestanding Pt NPs, which exhibited a pseudospherical structure and a similar size range (average: 3.6 nm), served as a control (Figure 50 and Figure 51).
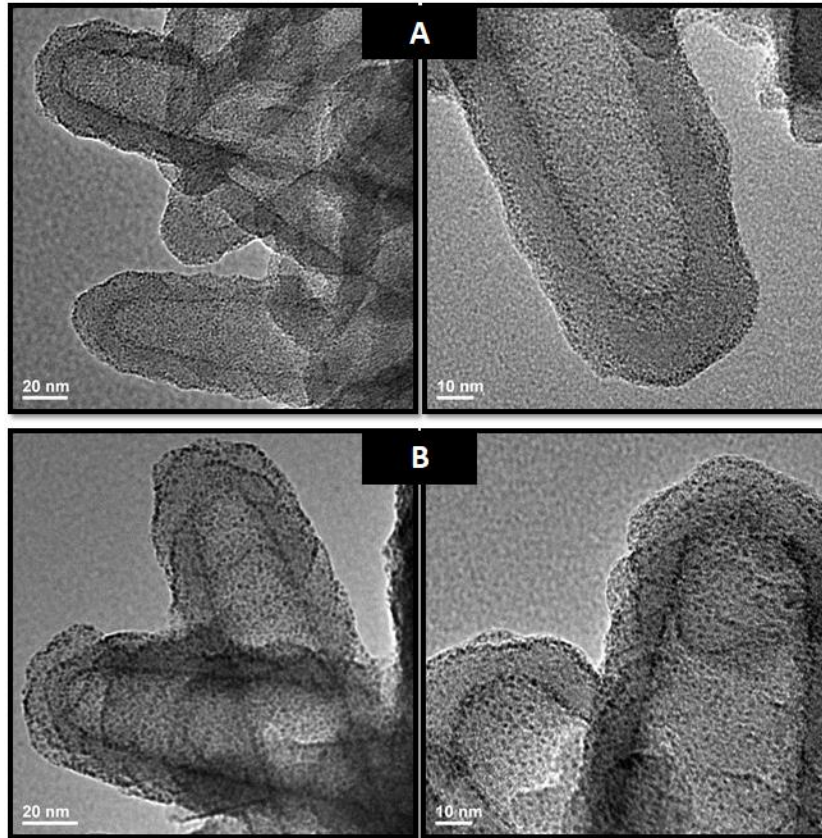
Figure 49. TEM imaging of Pt NCs-pSiNTs (A) 1.5 mM/4h (30-35 wt % Pt) and (B) 1.5 mM/24h (45-50 wt % Pt).
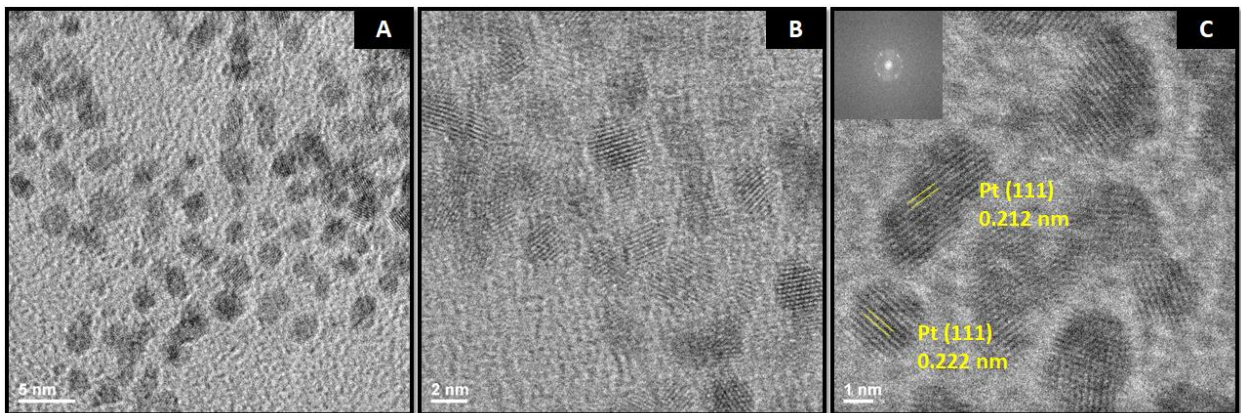
Figure 50. TEM imaging of (A) ultrasmall Pt NPs and (B and C) HR-TEM showing lattice spacing of Pt NPs.
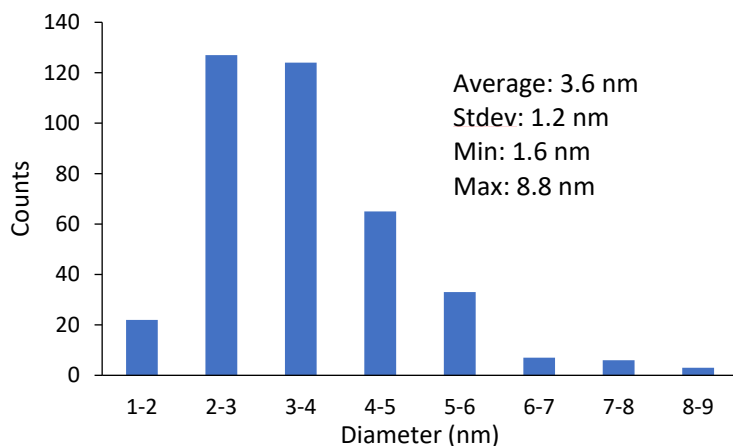
Figure 51. Size distribution of citrate-capped, free-standing Pt NPs.

4.3.2 Viability Assays

Based on the results obtained from *in vitro* viability assays, both types of Pt NCs-pSiNT [Pt Wt%: 30-35 % (1.5 mM/4 h) and 45-50 % (1.5 mM/24 h)] nanocomposites reduced cell viability to 60-80 % after 48 h and to less than 50 % after 72 and 96 h (Figure 52). At a higher concentration (50 μg/ml), cell viability was slightly lower but not statistically different than the lower doses (35 μg/ml), presumably owing to an increase in nanotube aggregation at a relatively higher concentration that reduced surface area and hampered cellular uptake. Since U-pSiNTs had no significant impact on cell viability even at the highest dose (35 μg/ml), cytotoxicity exerted by Pt NCs-pSiNTs presumably stemmed from the secondary nanostructure, i.e. Pt NCs components (Figure 53). Interestingly, by normalizing the toxicity to the amount of Pt species, 4-h formed Pt NCs appeared to be more toxic than the 24-h samples, presumably due to either smaller crystal size or amorphous morphology of Pt species formed after a shorter reaction time since no distinctive crystalline structure was detected by HR-TEM imaging. Thus, a higher concentration of Pt^{2+} was released and exerted greater damage compared to the more crystalline counterpart in a given time period.

With Pt^{2+} was shown to be responsible for the cytotoxicity profile of Pt NCs, two sources of Pt^{2+}: citrate-capped Pt NCs and K_2PtCl_4 were selected as the controls to evaluate the impact of Pt species identity to cell viability. Here, K_2PtCl_4 (25 µg/mL) with a comparable amount of Pt in the upper limit of Pt NC density in 1.5 mM/4h nanocomposites (i.e. 35 wt %) surprisingly yielded a higher cell viability (65-70%) even after 96 h, thereby suggesting a low intracellular bioavailability of K_2PtCl_4 (Figure 55A). Conversely, Pt NCs (17.5 µg/mL) elicited a similar toxicity level compared to that of Pt NCs-pSiNTs at a comparable Pt concentration (Figure 55B). Therefore, the results suggest cellular internalization of Pt NCs is necessary to elicit a higher toxicity by increasing bioavailability of Pt^{2+} inside cellular compartments.[165]
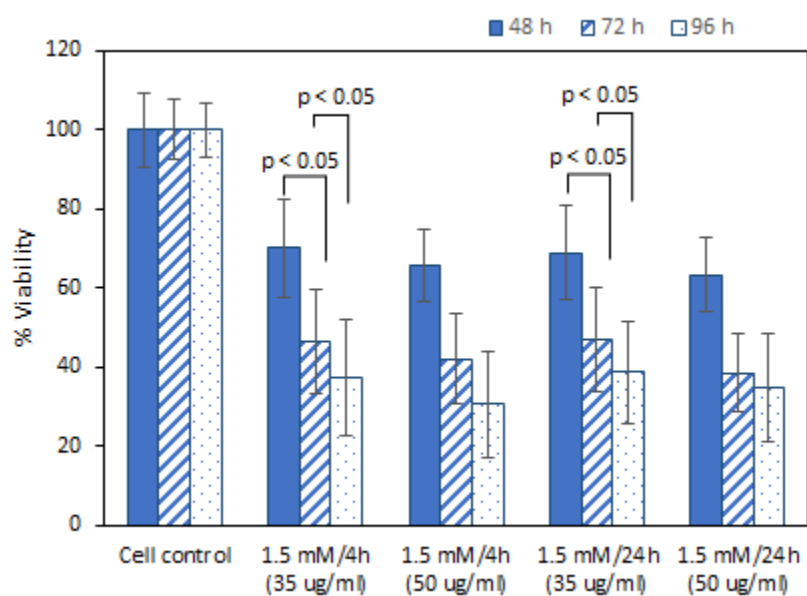
Figure 52. Viability of HeLa cells after treatment with Pt NCs-pSiNTs [(1.5 mM/4h (30-35 wt % Pt) and 1.5 mM/24h (45-50 wt % Pt)] at different doses (adapted from ref. 165).
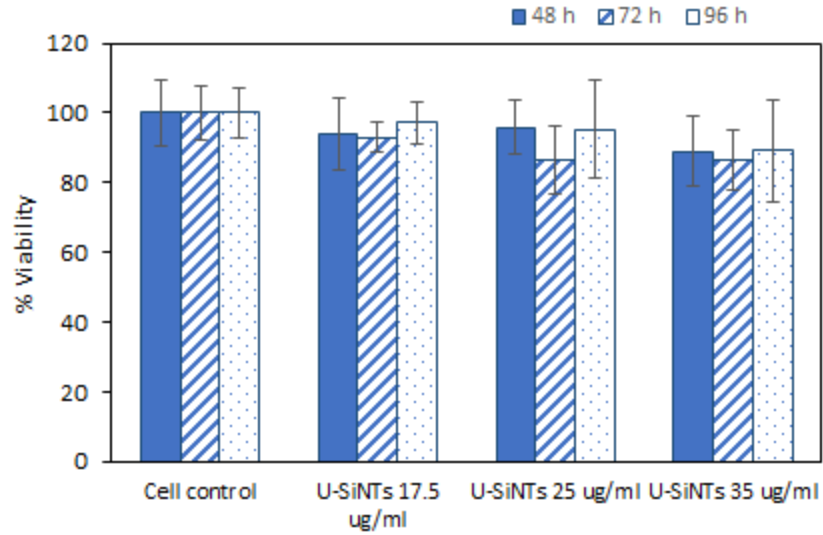
Figure 53. Viability of HeLa cells after treatment with U-pSiNTs at different doses (adapted from ref. 165).
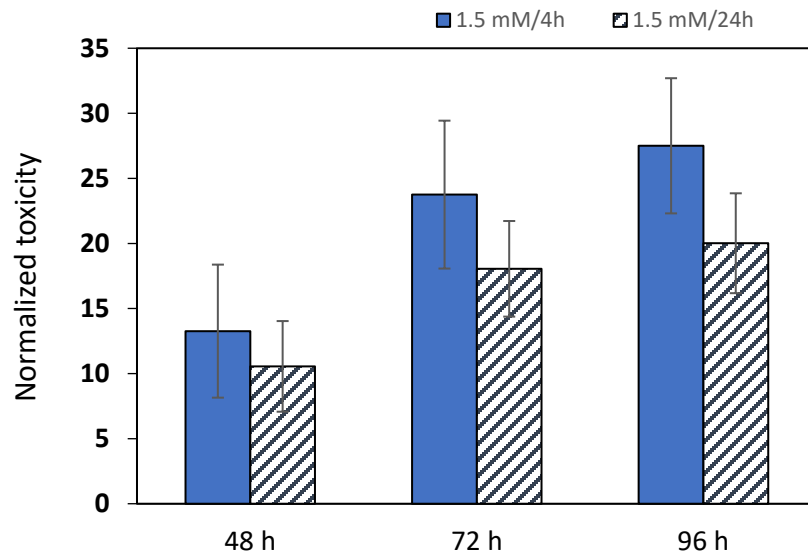
Figure 54. Normalized cytotoxicity based on wt % Pt obtained from TEM-EDX of Pt NCs-pSiNTs [(1.5 mM/4h (30-35 wt % Pt) and 1.5 mM/24h (45-50 wt % Pt)] (adapted from ref. 165).
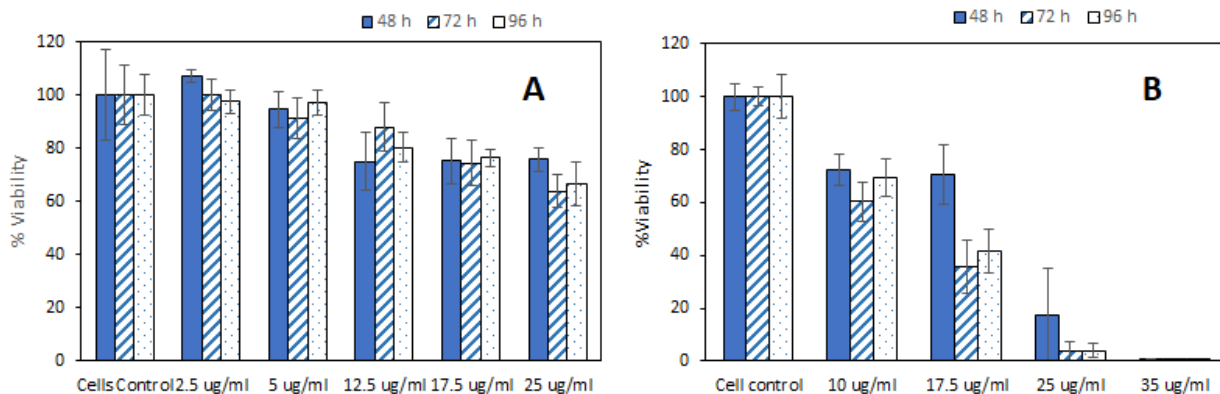
Figure 55. Cytotoxicity of A) K$_2$PtCl$_4$ and B) Pt NCs (3.5 ± 1.1 nm) exposed to HeLa cells at different doses (adapted from ref. 165).

4.3.3 Caspase 3/7 Assays

Apoptosis is a programmed cell death pathway that involves initial activation of initiator caspases (ex. caspase 8 and 9) followed by activation of the effector caspases (caspase 3 and 7), which subsequently trigger apoptotic events. Thus, to elucidate the mode of cell death occurring in Pt NCs/pSiNTs-treated cells, the activity of caspase 3/7 enzymes activated during apoptosis was evaluated and thus differentiate the mechanism from necrosis, which is an abnormal and harmful unprogrammed pathway. Consistent with viability assays, cytocompatibility of U-pSiNTs was confirmed since caspase 3/7 activity was comparable to untreated cells. On the other hand, elevated caspase activity ranging from a 1.5 to 2-fold increase was observed in cells after treatment with Pt NCs-pSiNTs regardless of the tested concentrations of the nanocomposites (Figure 56). Therefore, the data suggested Pt NCs-pSiNTs elicit cytotoxicity in an apoptotic manner. Since the peroxidase-like character (known for Pt NC systems) may also be involved in cellular functions, further mechanistic details remain to be elucidated.
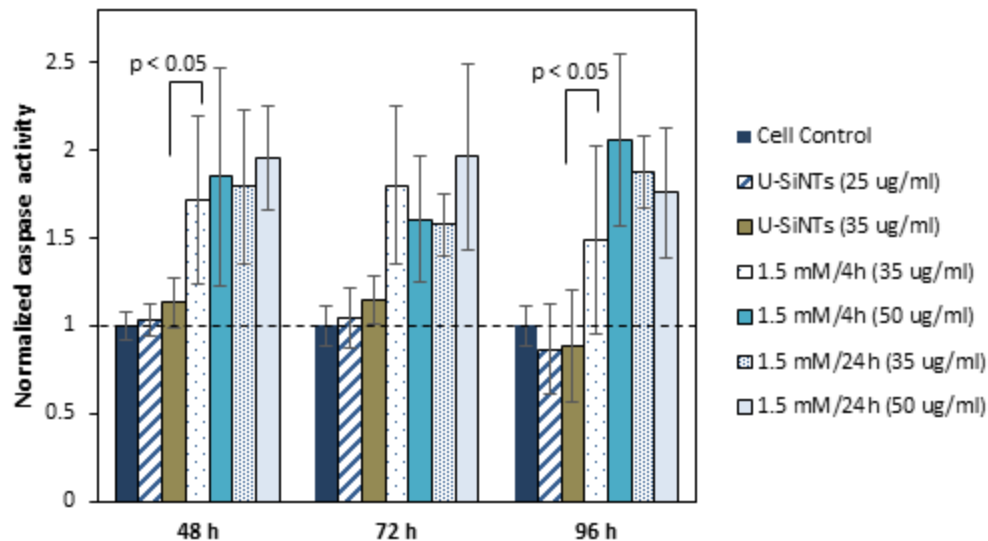
Figure 56. Caspase activity of HeLa cells after treatment with U-pSiNTs and Pt NCs-pSiNTs [(1.5 mM/4h (30-35 wt % Pt) and 1.5 mM/24h (45-50 wt % Pt)] (adapted from ref. 165).

4.3.4   Cellular Uptake

Based on viability and caspase assays, Pt NCs-pSiNTs must be able to internalize inside the cells to locally release a high concentration of Pt^{2+} from the NC surface. According to both non-fluorescent and fluorescent labeling studies, the nanocomposites were shown to accumulate around the cell nuclei of a measurable number of cells after 24 h, and the density of the internalized particles continuously escalated after 48 h and 72 h (Figure 57 and Figure 58). Since the significant reduction in cell viability was consistently within the same time frame as the increase in the nanoparticle concentration accumulating within the cells, toxicity elicited by the internalized Pt NCs-pSiNT nanocomposites was confirmed.[165]
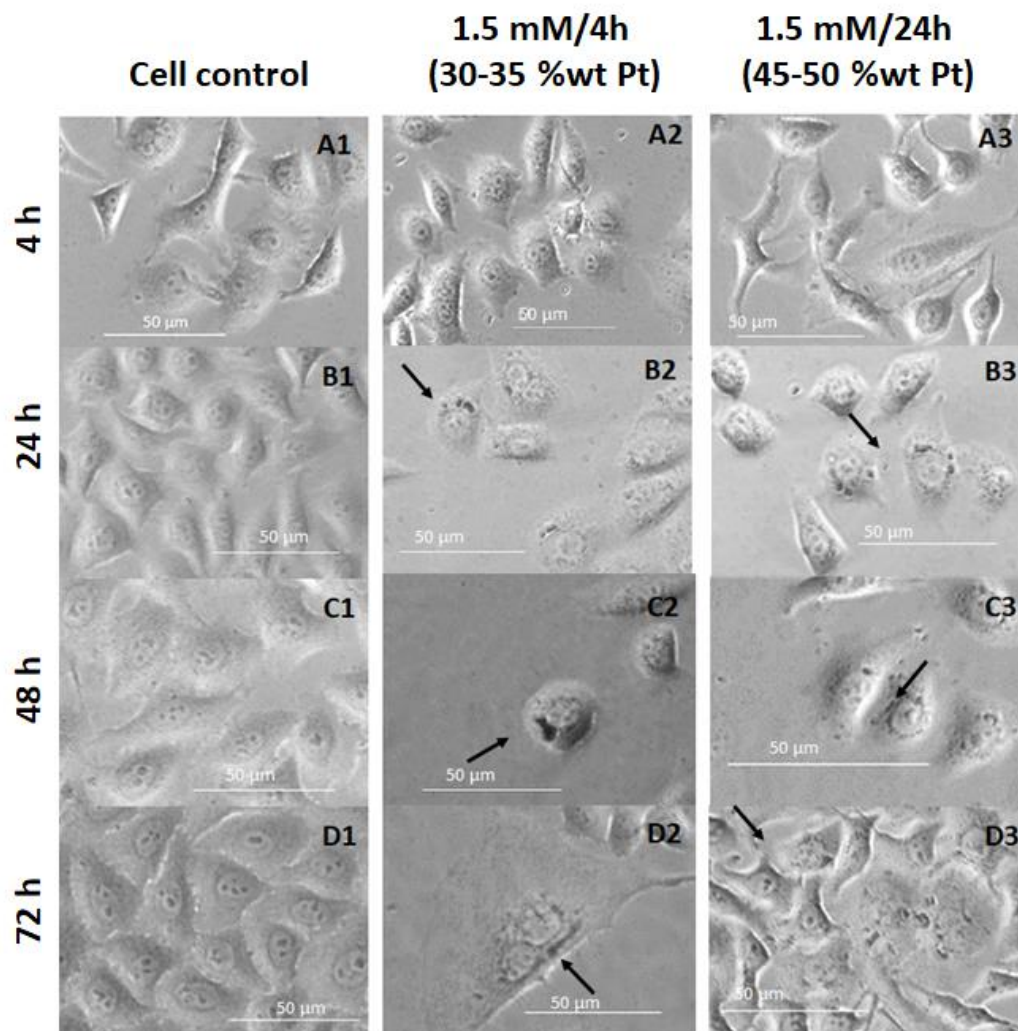
Figure 57. Localization of Pt NCs-pSiNTs in HeLa cells after 4h (A1-A3), 24h (B1-B3), 48h (C1-C3) and 72h (D1-D3) observed using visible light (brightfield mode) of fluorescence microscopy (non-fluorescence method). A1-D1: Cell with no treatment; A2-D2: 1.5 mM/4h (30-35 % wt Pt) Pt NCs-pSiNTs; A3-D3: 1.5 mM/24h (45-50 % wt Pt) Pt NCs-pSiNTs. Note: arrows show the presence of Pt NCs-pSiNTs (adapted from ref. 165).
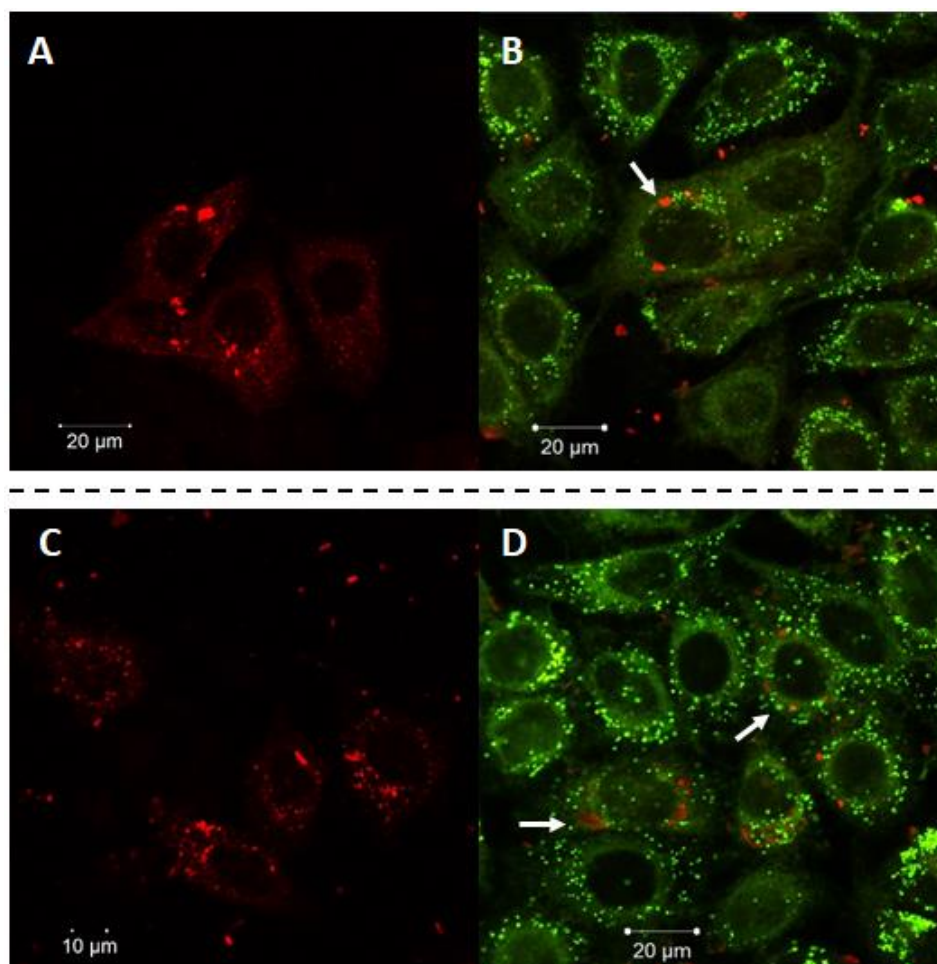
Figure 58. Confocal imaging showing cellular uptake of Pt NCs-pSiNTs after 48-h treatment with HeLa cells. (A) and (B): 1.5 mM/4h (30-35 %wt Pt); (C) and (D): 1.5 mM/24h (45-50 %wt Pt). A) and C) Accumulation of Alexa dye-stained composites (Red) around nuclei of the unstained HeLa cells (fluorescent method); B) and D) Accumulation of Alexa dye-stained composites (Red) in Green BODIPY-stained HeLa cells (Green) (fluorescent method). Note: arrows show the presence of Alexa dye-stained composites (adapted from ref. 165).

4.3.5 Dissolution of Pt NCs-pSiNTs in the Cell Culture Medium

To evaluate the role of pSiNT matrices in delivery of Pt NCs, evolution in structural morphology of Pt NCs-pSiNTs in the extracellular environment were assessed. After 24 h, most of the nanocomposites remained intact without considerable changes in the Pt composition, presumably owing to minimal dissolution of the nanotube matrices and Pt NCs during this time

period. Since cellular uptake studies indicate accumulation of the composites inside the cells after 24 h, the composites are assumed to mostly remain in intact form inside the cells. Conversely, significant structural evolution in conjunction with an increase in Pt and a decrease in Si concentration were observed after 48 h when the reduction in cell viability was also pronounced (Figure 59 and Table 11). It should be noted that upon accumulation inside the acidic intracellular organelles, the resorption of pSiNTs is expected to slow down along with an enhancement in dissolution of Pt NCs. Overall, based on the dissolution patterns of the nanocomposites, these results suggest biodegradability of pSiNTs was responsible for mediating cytotoxicity of the Pt NC components.

Thus, these studies presented here collectively suggest cytotoxicity of Pt NCs-pSiNT nanocomposites hinges on a "Trojan horse" mechanism. In this system, delivery of a high concentration of Pt NCs is mediated by the pSiNT matrix, whose dissolution along with the acidic microenvironment of endosome/lysosome readily facilitate the release of a high density of cytotoxic Pt^{2+} from the corrosive Pt NC surface inside the cells in a time-dependent manner.[165]
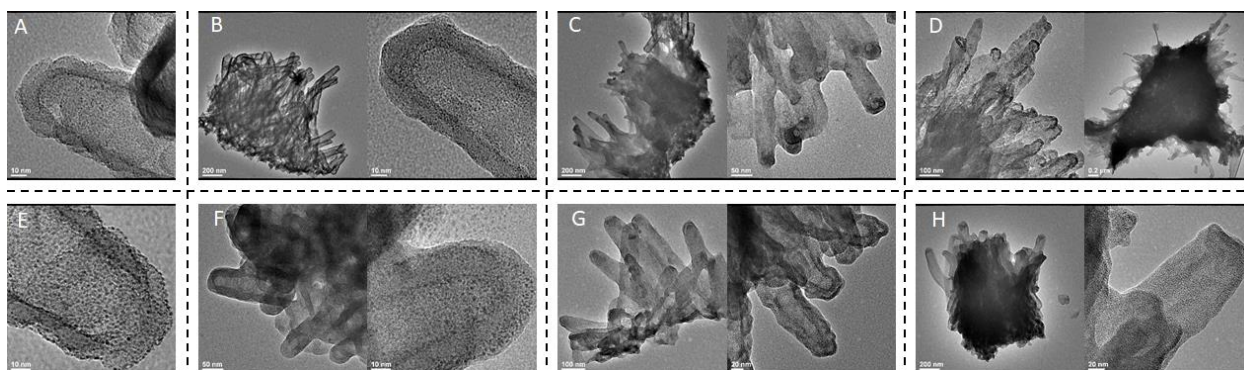
Figure 59. TEM images of Pt NCs-pSiNTs after dissolution in the DMEM growth medium showing gradual change in the morphology of the composites over incubation period. 30-35 wt% Pt: A: initial, B: 24 h, C: 48 h, D: 72 h; 45-50 wt% Pt: E: initial, F: 24 h, G: 48 h, H: 72 h (adapted ref. [165]).

Table 11. Elemental analysis of Pt NCs-pSiNTs after incubation in the cell growth medium (adapted from ref. 165).

1.5 mM/4 h Wt%	Si	O	Pt	Cl
Initial	44.1 ± 3.8	16.5 ± 2.3	38.2 ± 3.9	1.3 ± 0.1
24h	40.0 ± 5.5	15.6 ± 2.3	43.3 ± 3.9	1.0 ± 0.6
48h	14.5 ± 8.2	12.8 ± 3.0	70.6 ± 10.1	2.1 ± 0.9
72h	20.6 ± 15.2	13.8 ± 4.7	64.2 ± 18.5	1.4 ± 0.5

1.5 mM/24 h Wt%	Si	O	Pt	Cl
Initial	38.8 ± 4.8	14.4 ± 3.3	45.4 ± 4.8	1.2 ± 0.9
24h	38.1 ± 5.7	18.0 ± 3.9	34.8 ± 5.1	9.0 ± 2.0
48h	15.7 ± 11.7	8.4 ± 3.2	73.9 ± 13.6	1.9 ± 0.6
72h	14.7 ± 12.4	8.7 ± 2.8	74.3 ± 13.5	2.3 ± 1.3

4.4   Summary

This Chapter describes *in vitro* anticancer properties of Pt NCs-pSiNTs, whose time-dependent cytotoxicity is demonstrated as a consequence of leaching of Pt^{2+} from Pt NCs mediated partly by dissolution of pSiNT matrices. While *in vivo* studies are necessary to assess therapeutic potential of this type of novel nanocomposite in translational animal models, investigation into grafting additional targeting features (e.g. targeting peptides) is imperative in order to minimize deleterious side effects imposed on healthy cells. Also, since the presence of reactive oxygen species in the cellular environment has been shown to play a pivotal role in facilitating oxidation of metallic Pt^0 and thus govern the toxicity level of Pt NCs,[185] evaluation of cytotoxicity of Pt NCs-pSiNT nanocomposites in other cancer cell lines (e.g. liver cancer), which exhibit a relatively high oxidative potential, is also necessary to assess cell line-dependent cytotoxicity.

Chapter V

Porous Silicon Nanotubes as Gene Delivery Vectors

5.1 Introduction

To date, several chronic diseases, such as cancers and dementia (e.g. Alzheimer's disease), have been shown to associate with genetic disorders.[191-193] Typically, abnormal expression of single or multiple crucial proteins, such as those involved in cell cycle regulations (e.g. tumor suppressor p53), is deleterious to overall biological functions.[191, 194]

Conventional therapies normally involve small molecule drugs which target proteins of interest; however, these strategies are unappealing owing to reliance on the binding sites of the proteins.[195] In addition, although administration of recombinant proteins has been demonstrated lately, low biologic activity *in vivo* eventually hampers this therapeutic route.[195] Therefore, over the past few decades, treatments targeting the genetic level have been evaluated as an alternative approach in biologic therapy. Nowadays, nucleic acids, such as exogeneous DNA and RNA species [e.g. small interfering RNA (siRNA) and micro RNA (miRNA)], have been demonstrated as a unique class of therapeutic agents with great potential merit to cure genetic disorders.[195, 196] These nucleic acids have been shown to either extensively impede the production of overexpressing proteins or increase the concentration of the deficient proteins.[195, 197] Among therapeutic strategies, Clustered Regularly Interspaced Short Palindromic Repeats (CRISPR)-cas9 gene editing has been recently recognized as a simple and flexible strategy that allows modifying genes of interest in diverse organisms with extremely high accuracy.[198]

Unlike molecular drugs and active biologics which typically require extensive synthetic routes and purification steps, a large selection of nucleic acids can readily be achieved due to the ease of design and production processes, thereby implying flexibility in creating therapeutic nucleic acids suitable for a given pathological disease.[195]

Despite promising therapeutic features, administration of nucleic acids still encounters numerous hurdles since free nucleic acids are notorious for having low bioavailability owing to high potential of being degraded and eliminated by RNAses, exo-endonucleases and immune responses of the intrinsic defensive systems.[197] In addition, since cell membranes are mainly composed of lipid bilayers, diffusion of free nucleic acids across this barrier is highly restricted due to a combination of the large size, hydrophilic nature and the overall negative charge stemming from the phosphate and the sugar backbone.[199, 200] Also, since multiple intracellular barriers including endosomes/lysosomes hinder the therapeutic functions of nucleic acids, delivery vectors assisting the transport of nucleic acids in such complex biological systems are necessary to acquire desirable transfection outcomes.[201]

Since the movement of the genetic materials, especially those with size larger than 2 kbp, is highly restricted in the viscous environment of the cytoplasm, [202, 203] delivery vectors should not only continuously protect genetic cargoes from cytoplasmic enzymes but also need to assist translocation of the materials to the nuclear regions.

To date, a few gene therapies, which rely on viral vectors, have received FDA approval owing to high transfection efficiency attributed to the unique features of the vectors that enable efficient bypassing of cellular barriers.[204, 205] However, potential insertional mutagenesis, limited loading capacity, as well as manufacturing bottleneck (e.g. limited production capacity and high production cost) must be carefully considered in developing these delivery systems.[206-208] Alternatively, a number of non-viral carriers that offer safer approaches have been demonstrated.[209]

Among non-viral vectors, nanoparticles with a porous architecture can either confine and protect the genetic materials within the pores or immobilize them on the surface via electrostatic

interactions.[210] For these reasons, porous silicon (pSi) with the unique biodegradability features has been extensively evaluated in gene therapy. In an earlier study, the Coffer group has demonstrated oxidized stain-etched pSi (average size: 422 nm) functionalized with 3-(aminopropyl)triethoxysilane (APTES) as a feasible vector for *in vitro* delivery of small circular DNA molecules or plasmid DNA (pDNA) containing enhanced green fluorescent proteins (eGFP)-encoded reporter gene to HEK 293.[211] In another strategy, Cunin and colleagues evaluated conjugation of luciferase-encoded pDNA with pSi (average size ~ 200 nm) modified with positively charged amino acids (i.e. histidine and lysine), and a relatively high transfection efficiency in HEK293 has been observed.[212] Interestingly, promising initial results of *in vitro* gene delivery using plant-derived pSi have also been presented.[213] While extensive synthetic routes of anodic and stain-etched pSi poses critical challenges in scale-up production, plant-derived pSi is an ideal low-cost and eco-friendly alternative route of pSi-based gene delivery.

Since pSi employed in these preliminary studies are typically of a non-uniform particle morphology, evaluation of gene delivery using vectors with well-defined geometry are therefore of interest. In the studies presented in this Chapter, assessment of Si in a surface-functionalized nanotube architecture as potential gene carriers was evaluated via an *in vitro* model, in which transfection efficiency of reporter gene, eGFP-encoding pDNA, into HEK 293 was analyzed.

5.2   Experimental

5.2.1   Cell Culture

Human embryonic kidney (HEK) 293 cells were maintained under the same conditions as described in the experimental section of Chapter 2.

5.2.2 Purification of DNA Plasmids Encoding eGFP (pEGFP)

Escherichia coli (*E. coli*) bacteria containing the eFIRES plasmid with an eGFP insert (prepared by the Dr. Giridhar Akkaraju group)[214] were grown in lysogeny broth (LB) (2 ml) with ampicillin (100 μg/ml) at 37 °C overnight (16 h) in an incubator shaker. Next day, the bacterial culture (200 μl) was transferred into a flask containing LB (300 ml) and ampicillin (100 μg/ml), and the culture was incubated at 37 °C in an incubator shaker overnight again. After 16 h, the bacteria were harvested by centrifugation to remove the growth medium, and the plasmid was extracted and purified according to the manufacturer's protocol (QIAGEN Plasmid Midi Kit). Finally, the plasmid pellet was resuspended in TE buffer (150 μl). The purity and the concentration of the plasmids were characterized by measuring UV absorbance at 260 nm using Nanodrop spectrophotometer (Thermo Scientific Nanodrop 1000 model).

5.2.3 Immobilization of pEGFP to APTES-functionalized pSiNTs

pSiNTs were functionalized with APTES according to the protocol described in Chapter 2. APTES-pSiNTs were sterilized with 95 % EtOH and were dried *in vacuo*. APTES-pSiNTs were then dispersed in sterilized DI water and fragmented by ultrasonication for 5 min in an ice bath. The mixture of APTES-pSiNTs was diluted in sterilized DI H_2O to obtain the target concentration. APTES-pSiNTs, were incubated with pEGFP, and the sample was incubated for 5 min at room temperature with occasional mixing by tapping on the side of the tube. After incubation, samples were mixed by pipetting up and down prior to transfection. It should be noted that immobilization of pEGFP to APTES-pSiNTs was performed immediately prior to transfection experiments.

5.2.4 Evaluation of Conjugation Efficiency of pEGFP to APTES-pSiNTs

After 5-min incubation with pEGFP, the mixture was centrifuged for 10 min at 13000 rpm, and the supernatant was collected. The absorbance of the supernatant was measured using the

Nanodrop UV-Vis spectrophotometer to determine the concentration of the unbound pEGFP. Conjugation efficiency is determined according to the following equation:

$$CE = \frac{m_i - m_f}{m_i} \times 100 \,\%$$ (1)

where m_i is the initial mass of pDNA and m_f is the mass of pDNA remaining in the supernatant.

5.2.5 Transfection of Cells with pDNA/APTES-pSiNTs

HEK 293 cells were seeded in a 6-well plate (1×10^4 cells/well (~ 1042 cells/cm^2) or 2.5×10^4 cells/well (~2604 cells/cm^2)). For plating cells on the coverslips, cells (1×10^4 cells) were seeded on a collagen coated coverslip (d = 25 mm, Neuvitro Corporation) (~ 2038 cells/cm^2) and incubated at room temperature (25 °C) for 30 min, then complete medium was added to make up a total volume of 4 ml. Cells were incubated at 37 °C, 5% CO$_2$ for 24 h.

Next day, cells were transfected with pEGFP/APTES-pSiNTs, which were prepared as described in section 2.3. Then the plate was incubated in the incubator for 48 h and 72 h. Transfection of pEGFP by APTES-pSiNTs was assessed by visual detection using a fluorescent microscope equipped with GFP filter (Ex/Em 485/520) (Zeiss Axiovert 200) and semi-quantification by calculating the percentage of the area of cells expressing GFPs relative to the total cell area (Eq. 2). For the positive control, pEGF (100 ng) was conjugated with Lyovec (InvivoGen) (100 μl), which is a commercial transfection agent comprises of a mixture of phosphonolipids Di-tetradecylphosphoryl-N,N,N-trimethylmethanaminium chloride (DTCPTA) and 1,2-Diphytanoyl-sn-Glycero-3-Phosphoethanolamine (DiPPE) (Figure 60).

$$\% \, Transfection \, Efficiency = \frac{Area \, of \, Fluorescent \, cells}{Total \, cell \, area} \times 100 \,\%$$ (2)
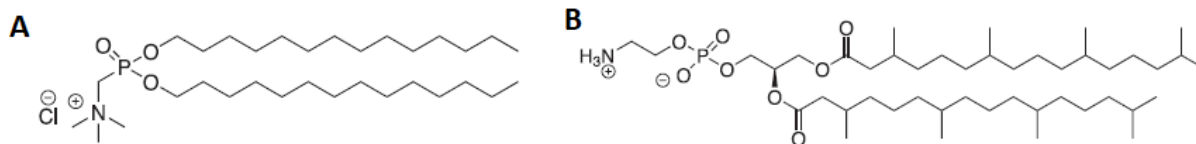
Figure 60. Molecular structure of A) DTCPTA and B) DiPPE.

5.3   Results and Discussion

5.3.1   Optimization of Conjugation Efficiency and Cellular Uptake

In this approach, initial efforts focused on increasing the density of the plasmids immobilized onto APTES-pSiNT surface by introducing a high concentration of the nanotubes. At concentrations greater than 0.2 mg/ml, extensive aggregation was observed, thus hampering cellular uptake process required for delivery of the genetic cargoes inside the cells. In addition, increasing incubation time of pEGFP with the nanotubes for more than 5 min also induced aggregation, presumably due to insufficient surface charge necessary for maintaining stability of the particles after the conjugation of the large-sized pEGFP (Figure 61). Thus, since highly dispersed particles are essential to achieve optimal cellular uptake, a short incubation time (i.e. 5 min) and a concentration of the functionalized pSiNTs of less than 0.2 mg/ml were essential, despite a relatively low conjugation efficiency (53.6 ± 1.9 CE %) and loading (0.53 ± 0.02 wt%).
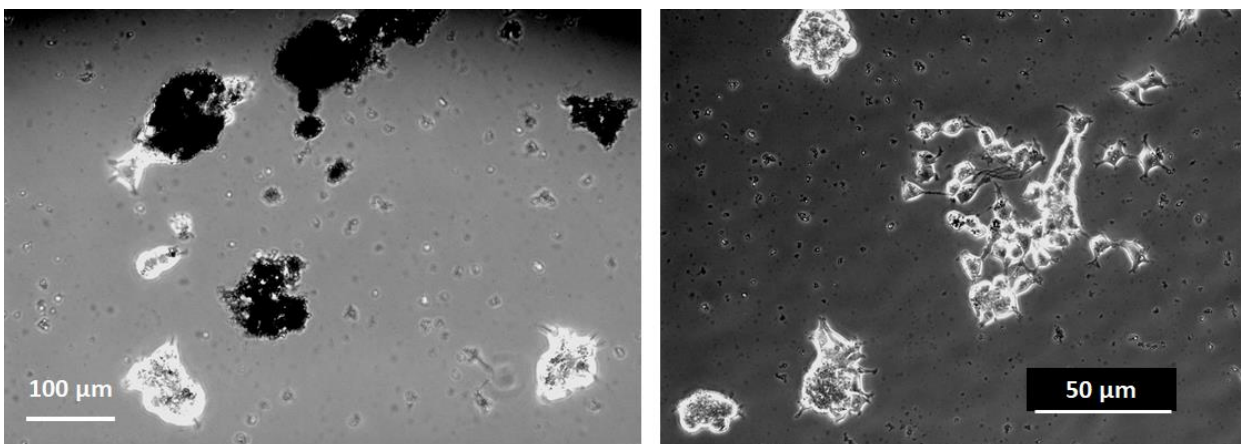
Figure 61. Brightfield imaging of HEK 293 cells interacting with pEGFP/APTES-pSiNTs. APTES-pSiNTs prepared at 0.2 μg/μl and incubated with 1μg pEGFP for A) 1 h and B) 5 min.

5.3.2 Delivery of pEGFP to HEK 293 Cells

Cells expressing eGFPs as a phenotype is an indication of successful pEGFP transfection. For the positive control using Lyovec, a high density of cells expressed eGFPs by day 2, thus suggesting the cationic lipids successfully complexed and delivered pEGFP into the cells (Figure 62 and Table 12). In addition, the data also confirms such purified pEGFP (260/280 > 1.80) extracted from E.coli can be effectively transcribed and translated into eGFP, thus serving as an efficient reporter gene.[214]

Nevertheless, it should be pointed out that although a high transfection efficiency (~ 50 %) could be achieved using the commercial agent, cells in these experiments appeared to be rounded up and detached from the well plate after 48 h, presumably owing to a high density of positive charges stemming from the cationic lipids that have been shown to be responsible for damaging cell membranes in earlier studies.[215-217]

Transfection using APTES-pSiNTs resulted in a relatively small number of HEK 293 cells expressing eGFPs at all the tested SiNT concentrations (Figure 63 and Table 13). Given the instability of the plasmid in an extracelluar environment, cells treated with free pEGFP expressed

no fluorescent protein (Figure 62C) and the eGFP expression observed here thus stemmed from pEGFP delivered inside the cells by SiNTs. After 72 h, a higher density of fluorescent cells was observed, but transfection efficiency was not statistically higher compared to that at 48 h, presumably owing to cell proliferation that yielded an increase in overall cell density.

Given the same nanotube concentration (10.4 µg/cm^2), an increase in cell confluency (from 1042 cells/cm^2 to 2604 cells/cm^2) yielded a slightly higher number of cells interacting with SiNTs and transfected with pEGFP, although the percentage of eGFP expression was insignificantly affected (Figure 64 and Table 14). Therefore, these results imply cellular association of SiNTs is essential for successful transfection. Increasing nanoparticle density relative to the cell coverage area (i.e. from 10.4 µg/2604 cells/cm^2 to 20.4 µg/2038 cells/cm^2) resulted in similar transfection efficiencies, which might be attributed to more aggregates formed at a higher particle concentration per surface area, thus hindering cellular internalization (Figure 64 and Table 14).

Although transfection efficiency was lower (2-5 %) compared to that transfected by Lyovec (~50 %) (partly due to a relatively low conjugation efficiency), HEK 293 cells not only exhibited a similar morphology compared to that of the untreated control but also proliferated normally; hence, confirming cytocompatibility of these SiNT materials to this cell line.

Based on these results, APTES-pSiNTs were assumed to be able to internalize inside the cells and escape the endosome, presumably via a mechanism similar to the proton-sponge effect, in which the unbound primary amino groups of APTES absorb protons and lead to an influx of Cl$^-$ along with water, thus eventually rupturing the endosomal membrane due to osmotic swelling. In addition, since it has been previously suggested that particles with sharp edges are more likely to rupture the endosomal membrane and reside in the cytoplasm compared to spherical

counterparts,[218] nanotube bundles might also presumably rely on their shape to escape endosomes. Overall, additional studies remain to elucidate the escape mechanism(s).

Since pEGFP must translocate into the nucleus to be translated, nuclear entry (in addition to cytoplasm trafficking) is a critical part to this process and has been identified as one of the main rate-limiting step in gene delivery.[219, 220] Although a series of nuclear pores formed on the nuclear envelope by nuclear pore complex (NPC) allows diffusion of certain molecules into the nuclei, the entrance of exogeneous DNA is greatly hindered (ascribed to its large size) and thus mainly relies on the breakdown of the nuclear envelope during mitosis.[221, 222] Hence, these hurdles collectively contribute to a relatively limited transfection efficiency of the SiNT delivery vectors employed in these experiments.
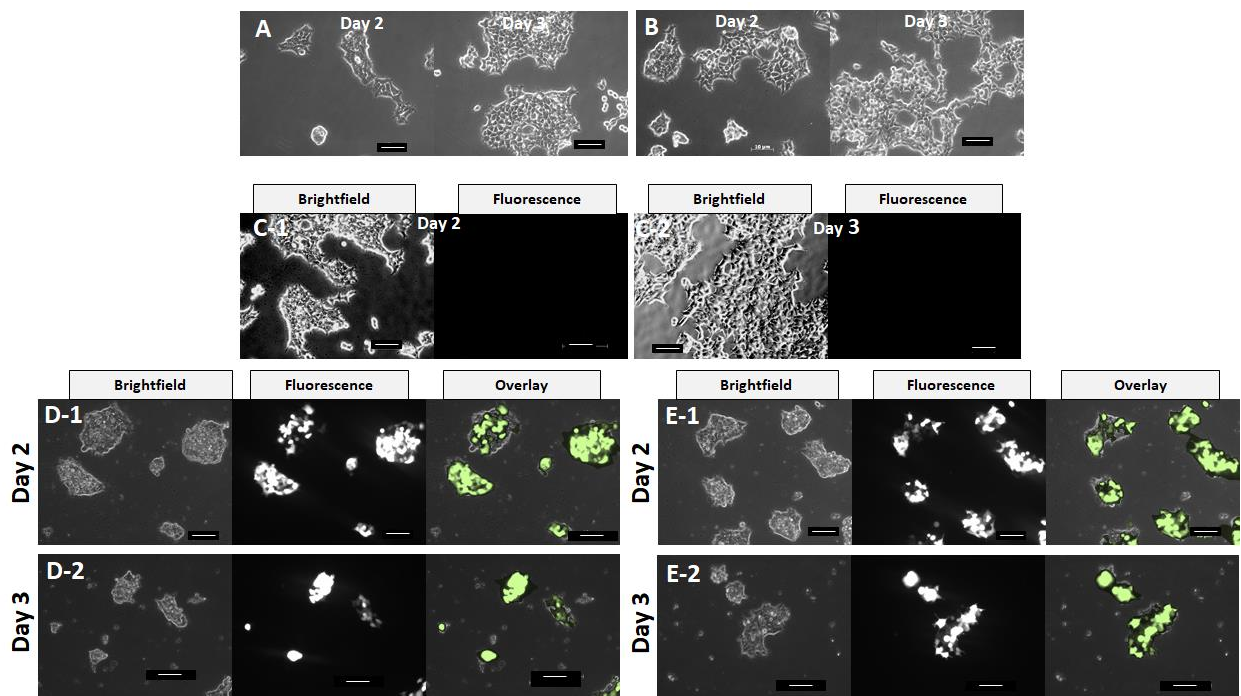
Figure 62. Microscopic imaging of HEK 293 cells. Untreated HEK 293 cells seeded at a density of A) 1×10^4 cells B) 2.5×10^4 cells; HEK293 cells treated with free pEGFP after 48 h (C-1) and 72 h (C-2); HEK 293 cells seeded at 1×10^4 cells (D) or 2.5×10^4 cells (E) transfected with pEGFP delivered by Lyovec. Scale bars: 50 μm.

Table 12. Transfection efficiency (%) of HEK 293 cells with Lyovec as transfection agent.

	$1x10^4$ cells (1042 cells/cm^2)		$2.5x10^4$ cells (2604 cells/cm^2)	
	Day 2	Day 3	Day 2	Day 3
	50.1 ± 10.7	65.3 ± 8.1	47.5 ± 7.5	54.7 ± 15.6

Table 13. Transfection efficiency (%) of HEK293 with APTES-pSiNTs as delivery vectors.

	$1x10^4$ cells (2038 cells/cm^2)			
$m_{APTES-pSiNTs}$	m_{pEGFP} (incubated)	m_{pEGFP} (bound)	Day 2	Day 3
100 µg	1 µg	~ 500 ng	3.2 ± 1.5	3.1 ± 2.8
50 µg	1 µg	~ 500 ng	2.7 ± 0.6	4.9 ± 9.7
50 µg	0.5 µg	~ 500 ng	3.0 ± 0.5	3.2 ± 1.8
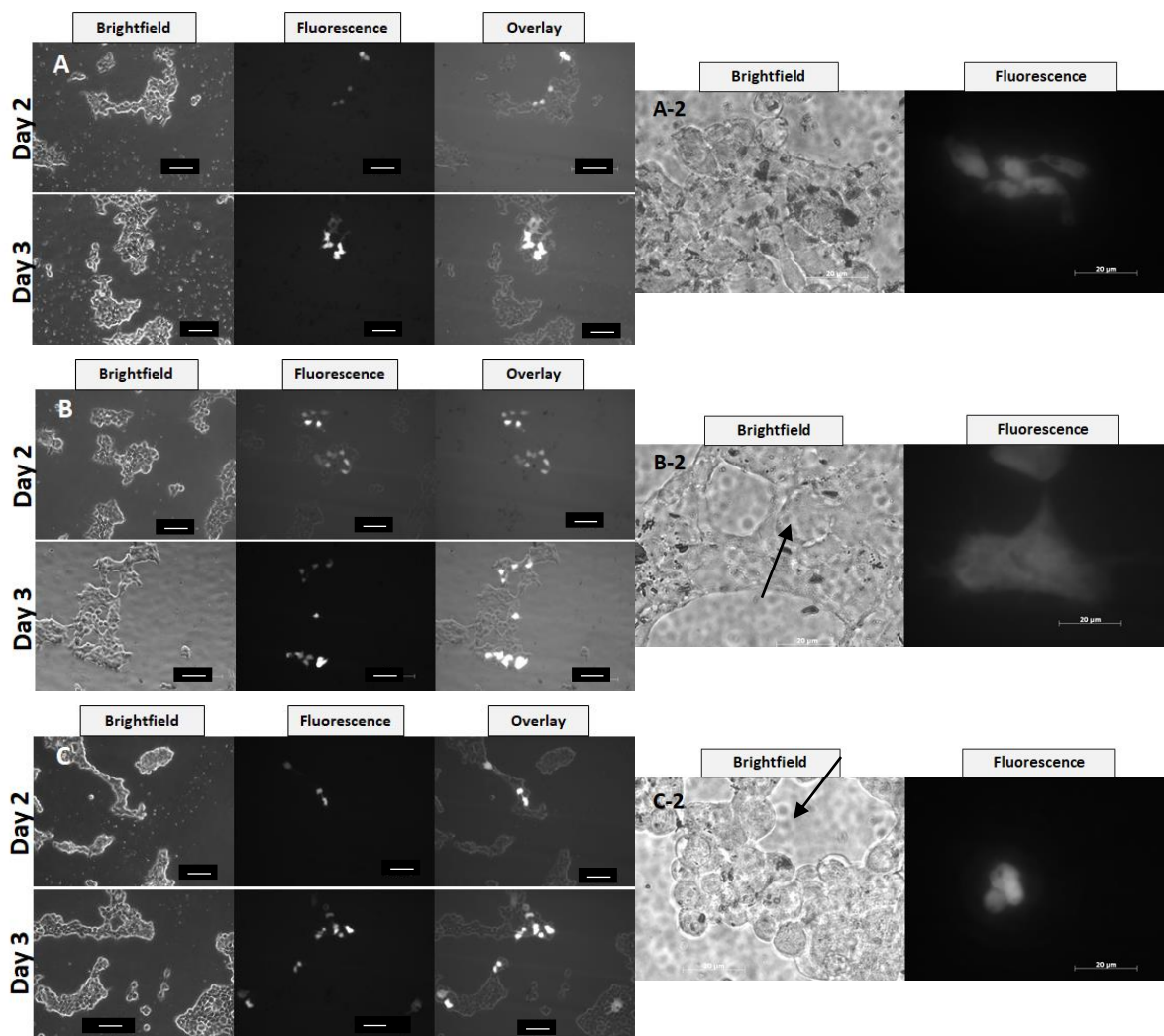
Figure 63. Brightfield and fluorescence imaging of HEK 293 (cell density: 1×10^4 cells seeded on coverslips (2038 cells/cm^2); after transfected with APTES-pSiNTs:pEGFP (incubated): A) 100 µg:1 µg, B) 50 µg:1 µg C) 50 µg: 0.5 µg. Scale bar: 100 µm. A-2, B-2 and C-2: imaging showing interactions between between pEGFP/APTES-pSiNTs and HEK293 cells at high magnification.
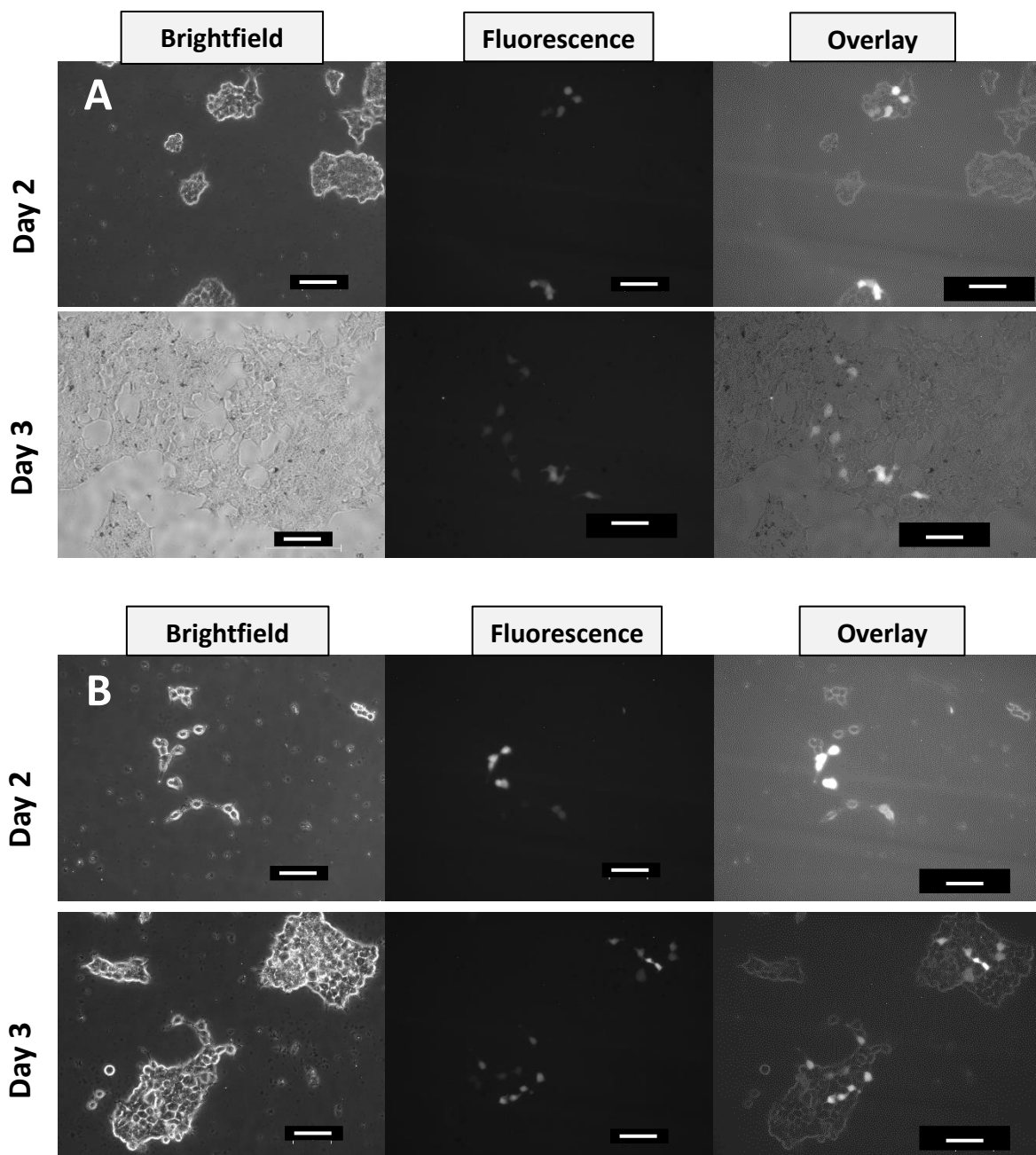
Figure 64. Brightfield and fluorescence imaging of HEK 293 cells plated at different densities; A) 2.5×10^4 cells (2604 cells/cm^2) and B) 10^4 cells (1042 cells/cm^2) after transfected with pEGFP/APTES-pSiNTs (100 μg) for 48 h and 72 h. Scale bars: 50 nm

Table 14. Expression of EGFPs (%) in different HEK293 cell densities.

	$1x10^4$ cells (2038 cells/cm^2)		$1x10^4$ cells (1042 cells/cm^2)		$2.5x10^4$ cells (2604 cells/cm^2)	
	20.4 μg/cm^2		10.4 μg/cm^2		10.4 μg/cm^2	
$m_{APTES\text{-}pSiNTs}$ 100 μg	Day 2	Day 3	Day 2	Day 3	Day 2	Day 3
	3.2 ± 1.5	3.1 ± 2.8	8.5 ± 5.7	5.9 ± 5.2	2.8 ± 2.4	3.0 ± 1.9

5.4 Summary

Initial *in vitro* gene delivery experiments described in this Chapter suggest the feasibility of biodegradable pSiNTs to serve as a nanocarrier for mediating internalization and expression of exogeneous genes, and thus signifies the potential merit of this type of nanoconstruct in delivery of other types of nucleic acids. Future investigations into increasing cargo loading, overcoming nuclear barriers as well as elucidating mechanisms of the intracellular fate of the materials are necessary to enhance transfection efficiency.

Chapter VI

Porous Silicon Nanotubes as Potential Nanocarriers for Delivering of Small Interfering RNA

6.1　Introduction

RNA interference pathway (RNAi) was first discovered by Matthew Fire and Craig Mello in 1998 when they were studying the phenotype effects of the double-stranded RNA (dsRNA) encoding a myofilament protein (*unc*-22 RNA) in the nematode worm *Caenorhabditis elegans* (*C. elegans*).[223] The injection of dsRNA resulted in a severe twitching motion which was correlated to a decrease in *unc-22* activity. Follow-up studies confirmed that dsRNAs recognize the complementary mRNA strands at the posttranscriptional level and trigger degradation pathways prior to translation, thereby leading to a reduction of the corresponding proteins.[224] Their findings revealed the significant role of dsRNAs in physiological gene silencing, pioneered a new era of RNA in molecular biology and therefore earned them a Nobel Prize in 2006.[225]

Based on *in vitro* studies using *Drosophila* embryo extracts and cultured cells, the silencing mechanism was revealed.[226-228] When dsRNAs are introduced inside a cell, endoribonuclease Dicer is recruited and cleaves the strands into shorter sequences of 21-23 nucleotides (3 nm×7.5 nm), so called small interfering RNA (siRNA). siRNAs are bound to Argonaute protein and other components of RNA-induced silencing complex (RISC), and the endonuclease Ago 2 of RISC catalyzes the unwinding of the siRNA duplex. After the unwinding process, the passenger strand of siRNA is released leaving the guide strand incorporated into the RISC; therefore, RISC can start searching for any mRNAs which have complementary sequence to the guide strand and cleave the target mRNA via an endonucleolytic process (Figure 65).

The advent of RNAi has profoundly contributed to an understanding of cellular functions and development of organisms.[229] To date, siRNA-mediated gene silencing is envisioned as a promising strategy to combat detrimental diseases.[230] However, administration of siRNAs still encounters numerous critical challenges owing to the nature of nucleic acids, thus requiring

effective delivery vectors that can harness the potential therapeutics of RNAi while minimizing

potential immune-related toxicities. In contrast to gene delivery, since siRNAs target

complementary mRNA in the cytoplasm, hurdles related to the nuclear entry described previously

in Chapter 5 are no longer the concerns in siRNA delivery.[231, 232]
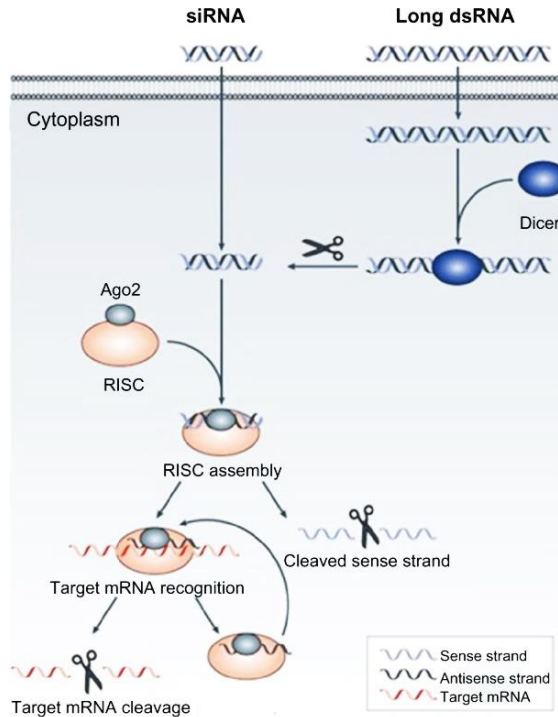
Figure 65. RNAi pathway (adapted from ref. 233)

Lipid nanoparticles (LNPs) have contributed to the great progress in siRNA delivery, such

as the cationic ionizable LNPs that serve as the central keys to the success of the first FDA-

approved siRNA-based therapy for treatment of peripheral nerve disease (polyneuropathy)

(Onpattro).[230] Inorganic NPs such as pSi have also been demonstrated as exceptional delivery

carriers of a variety of siRNAs in diverse disease models.

To date, multiple designs of pSi-based siRNA delivery vectors have been reported to

address multiple challenges in therapeutic delivery. Owing to the versatile surface chemistry of

pSi, a high loading of siRNAs can be readily achieved via surface functionalization of pSi with a

great diversity of cationic molecules (e.g. dendrimers, PEI).[142] In another approach, the Sailor group has demonstrated a novel loading method, so called calcium ion precipitation strategy, in which formation of the calcium silicate (Ca_2SiO_4) shell occurs simultaneously with the entrapment of siRNA within pSi. Therefore, not only a high loading of siRNAs is achieved (~20 wt %) but dissolution of the Si skeleton is also slowed down by the Ca_2SiO_4 shell in order to attain a sustained release of siRNAs from the pSi carriers.[234]

In addition, Shen and colleagues have evaluated discoidal pSi, which exhibits favorable flow dynamics (i.e. more likely to marginate and reach the vessel walls), in delivery of siRNA targeting the ataxia telangiectasia mutated (ATM) gene in human breast cancer cells via a multistage vector approach, and biocompatibility of this novel delivery system was also confirmed by *in vivo* studies.[235, 236]

Since nanoparticle shape plays a critical role in blood circulation and cellular interactions, in this Chapter, the potential of the 1D porous nanotube structure of Si (pSiNTs) to serve as delivery vectors for siRNA is demonstrated via two *in vitro* models, both of which involve pSiNTs functionalized with APTES to facilitate siRNA conjugation via electrostatic interactions. In the first model, delivery of siRNA (siGFP), targeting the enhanced green fluorescence protein (EGFP) reporter gene, which was transiently transfected in HeLa cervical cancer cells, was assessed. Knockdown efficiency of EGFP expression was quantitatively evaluated by measuring fluorescence intensity of the EGFPs, which mirrored the mRNA-GFP level. The second *in vitro* model involved delivery of therapeutic siRNA (siER) to downregulate estrogen receptors α (ERα), which are known to overly expressed in breast cancer cells.[237, 238] Knockdown efficiency by siER was characterized by quantification of ER-protein and ER-mRNA levels via Western blot protein analysis and Reverse Transcription-Real time Polymerase Chain Reaction (RT-qPCR)

respectively. Cellular uptake and dissolution of siRNA/APTES-SiNTs were also evaluated to elucidate the possible siRNA delivery mechanism.

6.2   Experimental

6.2.1   Cell Cultures

HeLa and MCF-7 (Breast cancer) cells were maintained in the same conditions as described in the experimental section of Chapter 2.

6.2.2   Fragmentation of APTES-pSiNTs

APTES-pSiNTs were sterilized and fractured for 5 min (delivery of siEGFP) or 10 min (delivery of siER) in diethyl pyrocarbonate (DEPC)-treated water (IBI Scientific) by ultrasonication as described in Chapter 2.

6.2.3   Preparation of siRNA/APTES-pSiNTs

The sonicated samples were further diluted with DEPC-treated water to obtain the target concentrations. APTES-pSiNTs were incubated with siRNAs [nonspecific siRNA (NS_siRNA), siGFP (Thermo Fisher Scientific) or siER (siGENOME, Smartpool, Horizon Discovery)] for 30 min at room temperature (RT) (~25 $^{\circ}$C).

For siER experiments, the samples were further centrifuged, and the pellet was resuspended in Opti-MEM reduced serum (Gibco, Thermo Fisher Scientific).

6.2.4   Characterization of siRNA/APTES-pSiNTs

a) Zeta Potential Measurements

After siRNA conjugation, the sample was centrifuged (13000 rpm, 10 min, 4°C), and the supernatant was collected. The nanoparticle pellet was washed twice and re-dispersed in ultrapure H$_2$O (2 ml). The sample was briefly ultrasonicated (~10 s) in the ice bath and the zeta potential

values were collected at RT (10 runs, 30 cycles/run and fit to *Smoluchowski's* model, which is used for determination of electrophoretic mobility of particles dispersed in aqueous media)).[150] Zeta potential of APTES-pSiNTs stock solution was also collected to evaluate changes in zeta potential before and after siRNA binding.

b) Conjugation Efficiency of siRNA to APTES-pSiNTs

The sonicated APTES-pSiNTs were diluted in DEPC-treated water to obtain the following concentrations: 0.02, 0.05 and 0.1 µg/µl, 145 µl, and the solutions were mixed with the same volume of siRNA stock (30 pmol, 5 µl) for 30 min at RT. The samples were centrifuged (13,300 rpm, 15 min, 4 °C), and the concentration of the unbound siRNA was analyzed by using a Nanodrop UV-Vis spectrophotometer. The conjugation efficiency (% CE) and % mass loading were determined according to the following equations:

$$\%Conjugation\ efficiency\ = \frac{m_{siRNA\ (Stock)} - m_{siRNA(Supernatant)}}{m_{siRNA(Stock)}} \times 100\% \qquad (1)$$

$$\%Mass\ loading\ = \frac{m_{siRNA}}{m_{siRNA} + m_{APTES-pSiNTs}} \times 100\% \qquad (2)$$

c) Release Kinetics of siRNA from APTES-pSiNTs

APTES-pSiNTs (20 µg, 0.05 µg/µl) were incubated with fluorescent FAM-labeled siRNA (80 pmol) (Ex/Em: 485/520) for 30 min at RT, and the sample was centrifuged at 4 °C (13,300 rpm, 10 min). The pellet was washed once with ultrapure water (200 µl), re-dispersed in PBS (400 µl) and incubated in the humidified incubator at 37 °C with 5 % CO_2 in air. At a specific time point, the sample was centrifuged (13,000 rpm, 10 min, 4 °C) to collect the supernatant, and the pellet was re-dispersed in fresh PBS (400 µl).

Two calibration curves were constructed using FAM-siRNA diluted in RNAse-free H_2O and PBS to determine mass loading and cumulative release of siRNA (Figure 66). Fluorescence readings were recorded using a microplate reader (Ex/Em 485/520).

A

Fluorescence intensity (a.u.)

$y = 3843.4x - 303.78$
$R^2 = 0.996$

[FAM-siRNA] (ng/ul)

B

Fluorescence intensity (a.u.)

$y = 23950x - 276.69$
$R^2 = 0.9983$

[FAM-siRNA] (ng/ul)
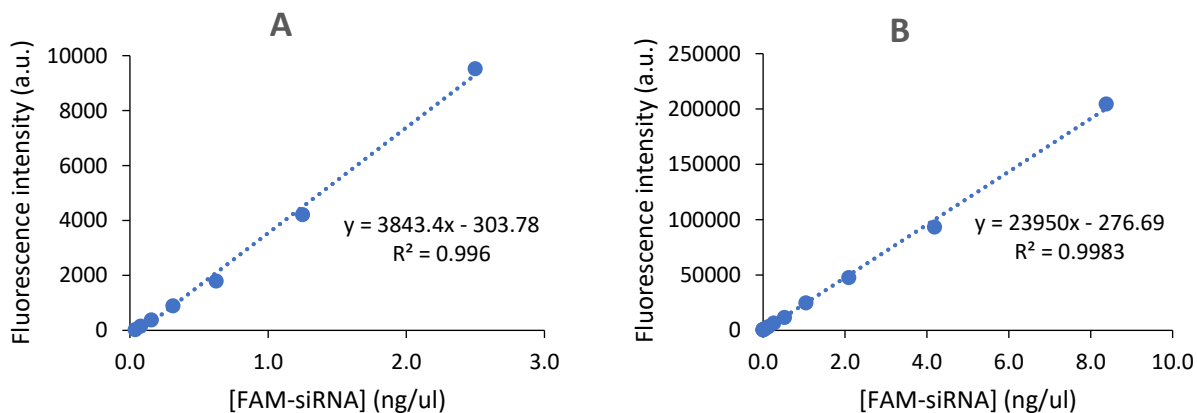
Figure 66. Calibration curve of FAM-siRNA diluted in A) H_2O and B) PBS.

d) Interaction of siRNA/APTES-pSiNTs with HeLa cells

Brightfield Imaging

HeLa cells were seeded at a density of 5000 cells/well (100 μl complete medium) in a 96-well plate and were incubated at 37 °C, 5% CO_2 for 24h. Next day, NS_siRNA/APTES-pSiNTs was prepared by incubating APTES-pSiNTs (2.5 μg) with siRNA (10 pmol) (per well) according to the procedure described above, and cells were transfected with this mixture (final conc. = 12.5 μg/ml) for 36 h. After transfection, cells were washed with PBS once (100 μl), incubated in the complete medium (50 μl) and imaged using the visible light (brightfield mode) of the fluorescence microscope (Zeiss Axiovert 200).

Confocal Microscopic Imaging

HeLa cells were seeded at a density of 7.5×10^4 cells (500 μl medium) on a cover slip (2.2 cm×2.2 cm) placed in a well of a 6-well plate and were incubated for 30 min at 37 °C. After 30

min, 2.5 ml of the complete medium was added into the well ($V_{medium\ (total)}$ = 3 ml), and the plate was placed in the incubator for 24 h.

The next day, a solution of APTES-pSiNTs prepared in DEPC-treated H_2O ((38 μg: 500 μl) was mixed with fluorescently labeled non-specific siRNA [Alexa Fluor 674 (AF 674 siRNA)] (40 pmol) for 30 min at RT. For the positive controls, AF 647 siRNA (40 pmol in 250 μl OptiMEM) was incubated with a commercial transfection reagent Optifect (Invitrogen) (12 μl in 250 μl OptiMEM) according to the manufacturer's protocol: Optifect was first diluted in Opti-MEM and incubated at RT for 5 min, then pEGFP diluted in Opti-MEM was combined with the Optifect solution, and the mixture was incubated at RT for 20 min. It should be noted that all the samples were protected from light during incubation period. Cells were then transfected with siRNA/APTES-pSiNTs and siRNA/Optifect, and cells were then incubated at 37°C for 4 h and 24 h.

At a specific time point, CellTracker Green BODIPY dye (0.5 mL, 10 μM) was added into each well, and cells were incubated at 37 °C for another 30 min. After incubation, cells were washed with PBS (1 ml) for 2 times to remove excess dye and fixed in a solution of 4 % paraformaldehyde (prepared in PBS) for 15 min. Cells were then thoroughly washed with PBS and mounted on a clean glass slide using *Fluoromount*-G Mounting Medium. Cells were observed using Laser Scanning Confocal microscope, and Ex/Em for AF 647 and Green BODIPY are selected to be 633/660-730 and 458/516-588 respectively

SEM Imaging

Cells were seeded and treated with siRNA/APTES-pSiNTs as described in the sample preparation for confocal microscopic imaging section. It should be pointed out that non-fluorescent

NS_siRNA (60 pmol) was utilized here. Cells were incubated for 4, 24, 48 and 72 h in the humidified incubator at 37 °C with 5 % CO_2 in air.

After a specific time point, cells remained attached on the coverslip were washed with phosphate buffer (0.2 M, pH 7.2) and incubated in a solution of 6 % paraformaldehyde and 8% glutaraldehyde prepared in phosphate buffer for 15 min (volume ratio is 1:1:1). Cells were then slowly dehydrated in a series of EtOH solution: 30%, 60%, 95% and 100% EtOH (5 min for each step). The coverslip was attached to a carbon tape adhered to an aluminum mount and subsequently sputter-coated with 8-nm gold thickness. The cells were imaged with FESEM using an accelerating voltage of 2 kV and a working distance of 10 mm.

6.2.5 *In vitro* Delivery of siRNA Targeting EGFP-mRNA

a) Cytotoxicity of APTES-pSiNTs

HeLa cells were seeded at a density of 5000 cells/well (100 μl complete medium) in a 96-well plate and were incubated at 37 °C, 5% CO_2 for 24h. Next day, to mimic siRNA delivery experiments (Section 1.1.4), the reduced serum medium (Opti-MEM, 50 μl) was added into each well followed by different concentrations of APTES-pSiNTs (50 μl) prepared in sterilized water. The final concentrations of APTES-pSiNTs in the well are: 2.5, 5.0, 12.5, 17.5, 25, 35 and 50 μg/ml. Cells with no nanoparticle treatment served as the control. Cells were incubated for 36 h, and cell viability was assessed by CellTiter-Glo assays.

b) Silencing eGFP Expression in HeLa cells Transiently Transfected with pEGFP

In this experiment, HeLa cells were transiently transfected with pEGFP and subsequently transfected with siGFP to suppress eGFP expression (Figure 67). For the negative control, cells were transfected with NS_siRNA.
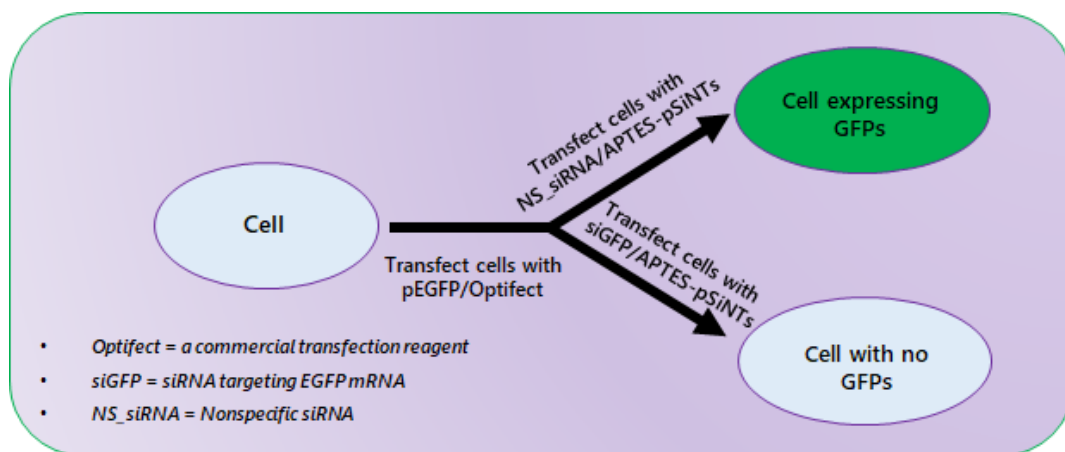
Figure 67. Experimental scheme of evaluating *in vitro* siGFP delivery by APTES-pSiNTs.

Transient Transfection of HeLa Cells with pEGFP

HeLa cells were seeded at a density of 5000 cells/well (100 μl complete medium) in a 96-well plate and were incubated at 37 °C, 5% CO_2 for 24 h. Next day, cells were transiently transfected with a solution (50 μl) containing 125 ng pEGFP/0.5 μl Optifect. Cells were then incubated for 8 h at 37°C prior to siRNA transfection.

siRNA Delivery for Silencing eGFP Expression

After 8-h incubation with pEGFP/Optifect, cells were transfected with siGFP (or NS_siRNA) delivered by either APTES-pSiNTs or the control. Here, siRNA/ APTES-pSiNTs was prepared by incubating APTES-pSiNTs (2.5 μg/50 μl) with siGFP (10 pmol). For the controls, siGFP or NS_siRNA (10 pmol, 25 μl OptiMEM) was combined with Optifect (0.5 μl diluted in 25 μl OptiMEM). It should be noted that siRNA/APTES-pSiNTs and siRNA/Optifect were freshly prepared before 8-h time point. Cells were incubated in the incubator at 37 °C for 36 h, and knockdown efficiency was analyzed.

Analysis of eGFP Knockdown

After 36 h, cells were gently washed with PBS (100 μl) twice to remove the excess

nanoparticles. Cells were incubated in the complete medium and were imaged using fluorescence microscope equipped with a GFP filter (Ex/Em 458/520 nm). After imaging, cells were washed again with PBS to completely remove the medium, and fresh PBS (100 μl) was added into each well. Cells were then lysed by a freeze-thaw method: the plate was incubated at -80 ℃ for 30 min and thawed to RT. Cell lysates were transferred into a 96-well black plate with opaque black bottom, and the fluorescence reading was recorded by using the multiplate reader (BMG Labtech FLUOstar Omega) (Ex/Em: 485/520)

Analysis of β-actin Expression

- **Protein Extraction**

Influence of siRNA transfection conditions to a housekeeping gene expression, in this case β-actin, was analyzed by Western blot analysis. In this method, cells were seeded and transfected as described above. For scale-up, 8 wells were prepared for 1 sample. After 36-h siRNA transfection, cells were washed with cold PBS (100 μl/well). SDS-lysis buffer was added into each well (50 μl/well), and the plate was incubated on ice for 15 min. The lysate was collected and cleared by centrifugation at 13,000 rpm for 10 min at 4 ℃. The supernatant (200 μl) of each sample was combined with 6X SDS (40 μl), and the samples were briefly vortexed, boiled at 95 ℃ in a dry bath incubator (Fisher Scientific) for 5 min. The samples were frozen immediately and stored at -20 ℃ for further use.

The protein concentration of each sample was determined by colorimetric Bradford protein assay, in which the acidified Coomassie Brilliant Blue G-250 binds to the proteins and yield blue complexes with maximum absorbance at 595 nm. The calibration curve was prepared according to the following protocol (Table 15 and Figure 68). Note: a new calibration curve was prepared for every Western blot experiment.

125

Table 15. Construction of calibration curve and determination of the concentration of the unknowns

BSA (mg/ml)	$V_{BSA\ (stock)}$ (μl)	$V_{0.15M\ NaCl}$ (μl)	$V_{bradford\ reagent}$ (μl)
0	0	10	190
0.5	1	9	190
1	2	8	190
2	4	6	190
4	8	2	190
Unknown sample (triplicate)	V (μl)	$V_{0.15M\ NaCl}$ (μl)	$V_{bradford\ reagent}$ (μl)
	1	9	190

y = 0.0913x + 0.0175
R² = 0.9996
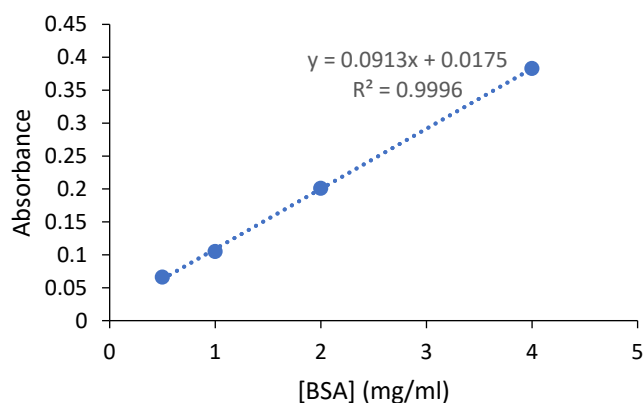
Figure 68. A typical calibration curve used for determining the total protein concentrations in the unknowns.

- **Western Blot**

A gel comprised of the separating gel and the stacking gel was prepared (Table 16). Equal amount of the samples (5.2 μg/each) and the protein ladder (5 μl) (Precision Plus Protein™ Dual Color Standards) were loaded into the wells, and gel electrophoresis was run at 100 V until the blue dye was close to the bottom of the gel. Electrophoretic transfer of the proteins to a PVDF membrane (Immobilon-P^SQ Transfer Membrane) was run at 100 V for 1 h, and the membrane was blocked with 5 % milk (prepared in TBST buffer) for 1 h. The membrane was incubated in primary

antibody β actin mouse monoclonal IgG (Santa Cruz Biotechnology) (1:1000), which was prepared in 5 % milk, for 30 min on a rocker at RT and then at 4 °C overnight.

Next day, the membrane was washed with 5 % milk on the orbital shaker for 3 times (10 min/time) and then incubated in the secondary antibody Goat-anti Mouse with Alkaline phosphatase (AP) conjugate (Santa Cruz Biotechnology) (1: 10,000) on the rocker for 1 h at RT. The membrane was then washed again using 5 % milk as described above and finally incubated in the AP substrate solution, which is comprised of 5-bromo-4-chloro-3'-indolyphosphate and nitro-blue tetrazolium (BCIP and NBT). Here, AP conjugated to the secondary antibodies hydrolyzes BCIP into inorganic phosphate and 5-bromo-4-chloro-3-indole and inorganic phosphate, which is further oxidized by NBT to form an insoluble dark blue-purple diformazan precipitate. Once the bands were developed, the membrane was then washed thoroughly with deionized water and dried in air on a filter paper.

Table 16. Preparation of separating gel and stacking gel.

Separating gel	Volume	Stacking gel	Volume
H_2O	3.6 ml	H_2O	2.33 ml
1.5 M TrisHCl, pH 8.8	2 ml	0.5 M TrisHCl, pH 6.8	1 ml
Acryl:Bis (37.5 : 1)	2.4 ml	Acryl:Bis (37.5 : 1)	0.67 ml
APS (10 %)	40 μl	APS (10 %)	20 μl
TEMED	10 μl	TEMED	2 μl

Notes: APS = Ammonium Persulfate ; TEMED = Tetramethylethylenediamine

Dissolution of siRNA/APTES-pSiNTs

Cell lysates remaining after eGFP knockdown experiments were collected, centrifuged and washed with DI H_2O. The pellets were re-dispersed in DI H_2O and the morphology of the NPs was

evaluated by Transmission electron microscope (TEM) imaging (JEOL JEM-2100 electron microscope, 200 kV).

6.2.6 Delivery of siRNA Targeting ER-encoding mRNA

a) Cytotoxicity of APTES-pSiNTs Against MCF-7 cells

MCF-7 cells (1×10^4 cells/well) were seeded in a 96 well plate and were incubated for 24 h. Next day, APTES-pSiNTs were sonicated and re-dispersed in OptiMEM as described in section 2.3. Cells were treated with APTES-pSiNTs, whose final concentrations in the wells were: 5 µg/ml, 12.5 µg/ml and 25 µg/ml. Cells were incubated for 48 h, and cell viability was assessed by CellTiter-Glo assays.

b) Cytotoxicity of siER

MCF-7 cells were seeded and incubated as described above. siER/APTES-pSiNTs were prepared as described in section 2.3 (Note: 0.02 µg/ml APTES-pSiNTs was incubated with 10 pmol siRNAs), and the samples were added into each well (final conc. = 5 µg/ml). After 48 h, cell viability was assessed by CellTiter-Glo assays.

For the controls, cells were transfected with APTES-pSiNTs, NS_siRNA/APTES-pSiNTs and siRNAs delivered by Optifect (0.5 µl Optifect/10 pmol siRNAs/50 µl OptiMEM).

c) Interaction of siRNA/APTES-pSiNTs with MCF-7 Cells

Brightfield Imaging

After 48-h transfection, cells were observed using the visible light (brightfield mode) of the fluorescence microscope.

SEM Imaging

MCF-7 cells (1×10^5 cells/500 µl) were seeded on a coverslip placed in a 6-well plate and

128

were incubated for 30 min at 37 ºC. Complete medium (2.5 ml) was added into the well, and cells were incubated for 24 h. Next day, APTES-pSiNTs (15 μg) were incubated with NS_siRNA (100 pmol) for 30 min at RT, and the samples were prepared as described in siER transfection section. Cells were transfected with NS_siRNA/APTES-pSiNTs for 4, 24 and 48 h. After each incubation time, cells were fixed and dehydrated according to the procedure as described above.

Confocal Imaging

MCF-7 cells were seeded and treated as described in the SEM imaging section. Here, APTES-pSiNTs (15 μg) were incubated with AF-647 (40 pmol). Cells were transfected with AF-647 NS_siRNA/APTES-pSiNTs for 4 h and 24 h. After each incubation time, cells were stained with Green BODIPY and fixed with 4 % paraformaldehyde as described in the siGFP section.

d) Western Blot for Analysis of ER Protein Expression

MCF-7 cells were seeded in a 96-well plate (1×10^4 cells/well and 8 wells/sample for scale-up) and transfected with siRNAs as described in the section 2.6.2. After 48 h, cells were washed with PBS (100 μl), trypsinized (25 μl) and quenched with the complete medium (175 μl). Cells were harvested and washed with cold PBS. Cell pellet was incubated in the radioimmunoprecipitation assay (RIPA) buffer supplemented with protease inhibitor (80 μl total) on ice for 15 min. Proteins extraction and Western blot were performed as described above. After blotting with 5 % milk, the membrane was cut into halves and each portion was incubated in a suitable primary antibody solution. Here, mouse primary ER α and β actin antibodies (1:1000) (Santa Cruz Biotechnology) were utilized.

In order to achieve the optimal signal for quantification, a WESTERNVIEW detection kit (Enzo Life Sciences) was utilized. Here, after incubation in the primary antibodies, membranes were washed with the kit's wash buffer for 10 min (3 times) and were incubated in the secondary

antibody (anti-mouse, AP conjugate) (1:100) at RT for 1 h. Membranes were washed again with the wash buffer and incubated in the NBT/BCIP solution of the kit in the dark without shaking until the purple bands develop (typically 1-2 min for β-actin and 10 min for ER). Membranes were quickly washed with plenty of DI water, and the membranes was immediately imaged.

Protein bands after Western blot were quantified by using ImageJ software. Here, ER protein was first normalized to the corresponding β-actin control, and the resulting ER/ β-actin ratio was normalized to the no treatment control to obtain the % ER expression.

e) **Reverse Transcription-quantitative Polymerase Chain Reaction (RT-qPCR)**

RNA Extraction

MCF-7 cells were transfected and harvested as described in the "Western blot" section. After the cells were washed with PBS, the samples were prepared according to the protocol of Maxwell® 16 LEV simplyRNA Purification Kits. RNA extraction was automatically performed by Maxwell 16 machine. Quantification of the total extracted RNA was determined by measuring absorbance at 260 nm using Nanodrop spectrophotometer. The purity of RNA samples was assessed by determining the 260/280 and 260/230 ratios, which should be around 2.0 for acceptable purity (Figure 69A).

RNA integrity was evaluated by gel electrophoresis. In this method, agarose solution (0.8 % agarose (0.2 g) in TAE buffer (25 ml)) containing 10,000× SYBR dye (2.5 μl) was prepared, and gel was poured once the solution was warm. RNA samples were prepared by mixing the extracted RNA (2 μl) with 6× loading dye (1.67 μl) and further diluted with DI water to make up a 10 μl solution. Gel was run at 100 V for 1 h and was imaged using Syngene G:Box chemi/fluor imaging system. RNA with acceptable integrity must exhibit two bands associated to 28S and 18S of ribosomal RNA (rRNA) (Figure 69B). It should be noted that the ladder utilized herein was

130

double stranded DNA, which was mainly used for confirming the efficiency of the gel electrophoresis.
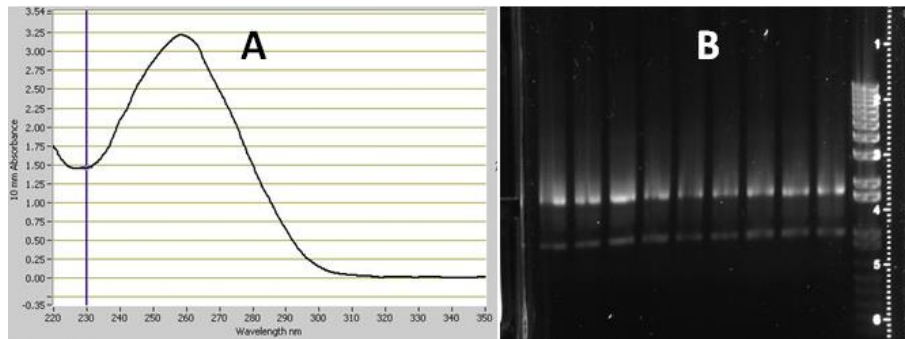
Figure 69. A typical UV-Vis spectrum of total extracted from RNA (here is RNA extracted from cells with no treatment) and B) Gel electrophoresis of the extracted RNAs from MCF-7 cells after a siRNA transfection experiment.

Synthesis of cDNA

RNA was further diluted with RNAse-free water and was combined with qScript cDNA SuperMix (QuantaBio) (8 μl : 2 μl) in 0.2 ml PCR tube (with domed-cap). The reaction was run using a thermal cycler (BIO-RAD T100), and the reaction conditions were set according to the manufacturer's protocol: 5 min at 25°C, 30 min at 42°C, 5 min at 85°C and hold at 4°C. After the reaction were completed, the product was centrifuged and transferred into a centrifuge tube containing 30 ml reverse transcription buffer.

To construct a calibration curve, RNA extracted from cells with no treatment was combined with the qScript cDNA Supermix (16 μl : 4 μl), and the resulting cDNA was diluted with RNAse-free water to obtain two-fold serial dilutions.

RT-qPCR

cDNA was combined with a reaction mixture containing PerfeCTa SYBR Green FastMix (QuantaBio) (2×), β-actin (or ER) primers (20 μM) and RNAse-free water, and the mixture was

131

added into a 96-well PCR plate (10 μl/well). The primer sequences designed for ER α and β-actin are the following:

Table 17. Primer sequences.

Primer	Sequences
ER α	Forward: 5'– GGC TTC TCT TGG TAT GTC TTG T - 3'
	Reverse: 5' – CTC CCA GAT TCT CAG TCC TTT G – 3'
β-actin	Forward: 5' – GGA TCA GCA AGC AGG AGT ATG – 3'
	Reverse: 5' – AGA AAG GGT GTA ACG CAA CTA A – 3'

<u>Note</u>: The primers were purchased from Integrated DNA Technologies.

The plate was sealed and spun at 1350 rpm for 3 min. The reaction was run according to the manufacturer's protocol; here, a "Fast 2-Step Cycling" setting was followed: Initial denaturation: 95 °C, 30 s, PCR cycling (40 cycles): 95 °C, 3-5 s and Collect data at end of extension step: 60 °C, 20-30 s. The reactions were performed by using CFX Connect Real-Time System (BIO-RAD).

In addition, PCR efficiency (or amplification efficiency) was analyzed based on the slope of the calibration curve. Since PCR efficiencies of both ER α and β actin were around 90 % (Figure 70), the design conditions of qPCR assays presented herein were successfully optimized.
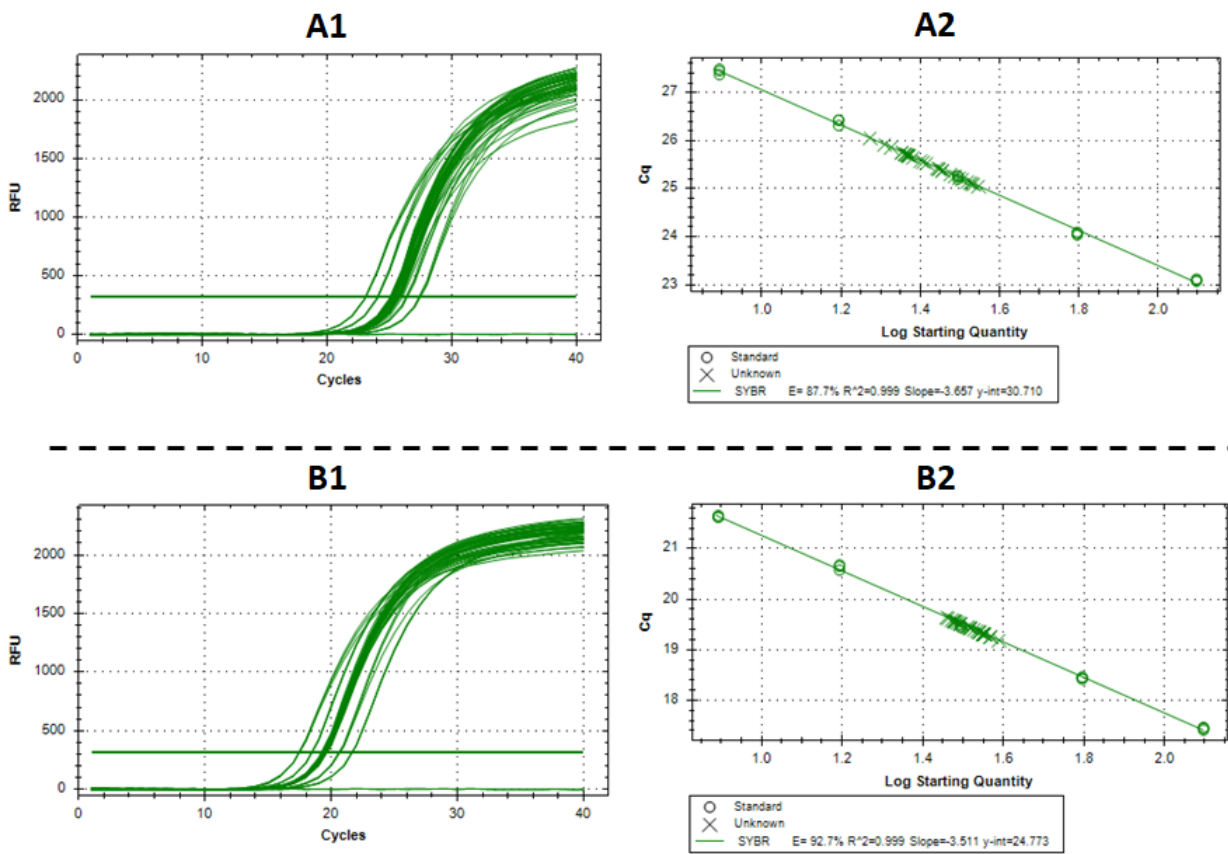
Figure 70. Amplification blots and standard curves of PCR products A) ER and B) β−actin.

6.3   Results and Discussion

6.3.1   Characterization of siRNA/APTES-pSiNTs

As discussed in the previous section, the negatively charged siRNA can be immobilized on the APTES-pSiNTs surface via electrostatic interactions. Here, an average of 23.1 % CE and 5 % of siRNA mass loading were respectively achieved at the lowest concentration of APTES-pSiNTs (0.02 µg/µl) (Table 18). An increase in APTES-pSiNTs concentration slightly enhanced CE% but yielded a decrease in % wt siRNA, presumably due to formation of large aggregates with relatively lower surface areas and a reduction in the amino group density available for conjugating with siRNAs.

After siRNA loading, the zeta potential analysis of siRNA/APTES-pSiNTs showed a drop of the potential value due to the shielding of the amino groups by the negatively charged nucleic acids (Table 19). Therefore, these results confirm successful immobilization of siRNAs to the functionalized nanotubes.

Table 18. Conjugation efficiency and mass loading of siRNA to APTES-pSiNTs

[APTES-pSiNTs]	CE%	% wt conjugated siRNA
0.02 µg/µl	23.1 ± 4.7	5.0 ± 1.0
0.05 µg/µl	38.1 ± 8.3	3.3 ± 0.7
0.1 µg/µl	52.4 ± 7.3	2.3 ± 0.3

Table 19. Zeta Potential measurements.

	Zeta Potential (mV)
APTES-pSiNTs	+20.55 ± 0.35
siRNA/APTES-pSiNTs	- 10.27 ± 0.26

With regard to the release kinetics of siRNAs from SiNT matrices, a burst release was observed at 4 h post incubation (Figure 71). After this time point, siRNA was released in a sustained manner. Although the cumulative release did not reach 100 %, presumably due to a loss of a small amount of the material during washing and transfer, the release profile of siRNA from SiNTs was insignificantly affected.

The gradual disappearance of the brown functionalized pSiNT particles during the course of the release experiment indicated dissolution of SiNTs, thereby implying the possibility that siRNA release was mediated by the dissolution of the pSiNT matrix.

It should be noted that although the complete medium more closely mimics biological conditions and enhances dissolution kinetics of SiNTs (Chapter 2), the complex components of the medium significantly interfered with siRNA measurements. Overall, the study presented herein provides the initial release profile of siRNA from the SiNT platforms and serve as a foundation for understanding the *in vitro* siRNA delivery.

Time (h)	% release
1	53.25
2	73.19
4	84.18
21	87.09
45	87.40
69	87.48
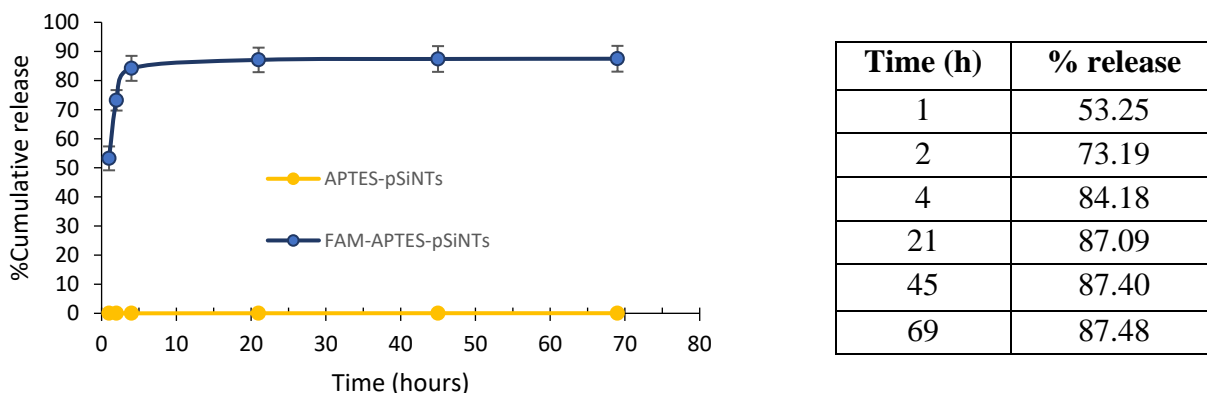
Figure 71. Release profile of FAM-labeled siRNA from APTES-pSiNTs.

6.3.2 Delivery of siGFP for Downregulation of eGFP Expression in HeLa cells

a) Cytotoxicity of APTES-pSiNTs

Since any nanoparticles can potentially exert adverse side effects to cell proliferation as well as transfection efficiency, *in vitro* cytotoxicity of APTES-pSiNTs was assessed. In this case, the viability of HeLa cells was above 90 % at all the tested doses after 36-h treatment, suggesting cytocompatibility of the NPs and the negligible influence of the diluted medium condition to cell viability (Figure 72).
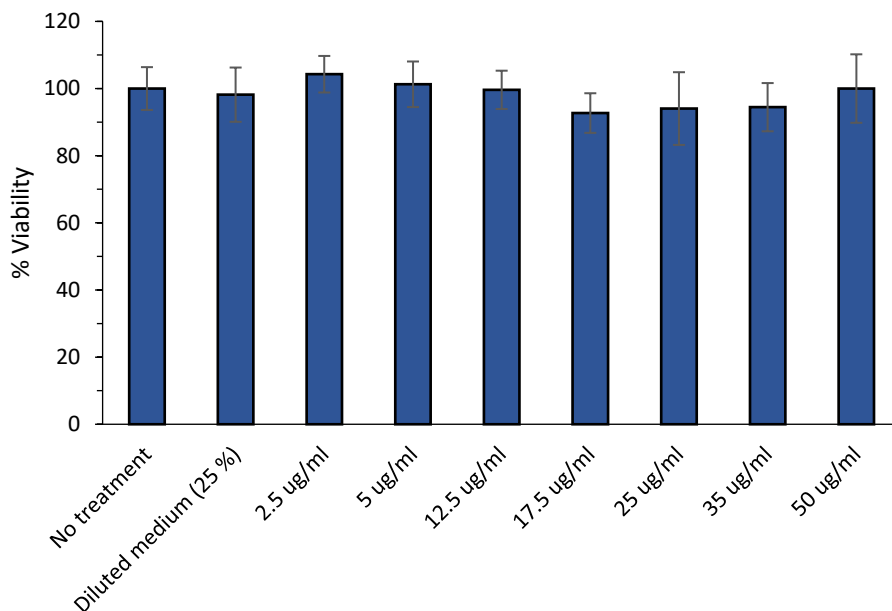
Figure 72. Viability of HeLa cells after 36-h treatment with APTES-pSiNTs.

b) **Interaction between siRNA/APTES-pSiNTs and HeLa cells**

In order to elucidate feasibility of APTES-pSiNTs as nanocarriers in intracellular delivery of siRNA, a combination of imaging techniques was performed to assess cellular internalization of the nanotubes as well as the siRNA components.

Brightfield Imaging

Optical imaging of HeLa cells after 36-h transfection with siRNAs/APTES-pSiNTs showed a significant density of particles accumulating around the nuclei, thus indicating cellular association and possible internalization of the NTs inside the cells.
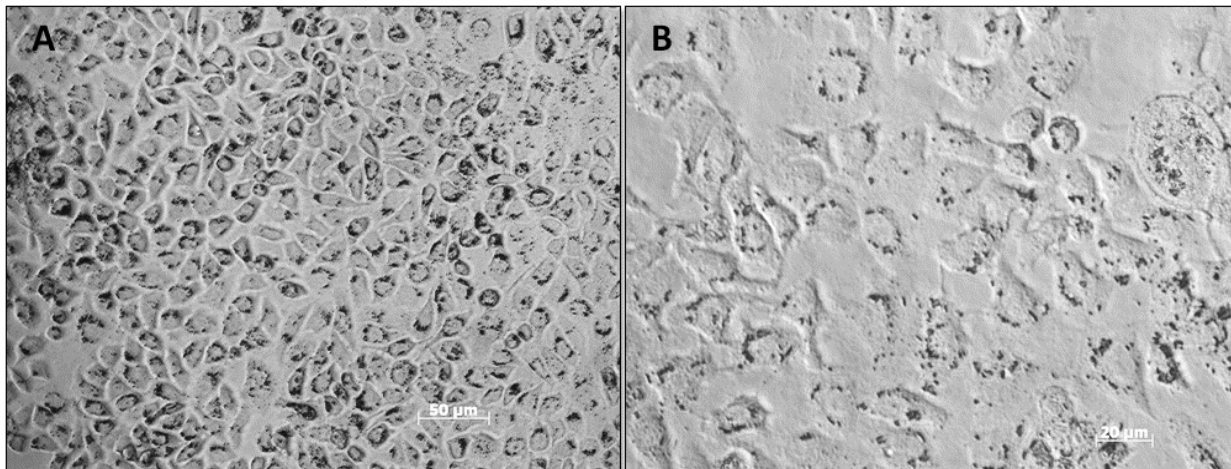
Figure 73. A) Brightfield imaging showing interactions between siRNA/APTES-pSiNTs with HeLa cells. B) High-resolution imaging showing accumulation of the NTs around the nuclei of HeLa cells. [APTES-pSiNTs] = 12.5 μg/ml.

Confocal Microscopic Imaging

In this study, delivery of the siRNA cargoes into HeLa cells was assessed via tracking fluorescently labeled siRNA. For transfection with free AF 647-siRNA, no fluorescent signal associated with siRNA was observed owing to instability of the cargoes in the extracellular environment (Figure 74A). Conversely, AF 647-siRNAs were shown to be associated with a considerable number of cells after 4 h and 24 h transfection with AF 647-siRNA/APTES-pSiNTs (Figure 74 D and E). Co-localization of the fluorescent siRNAs with the nanotube bundles (black spots located on cells (green channel)) confirmed conjugation of siRNAs to the SiNT matrices. In addition, internalization of siRNA after 4 h was confirmed via the confocal z-stack scanning (Figure 75). Therefore, the data presented here collectively provides evidence of the ability of SiNTs to immobilize, protect and mediate delivery of siRNAs inside the cells.

It is also necessary to point out that while both APTES-pSiNTs and the positive control Optifect were incubated with the same amount of siRNA, a greater concentration of siRNA was delivered by Optifect, presumably owing in part to a relatively higher conjugation efficiency.

137
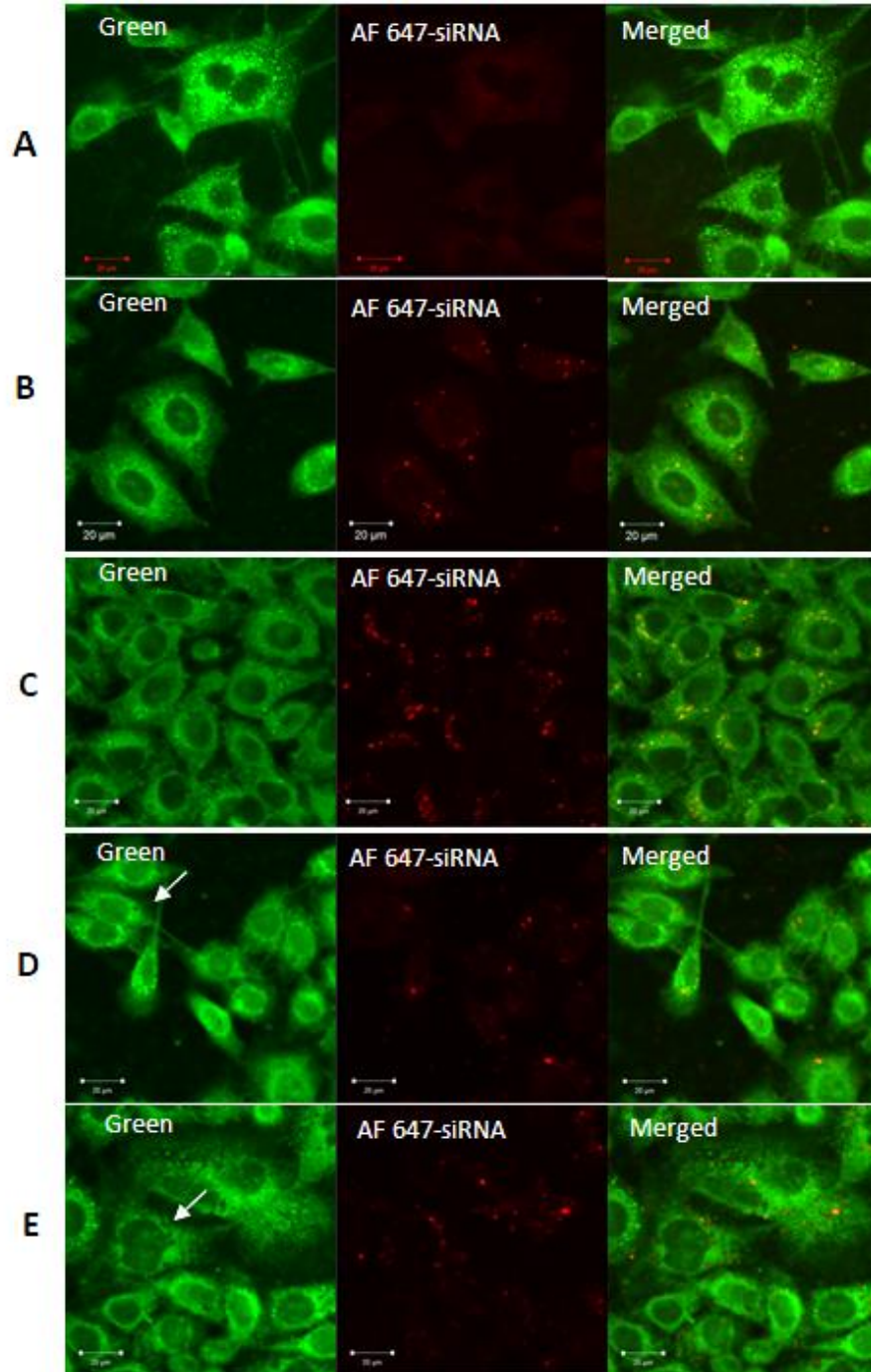
Figure 74. Confocal fluorescence imaging of HeLa cells and fluorescently labeled siRNA (AF 647) without delivery vector (A) and delivered by Optifect after 4 h (B) and 24 h (C) or by APTES-pSiNTs after 4 h (D) and 24 h (E). The arrows indicating the presence of the nanotube vectors. Scale bars: 20 μm.
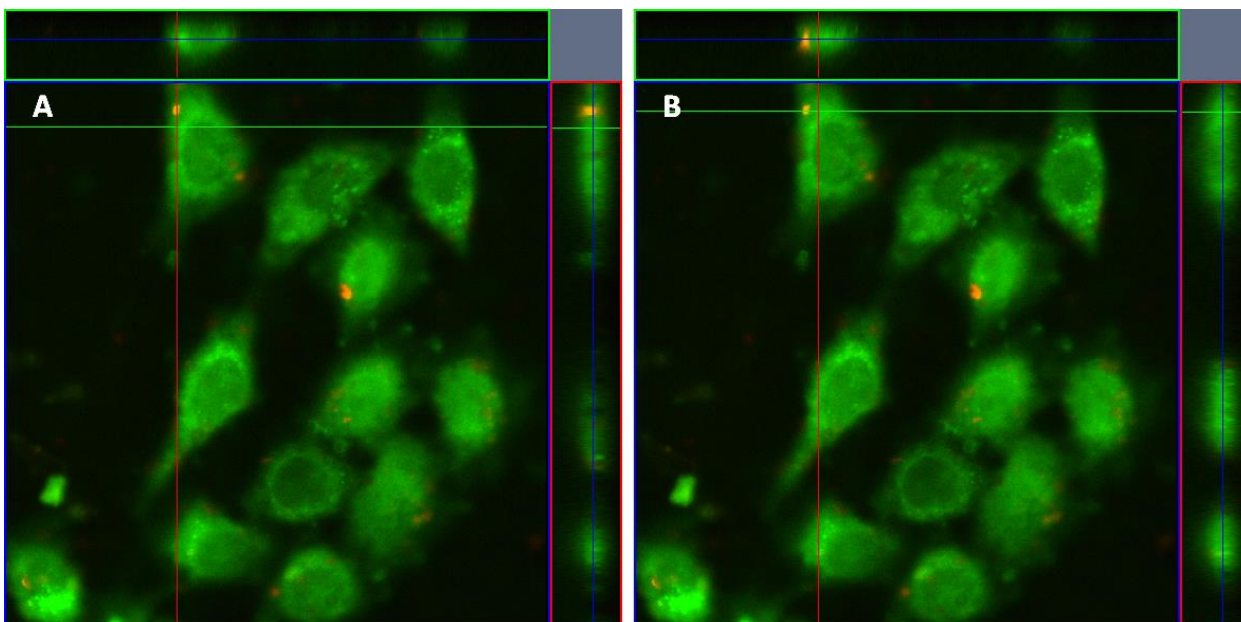
Figure 75. Z-stack scanning (confocal imaging) showing interactions between AF647-NS_siRNA/APTES-pSiNTs with cells after 4 h. (A) YZ plane (on the right of the XY image) and XZ plane (B) (above the XY image) showed association of siRNA with cells. Note: blue line: XY plane, green line: XZ plane and red line: YZ plane.

SEM Imaging

While confocal imaging is a powerful tool to validate intracellular delivery of siRNAs, 2D SEM imaging provides additional information regarding the interface between siRNA/APTES-pSiNTs and cells.

After 4-h transfection, the cell membrane was shown to wrap around the majority of the bundles. Even those within the largest size range (i.e. 4-5 μm) were also partially engulfed by cells at this time point (Figure 76). Based on SEM imaging, nanotube bundles can interact with cells via three main surfaces: A) closed-end; B) opened-end; and C) sideways (Figure 77). In all cases, the cell membrane appeared to favorably interact with all the surfaces and readily wrap around the bundles. Since nanotubes were shown to almost fully penetrate the cell membrane after 4 h (Figure

139

77 A and B), a relatively short nanotube length, i.e. submicron height, is favorable for an optimal cellular uptake process.

At a 24-h time point, a large number of cells exhibited protruding surfaces, which was not observed in the untreated cells (Figure 76 and Figure 78). Since the trace of the nanotubes was visible within these areas, these protrusions were the nanotube bundles being enclosed within the cell membrane. Interestingly, the density of the protrusions continuously escalated after 48 h and 72 h, thereby implying successful internalization of a high concentration of the nanotubes. Presumably due to variation in the intracellular pH as well as limited surface exposure of the bundles to the growth medium after membrane wrapping, the degradation of SiNT matrices was slowed down as the nanotube remnants were observed after 72 h.
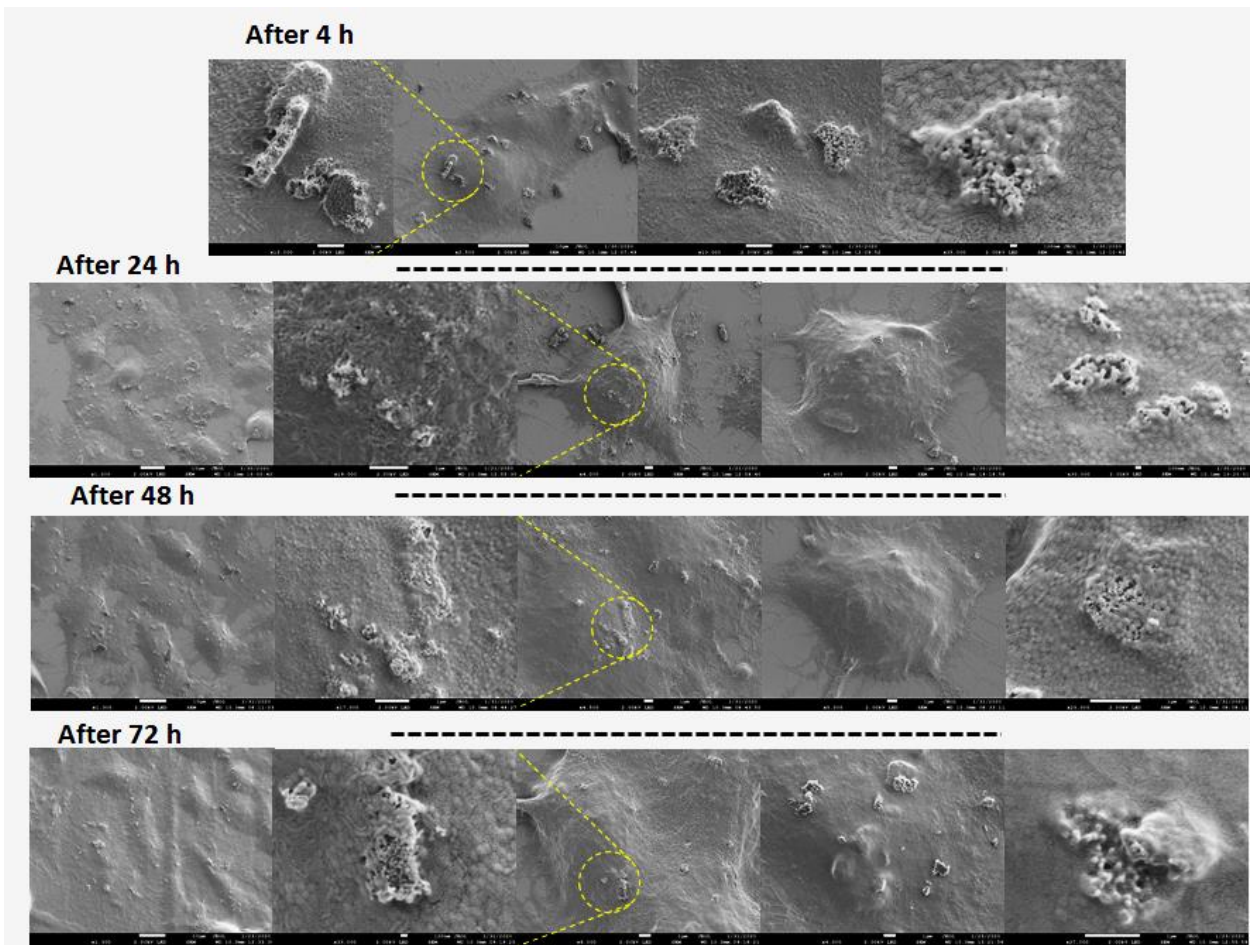
Figure 76. SEM imaging of HeLa cells after exposure to siRNA/APTES-pSiNTs for 4, 24, 48 and 72 h.
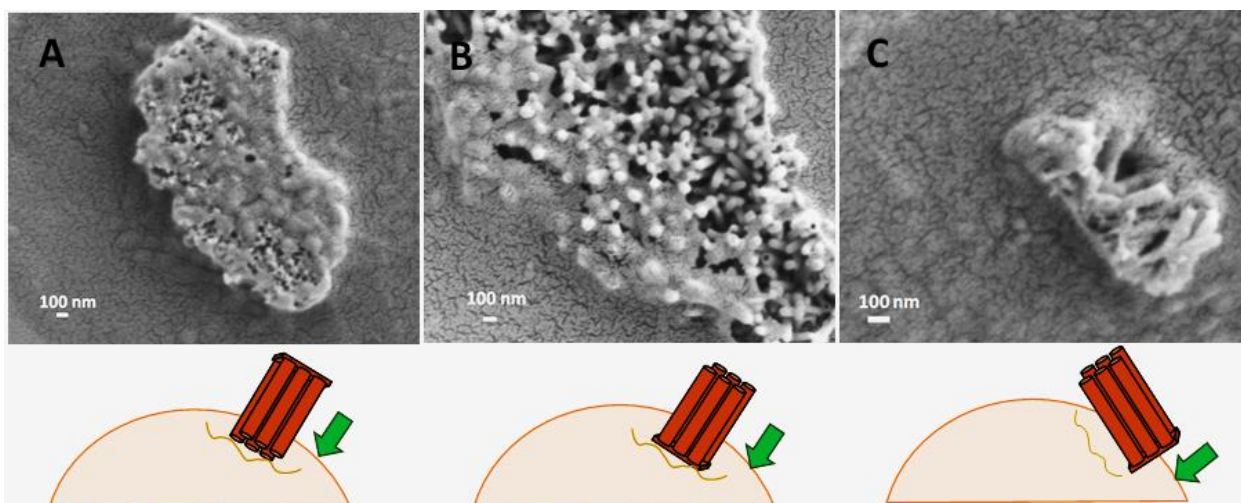
Figure 77. SEM imaging showing siRNA/APTES-pSiNT bundles positioned on the HeLa cells via: A) the closed-ends; B) the opened ends and C) sideways after 4-h incubation.
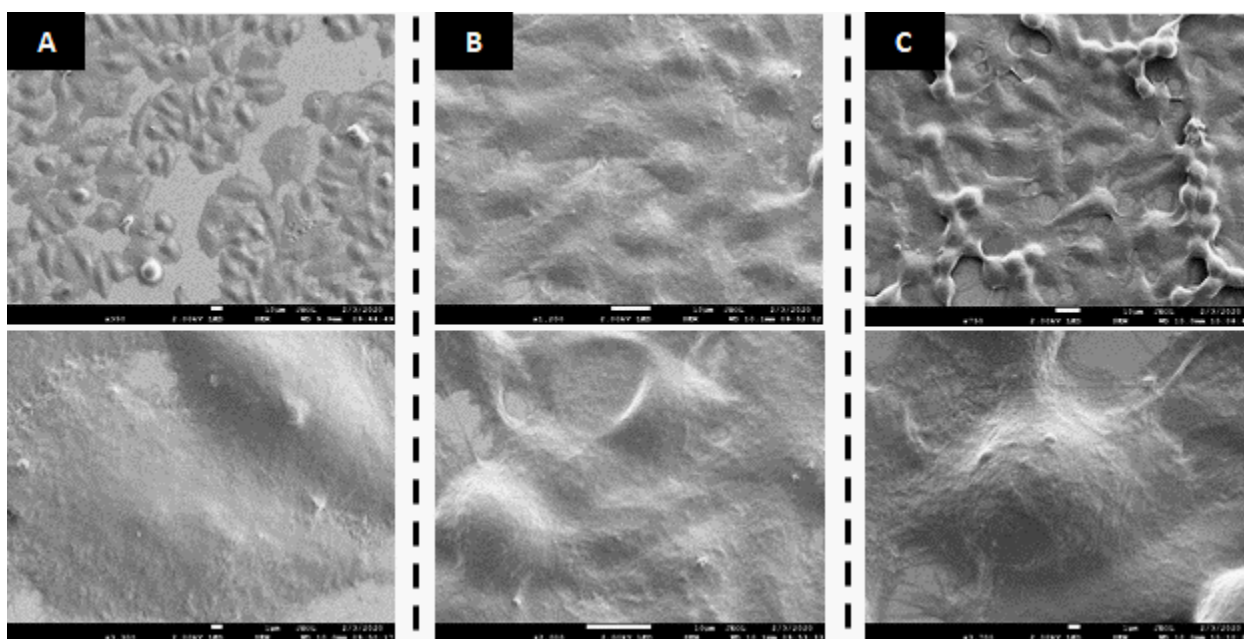
Figure 78. SEM imaging of untreated HeLa cells after A) 24 h, B) 48 h and C) 72 h.

6.3.3 Silencing of eGFP Expression in HeLa Cells by Delivery of siGFP

In these studies, the ability of APTES-pSiNTs to deliver siGFP was evaluated. Based on the fluorescence images and quantification of eGFP expression, a 50 % reduction in eGFP protein

level was observed after transfection with siGFP (3-4 pmol) delivered by the nanotubes. Since NS_siRNA/APTES-pSiNTs insignificantly affected eGFP expression, downregulation of eGFP was induced by siGFP delivered by APTES-pSiNTs rather than the nanotube matrices themselves (Figure 79 and Figure 80).

Although a higher % knockdown of eGFP was observed in the case of the commercial Optifect (~ 80-90 %), it should be pointed out that a total amount of 10 pmol siGFP were conjugated to Optifect, since complex formation with a higher siGFP density (100 pmol) did not yield a significant increase in eGFP knockdown.

With regard to NS_siRNA/Optifect, the level of eGFP knockdown varied randomly among trials (i.e. a large standard deviation). Since this significant fluctuation was not observed in siGFP/Optifect, this effect was not triggered by Optifect, but rather due to the off-target effects of NS_siRNAs, which have been reported to imperfectly bind to other mRNAs and potentially induce inflammatory responses.[239] While this off-target effect were not prominent in the case of NS_siRNA/APTES-pSiNTs, it was presumably due to a lower density of the NS_siRNA available ($n_{siRNA\ (conjugated)}$ = 3-4 pmol) to trigger a pronounced effect.

Since APTES-pSiNTs will always exhibit a relatively higher density of the exposed NH_2 groups compared to those with siRNA bound on the surface, APTES-pSiNTs are more likely to interact with the transiently delivered pEGFP via electrostatic interactions; therefore, eGFP expression from the transiently transfected pEGFP can be significantly interfered with. Therefore, this control was not performed in order to avoid complicating analysis.
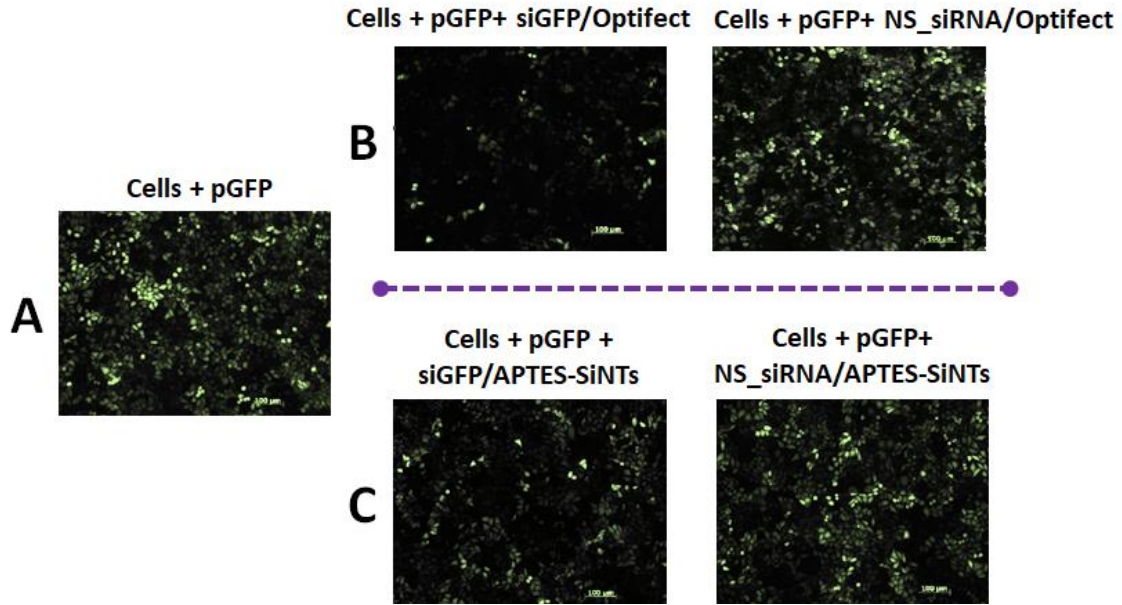
Figure 79. Fluorescent imaging of HeLa cells after transfected with pEGFP (A) and subsequently with siGFP (or NS_siRNA) delivered by Optifect (control) (B) or APTES-pSiNTs (C). Scale bars: 100 μm.
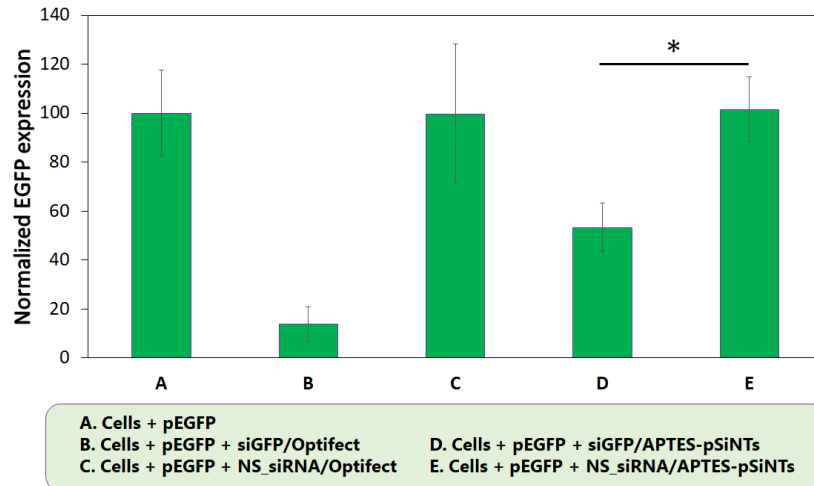
Figure 80. Normalized EGFP expression after 36-h siRNA transfection based on quantification of fluorescence intensity. * $p < 0.05$ (n = 4).

a) β-actin Expression

Housekeeping proteins are involved in basic cellular maintenance and is found in great abundance in many cell types.[240] Here, evaluation of the expression level of some proteins such as cytoskeletal β-actin, which are essential for cell motility and structural integrity,[241] is useful for assessment of a given treatment towards normal cellular functions.In this study described here, analysis of the β-actin protein by Western blot suggested that the transfection conditions as well as the APTES-pSiNT matrix itself insignificantly alter the level of β-actin protein, thus confirming specificity of the siGFP-mediated knockdown of GFP and cytocompatibility of the nanotube matrices (Figure 81).

peGFP	-	+	+	+	+	+	+
siGFP	-	-	+	-	+	-	-
Ns_siRNA	-	-	-	+	-	+	-
APTES-SiNTs	-	-	-	-	+	+	+
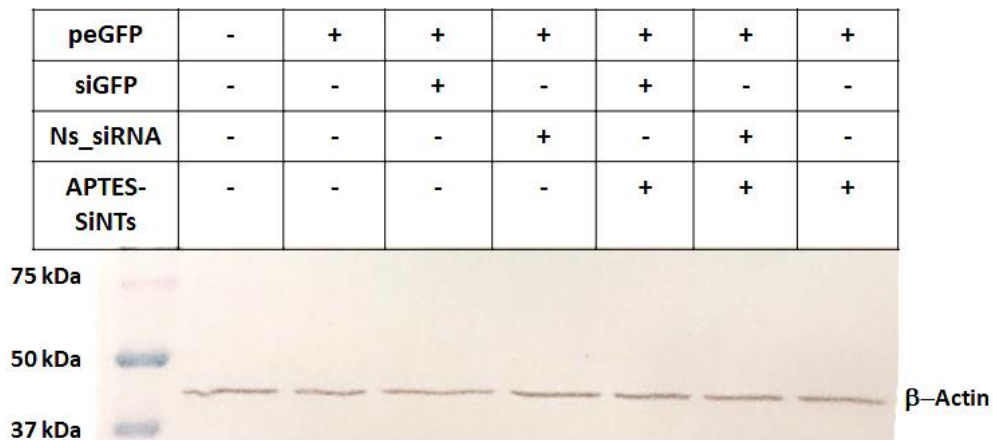
Figure 81. β-actin expression level in HeLa cells.

b) Dissolution of siRNA/APTES-pSiNTs

Since understanding the biofate of the delivery vectors after completing their functions is essential to assess potential health risks imposed by long-term accumulation, evaluation of the degradability of APTES-pSiNTs after siRNA transfection experiments is necessary. Here, assessment of the SiNT bundles remaining after 36 h based on TEM imaging revealed a complete

collapse of the defined nanotube structures, thereby indicating the dissolution of the nanocarriers during the delivery of siRNAs in biological media (Figure 82).
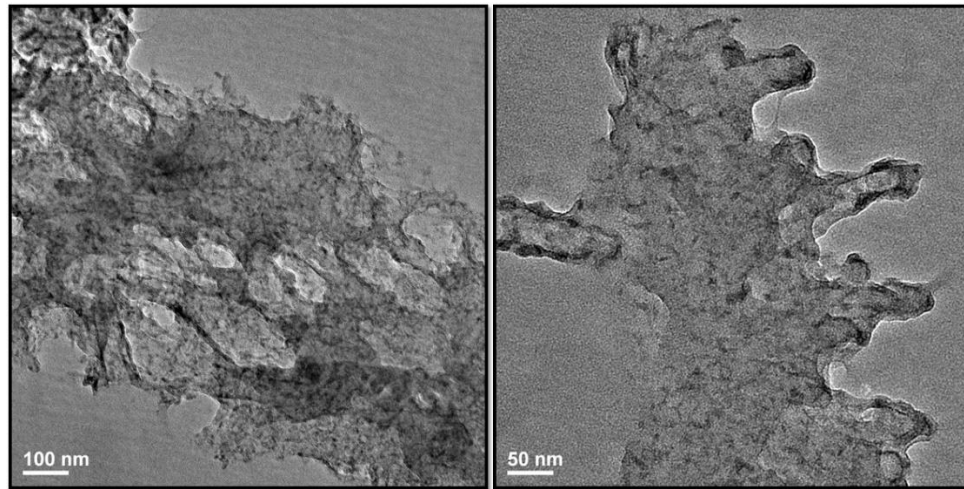
Figure 82. Dissolution of siRNA/APTES-pSiNTs in the complete growth medium after 36 h.

6.3.4 Delivery of siRNA Targeting mRNA Encoding Estrogen Receptor (siER)

In this section, a therapeutic model of siRNA delivery is described in which APTES-pSiNTs were employed to deliver siER to MCF-7 cells, whose ER α involved in cell proliferation is expressed at an abnormally high level.[237]

a) Cytotoxicity of APTES-pSiNTs to MCF-7 Cells

Based on *in vitro* cytotoxicity assays, cell viability of MCF-7 after treatment with APTES-pSiNTs at different doses was all above 90 %, thereby indicating cytocompatibility of the nanotube matrices to MCF-7 cells (Figure 83).
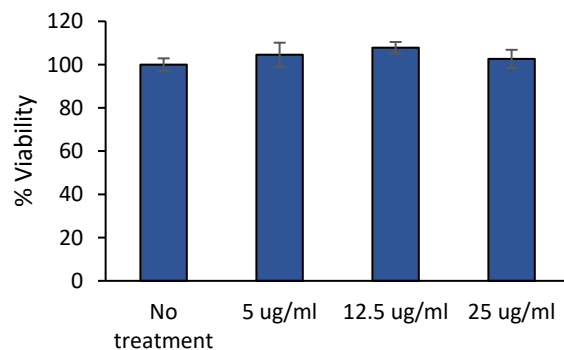
Figure 83. Viability of MCF-7 cells after treatment with APTES-pSiNTs.

b) **Association of siRNA/APTES-pSiNTs with MCF-7 Cells**

Based on optical imaging, nanotube bundles were more likely to distribute randomly on cytoplasm of MCF-7 cells rather than clustering around the nuclei as in HeLa cells, presumably owing in part to differences in cell morphology as well as biological pathways that mediate cellular internalization and intracellular trafficking. Hence, these results raised the logical question as to whether SiNTs were able to internalize inside MCF-7 cells (Figure 84).

SEM imaging provides insight into the nano-bio interface at proper resolution, siRNA/APTES-pSiNTs were shown to be partially engulfed by the cell membrane at 4 h and therefore imply initiation of the uptake process. As time proceeded, an increasing density of the protrusions, which have been discussed earlier, appeared on the cell surface, consistent with successful internalization of the materials into MCF-7 cells (Figure 85 and Figure 86).

While the optical and SEM imaging provide information regarding cellular association of siRNA/APTES-pSiNTs, confocal microscopic imaging enables one to address the question whether siRNA can be protected and delivered by the nanotube matrices. Here, fluorescence signals from AF 647-siRNA were detected on a considerable number of cells after treatment with siRNA/APTES-pSiNTs (Figure 87). In addition, interactions between siRNAs and the cell

147

membrane post 4-h transfection was evidenced via the z-stack scanning imaging (Figure 88). After 24 h, the fluorescence intensity of siRNA slightly decreased, presumably owing to the partial release of siRNA from the nanotube carriers. In terms of the positive control, Optifect was also shown to be able to deliver siRNAs into MCF-7 cells with a high transfection efficiency owing in part to a relatively greater conjugation efficiency.

Overall, the series of the cell imaging studies presented herein suggested that siRNAs can be delivered to MCF-7 breast cancer cells by APTES-pSiNTs.
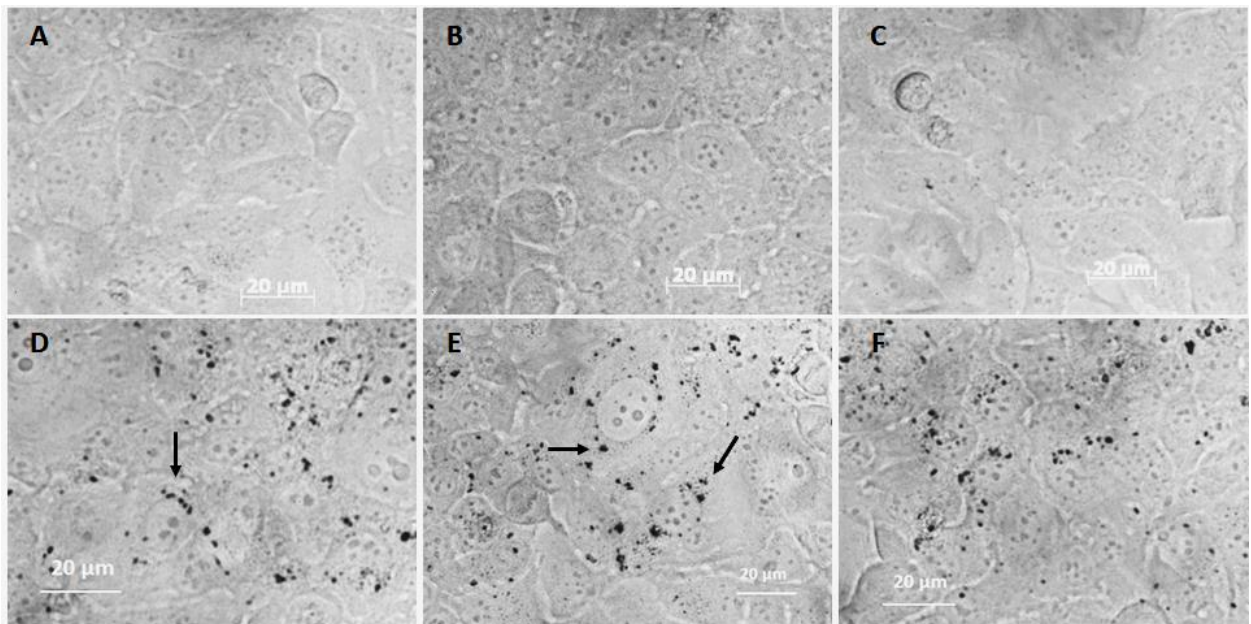
Figure 84. Bright field imaging showing the morphology of MCF-7 cells after siRNA transfection. A) No treatment, B) siER/Optifect, C) NS_siRNA/Optifect, D) siER/APTES-pSiNTs, E) NS_siRNA/APTES-pSiNTs, F) APTES-pSiNTs. [APTES-pSiNTs] = 5 μg/ml. Arrows showing the association of the nanotube matrices with MCF-7 cells.
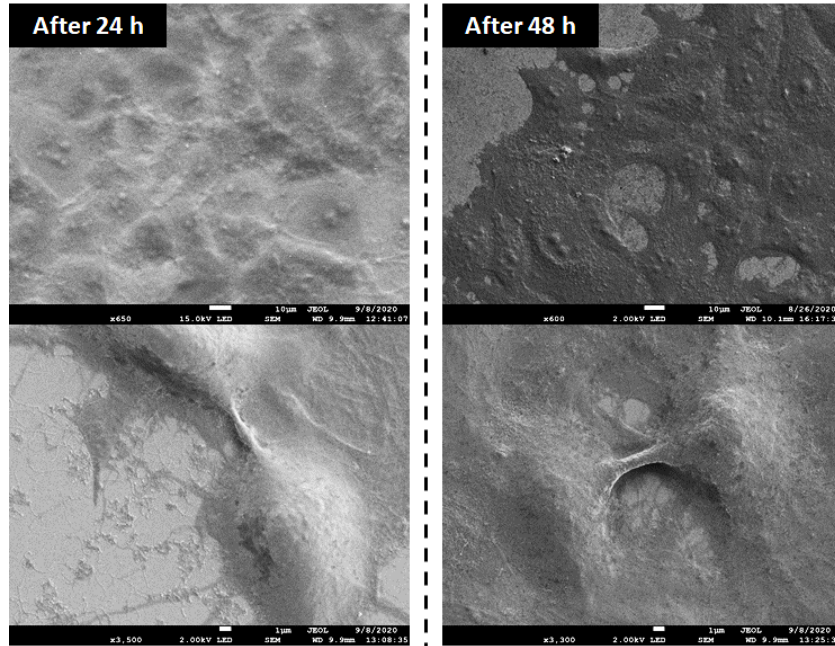
Figure 85. SEM imaging of untreated MCF-7 cells after 24 h and 48 h.
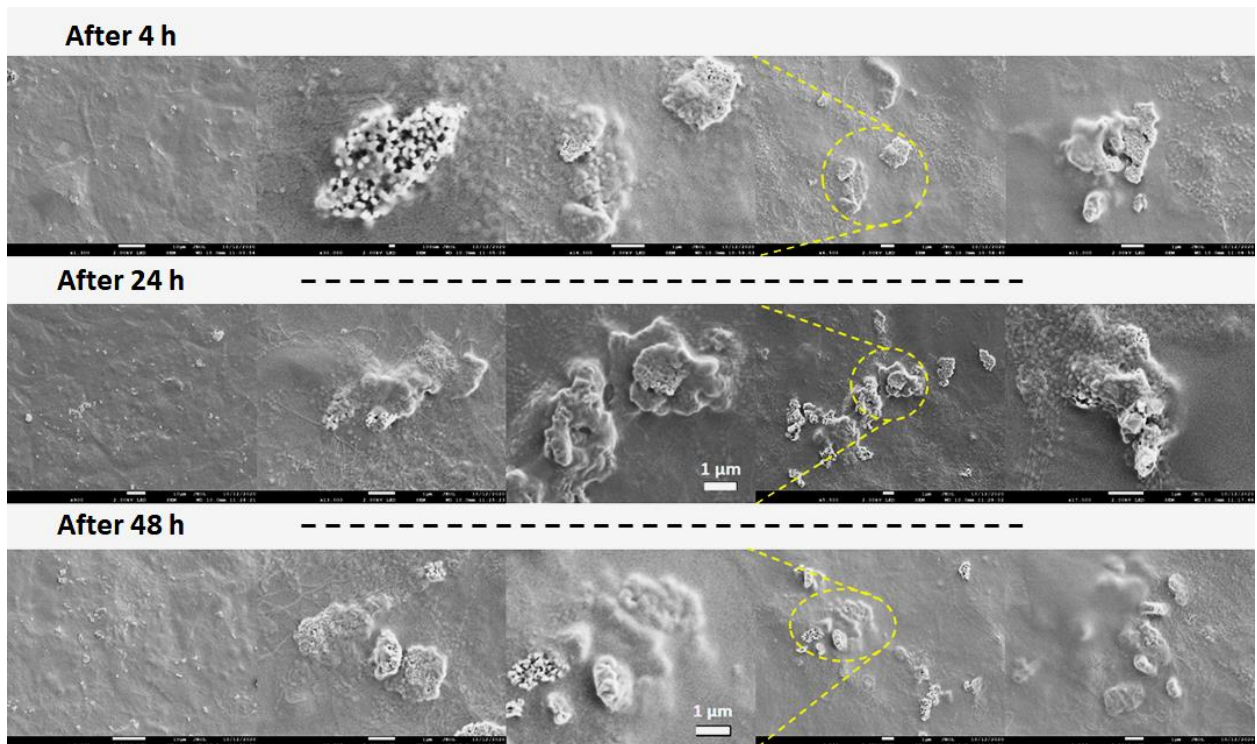
Figure 86. SEM imaging showing interactions between MCF-7 cells and NS_siRNA/APTES-siRNA.
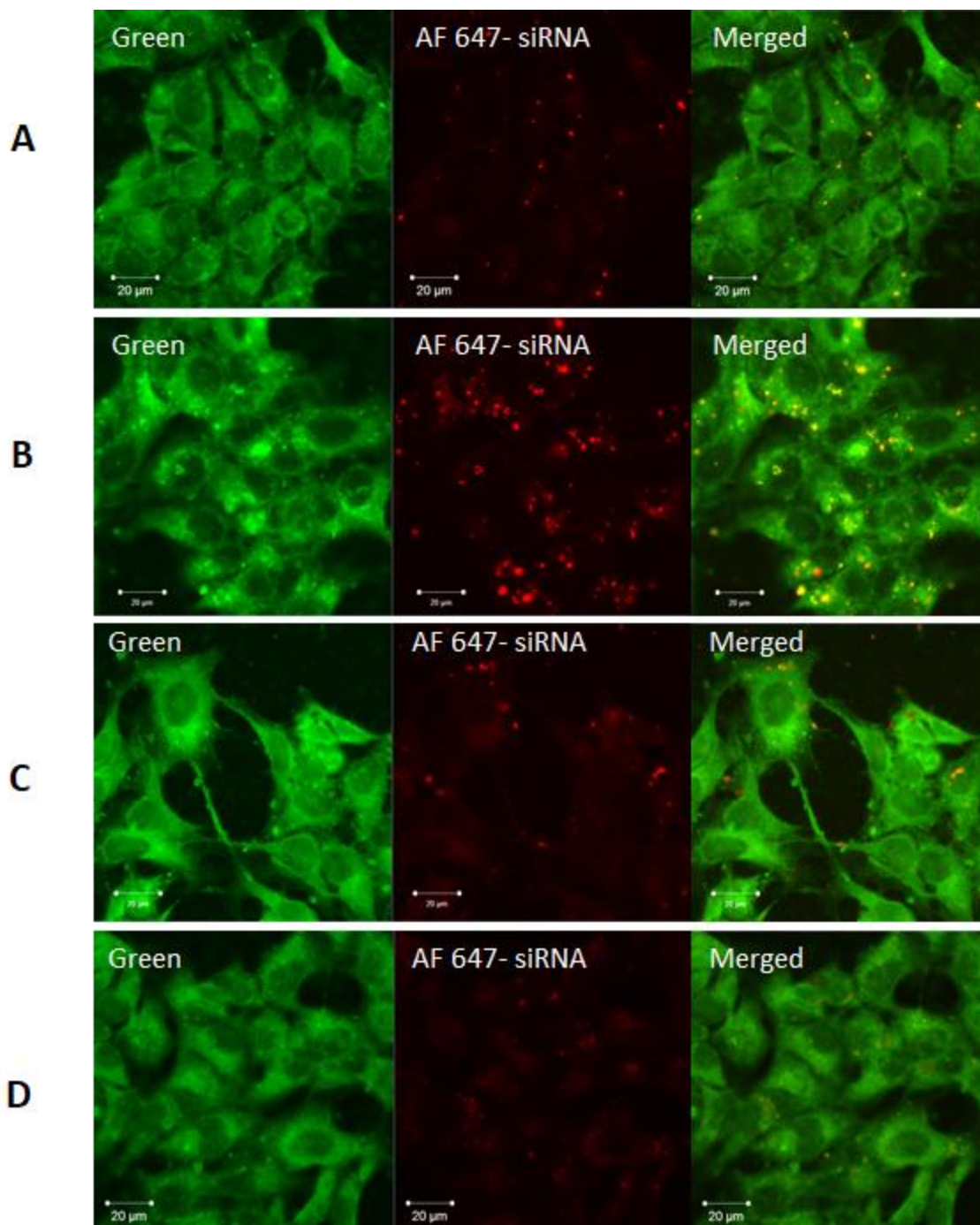
Figure 87. Confocal imaging of cellular uptake of AF647-labeled NS_siRNA delivered by Optifect after 4h (A) and 24 h (B); by APTES-pSiNTs after 4 h (C) and 24 h (D).
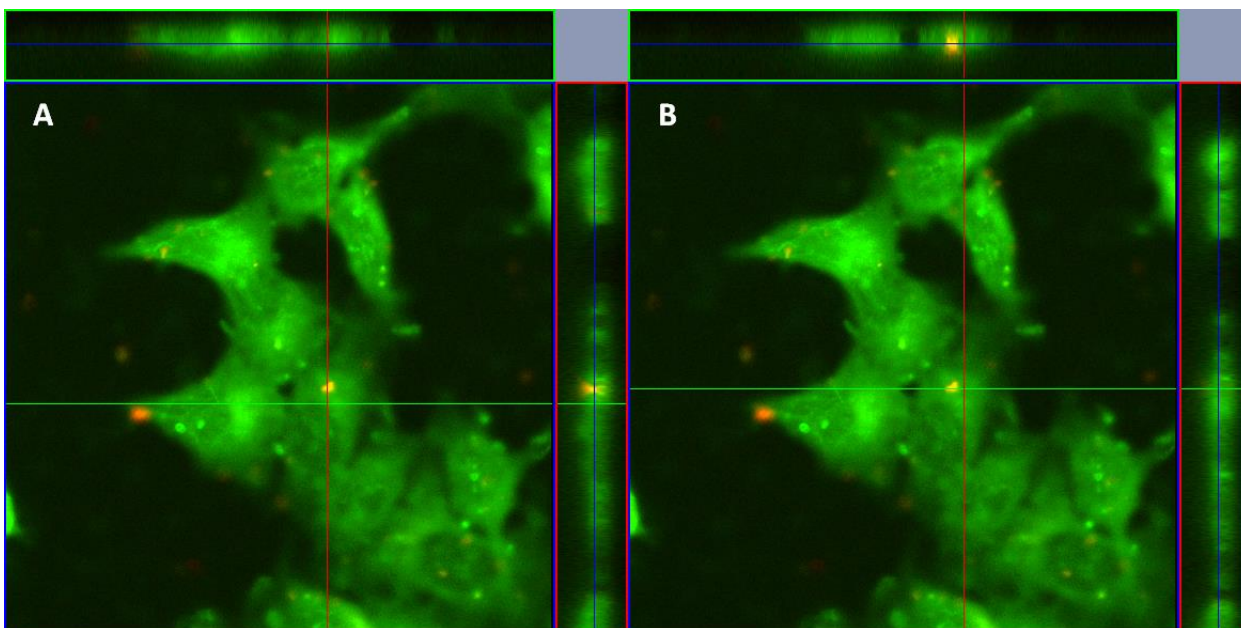
Figure 88. Z-stack scanning (confocal imaging) showing interactions between AF647-NS_siRNA/APTES-pSiNTs with cells after 4 h. (A) YZ plane (on the right of the XY image) and XZ plane (B) (above the XY image) showed association of siRNA with cells. Note: blue line: XY plane, green line: XZ plane and red line: YZ plane.

c) Effects of siER to Viability of MCF-7 Cells

Since ER α is known to be involved in promoting proliferation of MCF-7 cells, ER knockdown induced by siER was initially evaluated by assessing the reduction in cell viability. However, treatment with a high concentration of siER (10 pmol) delivered by Optifect, insignificantly hampered cell proliferation. Similarly, cells transfected with siER/APTES-pSiNTs ($n_{siER \, (conjugated)}$ = 2-3 pmol, [APTES-pSiNTs] = 5 μg/ml) were also negligibly affected in terms of cell viability (Figure 89). Hence, these initial results suggest that probing ER knockdown via cell viability is inefficacious since the reduction in ER level resulted herein might be insufficient to trigger a pronounced effect in cell proliferation. Therefore, in order to sensitively assess the knockdown efficiency, ER α-protein expression and ER α-mRNA levels were evaluated.
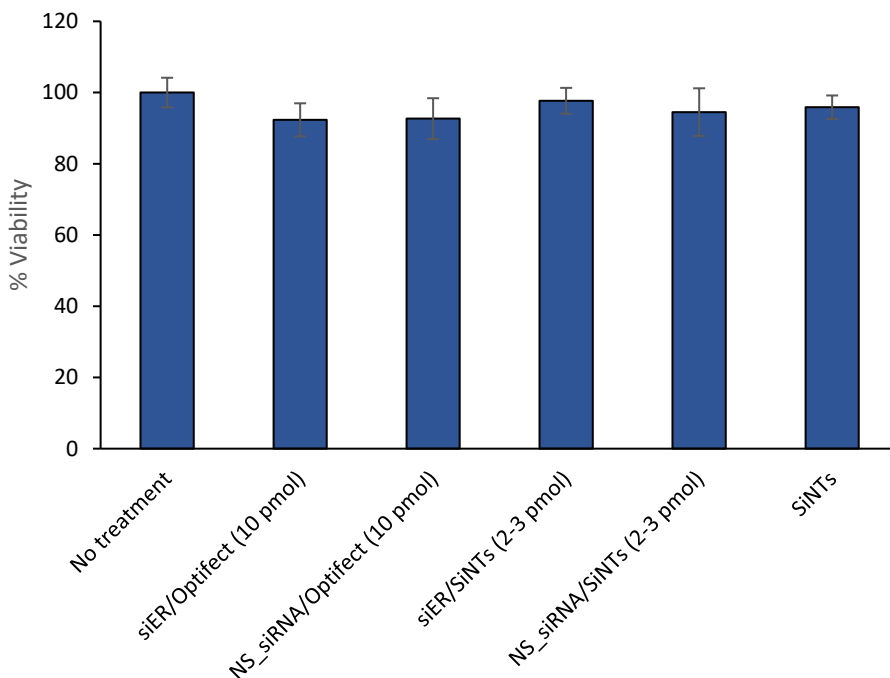
Figure 89. Viability of MCF-7 cells after transfection with siER and NS_siRNA delivered by Optifect and APTES-pSiNTs. Note: here APTES-pSiNTs is abbreviated as SiNTs.

d) Western blot Assays

In this study, siER (10 pmol) delivered by Optifect was clearly shown to downregulate ER expression by 50-65 % relative to the untreated control. On the other hand, the ER level in cells transfected with NS_siRNA/Optifect remained mostly unchanged, confirming specificity of siER in ER silencing.

With regard to transfection with siER/APTES-pSiNTs, although the knockdown level of ER was not as prominent as the positive control (siER/Optifect), presumably owing in part to a lower amount of siER (~2-3 pmol) conjugated to the nanotubes, this reduction level was higher than that of the treatment with NS_siRNA/APTES-pSiNTs (~20 % difference) (Figure 90). Since the surface chemistry of these two nanocomposites was similar to each other, a higher downregulation observed here stems from siER delivered by APTES-pSiNTs.

Although more siER can be introduced in order to enhance ER suppression by increasing the concentration of APTES-pSiNTs, siER-mediated knockdown of ER was no longer pronounced, presumably owing to unsuccessful internalization of the large aggregates formed at a relatively higher SiNT concentration.

This aggregation of siRNA/APTES-pSiNTs is an instrinsic effect, also induced during sample preparation in which the composites were centrifuged in order to replace H_2O with OptiMEM medium. Although this step can be omitted in order to circumvent this issue, significant reductions in ER levels were observed in all SiNT treatments where the growth medium was 25 % diluted with H_2O. Since earlier studies have demonstrated phenol red - a common pH indicator in many cell culture media (including OptiMEM) - can act as a weak estrogen to stimulate ER, a lower concentration of phenol red in the diluted medium might interfere with ER expression.[242] Therefore, this condition unfortunately created a fluctuating ER level, which is non-ideal for siER studies.

siER	-	+	-	+	-	-
NS_siRNA	-	-	+	-	+	-
Optifect	-	+	+	-	-	-
APTES-pSiNTs	-	-	-	+	+	+

75 kDa

ER α

50 kDa

β-actin

37 kDa
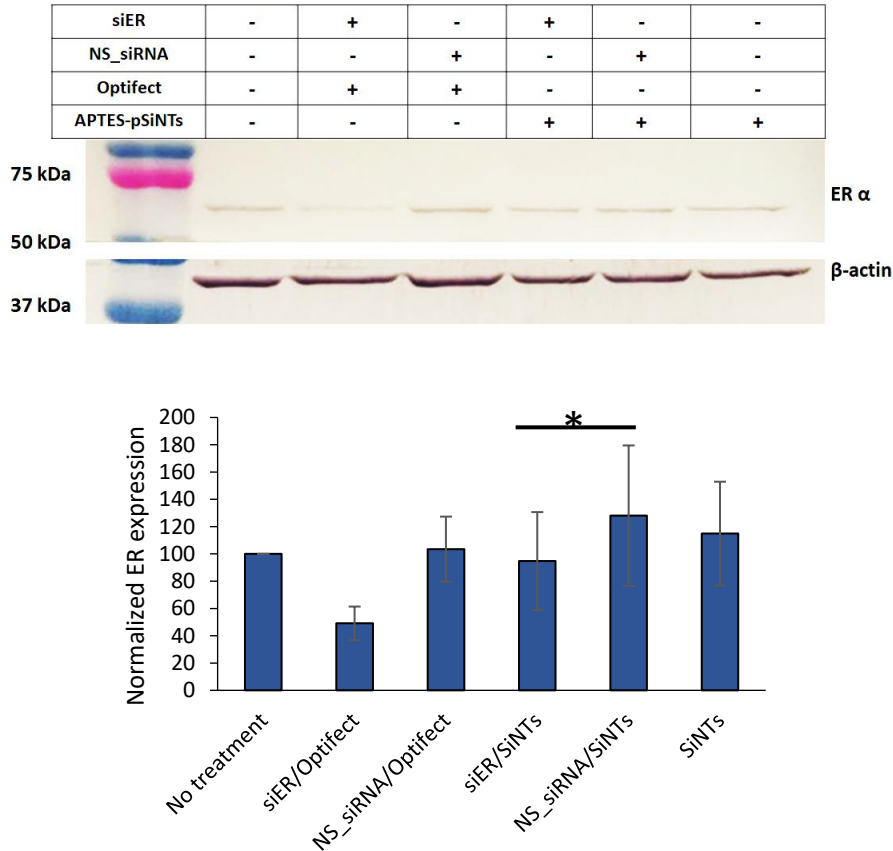
Figure 90. ER expression in MCF-7 after siRNA transfection, [APTES-pSiNTs] = 5 µg/ml, and the corresponding quantification of protein expression normalized relative to the no treatment control. (* $p < 0.1$). Note: APTES-pSiNTs is abbreviated here as SiNTs (n = 2).

e) RT-PCR

Complementary to Western blot experiments, RT-qPCR was performed, which provides a more sensitive measurement via direct quantification of ER-encoded mRNA levels (Figure 91). Consistent with Western blot results, ER-mRNA level was significantly reduced (32 %) after transfection with siER/Optifect (n_{siER} = 10 pmol). Although ER knockdown was also observed after treatment with NS_siRNA (delivered by Optifect), the large range of ER-mRNA expression was assumed to stem from the off-target effects of NS_ siRNAs, which has been discussed in the siGFP section. Interestingly, this decrease in mRNA level did not yield a pronounced reduction in

154

protein expression on the Western blot measurements; therefore, it is assumed that such a depletion level was below the detection limit of this protein assay.

Transfection with siER delivered by APTES-pSiNTs resulted in a 25 % reduction in mRNA level. Since the controls, i.e. NS_siRNA/APTES-pSiNTs and the non-functionalized nanotube matrices, yielded relatively higher mRNA levels, these results indicated that siER was effectively delivered by SiNTs to trigger a prominent reduction in ER-mRNA level. Also, based on the same reasons that have been discussed previously, the knockdown effects of NS_siRNA in this case were not significant.

Noticeably, the mRNA expression after transfection with both siRNAs delivered by APTES-pSiNTs appeared as a range, presumably attributed to non-uniform cellular uptake of the nanotube matrices, thereby resulting in variations in the siRNA concentration available for ER downregulation. On the other hand, with regard to APTES-pSiNTs, the higher density of the exposed amino groups relative to those with siRNA conjugated might exert more significant impacts on biological pathways as well as ER expression.
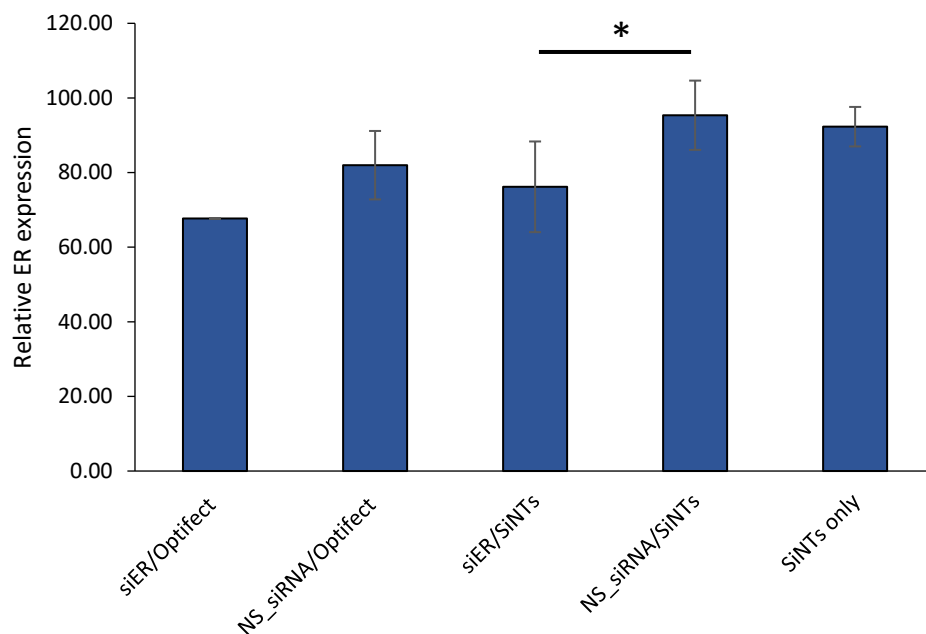
Figure 91. Expression of mRNA encoding ER in MCF-7 cells after transfection. * $p < 0.1$ (n = 3). Note: APTES-pSiNTs was abbreviated as SiNTs.

f) Dissolution of siRNA/APTES-pSiNTs

Similar to siGFP transfection, nanotubes remaining after 48-h transfection exhibited a gradual disappearance of the discrete structural boundaries (Figure 92). It should be noted that due to the low yield of the nanotubes utilized herein, the cumulative quantification of the dissolution of SiNTs as a function of time was not feasible in this case.
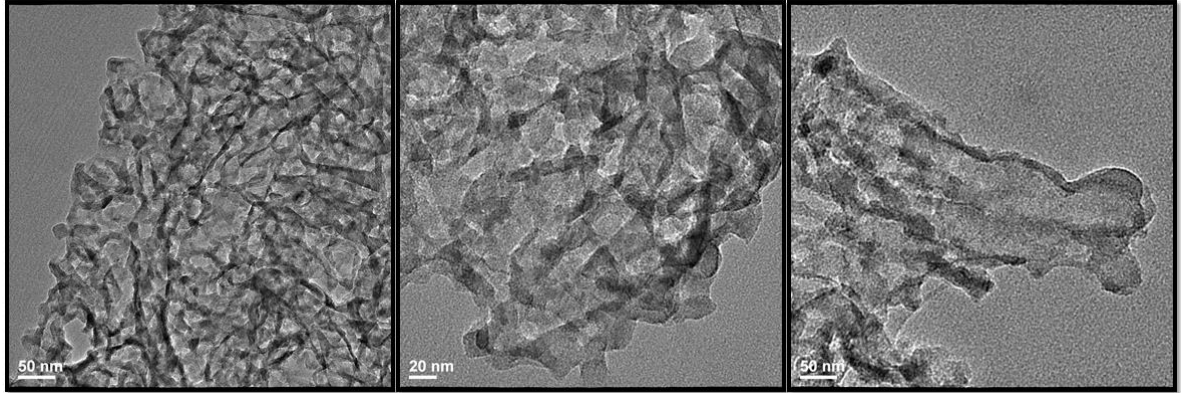
Figure 92. TEM imaging showing the remnant of siRNA/APTES-SiNTs after 48-h transfection.

6.4   Summary

Overall, to our knowledge, this is the first study that demonstrates freestanding SiNTs can serve as feasible delivery vectors for siRNA to downregulate selected target genes in different cell models. Based on cellular imaging, SiNTs readily interacted with cells and began the internalization process by 4 h. Since confocal imaging indicated the presence of the fluorescently labeled siRNA in the intracellular compartments, it is proposed that despite a burst release of siRNA, the internalization of the nanocarriers occurring at this early time point enabled a sufficiently high density of siRNA to be delivered inside the cells.

Based on the two *in vitro* models described here, eGFP and ER expressions were downregulated by 50 % and 25 % respectively after transfection with siGFP and siER delivered by APTES-pSiNTs. The initial evidence regarding the degradation of SiNTs after transfection imply the release of siRNA is readily facilitated by the dissolution of the nanotube matrices. Investigations into specific dissolution patterns of SiNTs in conjunction with siRNA release measurements are currently ongoing to elucidate the siRNA delivery mechanism operative in these systems.

157

Future studies will focus on enhancing knockdown efficiency by optimizing siRNA loading, grafting additional capping agents for controlling siRNA release and surface functionalization for minimizing SiNT aggregation. Additional targeting molecules and chemical agents that facilitate endosomal escape are also of utmost interest in the future work.

Chapter VII

Concluding Remarks

This dissertation describes the detailed synthesis and characterization of Si in a one-dimensional porous nanotube structure (pSiNTs) using a sacrificial ZnO nanowire template, and highlights several fundamental bio-relevant properties of these nanomaterials. With regard to the potential applications of pSiNTs in nanomedicine, the feasibility of pSiNTs to serve as a facile delivery vector of therapeutic molecules is also thoroughly described herein.

In Chapter 2, fabrication of pSiNTs via a ZnO NW-template method with a focus on length control and fragmentation of the nanotube arrays into smaller bundles (the majority in submicron regime) with a narrow size distribution is demonstrated, thereby suggesting feasibility of tuning the nanotube structures in a controlled manner. In addition, pSiNTs with oxide surface termination as well as modified with amino-alkoxysilane are shown to be degradable in biological environments and exert negligible cytotoxicity to the cancer cells at the tested concentrations. While these initial studies address limited aspects of the cytocompatibility of pSiNTs, the results do set the stage for evaluating the ability of pSiNTs as delivery platforms. In order to fully confirm the biocompatibility of pSiNTs and its derivatives, additional studies involving genotoxicity and the impact of the materials on animal models are of utmost necessity.

In Chapter 3, the story behind the discovery of the formation of ultrasmall platinum nanocrystals (Pt NCs) on pSiNTs functionalized with 3-aminopropyltriethoxysilane (APTES) is presented. These detailed studies demonstrate a uniform coverage of Pt species with relatively high crystalline domains on nanotubes is possible after incubation with cisplatin containing excess K_2PtCl_4, which typically serves as a common precursor in cisplatin synthesis. Additional studies demonstrate the concentration of Pt NCs formed on pSiNTs can readily be tuned (20-60 wt% Pt) via modulating the reaction time as well as the concentration of K_2PtCl_4 salt precursor, thereby

indicating a simple reductant-free route to achieve and stabilize a tunable density of the ultrasmall Pt NCs via APTES-functionalized pSiNT templates.

In Chapter 4, *in vitro* anti-cancer activity of Pt NCs-pSiNTs nanocomposites is demonstrated. The studies described in this chapter suggested the materials exerted cytotoxicity to HeLa cervical cancer cells via a "Trojan horse mechanism." In this system, a high concentration of Pt NCs is translocated into the cells via assistance from SiNTs, and the dissolution of the matrix along with the acidic environment of the intracellular organelles (e.g. endosomes and lysosomes) mediate the leaching of a high concentration of the cytotoxic Pt^{2+} from the Pt NC surface in a time-dependent manner. Future investigations into grafting additional targeting moieties are necessary to endow specificity feature to these nanohybrids.

Chapters 5 and 6 highlight the first studies showing the ability of free-standing pSiNTs to serve as nanocarriers for delivery of exogenous genes and siRNAs. In particular, APTES-functionalized pSiNTs conjugate with eGFP-pDNA via electrostatic interactions and deliver the cargos to human embryonic kidney cells (HEK 293) with a transfection efficiency of 3-5 % (Chapter 5). With the similar approach of immobilizing the nucleic acids, in Chapter 6, delivery of siGFP and siER were assisted by APTES-pSiNTs, and eGFP protein expression (in HeLa cells) were reduced by 50 % while the ER-mRNA level (in MCF-7 cells) were downregulated by 25 %. Given these promising initial results, enhancement of delivery efficacy and understanding the delivery mechanism (e.g. cellular uptake pathways) operative in these systems in greater detail are important investigations moving forward.

Overall, these studies presented here have demonstrated an exciting potential for SiNT-based technology in nanomedicine, thereby expanding the library of possible nanostructures of Si in therapeutic delivery. While current studies typically involve nanotubes in bundle form, delivery

studies focusing on discrete nanotubes are also of interest. In addition, since particle aggregation and multiple biological barriers impose critical challenges in therapeutic delivery, strategic designs of SiNT-based platforms that critically address these hurdles, along with scale-up production of these nanotubes are of utmost importance in order to achieve desirable therapeutic outcomes as well as opportunities for future clinical translation.

References

1.   'Plenty of room' revisited. *Nat. Nanotechnol.* **2009,** *4* (12), 781-781.
2.   Bayda, S.; Adeel, M.; Tuccinardi, T.; Cordani, M.; Rizzolio, F., The History of Nanoscience and Nanotechnology: From Chemical–Physical Applications to Nanomedicine. *Molecules* **2020,** *25* (1).
3.   Krajczewski, J.; Kołątaj, K.; Kudelski, A., Plasmonic nanoparticles in chemical analysis. *RSC Adv.* **2017,** *7* (28), 17559-17576.
4.   Freund, H.-J., Clusters and islands on oxides: from catalysis via electronics and magnetism to optics. *Surf. Sci.* **2002,** *500* (1), 271-299.
5.   Zhang, B.; Jie, J.; Zhang, X.; Ou, X.; Zhang, X., Large-Scale Fabrication of Silicon Nanowires for Solar Energy Applications. *ACS Appl. Mater. Interfaces* **2017,** *9* (40), 34527-34543.
6.   Xiang, D.; Wang, X.; Jia, C.; Lee, T.; Guo, X., Molecular-Scale Electronics: From Concept to Function. *Chem. Rev.* **2016,** *116* (7), 4318-4440.
7.   Shi, J.; Votruba, A. R.; Farokhzad, O. C.; Langer, R., Nanotechnology in Drug Delivery and Tissue Engineering: From Discovery to Applications. *Nano Lett.* **2010,** *10* (9), 3223-3230.
8.   Irvine, D. J.; Dane, E. L., Enhancing cancer immunotherapy with nanomedicine. *Nat. Rev. Immunol.* **2020,** *20* (5), 321-334.
9.   van der Meel, R.; Sulheim, E.; Shi, Y.; Kiessling, F.; Mulder, W. J. M.; Lammers, T., Smart cancer nanomedicine. *Nat. Nanotechnol.* **2019,** *14* (11), 1007-1017.
10.   Liu, Z.; Jiang, W.; Nam, J.; Moon, J. J.; Kim, B. Y. S., Immunomodulating Nanomedicine for Cancer Therapy. *Nano Lett.* **2018,** *18* (11), 6655-6659.
11.   Kandell, R. M.; Waggoner, L. E.; Kwon, E. J., Nanomedicine for Acute Brain Injuries: Insight from Decades of Cancer Nanomedicine. *Mol. Pharm.* **2020**.
12.   Gabizon, A. A., Pegylated Liposomal Doxorubicin: Metamorphosis of an Old Drug into a New Form of Chemotherapy. *Cancer Investig.* **2001,** *19* (4), 424-436.
13.   Senapati, S.; Mahanta, A. K.; Kumar, S.; Maiti, P., Controlled drug delivery vehicles for cancer treatment and their performance. *Signal Transduct. Target Ther.* **2018,** *3* (1), 7.
14.   Germain, M.; Caputo, F.; Metcalfe, S.; Tosi, G.; Spring, K.; Åslund, A. K. O.; Pottier, A.; Schiffelers, R.; Ceccaldi, A.; Schmid, R., Delivering the power of nanomedicine to patients today. *J. Control. Release* **2020,** *326*, 164-171.
15.   Bobo, D.; Robinson, K. J.; Islam, J.; Thurecht, K. J.; Corrie, S. R., Nanoparticle-Based Medicines: A Review of FDA-Approved Materials and Clinical Trials to Date. *Pharm. Res.* **2016,** *33* (10), 2373-2387.
16.   Liang, R.; Wei, M.; Evans, D. G.; Duan, X., Inorganic nanomaterials for bioimaging, targeted drug delivery and therapeutics. *Chem. Comm.* **2014,** *50* (91), 14071-14081.
17.   Ulery, B. D.; Nair, L. S.; Laurencin, C. T., Biomedical Applications of Biodegradable Polymers. *J Polym. Sci. B Polym. Phys.* **2011,** *49* (12), 832-864.
18.   Canham, L. T., Bioactive silicon structure fabrication through nanoetching techniques. *Adv. Mater.* **1995,** *7* (12), 1033-1037.
19.   Homola, J., Surface Plasmon Resonance Sensors for Detection of Chemical and Biological Species. *Chem. Rev.* **2008,** *108* (2), 462-493.
20.   Huang, X.; El-Sayed, M. A., Gold nanoparticles: Optical properties and implementations in cancer diagnosis and photothermal therapy. *J. Adv. Res.* **2010,** *1* (1), 13-28.
21.   Aldewachi, H.; Chalati, T.; Woodroofe, M. N.; Bricklebank, N.; Sharrack, B.; Gardiner, P., Gold nanoparticle-based colorimetric biosensors. *Nanoscale* **2018,** *10* (1), 18-33.

22.	Vines, J. B.; Yoon, J.-H.; Ryu, N.-E.; Lim, D.-J.; Park, H., Gold Nanoparticles for Photothermal Cancer Therapy. *Front. Chem.* **2019,** *7* (167).

23.	Gobin, A. M.; Lee, M. H.; Halas, N. J.; James, W. D.; Drezek, R. A.; West, J. L., Near-Infrared Resonant Nanoshells for Combined Optical Imaging and Photothermal Cancer Therapy. *Nano Lett.* **2007,** *7* (7), 1929-1934.

24.	O'Neal, D.; Hirsch, L. R.; Halas, N. J.; Payne, J.; West, J. L., Photo-thermal tumor ablation in mice using near infrared-absorbing nanoparticles. *Cancer Lett.* **2004,** *209* (2), 171-176.

25.	Rastinehad, A. R.; Anastos, H.; Wajswol, E.; Winoker, J. S.; Sfakianos, J. P.; Doppalapudi, S. K.; Carrick, M. R.; Knauer, C. J.; Taouli, B.; Lewis, S. C.; Tewari, A. K.; Schwartz, J. A.; Canfield, S. E.; George, A. K.; West, J. L.; Halas, N. J., Gold nanoshell-localized photothermal ablation of prostate tumors in a clinical pilot device study. *Proc. Natl. Acad. Sci.* **2019,** *116* (37), 18590-18596.

26.	Loo, C.; Lin, A.; Hirsch, L.; Lee, M.-H.; Barton, J.; Halas, N.; West, J.; Drezek, R., Nanoshell-Enabled Photonics-Based Imaging and Therapy of Cancer. *Technol. Cancer Res. Treat.* **2004,** *3* (1), 33-40.

27.	Miessler, G. L.; Tarr, D. A., *Inorganic chemistry*. 3rd ed.; Pearson Education: Upper Saddle River, N.J., 2004; p xiv, 706 p.

28.	Martynenko, I. V.; Litvin, A. P.; Purcell-Milton, F.; Baranov, A. V.; Fedorov, A. V.; Gun'ko, Y. K., Application of semiconductor quantum dots in bioimaging and biosensing. *J. Mater. Chem. B* **2017,** *5* (33), 6701-6727.

29.	Vlasceanu, G.; Grumezescu, A. M.; Gheorghe, I.; Chifiriuc, M. C.; Holban, A. M., Chapter 18 - Quantum dots for bioimaging and therapeutic applications. In *Nanostructures for Novel Therapy*, Ficai, D.; Grumezescu, A. M., Eds. Elsevier: 2017; pp 497-515.

30.	Zhu, X.; Zhang, J.; Liu, J.; Zhang, Y., Recent Progress of Rare-Earth Doped Upconversion Nanoparticles: Synthesis, Optimization, and Applications. *Adv. Sci.* **2019,** *6* (22), 1901358.

31.	Chen, G.; Qiu, H.; Prasad, P. N.; Chen, X., Upconversion Nanoparticles: Design, Nanochemistry, and Applications in Theranostics. *Chem. Rev.* **2014,** *114* (10), 5161-5214.

32.	Girma, W. M.; Fahmi, M. Z.; Permadi, A.; Abate, M. A.; Chang, J.-Y., Synthetic strategies and biomedical applications of I–III–VI ternary quantum dots. *J. Mater. Chem. B* **2017,** *5* (31), 6193-6216.

33.	Yan, C.; Tang, F.; Li, L.; Li, H.; Huang, X.; Chen, D.; Meng, X.; Ren, J., Synthesis of Aqueous CdTe/CdS/ZnS Core/shell/shell Quantum Dots by a Chemical Aerosol Flow Method. *Nanoscale Res. Lett.* **2009,** *5* (1), 189.

34.	Lin, X.; Wang, Y.; Chen, X.; Yang, R.; Wang, Z.; Feng, J.; Wang, H.; Lai, K. W. C.; He, J.; Wang, F.; Shi, P., Multiplexed Optogenetic Stimulation of Neurons with Spectrum-Selective Upconversion Nanoparticles. *Adv. Healthc. Mater.* **2017,** *6* (17), 1700446.

35.	Palanisamy, S.; Wang, Y.-M., Superparamagnetic iron oxide nanoparticulate system: synthesis, targeting, drug delivery and therapy in cancer. *Dalton Trans.* **2019,** *48* (26), 9490-9515.

36.	Liu, Z.; Robinson, J. T.; Tabakman, S. M.; Yang, K.; Dai, H., Carbon materials for drug delivery & cancer therapy. *Mater. Today* **2011,** *14* (7), 316-323.

37.	Gao, J.; Liang, G.; Zhang, B.; Kuang, Y.; Zhang, X.; Xu, B., FePt@CoS2 Yolk−Shell Nanocrystals as a Potent Agent to Kill HeLa Cells. *J. Am. Chem. Soc.* **2007,** *129* (5), 1428-1433.

38.	Croissant, J. G.; Butler, K. S.; Zink, J. I.; Brinker, C. J., Synthetic amorphous silica nanoparticles: toxicity, biomedical and environmental implications. *Nat. Rev. Mater.* **2020**.

39.   Salonen, J.; Laitinen, L.; Kaukonen, A. M.; Tuura, J.; Björkqvist, M.; Heikkilä, T.; Vähä-Heikkilä, K.; Hirvonen, J.; Lehto, V. P., Mesoporous silicon microparticles for oral drug delivery: Loading and release of five model drugs. *J. Control. Release* **2005,** *108* (2), 362-374.

40.   Kango, S.; Kalia, S.; Celli, A.; Njuguna, J.; Habibi, Y.; Kumar, R., Surface modification of inorganic nanoparticles for development of organic–inorganic nanocomposites—A review. *Prog. Polym. Sci.* **2013,** *38* (8), 1232-1261.

41.   Tang, H.; Zhao, W.; Yu, J.; Li, Y.; Zhao, C., Recent Development of pH-Responsive Polymers for Cancer Nanomedicine. *Molecules* **2019,** *24* (1).

42.   Ma, P. a.; Xiao, H.; Li, C.; Dai, Y.; Cheng, Z.; Hou, Z.; Lin, J., Inorganic nanocarriers for platinum drug delivery. *Mater. Today* **2015,** *18* (10), 554-564.

43.   Sanvicens, N.; Marco, M. P., Multifunctional nanoparticles - properties and prospects for their use in human medicine. *Trends Biotechnol.* **2008,** *26* (8), 425-433.

44.   Vega-Vásquez, P.; Mosier, N. S.; Irudayaraj, J., Nanoscale Drug Delivery Systems: From Medicine to Agriculture. *Front. Bioeng. Biotechnol.* **2020,** *8* (79).

45.   Patra, J. K.; Das, G.; Fraceto, L. F.; Campos, E. V. R.; Rodriguez-Torres, M. d. P.; Acosta-Torres, L. S.; Diaz-Torres, L. A.; Grillo, R.; Swamy, M. K.; Sharma, S.; Habtemariam, S.; Shin, H.-S., Nano based drug delivery systems: recent developments and future prospects. *J. Nanobiotechnology* **2018,** *16* (1), 71.

46.   Doucey, M.-A.; Carrara, S., Nanowire Sensors in Cancer. *Trends Biotechnol.* **2019,** *37* (1), 86-99.

47.   Tran, D. P.; Pham, T. T.; Wolfrum, B.; Offenhäusser, A.; Thierry, B., CMOS-Compatible Silicon Nanowire Field-Effect Transistor Biosensor: Technology Development toward Commercialization. *Materials* **2018,** *11* (5).

48.   Anselmo, A. C.; Mitragotri, S., A Review of Clinical Translation of Inorganic Nanoparticles. *AAPS J.* **2015,** *17* (5), 1041-1054.

49.   Wilhelm, S.; Tavares, A. J.; Dai, Q.; Ohta, S.; Audet, J.; Dvorak, H. F.; Chan, W. C. W., Analysis of nanoparticle delivery to tumours. *Nat. Rev. Mater.* **2016,** *1* (5), 16014.

50.   Naz, S.; Shamoon, M.; Wang, R.; Zhang, L.; Zhou, J.; Chen, J., Advances in Therapeutic Implications of Inorganic Drug Delivery Nano-Platforms for Cancer. *Int. J. Mol. Sci.* **2019,** *20* (4).

51.   Liu, Q.; Zhan, C.; Kohane, D. S., Phototriggered Drug Delivery Using Inorganic Nanomaterials. *Bioconjug. Chem.* **2017,** *28* (1), 98-104.

52.   Blanco, E.; Shen, H.; Ferrari, M., Principles of nanoparticle design for overcoming biological barriers to drug delivery. *Nat. Biotechnol.* **2015,** *33* (9), 941-951.

53.   Zhao, Z.; Ukidve, A.; Kim, J.; Mitragotri, S., Targeting Strategies for Tissue-Specific Drug Delivery. *Cell* **2020,** *181* (1), 151-167.

54.   Albanese, A.; Walkey, C. D.; Olsen, J. B.; Guo, H.; Emili, A.; Chan, W. C. W., Secreted Biomolecules Alter the Biological Identity and Cellular Interactions of Nanoparticles. *ACS Nano* **2014,** *8* (6), 5515-5526.

55.   García-Álvarez, R.; Hadjidemetriou, M.; Sánchez-Iglesias, A.; Liz-Marzán, L. M.; Kostarelos, K., In vivo formation of protein corona on gold nanoparticles. The effect of their size and shape. *Nanoscale* **2018,** *10* (3), 1256-1264.

56.   Rosenblum, D.; Joshi, N.; Tao, W.; Karp, J. M.; Peer, D., Progress and challenges towards targeted delivery of cancer therapeutics. *Nat. Commun.* **2018,** *9* (1), 1410.

57.   Oh, J. Y.; Kim, H. S.; Palanikumar, L.; Go, E. M.; Jana, B.; Park, S. A.; Kim, H. Y.; Kim, K.; Seo, J. K.; Kwak, S. K.; Kim, C.; Kang, S.; Ryu, J.-H., Cloaking nanoparticles with protein corona shield for targeted drug delivery. *Nat. Commun.* **2018,** *9* (1), 4548.

58.   Gunawan, C.; Lim, M.; Marquis, C. P.; Amal, R., Nanoparticle–protein corona complexes govern the biological fates and functions of nanoparticles. *J. Mater. Chem. B* **2014,** *2* (15), 2060-2083.

59.   Chen, D.; Ganesh, S.; Wang, W.; Amiji, M., Protein Corona-Enabled Systemic Delivery and Targeting of Nanoparticles. *AAPS J.* **2020,** *22* (4), 83.

60.   Akinc, A.; Maier, M. A.; Manoharan, M.; Fitzgerald, K.; Jayaraman, M.; Barros, S.; Ansell, S.; Du, X.; Hope, M. J.; Madden, T. D.; Mui, B. L.; Semple, S. C.; Tam, Y. K.; Ciufolini, M.; Witzigmann, D.; Kulkarni, J. A.; van der Meel, R.; Cullis, P. R., The Onpattro story and the clinical translation of nanomedicines containing nucleic acid-based drugs. *Nat. Nanotechnol.* **2019,** *14* (12), 1084-1087.

61.   Jokerst, J. V.; Lobovkina, T.; Zare, R. N.; Gambhir, S. S., Nanoparticle PEGylation for imaging and therapy. *Nanomedicine (Lond)* **2011,** *6* (4), 715-728.

62.   Alconcel, S. N. S.; Baas, A. S.; Maynard, H. D., FDA-approved poly(ethylene glycol)–protein conjugate drugs. *Polym. Chem.* **2011,** *2* (7), 1442-1448.

63.   Haute, D. V.; Berlin, J. M., Challenges in realizing selectivity for nanoparticle biodistribution and clearance: lessons from gold nanoparticles. *Ther Deliv* **2017,** *8* (9), 763-774.

64.   Nehoff, H.; Parayath, N. N.; Domanovitch, L.; Taurin, S.; Greish, K., Nanomedicine for drug targeting: strategies beyond the enhanced permeability and retention effect. *Int J Nanomedicine* **2014,** *9*, 2539-2555.

65.   Carboni, E.; Tschudi, K.; Nam, J.; Lu, X.; Ma, A. W. K., Particle Margination and Its Implications on Intravenous Anticancer Drug Delivery. *AAPS PharmSciTech* **2014,** *15* (3), 762-771.

66.   Ta, H. T.; Truong, N. P.; Whittaker, A. K.; Davis, T. P.; Peter, K., The effects of particle size, shape, density and flow characteristics on particle margination to vascular walls in cardiovascular diseases. *Expert Opin. Drug Deliv.* **2018,** *15* (1), 33-45.

67.   Gentile, F.; Chiappini, C.; Fine, D.; Bhavane, R. C.; Peluccio, M. S.; Cheng, M. M.-C.; Liu, X.; Ferrari, M.; Decuzzi, P., The effect of shape on the margination dynamics of non-neutrally buoyant particles in two-dimensional shear flows. *J. Biomech.* **2008,** *41* (10), 2312-2318.

68.   Cooley, M.; Sarode, A.; Hoore, M.; Fedosov, D. A.; Mitragotri, S.; Sen Gupta, A., Influence of particle size and shape on their margination and wall-adhesion: implications in drug delivery vehicle design across nano-to-micro scale. *Nanoscale* **2018,** *10* (32), 15350-15364.

69.   Zhu, X.; Vo, C.; Taylor, M.; Smith, B. R., Non-spherical micro- and nanoparticles in nanomedicine. *Mater. Horizons* **2019,** *6* (6), 1094-1121.

70.   Lee, S.-Y.; Ferrari, M.; Decuzzi, P., Shaping nano-/micro-particles for enhanced vascular interaction in laminar flows. *Nanotechnology* **2009,** *20* (49), 495101.

71.   Li, B.; Lane, L. A., Probing the biological obstacles of nanomedicine with gold nanoparticles. *WIREs Nanomed. Nanobiotechnol.* **2019,** *11* (3), e1542.

72.   Blanco, E.; Shen, H.; Ferrari, M., Principles of nanoparticle design for overcoming biological barriers to drug delivery. *Nat. Biotechnol.* **2015,** *33*, 941.

73.   New Insights into "Permeability" as in the Enhanced Permeability and Retention Effect of Cancer Nanotherapeutics. *ACS Nano* **2017,** *11* (10), 9567-9569.

74.   Kamata, R.; Yamamoto, T.; Matsumoto, K.; Maeda, H., A serratial protease causes vascular permeability reaction by activation of the Hageman factor-dependent pathway in guinea pigs. *Infect Immun* **1985,** *48* (3), 747-753.

75.   Tran, S.; DeGiovanni, P.-J.; Piel, B.; Rai, P., Cancer nanomedicine: a review of recent success in drug delivery. *Clin. Transl. Med.* **2017,** *6* (1), 44.

76. Dagogo-Jack, I.; Shaw, A. T., Tumour heterogeneity and resistance to cancer therapies. *Nat. Rev. Clin. Oncol.* **2018,** *15* (2), 81-94.

77. Guo, Y.; Terazzi, E.; Seemann, R.; Fleury, J. B.; Baulin, V. A., Direct proof of spontaneous translocation of lipid-covered hydrophobic nanoparticles through a phospholipid bilayer. *Sci. Adv.* **2016,** *2* (11), e1600261.

78. Mayor, S.; Pagano, R. E., Pathways of clathrin-independent endocytosis. *Nat. Rev. Mol. Cell Biol.* **2007,** *8* (8), 603-612.

79. Degors, I. M. S.; Wang, C.; Rehman, Z. U.; Zuhorn, I. S., Carriers Break Barriers in Drug Delivery: Endocytosis and Endosomal Escape of Gene Delivery Vectors. *Acc. Chem. Res.* **2019,** *52* (7), 1750-1760.

80. Bus, T.; Traeger, A.; Schubert, U. S., The great escape: how cationic polyplexes overcome the endosomal barrier. *J. Mater. Chem. B* **2018,** *6* (43), 6904-6918.

81. Varkouhi, A. K.; Scholte, M.; Storm, G.; Haisma, H. J., Endosomal escape pathways for delivery of biologicals. *J. Control. Release* **2011,** *151* (3), 220-228.

82. Foroozandeh, P.; Aziz, A. A., Insight into Cellular Uptake and Intracellular Trafficking of Nanoparticles. *Nanoscale Res. Lett.* **2018,** *13* (1), 339.

83. Jindal, A. B., The effect of particle shape on cellular interaction and drug delivery applications of micro- and nanoparticles. *Int. J. Pharm.* **2017,** *532* (1), 450-465.

84. Vácha, R.; Martinez-Veracoechea, F. J.; Frenkel, D., Receptor-Mediated Endocytosis of Nanoparticles of Various Shapes. *Nano Lett.* **2011,** *11* (12), 5391-5395.

85. Decuzzi, P.; Ferrari, M., The Receptor-Mediated Endocytosis of Nonspherical Particles. *Biophys. J.* **2008,** *94* (10), 3790-3797.

86. Champion, J. A.; Mitragotri, S., Role of target geometry in phagocytosis. *Proc. Natl. Acad. Sci. U.S.A.* **2006,** *103* (13), 4930.

87. Jiang, K.; Coffer, J. L.; Akkaraju, G. R., Silicon nanowire/polycaprolactone composites and their impact on stromal cell function. *J. Mater. Res.* **2013,** *28* (2), 185-192.

88. Zimmerman, J. F.; Parameswaran, R.; Murray, G.; Wang, Y.; Burke, M.; Tian, B., Cellular uptake and dynamics of unlabeled freestanding silicon nanowires. *Sci. Adv.* **2016,** *2* (12), e1601039.

89. Chithrani, B. D.; Ghazani, A. A.; Chan, W. C. W., Determining the Size and Shape Dependence of Gold Nanoparticle Uptake into Mammalian Cells. *Nano Lett.* **2006,** *6* (4), 662-668.

90. Hao, N.; Li, L.; Zhang, Q.; Huang, X.; Meng, X.; Zhang, Y.; Chen, D.; Tang, F.; Li, L., The shape effect of PEGylated mesoporous silica nanoparticles on cellular uptake pathway in Hela cells. *Microporous Mesoporous Mater.* **2012,** *162*, 14-23.

91. Kinnear, C.; Moore, T. L.; Rodriguez-Lorenzo, L.; Rothen-Rutishauser, B.; Petri-Fink, A., Form Follows Function: Nanoparticle Shape and Its Implications for Nanomedicine. *Chem. Rev.* **2017,** *117* (17), 11476-11521.

92. Yoo, J.-W.; Doshi, N.; Mitragotri, S., Endocytosis and Intracellular Distribution of PLGA Particles in Endothelial Cells: Effect of Particle Geometry. *Macromol. Rapid Commun.* **2010,** *31* (2), 142-148.

93. Granitzer, P.; Rumpf, K., Porous Silicon—A Versatile Host Material. *Materials* **2010,** *3* (2).

94. Venema, L., Silicon electronics and beyond. *Nature* **2011,** *479* (7373), 309-309.

95. Canham, L. T., 1 - Porous silicon for medical use: from conception to clinical use. In *Porous Silicon for Biomedical Applications*, Santos, H. A., Ed. Woodhead Publishing: 2014; pp 3-20.

96.   Li, W.; Liu, Z.; Fontana, F.; Ding, Y.; Liu, D.; Hirvonen, J. T.; Santos, H. A., Tailoring Porous Silicon for Biomedical Applications: From Drug Delivery to Cancer Immunotherapy. *Adv. Mater.* **2018,** *30* (24), 1703740.

97.   Kolasinski, K. W., Porous Silicon Formation by Stain Etching. In *Handbook of Porous Silicon*, Canham, L., Ed. Springer International Publishing: Cham, 2017; pp 1-21.

98.   Loni, A., Porous Silicon Formation by Anodization. In *Handbook of Porous Silicon*, Canham, L., Ed. Springer International Publishing: Cham, 2014; pp 11-22.

99.   Santos, A.; Kumeria, T., Electrochemical Etching Methods for Producing Porous Silicon. In *Electrochemically Engineered Nanoporous Materials: Methods, Properties and Applications*, Losic, D.; Santos, A., Eds. Springer International Publishing: Cham, 2015; pp 1-36.

100.   Chiappini, C.; Tasciotti, E.; Fakhoury, J. R.; Fine, D.; Pullan, L.; Wang, Y.-C.; Fu, L.; Liu, X.; Ferrari, M., Tailored Porous Silicon Microparticles: Fabrication and Properties. *ChemPhysChem* **2010,** *11* (5), 1029-1035.

101.   Qin, Z.; Joo, J.; Gu, L.; Sailor, M. J., Size Control of Porous Silicon Nanoparticles by Electrochemical Perforation Etching. *Part. Part. Syst. Charact.* **2014,** *31* (2), 252-256.

102.   Wan, Y.; Apostolou, S.; Dronov, R.; Kuss, B.; Voelcker, N. H., Cancer-targeting siRNA delivery from porous silicon nanoparticles. *Nanomedicine (Lond.)* **2014,** *9* (15), 2309-2321.

103.   Godin, B.; Chiappini, C.; Srinivasan, S.; Alexander, J. F.; Yokoi, K.; Ferrari, M.; Decuzzi, P.; Liu, X., Discoidal Porous Silicon Particles: Fabrication and Biodistribution in Breast Cancer Bearing Mice. *Adv. Funct. Mater.* **2012,** *22* (20), 4225-4235.

104.   Tasciotti, E.; Liu, X.; Bhavane, R.; Plant, K.; Leonard, A. D.; Price, B. K.; Cheng, M. M.-C.; Decuzzi, P.; Tour, J. M.; Robertson, F.; Ferrari, M., Mesoporous silicon particles as a multistage delivery system for imaging and therapeutic applications. *Nat. Nanotechnol.* **2008,** *3* (3), 151-157.

105.   Patolsky, F.; Zheng, G.; Lieber, C. M., Nanowire sensors for medicine and the life sciences. *Nanomedicine (Lond.)* **2006,** *1* (1), 51-65.

106.   Chiappini, C.; Martinez, J. O.; De Rosa, E.; Almeida, C. S.; Tasciotti, E.; Stevens, M. M., Biodegradable Nanoneedles for Localized Delivery of Nanoparticles in Vivo: Exploring the Biointerface. *ACS Nano* **2015,** *9* (5), 5500-5509.

107.   Huang, X.; Gonzalez-Rodriguez, R.; Rich, R.; Gryczynski, Z.; Coffer, J. L., Fabrication and size dependent properties of porous silicon nanotube arrays. *Chem. Comm.* **2013,** *49* (51), 5760-5762.

108.   Chiappini, C.; De Rosa, E.; Martinez, J. O.; Liu, X.; Steele, J.; Stevens, M. M.; Tasciotti, E., Biodegradable silicon nanoneedles delivering nucleic acids intracellularly induce localized in vivo neovascularization. *Nat. Mater.* **2015,** *14* (5), 532-539.

109.   Sailor, M. J., Chemical Reactivity and Surface Chemistry of Porous Silicon. In *Handbook of Porous Silicon*, Canham, L., Ed. Springer International Publishing: Cham, 2014; pp 355-380.

110.   Anglin, E. J.; Cheng, L.; Freeman, W. R.; Sailor, M. J., Porous silicon in drug delivery devices and materials. *Adv. Drug Deliv. Rev.* **2008,** *60* (11), 1266-1277.

111.   Low, S. P.; Williams, K. A.; Canham, L. T.; Voelcker, N. H., Generation of reactive oxygen species from porous silicon microparticles in cell culture medium. *J. Biomed. Mater. Res. A* **2010,** *93A* (3), 1124-1131.

112.   Coffinier, Y.; Boukherroub, R., 3 - Surface modification of semiconducting silicon nanowires for biosensing applications. In *Semiconducting Silicon Nanowires for Biomedical Applications*, Coffer, J. L., Ed. Woodhead Publishing: 2014; pp 26-61.

113. Sailor, M. J., Chemistry of Porous Silicon. In *Porous Silicon in Practice*, Wiley-VCH: Weinheim, 2012; pp 189-227.

114. Lee, S. H.; Kang, J. S.; Kim, D., A Mini Review: Recent Advances in Surface Modification of Porous Silicon. *Materials* **2018,** *11* (12).

115. Shabir, Q., Biodegradability of Porous Silicon. In *Handbook of Porous Silicon*, Canham, L., Ed. Springer International Publishing: Cham, 2014; pp 395-401.

116. Martinez, J. O.; Evangelopoulos, M.; Chiappini, C.; Liu, X.; Ferrari, M.; Tasciotti, E., Degradation and biocompatibility of multistage nanovectors in physiological systems. *J. Biomed. Mater. Res. A* **2014,** *102* (10), 3540-3549.

117. Croissant, J. G.; Fatieiev, Y.; Khashab, N. M., Degradability and Clearance of Silicon, Organosilica, Silsesquioxane, Silica Mixed Oxide, and Mesoporous Silica Nanoparticles. *Adv. Mater.* **2017,** *29* (9), 1604634.

118. Godin, B.; Gu, J.; Serda, R. E.; Bhavane, R.; Tasciotti, E.; Chiappini, C.; Liu, X.; Tanaka, T.; Decuzzi, P.; Ferrari, M., Tailoring the degradation kinetics of mesoporous silicon structures through PEGylation. *J. Biomed. Mater. Res. A* **2010,** *94A* (4), 1236-1243.

119. Martinez, J. O.; Chiappini, C.; Ziemys, A.; Faust, A. M.; Kojic, M.; Liu, X.; Ferrari, M.; Tasciotti, E., Engineering multi-stage nanovectors for controlled degradation and tunable release kinetics. *Biomaterials* **2013,** *34* (33), 8469-8477.

120. Tzur-Balter, A.; Shatsberg, Z.; Beckerman, M.; Segal, E.; Artzi, N., Mechanism of erosion of nanostructured porous silicon drug carriers in neoplastic tissues. *Nat. Commun.* **2015,** *6* (1), 6208.

121. Bamburowicz-Klimkowska, M.; Poplawska, M.; Grudzinski, I. P., Nanocomposites as biomolecules delivery agents in nanomedicine. *J. Nanobiotechnology* **2019,** *17* (1), 48.

122. Bowditch, A. P.; Waters, K.; Gale, H.; Rice, P.; Scott, E. A. M.; Canham, L. T.; Reeves, C. L.; Loni, A.; Cox, T. I., In-Vivo Assessment of Tissue Compatibility and Calcification of Bulk and Porous Silicon. *MRS Proceedings* **1998,** *536*, 149.

123. Liu, D.; Shahbazi, M. A.; Bimbo, L. M.; Hirvonen, J.; Santos, H. A., 7 - Biocompatibility of porous silicon for biomedical applications. In *Porous Silicon for Biomedical Applications*, Santos, H. A., Ed. Woodhead Publishing: 2014; pp 129-181.

124. Low, S. P.; Voelcker, N. H., Biocompatibility of Porous Silicon. In *Handbook of Porous Silicon*, Canham, L., Ed. Springer International Publishing: Cham, 2014; pp 381-393.

125. Kumeria, T.; McInnes, S. J. P.; Maher, S.; Santos, A., Porous silicon for drug delivery applications and theranostics: recent advances, critical review and perspectives. *Expert Opin. Drug Deliv.* **2017,** *14* (12), 1407-1422.

126. Arshavsky-Graham, S.; Massad-Ivanir, N.; Segal, E.; Weiss, S., Porous Silicon-Based Photonic Biosensors: Current Status and Emerging Applications. *Anal. Chem.* **2019,** *91* (1), 441-467.

127. Riikonen, J.; Correia, A.; Kovalainen, M.; Näkki, S.; Lehtonen, M.; Leppänen, J.; Rantanen, J.; Xu, W.; Araújo, F.; Hirvonen, J.; Järvinen, K.; Santos, H. A.; Lehto, V.-P., Systematic in vitro and in vivo study on porous silicon to improve the oral bioavailability of celecoxib. *Biomaterials* **2015,** *52*, 44-55.

128. Kalluri, J. R.; West, J.; Akkaraju, G. R.; Canham, L. T.; Coffer, J. L., Plant-Derived Tandem Drug/Mesoporous Silicon Microcarrier Structures for Anti-Inflammatory Therapy. *ACS Omega* **2019,** *4* (5), 8359-8364.

129. Tanaka, T.; Mangala, L. S.; Vivas-Mejia, P. E.; Nieves-Alicea, R.; Mann, A. P.; Mora, E.; Han, H.-D.; Shahzad, M. M. K.; Liu, X.; Bhavane, R.; Gu, J.; Fakhoury, J. R.; Chiappini,

C.; Lu, C.; Matsuo, K.; Godin, B.; Stone, R. L.; Nick, A. M.; Lopez-Berestein, G.; Sood, A. K.; Ferrari, M., Sustained Small Interfering RNA Delivery by Mesoporous Silicon Particles. *Cancer Res.* **2010,** *70* (9), 3687.

130. Kim, B.; Sun, S.; Varner, J. A.; Howell, S. B.; Ruoslahti, E.; Sailor, M. J., Securing the Payload, Finding the Cell, and Avoiding the Endosome: Peptide-Targeted, Fusogenic Porous Silicon Nanoparticles for Delivery of siRNA. *Adv. Mater.* **2019,** *31* (35), 1902952.

131. Xia, X.; Mai, J.; Xu, R.; Perez, J. E. T.; Guevara, M. L.; Shen, Q.; Mu, C.; Tung, H.-Y.; Corry, D. B.; Evans, S. E.; Liu, X.; Ferrari, M.; Zhang, Z.; Li, X. C.; Wang, R.-f.; Shen, H., Porous Silicon Microparticle Potentiates Anti-Tumor Immunity by Enhancing Cross-Presentation and Inducing Type I Interferon Response. *Cell Rep.* **2015,** *11* (6), 957-966.

132. Shahbazi, M.-A.; Hamidi, M.; Mäkilä, E. M.; Zhang, H.; Almeida, P. V.; Kaasalainen, M.; Salonen, J. J.; Hirvonen, J. T.; Santos, H. A., The mechanisms of surface chemistry effects of mesoporous silicon nanoparticles on immunotoxity and biocompatibility. *Biomaterials* **2013,** *34* (31), 7776-7789.

133. Shahbazi, M.-A.; Fernández, T. D.; Mäkilä, E. M.; Le Guével, X.; Mayorga, C.; Kaasalainen, M. H.; Salonen, J. J.; Hirvonen, J. T.; Santos, H. A., Surface chemistry dependent immunostimulative potential of porous silicon nanoplatforms. *Biomaterials* **2014,** *35* (33), 9224-9235.

134. Meraz, I. M.; Melendez, B.; Gu, J.; Wong, S. T. C.; Liu, X.; Andersson, H. A.; Serda, R. E., Activation of the Inflammasome and Enhanced Migration of Microparticle-Stimulated Dendritic Cells to the Draining Lymph Node. *Mol. Pharm.* **2012,** *9* (7), 2049-2062.

135. Gopal, S.; Chiappini, C.; Penders, J.; Leonardo, V.; Seong, H.; Rothery, S.; Korchev, Y.; Shevchuk, A.; Stevens, M. M., Porous Silicon Nanoneedles Modulate Endocytosis to Deliver Biological Payloads. *Adv. Mater.* **2019,** *31* (12), 1806788.

136. Marcon, L.; Boukherroub, R., 4 - Biocompatibility of semiconducting silicon nanowires. In *Semiconducting Silicon Nanowires for Biomedical Applications*, Coffer, J. L., Ed. Woodhead Publishing: 2014; pp 62-85.

137. Zhang, D.-X.; Esser, L.; Vasani, R. B.; Thissen, H.; Voelcker, N. H., Porous silicon nanomaterials: recent advances in surface engineering for controlled drug-delivery applications. *Nanomedicine (Lond.)* **2019,** *14* (24), 3213-3230.

138. Zou, S.; Wang, B.; Wang, C.; Wang, Q.; Zhang, L., Cell membrane-coated nanoparticles: research advances. *Nanomedicine (Lond.)* **2020,** *15* (6), 625-641.

139. Fontana, F.; Lindstedt, H.; Correia, A.; Chiaro, J.; Kari, O. K.; Ndika, J.; Alenius, H.; Buck, J.; Sieber, S.; Mäkilä, E.; Salonen, J.; Urtti, A.; Cerullo, V.; Hirvonen, J. T.; Santos, H. A., Influence of Cell Membrane Wrapping on the Cell−Porous Silicon Nanoparticle Interactions. *Adv. Healthc. Mater.* **2020,** *9* (17), 2000529.

140. Fontana, F.; Shahbazi, M.-A.; Liu, D.; Zhang, H.; Mäkilä, E.; Salonen, J.; Hirvonen, J. T.; Santos, H. A., Multistaged Nanovaccines Based on Porous Silicon@Acetalated Dextran@Cancer Cell Membrane for Cancer Immunotherapy. *Adv. Mater.* **2017,** *29* (7), 1603239.

141. Yong, T.; Zhang, X.; Bie, N.; Zhang, H.; Zhang, X.; Li, F.; Hakeem, A.; Hu, J.; Gan, L.; Santos, H. A.; Yang, X., Tumor exosome-based nanoparticles are efficient drug carriers for chemotherapy. *Nat. Commun.* **2019,** *10* (1), 3838.

142. Tieu, T.; Dhawan, S.; Haridas, V.; Butler, L. M.; Thissen, H.; Cifuentes-Rius, A.; Voelcker, N. H., Maximizing RNA Loading for Gene Silencing Using Porous Silicon Nanoparticles. *ACS Appl. Mater. Interfaces* **2019,** *11* (26), 22993-23005.

143.   Fagan, S. B.; Baierle, R. J.; Mota, R.; da Silva, A. J. R.; Fazzio, A., Ab initio calculations for a hypothetical material: Silicon nanotubes. *Phys. Rev. B* **2000,** *61* (15), 9994-9996.

144.   Seifert, G.; Köhler, T.; Urbassek, H. M.; Hernández, E.; Frauenheim, T., Tubular structures of silicon. *Phys. Rev. B* **2001,** *63* (19), 193409.

145.   Sha, J.; Niu, J.; Ma, X.; Xu, J.; Zhang, X.; Yang, Q.; Yang, D., Silicon Nanotubes. *Adv. Mater.* **2002,** *14* (17), 1219-1221.

146.   Castrucci, P.; Scarselli, M.; De Crescenzi, M.; Diociaiuti, M.; Chaudhari, P. S.; Balasubramanian, C.; Bhave, T. M.; Bhoraskar, S. V., Silicon nanotubes: Synthesis and characterization. *Thin Solid Films* **2006,** *508* (1), 226-230.

147.   Chen, Y.; Aslanoglou, S.; Murayama, T.; Gervinskas, G.; Fitzgerald, L. I.; Sriram, S.; Tian, J.; Johnston, A. P. R.; Morikawa, Y.; Suu, K.; Elnathan, R.; Voelcker, N. H., Silicon-Nanotube-Mediated Intracellular Delivery Enables Ex Vivo Gene Editing. *Adv. Mater.* **2020,** *32* (24), 2000036.

148.   Le, T. N.; Tian, Y.; Gonzalez-Rodriguez, R.; Coffer, L. J., Silicon Nanotubes as Potential Therapeutic Platforms. *Pharmaceutics* **2019,** *11* (11), 571.

149.   Decuzzi, P.; Godin, B.; Tanaka, T.; Lee, S. Y.; Chiappini, C.; Liu, X.; Ferrari, M., Size and shape effects in the biodistribution of intravascularly injected particles. *J. Control. Release* **2010,** *141* (3), 320-327.

150.   Ohshima, H., Zeta Potential. In *Encyclopedia of Colloid and Interface Science*, Tadros, T., Ed. Springer Berlin Heidelberg: Berlin, Heidelberg, 2013; pp 1423-1436.

151.   Canham, L., Color of Porous Silicon. In *Handbook of Porous Silicon*, Canham, L., Ed. Springer International Publishing: Cham, 2018; pp 395-402.

152.   Vayssieres, L.; Keis, K.; Hagfeldt, A.; Lindquist, S.-E., Three-Dimensional Array of Highly Oriented Crystalline ZnO Microtubes. *Chem. Mater.* **2001,** *13* (12), 4395-4398.

153.   Greene, L. E.; Law, M.; Goldberger, J.; Kim, F.; Johnson, J. C.; Zhang, Y.; Saykally, R. J.; Yang, P., Low-Temperature Wafer-Scale Production of ZnO Nanowire Arrays. *Angew. Chem. Int. Ed.* **2003,** *42* (26), 3031-3034.

154.   Guertin, D. A. S., David, M., Cell Size Control. *ELS* **2006**.

155.   Lowe, B. M.; Skylaris, C.-K.; Green, N. G., Acid-base dissociation mechanisms and energetics at the silica–water interface: An activationless process. *J. Colloid Interface Sci.* **2015,** *451*, 231-244.

156.   Pick, C.; Argento, C.; Drazer, G.; Frechette, J., Micropatterned Charge Heterogeneities via Vapor Deposition of Aminosilanes. *Langmuir* **2015,** *31* (39), 10725-10733.

157.   Salonen, J.; Kaukonen, A. M.; Hirvonen, J.; Lehto, V.-P., Mesoporous silicon in drug delivery applications. *J. Pharm. Sci.* **2008,** *97* (2), 632-653.

158.   Johnstone, T. C.; Suntharalingam, K.; Lippard, S. J., The Next Generation of Platinum Drugs: Targeted Pt(II) Agents, Nanoparticle Delivery, and Pt(IV) Prodrugs. *Chem. Rev.* **2016,** *116* (5), 3436-3486.

159.   Goodsell, D. S., The Molecular Perspective: Cisplatin. *Stem Cells* **2006,** *24* (3), 514-515.

160.   Reishus, J. W.; Martin, D. S., cis-Dichlorodiammineplatinum(II). Acid Hydrolysis and Isotopic Exchange of the Chloride Ligands1. *J. Am. Chem. Soc.* **1961,** *83* (11), 2457-2462.

161.   Kauffman, G.; Cowan, D.; Slusarczuk, G.; Kirschner, S., cis- and trans-Dichlorodiammineplatinum(II). 1963; Vol. 7, pp 239-245.

162.   Wilson, J. J.; Lippard, S. J., Synthetic Methods for the Preparation of Platinum Anticancer Complexes. *Chem. Rev.* **2014,** *114* (8), 4470-4495.

163.   Gao, C.; Lu, Z.; Yin, Y., Gram-Scale Synthesis of Silica Nanotubes with Controlled Aspect Ratios by Templating of Nickel-Hydrazine Complex Nanorods. *Langmuir* **2011,** *27* (19), 12201-12208.

164.   Soto-Cantu, E.; Cueto, R.; Koch, J.; Russo, P. S., Synthesis and Rapid Characterization of Amine-Functionalized Silica. *Langmuir* **2012,** *28* (13), 5562-5569.

165.   Le, N. T.; Akkaraju, G. R.; Coffer, J. L., Formation of Platinum Nanocrystals on Silicon Nanotubes and Corresponding Anti-Cancer Activity in Vitro. *ACS Appl. Bio Mater.* **2020,** *3* (1), 208-216.

166.   Harraz, F. A.; Tsuboi, T.; Sasano, J.; Sakka, T.; Ogata, Y. H., Metal deposition onto a porous silicon layer by immersion plating from aqueous and nonaqueous solutions. *J Electrochem Soc* **2002,** *149* (9), C456-C463.

167.   Park, J. S.; Kinsella, J. M.; Jandial, D. D.; Howell, S. B.; Sailor, M. J., Cisplatin-Loaded Porous Si Microparticles Capped by Electroless Deposition of Platinum. *Small* **2011,** *7* (14), 2061-2069.

168.   Dong, H.; Chen, Y. C.; Feldmann, C., Polyol synthesis of nanoparticles: status and options regarding metals, oxides, chalcogenides, and non-metal elements. *Green Chem.* **2015,** *17* (8), 4107-4132.

169.   Aslam, M.; Fu, L.; Su, M.; Vijayamohanan, K.; Dravid, V. P., Novel one-step synthesis of amine-stabilized aqueous colloidal gold nanoparticles. *J. Mater. Chem.* **2004,** *14* (12), 1795-1797.

170.   Newman, J. D. S.; Blanchard, G. J., Formation of Gold Nanoparticles Using Amine Reducing Agents. *Langmuir* **2006,** *22* (13), 5882-5887.

171.   Selvakannan, P. R.; Kumar, P. S.; More, A. S.; Shingte, R. D.; Wadgaonkar, P. P.; Sastry, M., One Pot, Spontaneous and Simultaneous Synthesis of Gold Nanoparticles in Aqueous and Nonpolar Organic Solvents Using a Diamine-Containing Oxyethylene Linkage. *Langmuir* **2004,** *20* (2), 295-298.

172.   Yuan, T. Germanium-based Nanomaterial Cytocompatibility and Gene Delivery. Dissertation, Texas Christian University, Fort Worth, 2014.

173.   Ullah, M. H.; Chung, W.-S.; Kim, I.; Ha, C.-S., pH-Selective Synthesis of Monodisperse Nanoparticles and 3D Dendritic Nanoclusters of CTAB-Stabilized Platinum for Electrocatalytic O2 Reduction. *Small* **2006,** *2* (7), 870-873.

174.   Nejdl, L.; Kudr, J.; Moulick, A.; Hegerova, D.; Ruttkay-Nedecky, B.; Gumulec, J.; Cihalova, K.; Smerkova, K.; Dostalova, S.; Krizkova, S.; Novotna, M.; Kopel, P.; Adam, V., Platinum nanoparticles induce damage to DNA and inhibit DNA replication. *PLoS One* **2017,** *12* (7), e0180798.

175.   Le Guével, X.; Trouillet, V.; Spies, C.; Jung, G.; Schneider, M., Synthesis of Yellow-Emitting Platinum Nanoclusters by Ligand Etching. *J. Phys. Chem. C* **2012,** *116* (10), 6047-6051.

176.   Tanaka, S.-I.; Miyazaki, J.; Tiwari, D. K.; Jin, T.; Inouye, Y., Fluorescent Platinum Nanoclusters: Synthesis, Purification, Characterization, and Application to Bioimaging. *Angew. Chem. Int. Ed.* **2011,** *50* (2), 431-435.

177.   Asharani, P. V.; Xinyi, N.; Hande, M. P.; Valiyaveettil, S., DNA damage and p53-mediated growth arrest in human cells treated with platinum nanoparticles. *Nanomedicine (Lond.)* **2009,** *5* (1), 51-64.

178.   Xia, H.; Li, F.; Hu, X.; Park, W.; Wang, S.; Jang, Y.; Du, Y.; Baik, S.; Cho, S.; Kang, T.; Kim, D.-H.; Ling, D.; Hui, K. M.; Hyeon, T., pH-Sensitive Pt Nanocluster Assembly

Overcomes Cisplatin Resistance and Heterogeneous Stemness of Hepatocellular Carcinoma. *ACS Cent. Sci.* **2016,** *2* (11), 802-811.

179. Chen, A.; Holt-Hindle, P., Platinum-Based Nanostructured Materials: Synthesis, Properties, and Applications. *Chem. Rev.* **2010,** *110* (6), 3767-3804.

180. Ye, R.; Hurlburt, T. J.; Sabyrov, K.; Alayoglu, S.; Somorjai, G. A., Molecular catalysis science: Perspective on unifying the fields of catalysis. *Proc. Natl. Acad. Sci.* **2016,** *113* (19), 5159.

181. Ma, Z.; Zhang, Y.; Zhang, J.; Zhang, W.; Foda, M. F.; Dai, X.; Han, H., Ultrasmall Peptide-Coated Platinum Nanoparticles for Precise NIR-II Photothermal Therapy by Mitochondrial Targeting. *ACS Appl. Mater. Interfaces* **2020,** *12* (35), 39434-39443.

182. Manikandan, M.; Hasan, N.; Wu, H.-F., Platinum nanoparticles for the photothermal treatment of Neuro 2A cancer cells. *Biomaterials* **2013,** *34* (23), 5833-5842.

183. Samadi, A.; Klingberg, H.; Jauffred, L.; Kjær, A.; Bendix, P. M.; Oddershede, L. B., Platinum nanoparticles: a non-toxic, effective and thermally stable alternative plasmonic material for cancer therapy and bioengineering. *Nanoscale* **2018,** *10* (19), 9097-9107.

184. Chien, C.-T.; Yan, J.-Y.; Chiu, W.-C.; Wu, T.-H.; Liu, C.-Y.; Lin, S.-Y., Caged Pt Nanoclusters Exhibiting Corrodibility to Exert Tumor-Inside Activation for Anticancer Chemotherapeutics. *Adv. Mater.* **2013,** *25* (36), 5067-5073.

185. Shoshan, M. S.; Vonderach, T.; Hattendorf, B.; Wennemers, H., Peptide-Coated Platinum Nanoparticles with Selective Toxicity against Liver Cancer Cells. *Angew. Chem. Int. Ed.* **2019,** *58* (15), 4901-4905.

186. Tsung, C.-K.; Kuhn, J. N.; Huang, W.; Aliaga, C.; Hung, L.-I.; Somorjai, G. A.; Yang, P., Sub-10 nm Platinum Nanocrystals with Size and Shape Control: Catalytic Study for Ethylene and Pyrrole Hydrogenation. *J. Am. Chem. Soc.* **2009,** *131* (16), 5816-5822.

187. Jeyaraj, M.; Gurunathan, S.; Qasim, M.; Kang, M.-H.; Kim, J.-H., A Comprehensive Review on the Synthesis, Characterization, and Biomedical Application of Platinum Nanoparticles. *Nanomaterials* **2019,** *9* (12).

188. Gehrke, H.; Pelka, J.; Hartinger, C. G.; Blank, H.; Bleimund, F.; Schneider, R.; Gerthsen, D.; Bräse, S.; Crone, M.; Türk, M.; Marko, D., Platinum nanoparticles and their cellular uptake and DNA platination at non-cytotoxic concentrations. *Arch. Toxicol.* **2011,** *85* (7), 799-812.

189. Konieczny, P.; Goralczyk, A. G.; Szmyd, R.; Skalniak, L.; Koziel, J.; Filon, F. L.; Crosera, M.; Cierniak, A.; Zuba-Surma, E. K.; Borowczyk, J.; Laczna, E.; Drukala, J.; Pyza, E.; Semik, D.; Woznicka, O.; Klein, A.; Jura, J., Effects triggered by platinum nanoparticles on primary keratinocytes. *Int J Nanomedicine* **2013,** *8*, 3963-3975.

190. Wu, G.-W.; He, S.-B.; Peng, H.-P.; Deng, H.-H.; Liu, A.-L.; Lin, X.-H.; Xia, X.-H.; Chen, W., Citrate-Capped Platinum Nanoparticle as a Smart Probe for Ultrasensitive Mercury Sensing. *Anal. Chem.* **2014,** *86* (21), 10955-10960.

191. Vogelstein, B.; Kinzler, K. W., Cancer genes and the pathways they control. *Nat. Med.* **2004,** *10* (8), 789-799.

192. Van Cauwenberghe, C.; Van Broeckhoven, C.; Sleegers, K., The genetic landscape of Alzheimer disease: clinical implications and perspectives. *Genet. Med.* **2016,** *18* (5), 421-430.

193. Farrer, M. J., Genetics of Parkinson disease: paradigm shifts and future prospects. *Nat. Rev. Genet.* **2006,** *7* (4), 306-318.

194. Muñoz-Fontela, C.; Mandinova, A.; Aaronson, S. A.; Lee, S. W., Emerging roles of p53 and other tumour-suppressor genes in immune regulation. *Nat. Rev. Immunol.* **2016,** *16* (12), 741-750.

195.   Shin, H.; Park, S.-J.; Yim, Y.; Kim, J.; Choi, C.; Won, C.; Min, D.-H., Recent Advances in RNA Therapeutics and RNA Delivery Systems Based on Nanoparticles. *Adv. Ther.* **2018,** *1* (7), 1800065.

196.   Dunbar, C. E.; High, K. A.; Joung, J. K.; Kohn, D. B.; Ozawa, K.; Sadelain, M., Gene therapy comes of age. *Science* **2018,** *359* (6372), eaan4672.

197.   Lostalé-Seijo, I.; Montenegro, J., Synthetic materials at the forefront of gene delivery. *Nat. Rev. Chem.* **2018,** *2* (10), 258-277.

198.   Adli, M., The CRISPR tool kit for genome editing and beyond. *Nat. Commun.* **2018,** *9* (1), 1911.

199.   Ni, R.; Feng, R.; Chau, Y., Synthetic Approaches for Nucleic Acid Delivery: Choosing the Right Carriers. *Life* **2019,** *9* (3).

200.   Desai, A. S.; Hunter, M. R.; Kapustin, A. N., Using macropinocytosis for intracellular delivery of therapeutic nucleic acids to tumour cells. *Philos. Trans. R. Soc. Lond., B, Biol. Sci.* **2019,** *374* (1765), 20180156.

201.   Zhao, Y.; Huang, L., Chapter Two - Lipid Nanoparticles for Gene Delivery. In *Advances in Genetics*, Huang, L.; Liu, D.; Wagner, E., Eds. Academic Press: 2014; Vol. 88, pp 13-36.

202.   Lukacs, G.; Haggie, P.; Seksek, O.; Lechardeur, D.; Freedman, N.; Verkman, A. S., Size-dependent DNA Mobility in Cytoplasm and Nucleus. *J. Biol. Chem* **2000,** *275*, 1625-1629.

203.   Zhou, R.; Geiger, R. C.; Dean, D. A., Intracellular trafficking of nucleic acids. *Expert Opin. Drug Deliv.* **2004,** *1* (1), 127-140.

204.   FDA approves hereditary blindness gene therapy. *Nat. Biotechnol.* **2018,** *36* (1), 6-6.

205.   Gene therapy's next installment. *Nat. Biotechnol.* **2019,** *37* (7), 697-697.

206.   Pack, D. W.; Hoffman, A. S.; Pun, S.; Stayton, P. S., Design and development of polymers for gene delivery. *Nat. Rev. Drug Discov.* **2005,** *4* (7), 581-593.

207.   Gray, S. J.; Woodard, K. T.; Samulski, R. J., Viral vectors and delivery strategies for CNS gene therapy. *Ther Deliv* **2010,** *1* (4), 517-534.

208.   Durymanov, M.; Reineke, J., Non-viral Delivery of Nucleic Acids: Insight Into Mechanisms of Overcoming Intracellular Barriers. *Front Pharmacol.* **2018,** *9* (971).

209.   Yin, H.; Kanasty, R. L.; Eltoukhy, A. A.; Vegas, A. J.; Dorkin, J. R.; Anderson, D. G., Non-viral vectors for gene-based therapy. *Nat. Rev. Genet.* **2014,** *15* (8), 541-555.

210.   Carvalho, A. M.; Cordeiro, R. A.; Faneca, H., Silica-Based Gene Delivery Systems: From Design to Therapeutic Applications. *Pharmaceutics* **2020,** *12* (7).

211.   Wareing, N.; Szymanski, K.; Akkaraju, G. R.; Loni, A.; Canham, L. T.; Gonzalez-Rodriguez, R.; Coffer, J. L., In Vitro Gene Delivery with Large Porous Silicon Nanoparticles Fabricated Using Cost-Effective, Metal-Assisted Chemical Etching. *Small* **2017,** *13* (3), 1602739.

212.   Chaix, A.; Cueto-Diaz, E.; Delalande, A.; Knezevic, N.; Midoux, P.; Durand, J.-O.; Pichon, C.; Cunin, F., Amino-acid functionalized porous silicon nanoparticles for the delivery of pDNA. *RSC Adv.* **2019,** *9* (55), 31895-31899.

213.   Kalluri, J. R. Sustainable routes to porous silicon nanostructures as drug and gene delivery vehicles. Texas Christian University, Fort Worth, 2018.

214.   Szymanski, K. Investigation of Gene Delivery via Silicon Nanotubes using the Reporter Gene eGFP. Honor Thesis, Texas Christian University, Texas Christian University, 2015.

215.   Wei, X.; Shao, B.; He, Z.; Ye, T.; Luo, M.; Sang, Y.; Liang, X.; Wang, W.; Luo, S.; Yang, S.; Zhang, S.; Gong, C.; Gou, M.; Deng, H.; Zhao, Y.; Yang, H.; Deng, S.; Zhao, C.; Yang, L.; Qian, Z.; Li, J.; Sun, X.; Han, J.; Jiang, C.; Wu, M.; Zhang, Z., Cationic nanocarriers

induce cell necrosis through impairment of Na+/K+-ATPase and cause subsequent inflammatory response. *Cell Res.* **2015,** *25* (2), 237-253.

216.   Fröhlich, E., The role of surface charge in cellular uptake and cytotoxicity of medical nanoparticles. *Int J Nanomedicine* **2012,** *7*, 5577-5591.

217.   Babaei, M.; Eshghi, H.; Abnous, K.; Rahimizadeh, M.; Ramezani, M., Promising gene delivery system based on polyethylenimine-modified silica nanoparticles. *Cancer Gene Ther.* **2017,** *24* (4), 156-164.

218.   Chu, Z.; Zhang, S.; Zhang, B.; Zhang, C.; Fang, C.-Y.; Rehor, I.; Cigler, P.; Chang, H.-C.; Lin, G.; Liu, R.; Li, Q., Unambiguous observation of shape effects on cellular fate of nanoparticles. *Sci. Rep.* **2014,** *4* (1), 4495.

219.   Cohen, R. N.; van der Aa, M. A. E. M.; Macaraeg, N.; Lee, A. P.; Szoka, F. C., Quantification of plasmid DNA copies in the nucleus after lipoplex and polyplex transfection. *J. Control. Release* **2009,** *135* (2), 166-174.

220.   Dowty, M. E.; Williams, P.; Zhang, G.; Hagstrom, J. E.; Wolff, J. A., Plasmid DNA entry into postmitotic nuclei of primary rat myotubes. *Proc. Natl. Acad. Sci.* **1995,** *92* (10), 4572.

221.   Dean, D. A.; Strong, D. D.; Zimmer, W. E., Nuclear entry of nonviral vectors. *Gene Ther.* **2005,** *12* (11), 881-890.

222.   van der Aa, M. A. E. M.; Mastrobattista, E.; Oosting, R. S.; Hennink, W. E.; Koning, G. A.; Crommelin, D. J. A., The Nuclear Pore Complex: The Gateway to Successful Nonviral Gene Delivery. *Pharm. Res.* **2006,** *23* (3), 447-459.

223.   Fire, A.; Xu, S.; Montgomery, M. K.; Kostas, S. A.; Driver, S. E.; Mello, C. C., Potent and specific genetic interference by double-stranded RNA in Caenorhabditis elegans. *Nature* **1998,** *391* (6669), 806-811.

224.   Montgomery, M. K.; Xu, S.; Fire, A., RNA as a target of double-stranded RNA-mediated genetic interference in <em>Caenorhabditis elegans</em&gt. *Proc. Natl. Acad. Sci.* **1998,** *95* (26), 15502.

225.   Ahmadzada, T.; Reid, G.; McKenzie, D. R., Fundamentals of siRNA and miRNA therapeutics and a review of targeted nanoparticle delivery systems in breast cancer. *Biophys Rev* **2018,** *10* (1), 69-86.

226.   Tuschl, T.; Zamore, P. D.; Lehmann, R.; Bartel, D. P.; Sharp, P. A., Targeted mRNA degradation by double-stranded RNA in vitro. *Genes Dev.* **1999,** *13* (24), 3191-3197.

227.   Parrish, S.; Fleenor, J.; Xu, S.; Mello, C.; Fire, A., Functional Anatomy of a dsRNA Trigger: Differential Requirement for the Two Trigger Strands in RNA Interference. *Mol. Cell* **2000,** *6* (5), 1077-1087.

228.   Hammond, S. M.; Bernstein, E.; Beach, D.; Hannon, G. J., An RNA-directed nuclease mediates post-transcriptional gene silencing in Drosophila cells. *Nature* **2000,** *404* (6775), 293-296.

229.   Agrawal, N.; Dasaradhi, P. V. N.; Mohmmed, A.; Malhotra, P.; Bhatnagar, R. K.; Mukherjee, S. K., RNA Interference: Biology, Mechanism, and Applications. *Microbiol. Mol. Biol. Rev.* **2003,** *67* (4), 657.

230.   Setten, R. L.; Rossi, J. J.; Han, S.-p., The current state and future directions of RNAi-based therapeutics. *Nat. Rev. Drug Discov.* **2019,** *18* (6), 421-446.

231.   Paddison, P. J.; Caudy, A. A.; Bernstein, E.; Hannon, G. J.; Conklin, D. S., Short hairpin RNAs (shRNAs) induce sequence-specific silencing in mammalian cells. *Genes Dev.* **2002,** *16* (8), 948-958.

232. Sui, G.; Soohoo, C.; Affar, E. B.; Gay, F.; Shi, Y.; Forrester, W. C.; Shi, Y., A DNA vector-based RNAi technology to suppress gene expression in mammalian cells. *Proc. Natl. Acad. Sci.* **2002,** *99* (8), 5515.

233. Chen, S.; Ge, X.; Chen, Y.; Lv, N.; Liu, Z.; Yuan, W., Advances with RNA interference in Alzheimer's disease research. *Drug Des Devel Ther* **2013,** *7*, 117-125.

234. Kang, J.; Joo, J.; Kwon, E. J.; Skalak, M.; Hussain, S.; She, Z.-G.; Ruoslahti, E.; Bhatia, S. N.; Sailor, M. J., Self-Sealing Porous Silicon-Calcium Silicate Core–Shell Nanoparticles for Targeted siRNA Delivery to the Injured Brain. *Adv. Mater.* **2016,** *28* (36), 7962-7969.

235. Shen, H.; Rodriguez-Aguayo, C.; Xu, R.; Gonzalez-Villasana, V.; Mai, J.; Huang, Y.; Zhang, G.; Guo, X.; Bai, L.; Qin, G.; Deng, X.; Li, Q.; Erm, D. R.; Aslan, B.; Liu, X.; Sakamoto, J.; Chavez-Reyes, A.; Han, H.-D.; Sood, A. K.; Ferrari, M.; Lopez-Berestein, G., Enhancing Chemotherapy Response with Sustained EphA2 Silencing Using Multistage Vector Delivery. *Clin. Cancer Res.* **2013,** *19* (7), 1806.

236. Zhang, M.; Xu, R.; Xia, X.; Yang, Y.; Gu, J.; Qin, G.; Liu, X.; Ferrari, M.; Shen, H., Polycation-functionalized nanoporous silicon particles for gene silencing on breast cancer cells. *Biomaterials* **2014,** *35* (1), 423-431.

237. Xue, M.; Zhang, K.; Mu, K.; Xu, J.; Yang, H.; Liu, Y.; Wang, B.; Wang, Z.; Li, Z.; Kong, Q.; Li, X.; Wang, H.; Zhu, J.; Zhuang, T., Regulation of estrogen signaling and breast cancer proliferation by an ubiquitin ligase TRIM56. *Oncogenesis* **2019,** *8* (5), 30.

238. Kang, H.-J.; Lee, M.-H.; Kang, H.-L.; Kim, S.-H.; Ahn, J.-R.; Na, H.; Na, T.; Kim, Y.; Seong, J.-K.; Lee, M.-O., Differential Regulation of Estrogen Receptor Expression in Breast Cancer Cells by Metastasis-Associated Protein 1. *Cancer Res.* **2014,** *74*.

239. Jackson, A. L.; Linsley, P. S., Recognizing and avoiding siRNA off-target effects for target identification and therapeutic application. *Nat. Rev. Drug Discov.* **2010,** *9* (1), 57-67.

240. Ferguson, R. E.; Carroll, H. P.; Harris, A.; Maher, E. R.; Selby, P. J.; Banks, R. E., Housekeeping proteins: A preliminary study illustrating some limitations as useful references in protein expression studies. *PROTEOMICS* **2005,** *5* (2), 566-571.

241. Procaccio, V.; Salazar, G.; Ono, S.; Styers, M. L.; Gearing, M.; Davila, A.; Jimenez, R.; Juncos, J.; Gutekunst, C.-A.; Meroni, G.; Fontanella, B.; Sontag, E.; Sontag, J. M.; Faundez, V.; Wainer, B. H., A Mutation of β-Actin That Alters Depolymerization Dynamics Is Associated with Autosomal Dominant Developmental Malformations, Deafness, and Dystonia. *Am. J. Hum. Genet.* **2006,** *78* (6), 947-960.

242. Berthois, Y.; Katzenellenbogen, J. A.; Katzenellenbogen, B. S., Phenol red in tissue culture media is a weak estrogen: implications concerning the study of estrogen-responsive cells in culture. *Proc. Natl. Acad. Sci.* **1986,** *83* (8), 2496.

Vita

Nguyên Tấn Khánh Lê was born in Biên Hòa, Đồng Nai, Việt Nam on September 07, 1992, and is the middle child of Thống Lê and Diệp Trần. In 2009, she began studying abroad in the United States. She finished senior year in high school at Faith Christian High School in Yuba city, California and obtained High School Diploma in 2010. She enrolled in Yuba Community College from 2010-2012 and transferred to Texas Christian University (TCU) in 2012. She graduated Magna cum Laude with a Bachelor of Science in Biochemistry and Minor in Mathematics from TCU in May 2015. After graduation, she enrolled in Chemistry PhD program at TCU in August 2015 and was supervised by Dr. Jeffery L. Coffer. Her PhD project is about evaluation of biological properties and applications of Silicon nanomaterials.

Abstract

SILICON IN A ONE-DIMENSIONAL POROUS NANOTUBE STRUCTURE AND ITS EVALUATION AS DRUG DELIVERY VECTOR *IN VITRO*

by Nguyen Tan Khanh Le

Department of Chemistry and Biochemistry

Dissertation Advisor: Professor Jeffery L. Coffer

Drug delivery is a promising therapeutic approach to achieve sustainable drug release while minimizing adverse side effects triggered by non-specificity of the free drugs. Among delivery vectors, biodegradable nanomaterials are of utmost interest for minimizing deleterious consequences stemming from long-term carrier accumulation. With regard to inorganic nanomaterials, porous silicon (pSi) is among a few that can degrade and release non-toxic byproducts (i.e. orthosilicic acid), and dissolution kinetics of the materials can readily be controlled via modulating structural morphology as well as surface chemistry.

To date, a great number of pSi-based delivery vectors with intricate designs have been presented to address multiple challenges in therapeutic delivery. Since the shape of the nanocarriers have been shown to influence interactions with multiple biological components, pSi with various geometrical shapes (i.e. discoidal, hemisphere and platelet shapes) have been introduced in recent years, and promising therapeutic efficacy has also been demonstrated in various disease models. Recently, via a sacrificial ZnO template method developed by our group, we have shown that one-dimensional (1D) porous nanotube structure of Si (pSiNTs) with well-

defined shell thickness, inner diameter and length can readily be achieved. Since the materials can degrade in biological media and exert negligible effects to viability of both normal (e.g. human embryonic kidney, HEK 293) and cancer (e.g. HeLa cervical cancer) human cells, it is of great interest to evaluate pSiNTs as potential therapeutic platforms.

Interestingly, we have also demonstrated pSiNTs can also serve as a facile template for facilitating formation of a secondary nanostructure, so called platinum nanocrystals (Pt NCs) with potential anti-cancer properties. Evaluation of *in vitro* anti-cancer activity of this novel nanohybrid revealed the viability of HeLa cells was reduced in a time-dependent manner as a consequence of a "Trojan horse" mechanism, in which a high concentration of Pt NCs are internalized within cells assisted by pSiNTs and subsequently released via dissolution of the nanotube matrix.

In addition, pSiNTs are also evaluated as potential therapeutic delivery vectors for nucleic acids. Preliminary *in vitro* studies suggest the materials can deliver reporter plasmids DNA (circular DNA) encoding green fluorescent proteins (eGFP) into HEK 293 cells. In another study, downregulations of eGFP (in HeLa) and estrogen receptors (ER) (in MCF-7 breast cancer cells) are also demonstrated via delivery of small interfering RNA (siRNAs) targeting eGFP-mRNA (siGFP) and ER-mRNA (siER) by pSiNTs.

All in all, these studies presented herein demonstrate the potential merit of pSiNTs in drug delivery and serve as a foundation for future studies to design pSiNTs-based platforms that can successively address multiple biological barriers encountered upon systemic administration. Such studies expand the library of possible pSi structures in nanomedicine for suitable disease models and associated applications.